MODEL AIDED OBSERVATIONAL STUDY OF PHYSICAL PROCESSES IN THE NORTHWESTERN ARABIAN / PERSIAN GULF IN RESPONSE TO THE SHAMAL WIND EVENT

A Dissertation

by

FAHAD AL SENAFI

Submitted to the Office of Graduate and Professional Studies of
Texas A&M University
in partial fulfillment of the requirements for the degree of

DOCTOR OF PHILOSOPHY

Chair of Committee,	Ayal Anis
Committee Members,	Alejandro Orsi
	Don Conlee
	Rainer Amon
Head of Department,	Debbie Thomas

May 2015

Major Subject: Oceanography

ABSTRACT

In the present study we define a Shamal event as a WNW-N wind with an hourly average speed ≥ 9.85 m/s blowing during at least 3 hours/day. These events have a significant impact on surface heat fluxes (shortwave, longwave, sensible and latent), momentum fluxes, and as a result on vertical water column stratification, currents, and mixing intensities. We examined mixing processes and volume transport in response to Shamal events using observational data (time-series of temperature, dissolved oxygen, light intensity, and currents as well as surface meteorological data) collected over two periods (mid-January to mid-April 2013 and mid-October to mid-January 2014) in the vicinity of Qarooh Island, Kuwait. We further estimated turbulence parameters (Reynolds stresses, eddy diffusivities, TKE, and its dissipation rates) and compared them to two equation turbulence model simulations (k-kl and k-ε) during three Shamal events. The comparison of the measured and simulated turbulence parameters demonstrated satisfactory agreement between the two. Mixing in the bottom boundary layer was mainly controlled by two main forcings. The first forcing was the increase in mixing resulting from the current shear frequency generated by tides. The second was by the Shamal induced convection.

Using time-series of the observational current structure, we show that winds parallel to the coast generated a subsurface volume transport that was perpendicular to the coast causing upwelling / downwelling. The extent of the upwelling / downwelling region was found to be confined in the region near the coast and did not extend to Qarooh Island (24 nm offshore). The thermal structure at Qarooh was mainly influenced by a warm tongue that extended across the Gulf from the SE.

ACKNOWLEDGEMENTS

First and foremost I would like to thank my academic father and mentor, Dr. Ayal Anis, whom to me was more than just an advisor. I especially thank him for making me a better person and a better young scientist. Dr. Anis encouraged me to always strive for excellence and not settle for anything less than perfection. Words cannot express how thankful I am for the last five years and the years to come. I would also like to extend my gratitude to Mrs. Ruthy Anis for pushing me through the toughest times and always making sure I smile. I will never forget the smell of her amazing cooking! Furthermore, I would like to thank the rest of the Anis Family (Idan, Sara, Yoed, Natasha, Dor, Katharine, young Maya and little Noa) for making me part of their family. In addition, I would like to thank all the Anis Family for making the acknowledgment section meaningful and breath-taking to write. You guys have made this section harder to write than any other section in the dissertation. I am also thankful to Dr. Rainer Amon, Dr. Alejandro Orsi, and Dr. Don Conlee for willingly being members of my committee. Their comments and availability whenever needed are truly acknowledged. I also thank Amy Caton for polishing my English.

Thanks to the Kuwaiti squad (Mohammad Al Mukaimi and Tariq Al Rushaid) who have looked after me the last four years and made sure I was taking care of when I needed it the most. I thank them for being there through my roughest times. Thanks to my lab buddies (Zhang Zheng, Arjun Adkhiri, Burkley Pettijohn and Dapeng Lee) and my close friend Joshua Williams for their support.

I thank Mr. Hassan Dashti, Mr. Mohammad Karam, and Mr. Nawaf Hassan of the Kuwait Meteorological Office for providing part of the observational data.

Thanks to the Kuwait Foundation for the Advancement of Sciences for providing all necessary funds for this project. Thanks to the Kuwait Coast Guard senior officers (Mubarak Al Sabah, Omair Al Rushidi, Talal Mwanas, and Ibrahim Al Wiziq) and the young officers (Fahad Al Kandari, Mohammed Al Harbi, Waleed Al Shatti, Saad Al Ajmi, and Abdulaziz Al Majid) for their very much needed field support. A special thanks to Captain Ali Drayi for taking care of the meteorological station on Qarooh Island for 1.5 years. I would also like to thank the scientific divers Abdulla Al Kandari, Raid Al Kandari, Ali Al Hamad, and Bader Al Atar for their outstanding underwater work.

Thanks to the Watan TV channel for making me feel at home late at night when feeling homesick. Thanks specifically to the Malaab Al Watan crew and specially Mr. Mohammad Karam for making me smile every night before bed.

I would like to thank my father (Suliman) and mother (Khalidah) for being patient with my stubbornness and encouraging me all these years and hope this accomplishment makes you proud of me. Thanks to my brother (Abdulaziz), two sisters (Basemah and Sharifah), uncles (Tariq, Faisel and Ali), and aunts (Nadia and Hoda) for lifting my spirits and providing encouragement. Finally, the most important support came from the biggest love of my life, my daughter Lulu (Leemar). Thanks for your patience and love my little Dora the Explorer.

NOMENCLATURE

ADCP	acoustic Doppler current profiler
ADCP-HR	acoustic Doppler current profiler - high resolution
ADV	acoustic Doppler velocimeters
AS	along shore current velocity
ASL	above sea level
B	buoyancy production
BAH	Bahrain International Airport
BBL	bottom boundary layer
CA	Canuto stability function
C_D	drag coefficient
C_{Kol}	Kolmogorov constant
C_p	specific heat of sea water
CPC	Climate Prediction Center
CS	cross shore current velocity
CTD	Conductivity Temperature Depth sensor
D	layer thickness
D_k	sum of the viscous and turbulence transport terms
DO	dissolved oxygen
DU	dust aerosols optical depth at 550 nm
E	energy spectra
ECMWF	European Center for Medium-Range Weather Forecast
ENSO	El Nino Southern Oscillation
GEMS	Global Earth-system Monitoring using Satellite

GHRSST	Group for High Resolution Sea Surface Temperature
GOTM	General Ocean Turbulence Model
Gulf	Arabian/Persian Gulf
Hum	relative humidity
I	shortwave radiation in water
J_q^{bbl}	BBL net heat flux
J_b^0	surface buoyancy flux
J_q^L	latent heat
J_q^{lw}	net longwave radiation
J_q^0	surface net heat flux
J_q^S	sensible heat
J_q^{sw}	net shortwave radiation
JAMSTEC	Japanese Agency for Marine-Earth Science
K	wave number
K_z	vertical eddy diffusivity
KMO	Kuwait Meteorological Office
KSA	Qaisumah, Saudi Arabia
L	Monin-Obukov scale
M_{as}	AS net water volume transport
M_{cs}	CS net water volume transport
MODIS	Moderate Resolution Imaging Spectroradiometer
P	shear production
PSD	power spectrum density
$Pres$	barometric pressure
IOD	Indian Ocean Dipole

K_M	eddy viscosity
K_H	eddy diffusivity
MBE	mean bias error
N	buoyancy frequency
N_s	Nash-Sutcliffe coefficient of efficiency
NAO	North Atlantic Oscillation
NCDC	National Climatic Data Center
NOAA	National Oceanic and Atmospheric Administration
Ri	Richardson number
$RMSE$	root mean square error
S	shear frequency
SBL	surface boundary layer
SST	sea surface temperature
T	water temperature
$Temp$	air temperature
UNEP	United Nations Environmental Programme
V	horizontal current speed
Vis	visibility
WMO	World Meteorological Organization
c_ε	empirical constants used in the $k-\varepsilon$ model
c_l	empirical constants used in the $k-kl$ model
c_μ	CA non-dimensional stability function
f	Coriolis frequency
g	asymmetry factor
g	gravitational acceleration

k	turbulent kinetic energy
l	turbulence length scale
l_z	diagnostic length scale
$lower_{as}$	AS bottom (8 m to seabed) water volume transport
$lower_{cs}$	CS bottom (8 m to seabed) water volume transport
s	salinity
r	mixing ratio
r	Pearsons correlation
u	velocity in the x-direction
u_w	cross shore velocity
u_*	water surface frictional velocity
$upper_{as}$	AS top (surface to 8 m) water volume transport
$upper_{cs}$	CS top (surface to 8 m) water volume transport
v	velocity in the y-direction
v_w	along shore velocity
w	velocity in the z-direction
α_{ei}	mass extinction
α_N	non-dimensional buoyancy number
α_S	non-dimensional shear number
α_T	thermal expansion coefficient
ε	turbulent kinetic energy dissipation rate
κ	Von Karman constant
λ	wavelength
ω	albedo
ρ_a	air density

ρ_b	BBL sea water density
ρ_o	surface sea water density
σ	standard deviation
$\sigma_{k,\varepsilon}$	empirical constants
Γ	mixing efficiency
τ	wind stress
τ_b	Reynolds stress at the BBL
ν	eddy viscosity
ν'	eddy diffusivity

TABLE OF CONTENTS

Page

LIST OF FIGURES

FIGURE Page

LIST OF TABLES

TABLE Page

1. INTRODUCTION

The dissertation herein describes research conducted in the N Arabian / Persian Gulf (hereafter called Gulf), investigating the dominant wind (Shamal and Kous) impacts on the regional hydrodynamics. This work is significant considering the lack of comprehensive observational and numerical studies of wind driven hydrodynamics in the region. None of the previously documented comprehensive observational studies by Emery (1956), Brewer and Dyrssen (1985), Reynolds (1993), and Swift and Bower (2003) investigated the wind driven hydrodynamics of northern part of the Gulf. This work strives to increase knowledge and understanding by evaluating the responses of the Gulf to wind events.

The Gulf is 990 km long, has a maximum width of 370 km, and a surface area of 239,000 km^2 (Emery, 1956). The average depth of the Gulf is about 35 m. The shallow regions ($<$ 20 m deep) are found along the coast of United Arab Emirates, Bahrain, and at the Gulf's head. The deeper regions ($>$ 40 m deep) are found along the Iranian Coast continuing into the Strait of Hormuz, which has a width of 56 km and connects the Gulf with the N Indian Ocean via the Gulf of Oman.

The Gulf is situated between 24 - 30 ^{o}N in the subtropical high pressure region, where most Earth's deserts are located. The descending air commonly produces clear skies and arid conditions with high evaporation rates of 1.3 m/yr (Privett, 1959) and low precipitation rates of 0.03 - 0.11 m/yr (Almazroui, Islam, et al., 2012). The main winds in the Gulf are from the northwest, known as 'Shamal' (literally meaning north), and from the southeast, known as 'Kous'. The Shamal is the most well-known phenomenon in the Gulf and designates strong northwesterly winds (up to 23 m/s) that blow mainly in summer (Rao et al., 2003) and winter (Rao et al., 2001).

Summer and winter Shamals are generated differently. Summer Shamals are a product of two main pressure systems. The first is the stationary summer monsoon low pressure system centered over NW India and extending W to the SE Gulf. The second is the stationary high pressure system over the E Mediterranean with a ridge extending SE towards the NW Gulf. These two systems result in a steep pressure gradient in between, which lies over the NE Gulf and produces the strong summer Shamal winds (Nasrallah et al., 2004). Summer Shamals blow on a continuous base that can last up to weeks (Wilkerson, 1991). Winter Shamals are associated with frontal systems that build up in the E Mediterranean and progress towards the Gulf (Thoppil & Hogan, 2010). Durations of winter Shamals vary between 2 - 5 days, which depend on the speed of the frontal system crossing the region (Ali, 1994).

The dissertation is subdivided into three main chapters which are related through the objective in understanding the winds in the N Gulf and their effects on the regional hydrodynamics.

Chapter 2, titled 'Shamals and climate variability in the Northern Arabian / Persian Gulf from 1973 to 2012', presents key results from analysis of surface meteorological observations collected in the N Gulf (Kuwait, Bahrain and NE Saudi Arabia), which spans a 40-year period (1973 - 2012). The first part of this study analyzes climate variability in the N Gulf and relates them to teleconnection patterns (North Atlantic Oscillation, El Nino Southern Oscillation, and Indian Ocean Dipole). Results of the analysis indicate that during the study period the climate in the region experienced a general trend of increase in temperature (0.8 ^{0}C), decrease in barometric pressure (1 mb), reduction in humidity (6%), and decrease in visibility (9%). Significant correlations were found between the three teleconnection patterns and the meteorological conditions suggesting that seasonal variabilities in air temperature, barometric pressure, and precipitation are closely related to the

teleconnection patterns. The second part of this study examines the 40-year variability of Shamal events (strong NW winds that commonly generate significant dust storms). The data suggests that on average Shamal events occur at a rate of 10 events/year with 85% of the events occurring during the summer and winter. The number of these events have increased in the past 14 years of the study period. These events resulted in abrupt changes in meteorological conditions: an increase in wind speed of 2.7 m/s, a decrease in visibility of 1.7 km, and reduction in humidity of 4.3 %. Seasonal variations in temperature (an increase in temperature during summer of 0.8 ^{0}C, and a decrease of 1.5 ^{0}C during winter) and barometric pressure (a decrease in barometric pressure during summer of 0.6 mb and an increase of 7.8 mb during winter) were observed during Shamal events.

Chapter 3, titled 'Mixing Induced by Winter Shamals in the Northwestern Gulf', examines Shamal events and their effect on the hydrodynamics, mixing processes, and surface net heat fluxes in the NW Gulf using observation data and compares them to numerical simulations using two equation turbulence models ($k-\varepsilon$ and $k-kl$). Observational data collected from mid-Jan to mid-Apr 2013 at two locations in the vicinity of Qarooh Island, Kuwait waters are described. These data constitute the first part of the observational work. The observational data included time-series of temperature, dissolved oxygen, light intensity, and currents as well as surface meteorological data which were used to force the numerical models. Turbulence properties including Reynolds stresses, eddy diffusivities, turbulent kinetic energies, and its dissipation rates computed from a high-resolution Acoustic Doppler Current Profiler were compared to model results using several statistical methods (mean bias error, root mean square error, Nash-Sutcliffe coefficient of efficiency, and Pearson's correlation) to evaluate the performance of the models in simulating mixing induced by Shamal events. The comparison of the measured and simulated turbu-

lence parameters demonstrated satisfactory agreement between the two. Mixing in the bottom boundary layer was mainly controlled by two main forcings. The first forcing was the increase in mixing resulting from the current shear frequency generated by tides. The second was by the Shamal induced convection. Both forcings were well described by the two equation turbulence models ($k-\varepsilon$ and $k-kl$).

Chapter 4, titled 'Wind driven flow dynamics off the coast of Kuwait', investigates wind driven hydrodynamics and their influence on the water properties (temperature and salinity) off the Kuwaiti Coast. Observational meteorological and hydrographical data were collected over two periods (mid-January to mid-April 2013 and mid-October to mid-January 2014) at two locations (Qarooh Island and Sea Island) in Kuwait. Using time-series of the observational current structure, we show that winds parallel to the coast generated a subsurface volume transport that was perpendicular to the coast causing upwelling/downwelling. The upwelling conditions resulted in cooler surface water temperatures. The extent of the upwelling/downwelling region was found to be confined in the region near the coast and did not extend to Qarooh Island (24 nm offshore). The thermal structure at Qarooh was mainly influenced by a warm tongue that extended across the Gulf from the southeast. The progression and regression of the tongue was in response to the general wind direction. Numerical simulations of the thermal structure at Qarooh were run using a 1D model that is based on the two equation k-ε turbulence model. The model was tested in its ability to capture the influence of heat advection following the progression/regression of the warm tongue. Overall, the agreement between the observations and simulations during five wind events were in a good agreement. However, the model overestimated vertical mixing during these events causing mean bias errors up to 0.1 ^{o}C.

2. SHAMALS AND CLIMATE VARIABILITY IN THE NORTHERN ARABIAN / PERSIAN GULF FROM 1973 TO 2012 [1]

2.1 Introduction

Effects of global climate change on the relative increase of surface temperatures (Jones, 2003; Attrill, 2009), droughts (van Vliet et al., 2013), flooding (Mirza, 2002), and intensity of weather events such as monsoons (Naidu et al., 2012) and hurricanes (Arpe & Leroy, 2009) have been increasing steadily. The rise in number of environmental catastrophes due to severe weather events in the last 50 years (Leroy, 2006) has further motivated scientists to better understand the impacts of global climate change on weather systems and phenomena (e.g. IPCC, 2014). In the Arabian/Persian Gulf (hereafter called the Gulf) (Fig. 2.1), a unique weather phenomena occurs throughout the year and has substantial impact on the society, economy, transportation, and the natural environment; it is known as a Shamal event (details of Shamals in section 2.1.2).

In this chapter, our first aim is to describe climate variability in the N Gulf region based on three (Kuwait, Bahrain and NE Saudi Arabia) 40 year long datasets, covering the period from 1973 - 2012, and relate teleconnection patterns (large scale modes of climate variability) to climate variability. To the best of our knowledge, there are no published studies documenting the long term variability of Shamal events as reported in the present study. The only other long term study of Shamals was presented by Rao et al. (2001). The latter study discusses the effects of Shamals on meteorological parameters (barometric pressure, wind speed, humidity, and air

[1] Reprinted with permission from 'Shamals and climate variability in the Northern Arabian / Persian Gulf from 1973 to 2012' by Al Senafi, A. and Anis, A., 2015, International Journal of Climatology, DOI: 10.1002/joc.4302, Copyright(2015) by Wiley.

temperature) and quantifies the frequency of events over a decade (1990 to 2000) at Doha, Qatar.

The second aim is to describe the variability of Shamal events and its effect on various meteorological parameters. Shamal events have a significant impact on surface heat fluxes (shortwave, longwave, sensible and latent), momentum fluxes, and, as a result, on vertical water column stratification, currents, and mixing intensities (Thoppil & Hogan, 2010). The importance of Shamal events in the region and the relation to climate variability have motivated the second aim of the present study and an ongoing oceanographic field experiment.

To set the stage we proceed by describing the climate characteristics in the region focusing on the seasons and the general synoptic conditions during each season (section 2.1.1). This is followed by a definition of Shamal events and related definitions used by other authors (section 2.1.2). Section 2.1.3 summarizes the relevant background information on the three teleconnection patterns that are discussed in the paper. Observational and reanalysis data sources, as well as how various parameters were computed, are described in section 2.2. Section 2.3.1 describes results and discusses the climate variability of the N Gulf region in the past 40 years in relation to teleconnection patterns as well as the meteorological and anthropogenic influences on visibility. The variability of Shamal events from 1973 to 2012 and their influence on meteorological parameters are described in section 2.3.2. A short summary and conclusion is given in section 2.4.

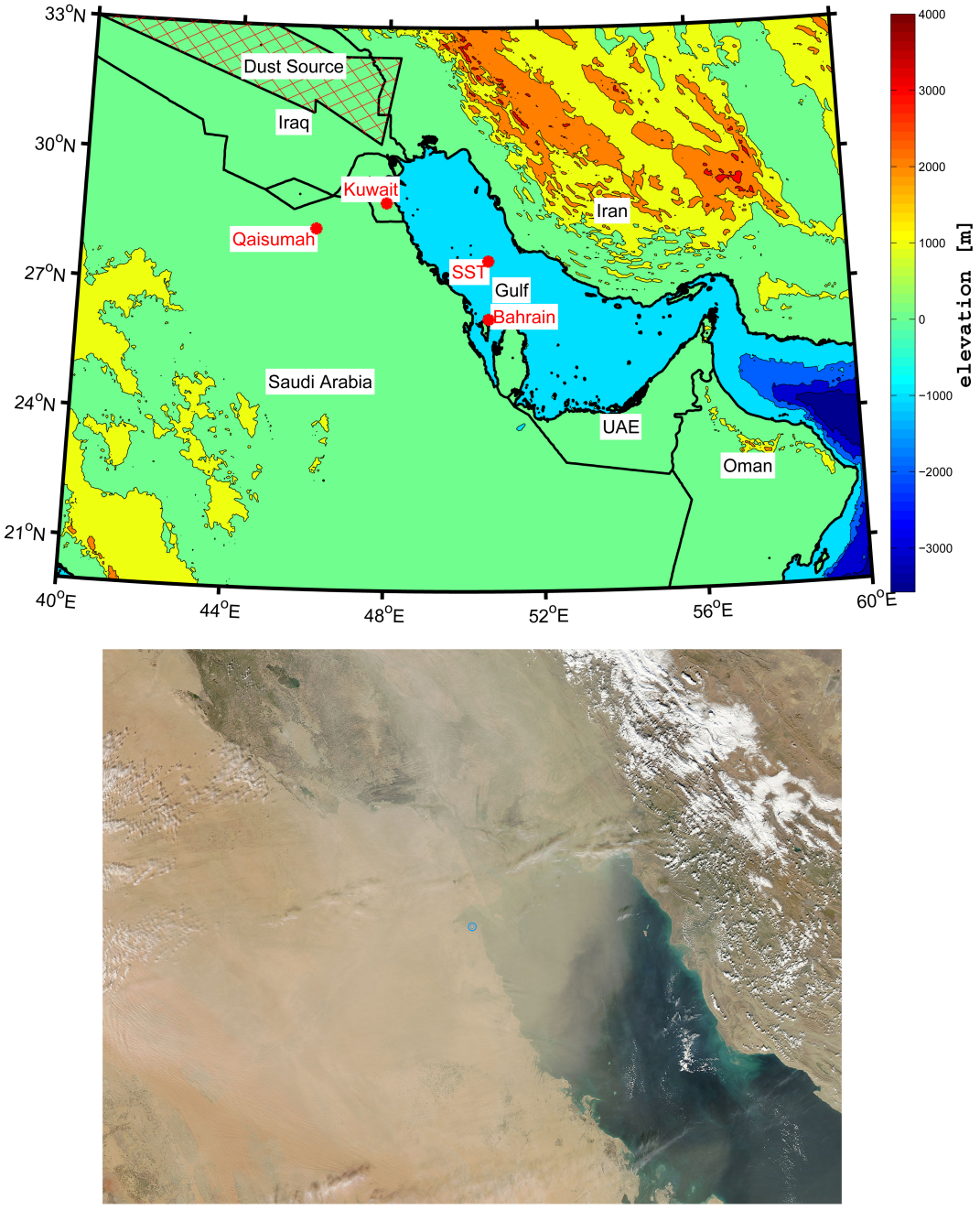

Figure 2.1: (Top) topographic map of the Gulf and the Mesopotamian dust source region (hatched) with the locations of the three meteorological stations and SST used in the study indicated in red circle; (Bottom) true color aqua satellite image of N Gulf dust storm on 8-Jan-2013. The blue circle shows the location of Kuwait City (NASA, 2013).

2.1.1 Climate characteristics

The Gulf is located in the subtropical high pressure region, where the climate is classified as arid. The combination of high evaporation (1.4 m/yr) (Privett, 1959) and low precipitation rates (0.03 - 0.11 m/yr) (Almazroui, Islam, et al., 2012) renders the ecosystem, and the society in particular, vulnerable to global warming effects.

The climate in the Gulf can be divided into two main seasons with two transition periods: summer season (Jun - Sep), fall transition (Oct - Nov), winter season (Dec - Mar), and spring transition (Apr - May) (Walters, 1990). During transition periods, weather is commonly unstable with no well defined weather patterns, and tropical storms are common.

2.1.1.1 summer season

Summer in the N Gulf is influenced by two main pressure systems. The first is the stationary summer monsoon low pressure system centered over NW India and extending W to the SE Gulf. The second is the stationary high pressure system over the E Mediterranean with a ridge extending SE towards the NW Gulf. These two systems produce a steep pressure gradient in between, which lies over the NE Gulf (Nasrallah et al., 2004) and produces strong NW winds (7 - 13 m/s) (Bartlett, 2004) known as summer Shamals (Rao et al., 2003); these may last up to weeks at a time (Wilkerson, 1991). The summer Shamals commonly bring dust or 'blazes' of hot (up to 51 ^{0}C) and dry air called Simoom (literally meaning poison). The adiabatic ascent and descent of air passing the Zagros Mountains in NW Iran from the E results in extreme hot Simoom air. These conditions are common in the first part of summer (May - Jun), when the summer monsoon low is at its lowest.

From our analysis, the combination of high temperatures (average high 41 ^{0}C), zero precipitation, and lower (550 m^3/s) than yearly average (703 m^3/s) river dis-

charge from the Euphrates and Tigris (Janabi, 2010) during this period induces mineral crust formation, as shallow streams on the Mesopotamian floodplain (951,000 km^2) dry out (Partow, 2001). These processes, and the average high wind speeds (5.3 m/s) during this time of the year, contribute to rising dust formation making this period the lowest in visibility (8.1 km). Furthermore, a correlation of -0.83 (95% confidence interval of -0.51, -0.97) between wind speed and visibility suggests that winds are a major controlling factor of visibility throughout the year. Other characteristics of this period are relatively low barometric pressure (1000.4 mb) and low relative humidity (21%) (Fig. 2.2). The second part of summer (Jul - Aug) exhibits weakening, and eventually a breakdown of the summer monsoon low pressure system into two pressure systems centered over the SE Gulf and Iran. The weather in the N Gulf is controlled by the low pressure system in the SE (Nasrallah et al., 2004) bringing about higher humidities (28%), weaker SE winds (4.2 m/s), and a slight increase in average visibility (8.7 km) (Fig. 2.2).

2.1.1.2 winter season

The winter season in the N Gulf is influenced by cold air carried into the region by the quasi-stationary Siberian high pressure system in the E (Crook, 2009). This climate is often interrupted by frontal systems that build up in the E Mediterranean and move SE due to the upper-westerlies (Polar Front Jet). These moisture bearing frontal systems are the primary source of precipitation in the region (Barlow et al., 2005). As the frontal system moves towards the Gulf, the Polar Front Jet behind the frontal system and the Sub-Tropical Jet ahead of it converge, strengthen the system, and generate strong winds at the front. On the passage of the front over the N Gulf, strong NW winds develop with fivefold the initial speed and reach values up to 15 - 20 m/s near the surface at the center of the Gulf (Thoppil & Hogan, 2010); these are

known as winter Shamals. The duration of a winter Shamal event depends on how fast the upper air trough moves through the region, however, typical duration of a Shamal event is 2 - 5 days (Ali, 1994). From our analysis, the general characteristics of this period are: colder temperatures (15 ^{0}C), higher relative humidity (55%), lower wind speed (3.7 m/s), higher barometric pressure (1019 mb), and increased visibility (8.8 km) when compared to other periods throughout the year (Fig. 2.2).

2.1.2 Shamal events

Dominating winds, referred to as Shamal winds, in the region are mainly from the N-NW throughout the year (Fig. 2.3). These winds are sometimes interrupted by rare, more localized SE winds locally known as 'Kaus', lasting from a few hours to a few days (Chao et al., 1992). Shamal winds can intensify well above the average and turn into what are considered 'Shamal events'. Topography of the region also plays a major role in strengthening the wind with the high terrain along the Iranian Coast (Zagros Mountains) and the W coast of Saudi Arabia (Fig. 2.1) producing a 'wind funnel' like structure (Giannakopoulou & Toumi, 2012). Commonly, Shamal events occur in the summer and winter seasons. Shamal events are accompanied by rising dust originating from the Mesopotamian region (Iraq, E Syria and SE Turkey) (Wilkerson, 1991), that can lead to dust storms (Fig. 2.1). The standard definition of dust storms is when visibility falls to $\leq$ 1 km due to dust (Kutiel & Furman, 2003; Goudie, 2009; Zhao et al., 2010; Al-dousari & Al-awadhi, 2012).

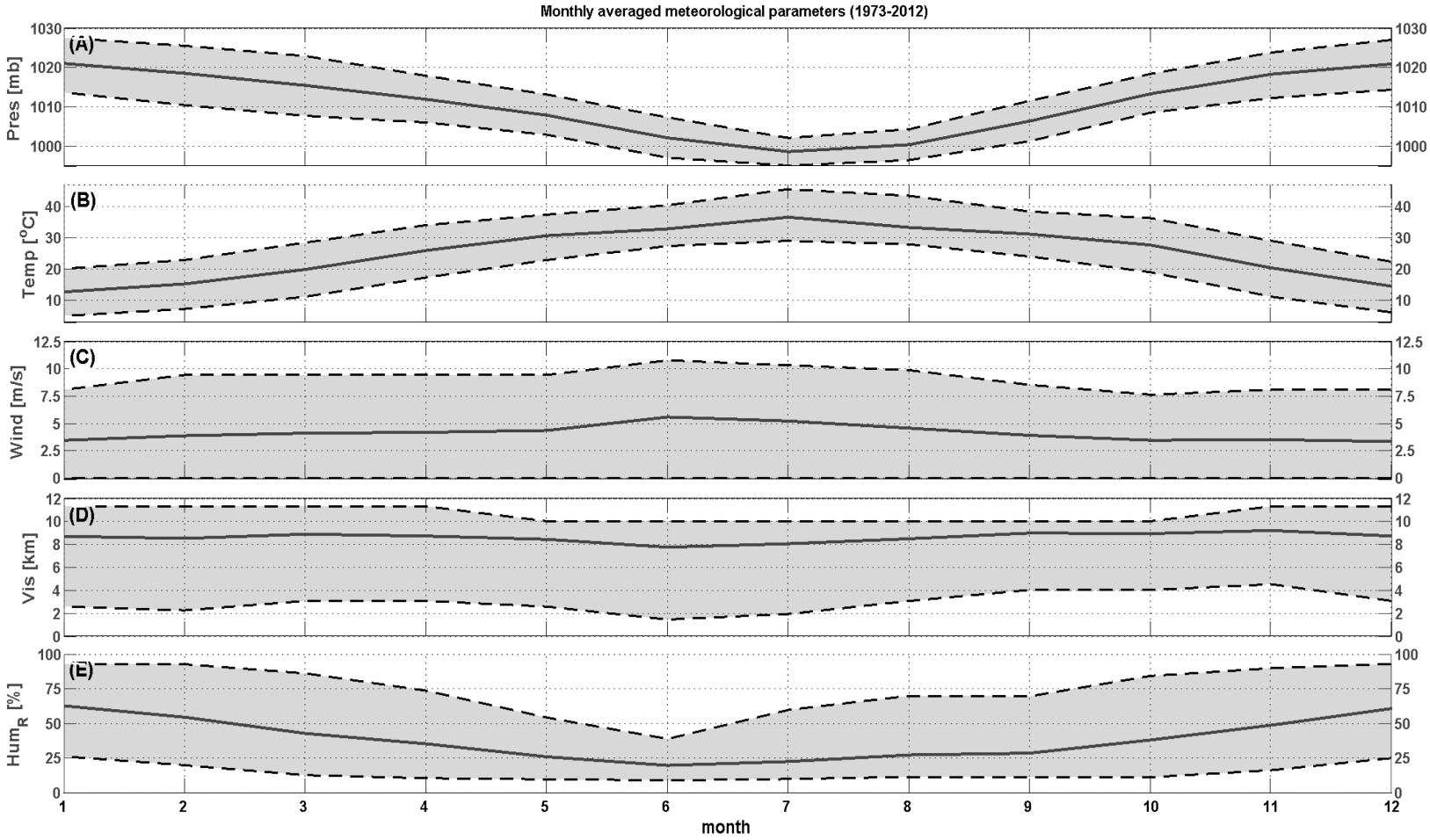

Figure 2.2: Hourly averaged wind speed, direction (from where wind blows), and frequency of occurrence (in %) during mid-Jan to mid-Apr 2013 at Qarooh Island, Kuwait.

Presently there is no agreed upon and clear definition of a Shamal event. Rao et al. (2001) define a Shamal event as a NW-N wind with an average speed ≥ 8.75 m/s during at least 3 hours of the day. Vishkaee et al. (2012) argue that for a Shamal to be characterized as an event five out of the six following conditions must be met: (i) decrease in humidity, (ii) decrease in surface temperature , (iii) increase in barometric pressure , (iv) Northerly winds, (v) wind speed > 6 m/s, and (vi) abrupt drop in visibility rate (3 km/hr). Perrone (1979), the first known author to publish about Shamals, and Walters (1990) subdivide Shamal events into two types. The first is a short duration (24 - 36 hours) event with NW winds ≥ 15.5 m/s, and the second is a long duration (3 - 5 days) event with NW winds up to 25.7 m/s. Next, we describe the operational definition of a Shamal event used in this study.

First, we note that associated with Shamal events is a reduction in visibility either due to rising dust or dust storms (visibility ≤ 1 km; Kutiel & Furman, 2003). We define a wind speed threshold value required to lift dust into the air, based on results of a comprehensive study by the US Army Natick Laboratories on wind borne dust in desert areas of various nature (sand dunes, desert flats, dry wash regions, desert pavements, alluvial fans and playas). The study concluded that a speed of 9.85 m/s is required in a dry wash region to suspend dust into the air (Clements et al., 1963). The Mesopotamian region is such a dry wash region that river streams are dry throughout most of the year. Furthermore, this threshold value is consistent with the range 8.95 - 11.18 m/s (UCAR/COMET, 2010) adopted by the Kuwait Meteorological Office and the United Nations Environment Programme (UNEP, 2013) for rising dust.

The operational definition of a Shamal day in this study is a WNW-N ($287^0 <$ direction $< 360^0$) wind with an hourly average speed ≥ 9.85 m/s blowing during at least 3 hours/day. Two consecutive Shamal days are required for a Shamal to be classified as a Shamal event. Using two consecutive Shamal days to define an

event is similar to the minimum number of days used by Reynolds (1993). Note that the conditions of winds blowing for at least 3 hours/day effectively filters out short duration wind events, such as sea-land breezes. Such breezes occur during more than 70% of the days in a year in this region and have wind speeds $\geq$ 10 m/s for less than 3 hours/day (Eager et al., 2008).

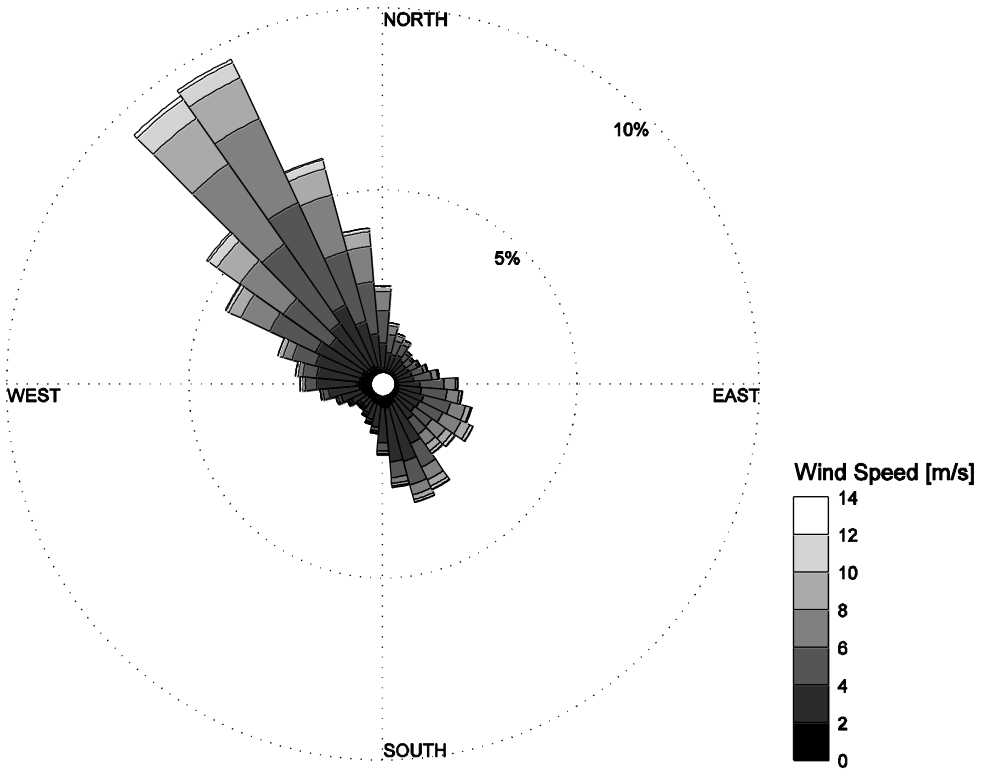

Figure 2.3: Hourly averaged wind speed, direction (from where wind blows) and frequency of occurrence (in %) during 1973 - 2012. Data source: Kuwait Meteorological Office at Kuwait Airport station.

2.1.3 Teleconnection patterns

Various teleconnection patterns have been linked to the interannual variability in sea surface temperature (SST) (Saji et al., 1999), air temperature (Philandras et al., 2013), humidity (Dai, 2006), precipitation (Chang et al., 2000), and also global warming (Cohen & Barlow, 2005) and droughts (Cullen & Demenocal, 2000). In this study we focus on the three teleconnection patterns: North Atlantic Oscillation (NAO), El Nino Southern Oscillation (ENSO), and Indian Ocean Dipole (IOD). These have been found in this study to have an influence on the N Gulf interannual barometric pressure, air temperature and precipitation.

The NAO index is defined as the standardized difference between the sea level barometric pressure of the Azores high (station at Lisbon, Portugal) and Icelandic low (station at Reykjavik, Iceland) (Hurrell, 1995). The NAO peaks in its positive phase during the Northern Hemisphere winter season in response to the increased difference between air-sea temperatures (Cullen & Demenocal, 2000). A positive NAO phase results in a stronger subtropical high over the Azores that extends to the E Mediterranean and deepening of the Icelandic barometric low (Meehl & Loon, 1979). The ENSO index is defined as the area average of SST anomalies cross the E Equatorial Pacific (5^o S - 10^o N, 150^o W - 90^o W). The ENSO starts to develop in its positive phase during the months of Mar - Jun producing warmer SST's along the central Pacific Ocean as the trade winds weaken and tropical convection shifts E (Torrence & Webster, 1999). The shift of tropical convection and warming of the central Pacific Ocean SST causes disturbances to the Asian summer monsoon (Soman & Slingo, 1997), which controls the N Gulf summer season climate (details in section 2.1.1). The IOD index is the standardized difference in SST between the W Indian Ocean (5^o S - 10^o N, 50^o E - 70^o E) and E Indian Ocean (10^o S - 0^o S, 90^o

E - 110^o E) (Arun et al., 2005). The change in trade winds direction from westerlies to easterlies produces warmer SST's in the W Indian Ocean and cooler SST's in the E Indian Ocean, which similar to ENSO, also effects the Asian summer monsoon (Saji & Yamagata, 2003). The IOD starts to develop in its positive phase during the months of May - Jun (Saji et al., 1999).

2.2 Methods

2.2.1 Data source

The observational dataset includes available hourly meteorological data of wind speed (Vaisala WS425 Ultrasonic), visibility (Vaisala FD12), barometric pressure (Vaisala PRB 100), and relative humidity (Vaisala HMP45D) and air temperature (Vaisala HMP45A) mounted in a radiation shield (Vaisala DTR503A) from 1973 to 2012 at the Kuwait Airport (29.242^0 N, 47.972^0 E, elevation 45 m; Fig. 2.1), obtained from the Kuwait Meteorological Office (KMO). The sensors were set to take measurements once a minute and averaged and logged every 10 minutes. The 10 minutes data were then averaged over an hour. There were no major gaps in the dataset except from Aug/1990 to Jul/1991 due to the 1st Gulf War. The study was limited to 1973 as no observational hourly data prior to 1973 in the region was available. Furthermore, this dataset is unique since, to the best of our knowledge, no other dataset in the region has similar temporal resolution and detail. From this dataset, the variability in meteorological parameters over 40 years were estimated, as well as occurrence frequency of Shamal events. Other observational hourly datasets of temperature and barometric pressure at Qaisumah, Saudi Arabia (KSA) (28.335^0 N, 46.125^0 E, elevation 357 m; Fig. 2.1) and Bahrain International Airport (BAH) (26.271^0 N, 50.634^0 E, elevation 1 m; Fig. 2.1) available from the National Oceanic and Atmospheric Administration - National Climatic Data Center (NOAA-NCDC) from 1973 to 2012

were used in addition to the KMO data to analyze climate variability. Due to the very limited temporal resolution, continuity, and quality of precipitation data at the BAH and KSA stations, only the KMO precipitation data was used for analysis.

2.2.2 Climate variability

Yearly averages (1973 - 2012) and 95% confidence intervals of observed meteorological parameters were computed using the bootstrap method (Efron & Tibshirani, 1986). A linear fit to the yearly averaged data (e.g. Yosef et al., 2009; Philandras et al., 2013) was computed using the robust regression method (Huber & Ronchetti, 2009). From the fitted slope, changes in meteorological parameters, as well as changes in Shamal event occurrence frequency over the study period were estimated.

The effect of teleconnection patterns on the Gulf were generally more pronounced seasonally (winter: Dec - Mar and summer: Jun - Sep) than annually (more details in 2.1.3). Therefore, we focus on interannual seasonal variability in meteorological parameters to quantify the variability of a specific season in reference to the 40 year average. We define

$$interannual\ seasonal\ variability = y - \overline{y} \quad , \tag{2.1}$$

where y is a seasonal average of an observational meteorological parameter (e.g. air temperature) and its 40 year seasonal average is noted with an overline. The interannual seasonal variability was then standardized (Eq. 2.2), in a similar approach to that taken by Philandras et al. (2013) and Saji et al. (1999), who analyzed the influence of teleconnection patterns on meteorological parameters over the E Mediterranean and Indian Ocean, respectively. Thus

$$z = \frac{y - \overline{y}}{\sigma} \quad , \tag{2.2}$$

where z is the standardized interannual seasonal anomaly of an observational meteorological parameter y, and σ is the 40 year standard deviation. Spatial anomalies were computed from NCEP reanalysis (for details see Kanamitsu et al., 2002) meteorological data at 6 hour intervals and global coverage at a resolution of 1.875^0. Spatial anomaly charts of meteorological parameters were constructed to assess the linkage between climate variability and teleconnection patterns.

To investigate the relation between the teleconnection patterns and meteorological anomalies, two goodness of fit statistics were computed. The first method is the Nash-Sutcliffe coefficient of efficiency (N_s; Nash & Sutcliffe, 1970) that determines how good the plot of the standardized teleconnection patterns indices versus the standardized meteorological anomalies fits the 1:1 line:

$$N_s = 1 - \frac{\sum_{i=1}^{n}(z_i - x_i)^2}{\sum_{i=1}^{n}(z_i - \overline{z})^2} \quad , \tag{2.3}$$

where x represents the standardized teleconnection pattern seasonal index, i is the yearly seasonal data point index, and n is the total number of years. The values of N_s range between -∞ to +1, with 1 indicating a perfect relation, $N_s = 0$ indicating that the standardized meteorological seasonal anomaly is only as good as the standardized teleconnection pattern seasonal index average and $0 > N_s$ indicating a weak relation (Elsanabary & Gan, 2013). Generally, values between 0 and 1 are viewed as acceptable (Gupta & Kling, 2011). The second method used is the Pearson correlation defined as:

$$r = \sum_{i=1}^{n} \frac{(x_i - \overline{x})(z_i - \overline{z})}{(n-1)\sigma_x \sigma_z} \quad , \tag{2.4}$$

where the value of r ranges between -1 and 1, with $r = 1$ and $r =$ -1 indicating a perfect relation, and $r = 0$ indicating a poor relation. This method assesses the degree

of collinearity between the standardized teleconnection patterns seasonal indices and the standardized meteorological parameter seasonal anomalies. Furthermore, this method was tested for significance (P_{value}) using the student's t-test with a critical value of 0.05 (Press et al., 2007). Pearson correlations were used by Donat et al. (2014) when linking teleconnection patterns to the extreme changes in temperature and precipitation in the Middle-East.

For the indices of NAO, ENSO, and IOD, we used the monthly available data provided by NOAA Climate Prediction Center (CPC) and the Japanese Agency for Marine-Earth Science and Technology (JAMSTEC) from 1973 - 2010. These data are based on the standardized (1970 - 2010 base period) latitudinal sea level pressure differences for NAO (Barnston & Livezey, 1987), and on the standardized longitudinal SST differences for ENSO and IOD (Saji et al., 1999) (see further details in 2.1.3). These three (NAO, ENSO, and IOD) monthly indices have been further averaged over 3 months (seasonal average) to be consistent with our observational datasets (KMO, KSA, and BAH). This is similar to the approach used by Donat et al. (2014) and Elsanabary and Gan (2013) to examine the interannual seasonal variability of temperature and precipitation. Furthermore, the longest spatial available dust dataset for the study region was obtained from GEMS (Global and regional Earth-system Monitoring using Satellite and in-situ data; Hollingsworth et al., 2008) developed by ECMWF-IFS (European Centre for Medium-Range Weather Forecasts-Integrated Forecast System; Benedetti et al., 2009) between 2003 to 2012 in the form of Dust Aerosol Optical Depth at 550 nm (DU). This data is derived from the reanalysis of four-dimensional variational (4D-Var) aerosol assimilation using a combination of satellite-based (Moderate Resolution Imaging Spectroradiometer-MODIS) and background meteorological data such as wind at 10 m to forecast the dust distribution and trajectory (Morcrette et al., 2008). The observational DU from MODIS is de-

termined using the dusts specific physical and optical properties (mass extinction, α_{ei}, single scattering albedo, ω, and asymmetry factor, g; Table 2.1) at 550 nm wavelength, λ, (Reddy, 2005) by

$$DU = \sum_{i=1}^{n} \int_{Pres}^{0} \alpha_{ei}(\lambda, Hum(Pres)) r_i(Pres) \frac{dp}{g} \quad , \tag{2.5}$$

where n is the number of dust aerosols, $Pres$ is the surface pressure, Hum is the relative humidity, r is the mass mixing ratio and dp is the model layer pressure (Benedetti et al., 2009). The 10 year DU spatial dataset was used to compare the variability of the observed visibility data and to investigate the controlling factors (anthropogenic activity and meteorological parameters) that may have led to fluctuations in the interannual variability of DU.

Table 2.1: Dust aerosol optical properties at 550 nm wavelength (Benedetti et al., 2009).

Dust Type	α_{ei} $[\mathrm{m^2 g^{-1}}]$	ω	g
$0.03 - 0.55\mu m$	2.6321	0.9896	0.7300
$0.66 - 0.90\mu m$	0.8679	0.9672	0.5912
$0.90 - 20.0\mu m$	0.4274	0.9441	0.7788

2.2.3 Metrics of Shamal effects

The influence of Shamal events on meteorological parameters during 1973 - 2012 is determined by quantifying both average and extreme parameter values of the difference between preShamal (a day before Shamal) to Shamal event conditions. These are summarized in the following equations and are based on wind speed (Eq. 2.6 and 2.7), visibility (Eq. 2.8 and 2.9), air temperature (Eq. 2.10 and 2.11), relative humidity (Eq. 2.12 and 2.13), and barometric pressure (Eq. 2.14 and 2.15):

$$\Delta Wind_{avr} = Shamal\,average\,Wind - preShamal\,average\,Wind \quad , \tag{2.6}$$

$$\Delta Wind_{max} = Shamal\,hourly\,max\,Wind - preShamal\,hourly\,max\,Wind \quad , \tag{2.7}$$

$$\Delta Vis_{avr} = Shamal\,average\,Vis - preShamal\,average\,Vis \quad , \tag{2.8}$$

$$\Delta Vis_{min} = Shamal\,hourly\,min\,Vis - preShamal\,hourly\,min\,Vis \quad , \tag{2.9}$$

$$\Delta Temp_{avr} = Shamal\,average\,Temp - preShamal\,average\,Temp \quad , \tag{2.10}$$

$$\Delta Temp_{max} = Shamal\,hourly\,max\,Temp - preShamal\,hourly\,max\,Temp \quad , \tag{2.11}$$

$$\Delta Hum_{r\ avr} = Shamal\,average\,Hum - preShamal\,average\,Hum \quad , \tag{2.12}$$

$$\Delta Hum_{r\ max} = Shamal\,hourly\,max\,Hum - preShamal\,hourly\,max\,Hum \quad , \tag{2.13}$$

$$\Delta Pres_{avr} = Shamal\,average\,Pres - preShamal\,average\,Pres \quad , \tag{2.14}$$

$$\Delta Pres_{max} = Shamal\,hourly\,max\,Pres - preShamal\,hourly\,max\,Pres \quad , \tag{2.15}$$

where $Wind$ is wind speed, Vis is visibility and $Temp$ is air temperature.

2.3 Results and Discussion

2.3.1 Climate variability in the N Gulf (1973 - 2012)

The increase of carbon dioxide (from 280 to 390ppm; Blasing, 2013) and other greenhouse gases due to the burning of fossil fuels since the industrial revolution (1750) has led to a pronounced increase in global temperature (Preining, 1992) of 0.4 - 0.8 ^{0}C during the past century (EPA, 2012). Our analysis suggests that the temperature in the N Gulf has increased by 0.8 ^{0}C just in the past 40 years and may continue to increase at a rate of 0.02 ^{0}C/yr (0.01, 0.04) if we assume a similar trend of increase in air temperature (Fig. 2.4A). This is lower compared to the average 0.06 ^{0}C/yr across Saudi Arabia (27 observational sites) reported by Almazroui, Nazrul Islam, et al. (2012) between 1979 and 2009. Moreover, a previous study by Nasrallah and Balling (1995) reported large variations (-0.09 to 0.07 ^{0}C/decade) in temperature trends at three locations in Saudi Arabia (30^o N, 40^o E; 25^o N, 50^o E; 20^o N, 40^o E), using an updated version of gridded points created by Jones et al. (1986) between 1950 - 1990. Nasrallah and Balling (1995) linked 30% (correlation of 0.55) of the temperature trend variances in Saudi Arabia as well as the Middle East to anthropogenic induced desertification. Air surface temperature plays a major role in influencing other meteorological parameters such as humidity and barometric pressure. Although air at higher temperatures can contain more water vapor (Hansen et al., 1984), observed humidities were not higher in the N Gulf region. The relative humidity level has dropped by 6% between 1973 and 2012 (Fig. 2.4B), in agreement with climate models that show a similar decrease in humidity in the Middle East as a result of global warming (Dai, 2006). Another meteorological parameter impacted by global warming in the N Gulf is barometric pressure. The increase of land and SST's following the increase in near surface air temperature results in increased

loss of longwave (infrared) radiation from the land and sea bodies, contributing to a reduction in barometric pressure by an overall of 0.8 mb (0.02 mb/yr) between 1973 and 2012 (Fig. 2.4C). The decrease in barometric pressure reported in this study is similar to that reported by El Kenawy et al. (2012), whose study suggested a decrease of 0.02 mb/yr between 1920 to 2006 for the W Mediterranean region. Barometric pressure and surface air temperature were found to fluctuate throughout the study period in response to the NAO and ENSO teleconnection patterns. A previous study by Cullen and Demenocal (2000), used monthly air temperature and precipitation observations at 770 stations, extending from the Iberian Peninsula to the Middle East (20^o N - 50^o N and 10^o W - 50^o E), to construct yearly winter season temperature and precipitation anomaly indices from 1930 to 1995 and link these to the NAO index. Their study suggests that the effect of a positive NAO phase during winter extends to the Mesopotamian region causing cooler temperatures by 18% (correlations of -0.42) and a reduction in precipitation of 27% (correlations of -0.52). Similarly, a study by Donat et al. (2014) used 61 observational stations measuring daily air temperature and precipitation across the Arab region; including two of the three stations used in the present study (KIA and BAH), which suggests a correlation of -0.2 between winter air temperatures and NAO for the N Gulf region from 1961 to 2010. These conditions are a result of the Azores High and Icelandic Low shifting the moisture bearing Jet Stream poleward and bringing wetter and warmer conditions to N Europe and cooler and drier conditions to the Mediterranean and Mesopotamian regions (Chang et al., 2000; Cullen & Demenocal, 2000), thus providing a possible link of precipitation, air temperature and barometric pressure in the Mesopotamian region to the NAO. The observational results reported here for the winter seasons of 1973 - 2012 in the N Gulf are consistent with those of Cullen and Demenocal (2000) and Donat et al. (2014) for the Mesopotamian region and suggests that the win-

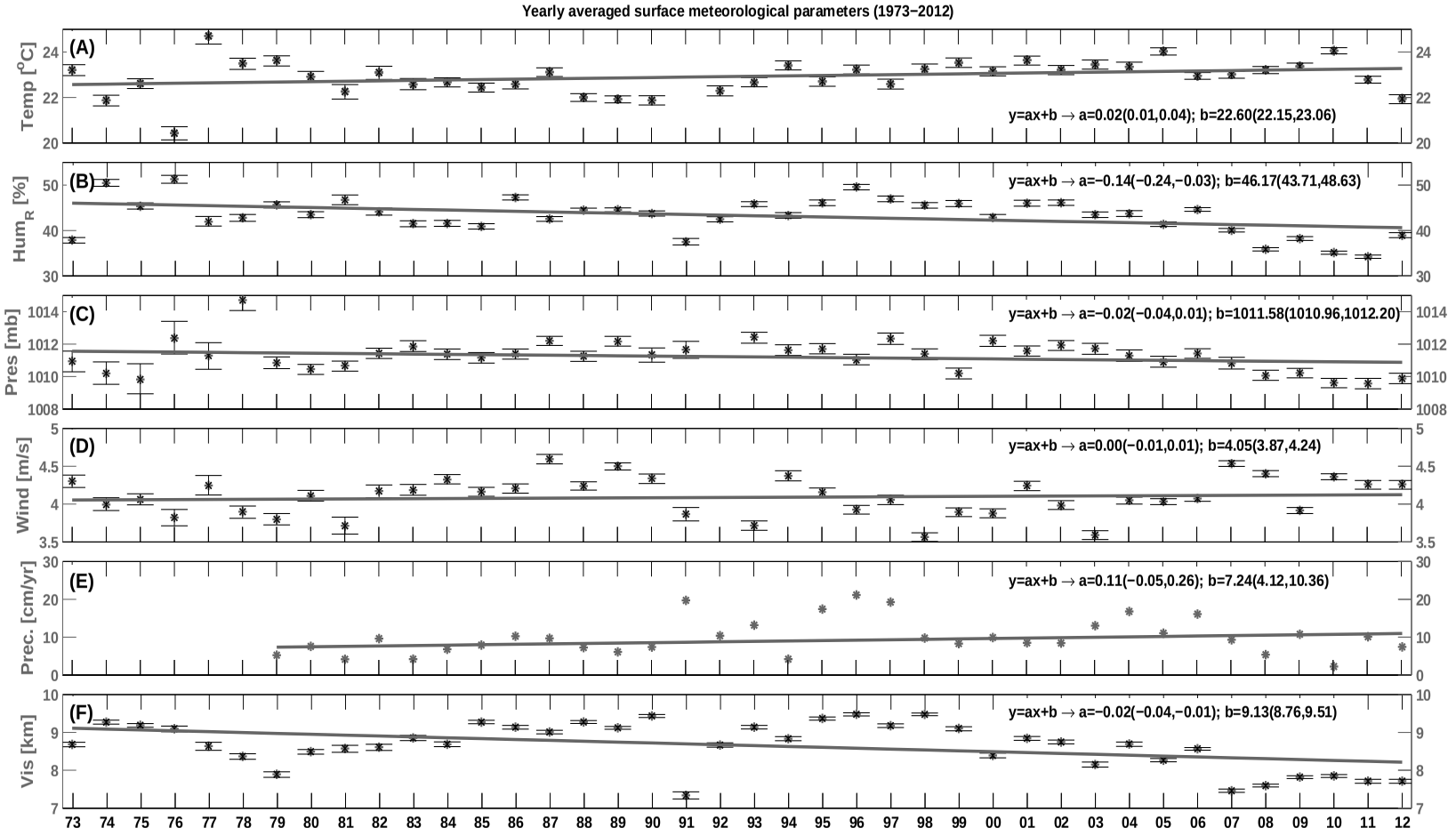

Figure 2.4: Yearly averaged surface meteorological parameters observed at KMO from 1973 to 2012 and their 95% bootstrap confidence interval error bars. A linear fit to the data, using robust regression is represented by the solid lines: (A) air temperature, (B) relative humidity, (C) barometric pressure, (D) wind speed, (E) precipitation and (F) visibility.

ter barometric pressure anomalies (Fig. 2.5A) and air temperature anomalies (Fig. 2.5E) in the N Gulf are impacted by the NAO with positive N_s values and significant ($p_{value} < 0.05$) correlation values ranging from 0.34 to 0.37 and -0.42 to -0.46, respectively (Fig. 2.6A). The impact of strong (index ≥ 1) NAO positive periods (1978/79, 1986/87 and 1993/94; Fig. 2.5A and E) have caused relative higher winter barometric pressure and cooler surface air temperatures by up to 2.8 mb (0.4%) and -2.4 ^{0}C (-22%), respectively (Table 2.2). Furthermore, the strong NAO positive index (≥ 1) periods were examined spatially for winters 1978/79, 1986/87 and 1993/94 barometric pressure anomalies and temperature anomalies (Fig. 2.5B-D and F-H). The barometric spatial anomaly results show a positive anomaly extending from NE Africa towards the N Gulf in winters of 1978/79 and 1993/94 (Fig. 2.5B and D) and at times covering all the Gulf in winter 1986/87 (Fig. 2.5C). The spatial air temperature anomalies (Fig. 2.5 F-H) followed a similar pattern to that of barometric pressure anomalies with negative anomalies extending from NE Africa towards the N Gulf. An exception was during the 1978/79 winter when the temperature anomaly at BAH and KSA was $\sim$0 compared to the negative anomaly of -1 at KMO (Fig. 2.5E). This may be explained by the negative air temperature anomaly centered over the Gulf (indicated by the red arrow Fig. 2.5F) and not extending to Kuwait. Moreover, possible connection between NAO and SST was quantitatively explored using the SST anomalies computed from the NCEP SST reanalysis data for the period 1979 to 2010 at a location centered in the N Gulf region (Fig. 2.1). During positive NAO phases SST anomalies were found to decrease, following a similar pattern to that of air temperature (Fig. 2.5E). Further analysis revealed a consistent lag of SST behind NAO, suggesting a delayed response of SST to NAO of about one month compared to the relatively immediate response of air temperature. The influence of the NAO on the variability in precipitation reported by Cullen and Demenocal (2000) has not

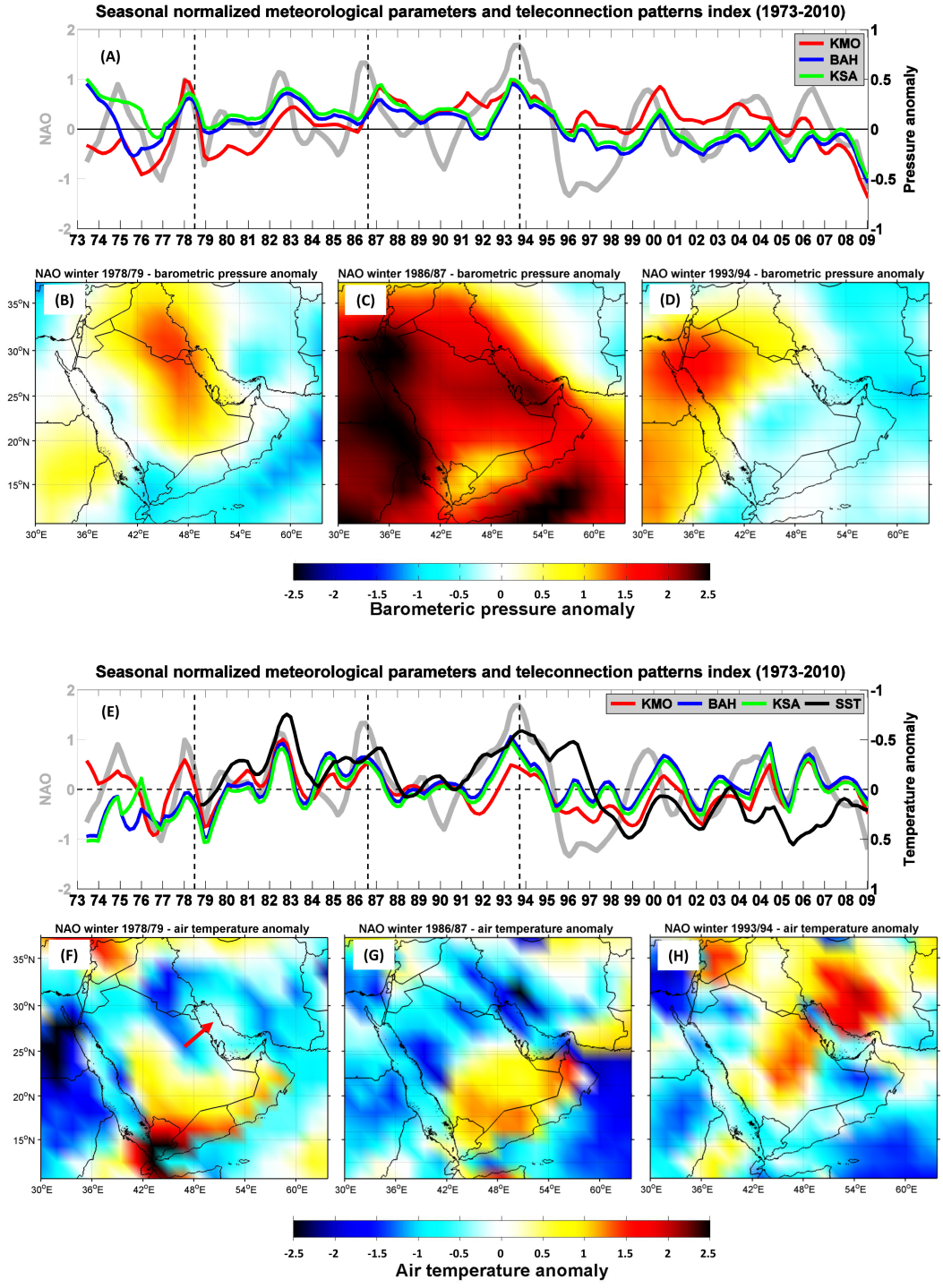

Figure 2.5: (A) Winter averaged NAO index (grey) and winter barometric pressure anomalies (Eq. 2.2; KMO-red; BAH-blue, KSA-green). Vertical broken lines indicate strong (index ≥ 1) positive NAO phases. (B-D) Winter barometric pressure anomalies computed as in Eq. 2.2 using NCEP barometric pressure data. (E-H) are similar to A-D but for air temperature anomalies.

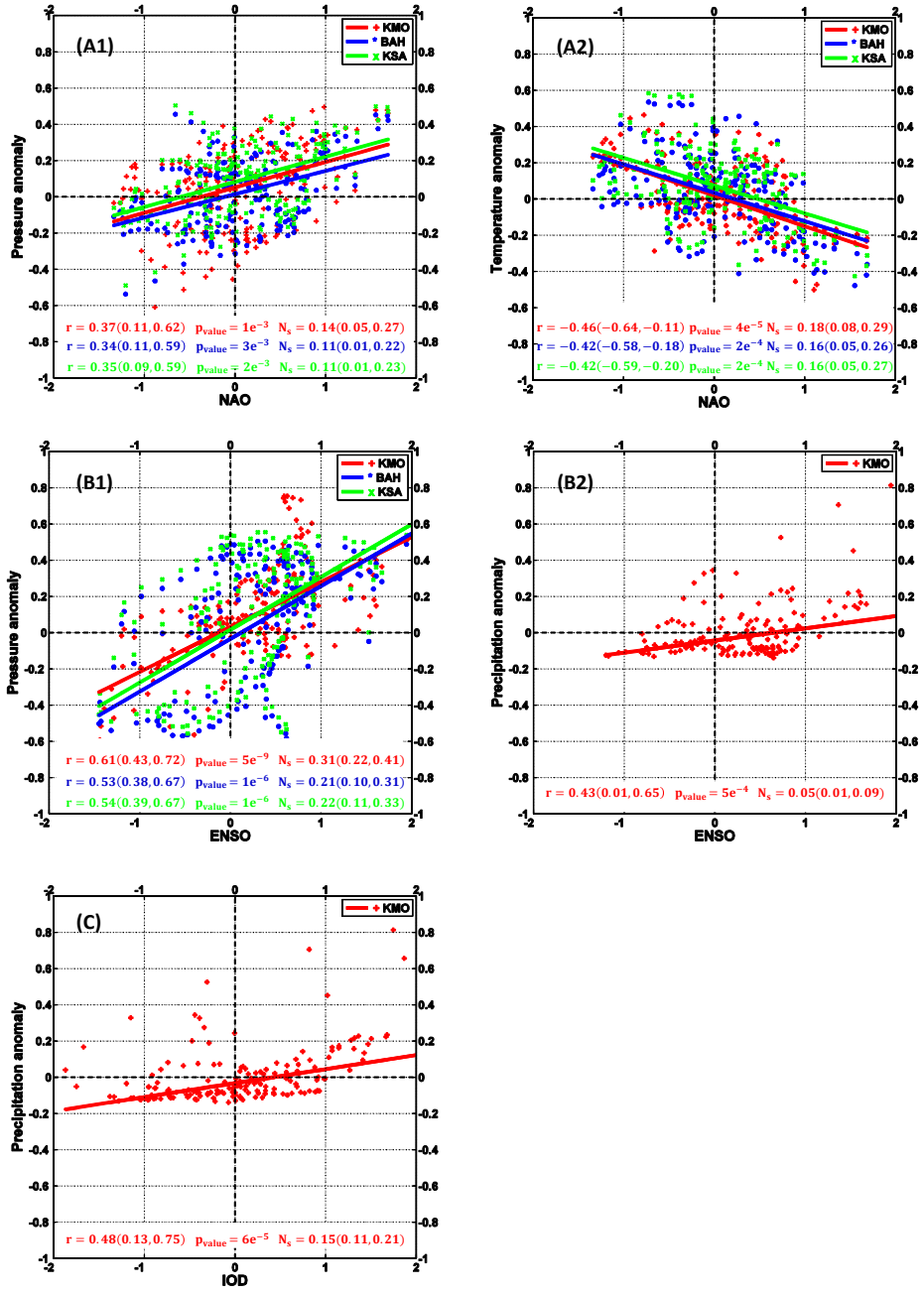

Figure 2.6: Seasonal averaged teleconnection patterns indices versus meteorological parameters anomalies (1973 - 2012) scatter plots at KMO (red), BAH (blue) and KSA (green), with their respective correlations, p-values and Nash-Sutcliffe coefficient. A linear fit to the data, using robust regression is represented by the solid lines: (A1) NAO index versus barometric pressure anomaly observations, (A2) NAO index versus air temperature anomaly observations, (B1) ENSO index versus barometric pressure anomaly observations, (B2) ENSO index versus precipitation anomaly observations, and (C) IOD index versus precipitation anomaly observations.

Table 2.2: Interannual seasonal variability of meteorological parameters (Eq. 2.1) at the KMO during teleconnection pattern events. 95% bootstrap confidence intervals are given in parentheses.

	Event Year	ΔPressure [mb]	ΔTemperature [^{0}C]	Tele. Index
NAO	1978/79 Winter	2.8 (1.8,3.8)	-2.4 (-3.2,-1.5)	1.0
	1986/87 Winter	1.4 (1.1,1.6)	-1.5 (-1.7,-0.9)	1.1
	1993/94 Winter	2.3 (1.7,2.9)	-1.6 (-2.0,-1.3)	1.7
		ΔPressure [mb]	ΔPrecipitation [cm/month]	
ENSO	1982 Summer	0.6 (0.6,0.7)	1.3 (1.2,1.6)	1.6
	1987 Summer	1.1 (1.0,1.2)	0.9 (0.8,1.2)	1.7
	1997 Summer	1.6 (1.5,2.1)	4.5 (4.3,5.3)	2.3
		ΔPrecipitation [cm/month]		
IOD	1982 Summer	1.3 (1.2,1.6)		1.4
	1994 Summer	1.4 (1.1,1.6)		1.7
	1997 Summer	4.5 (4.3,5.3)		2.3

been observed in our KMO dataset.

Similar to the NAO, ENSO is another large scale mode of climate variability (Jin, 2003). Of particular importance to the present study region is the weakening of the summer monsoon during positive phase ENSO events. During these events, the tropical convection shifts eastward causing a weaker low pressure monsoon over India, which in turn induces a disturbance to the Jet Stream (Shakula & Paolino, 1983; Joseph et al., 1994; Webster, 1995; Webster et al., 1998). It is of interest to note that the impact of ENSO on the summer monsoon (barometric pressure, air temperature and precipitation) was first introduced by Walker and Bliss (1937). The disturbance to the low pressure summer monsoon during the three analyzed ENSO events (1982, 1987, 1997; Table 2.2) was observed to result in higher barometric pressure (up to 1.6 mb (0.02%) in summer 1997; Table 2.2) and an increase in precipitation (up to 4.5 cm/month (31%) in summer 1997; Table 2.2). The increase in their respective anomalies is shown in Figures 2.7A and E. Correlation values between barometric pressure anomalies and ENSO index ranged between 0.53 to 0.61 and the correlation value of precipitation anomalies and ENSO index was 0.43, with positive N_s values suggesting a significant ($p_{value} < 0.05$) relation between these parameters and the ENSO event (Fig. 2.6B). Spatial anomaly results for barometric pressure during ENSO events show positive anomalies extending from the Arabian Sea and W India towards the Gulf (Fig. 2.7B-D). Spatial anomaly results for precipitation (Fig. 2.7F-H) show a scatter of positive anomalies over the Gulf region covering Kuwait, United Arab Emirates, Oman, and parts of Saudi Arabia and Qatar. Similar conclusions for the influence of ENSO on the increase of regional precipitation have been observed by Kumar and Ouarda (2014) and Arun et al. (2005). Both studies found correlations > 0.4 between precipitation values and ENSO index using monthly observations at six sites located in the United Arab Emirates between the years 1981

- 2011 (Kumar & Ouarda, 2014) and NCEP reanalysis data across Saudi Arabia between 1958 - 2012 (Arun et al., 2005). The increased precipitation due to ENSO appears to be in contrast to the observations of Donat et al. (2014) for the N Gulf, whose study suggests a weak relation between winter precipitation and ENSO for the period of 1961 to 2010. We suggest that the effect of ENSO on the regional precipitation is a result of its influence on the summer monsoon, thus, influencing the N Gulf during summer when the monsoon reaches its highest latitude and therefore is closest to the N Gulf (see further details in 2.1.1). Furthermore, the largest summer precipitation (4.5 cm/month, 31%) in the N Gulf was observed in 1997, when the strongest ENSO event was recorded (Jin, 2003). During 1997 the IOD was also in a strong (index ≥ 1) positive phase. During a positive IOD event the E Indian Ocean becomes relatively colder, while the W Indian Ocean becomes relatively warmer. These unusual temperature conditions suppress atmospheric convection in the E Indian Ocean, while enhancing atmospheric convection in the W Indian Ocean. This impacts the Indian summer monsoon low pressure system (Saji et al., 1999) causing an increase in precipitation over the W Indian Ocean region (Goes et al., 2005). An increase in precipitation was observed during the 1982, 1994 and 1997 summer events (Fig. 2.8A-D; Table 2.2). Furthermore, the correlation between precipitation and the IOD index was 0.48, with a positive N_s value suggesting a significant ($p_{value} < 0.05$) relation between the two (Fig. 2.6C). Similarly, a study by Webster et al. (1999) suggests a strong correlation (0.62) between E African precipitation and the IOD, based on NCEP reanalysis SST and upward longwave radiation (as a proxy for precipitation) for 1997 - 1998 across the Indian Ocean, when compared to 40 year observational climate variability in the region. Based on these results, Webster et al. (1999) suggests that during IOD events the precipitation over the W Indian Ocean region is above average while below average over the E Indian Ocean region.

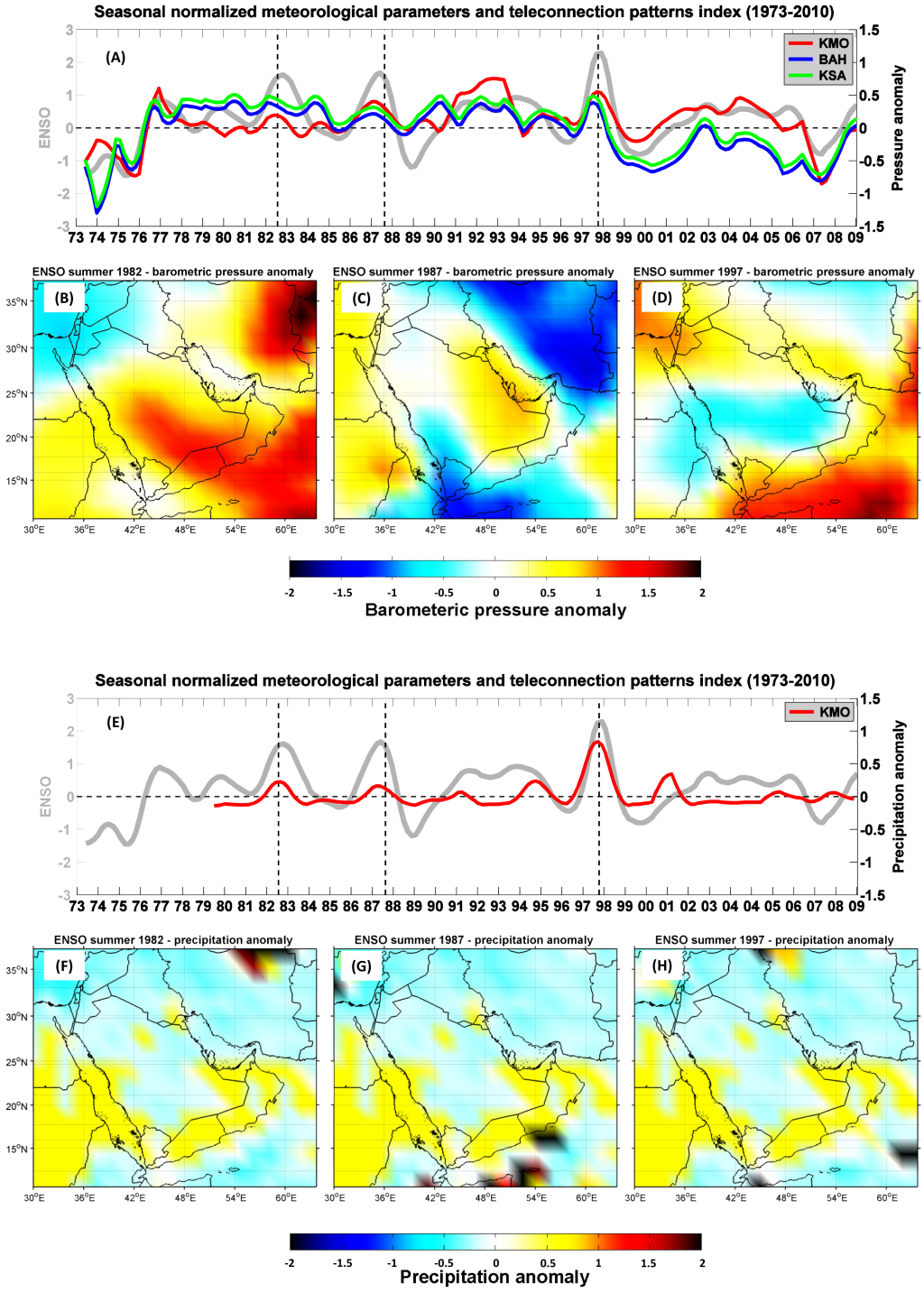

Figure 2.7: (A) Summer averaged ENSO index (grey) and summer barometric pressure anomalies (Eq. 2.2; KMO-red; BAH-blue, KSA-green). Vertical broken lines indicate strong (index ≥ 1) positive ENSO phases. (B-D) Summer barometric pressure anomalies computed as in Eq. 2.2 using NCEP barometric pressure data. (E-H) are similar to A-D but for precipitation anomalies.

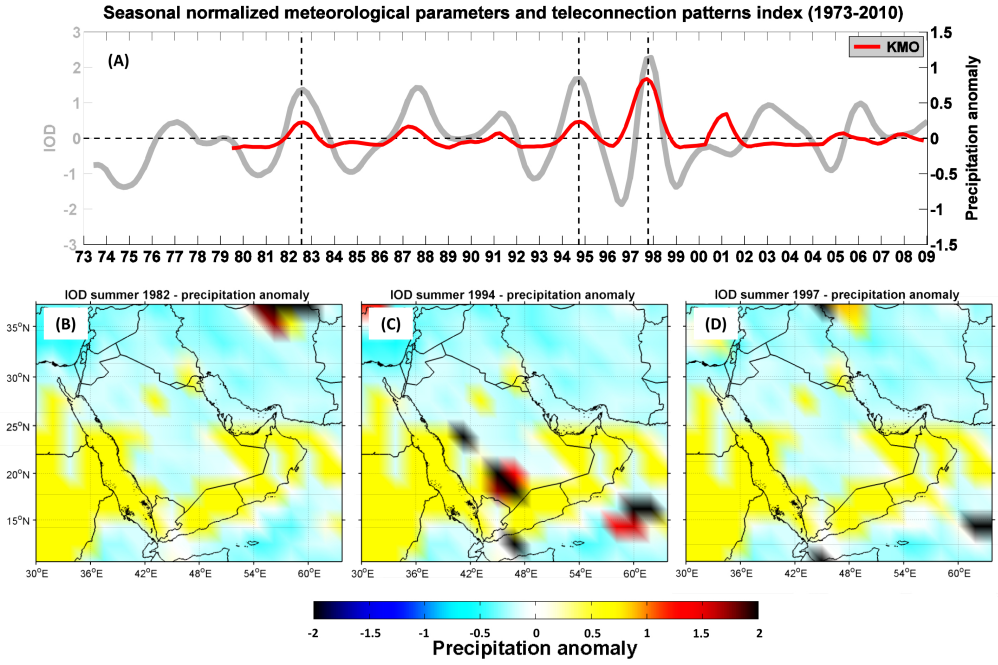

Figure 2.8: (A) Summer averaged IOD index (grey) and summer precipitation anomalies (Eq. 2.2; KMO-red). Vertical broken lines indicate strong (index ≥ 1) positive IOD phases. (B-D) Summer precipitation anomalies computed as in Eq. 2.2 using NCEP precipitation data.

The controlling factor of visibility in the Gulf is dust, with fog being uncommon. The DU data (Fig. 2.9) was found to be significantly ($p_{value} < 0.05$) correlated to the KMO visibility data (Fig. 2.4F) with a value of 0.76 (0.30, 0.93), suggesting dust to be indeed a main controlling factor of visibility. For dust to be lifted into the air a lifting force is required and is commonly supplied by the action of the wind. Another important factor controlling the amount of dust lifted into the air is related to the state and properties of the land surface, e.g. dry vs wet desert surface. During the last 10 years of the dataset (2003 - 2012), the DU has fluctuated in response to the wind strength and local precipitation (Fig. 2.10), such that the relative increase in precipitation and reduction in wind speed resulted in lower DU. However, in 2003 the above (31%) than 40 year average in precipitation and lower (11%) than 40 year average in wind speed did not result in relatively lower observed DU as for other years (Fig. 2.10). This may suggest other contributing factors. A previous study by Koch and El-Baz (1998) outlines the changes between pre- and post-war desert conditions (Iran - Iraq War in 1980 - 1988 and 1st Gulf War in 1990 - 1991) and suggests that military activities have changed desert morphology and environmental conditions of 22% of the desert areas. These morphological changes are mainly a result of disturbances caused to the desert pavement layer, which protects sand particles from exposure to wind erosion, leading to weaker pick-up wind speeds required to suspend dust into the air. Based on the above, we are led to suggest that environmental changes in desert morphology, possibly related to 'Operation Iraqi Freedom' in 2003, may have led to the observed increase in DU in 2003. Furthermore, a case study by Saeed et al. (2014) during 'Operation Iraqi Freedom' suggested an increase in dust storm intensity in the N Gulf as a result of military activity.

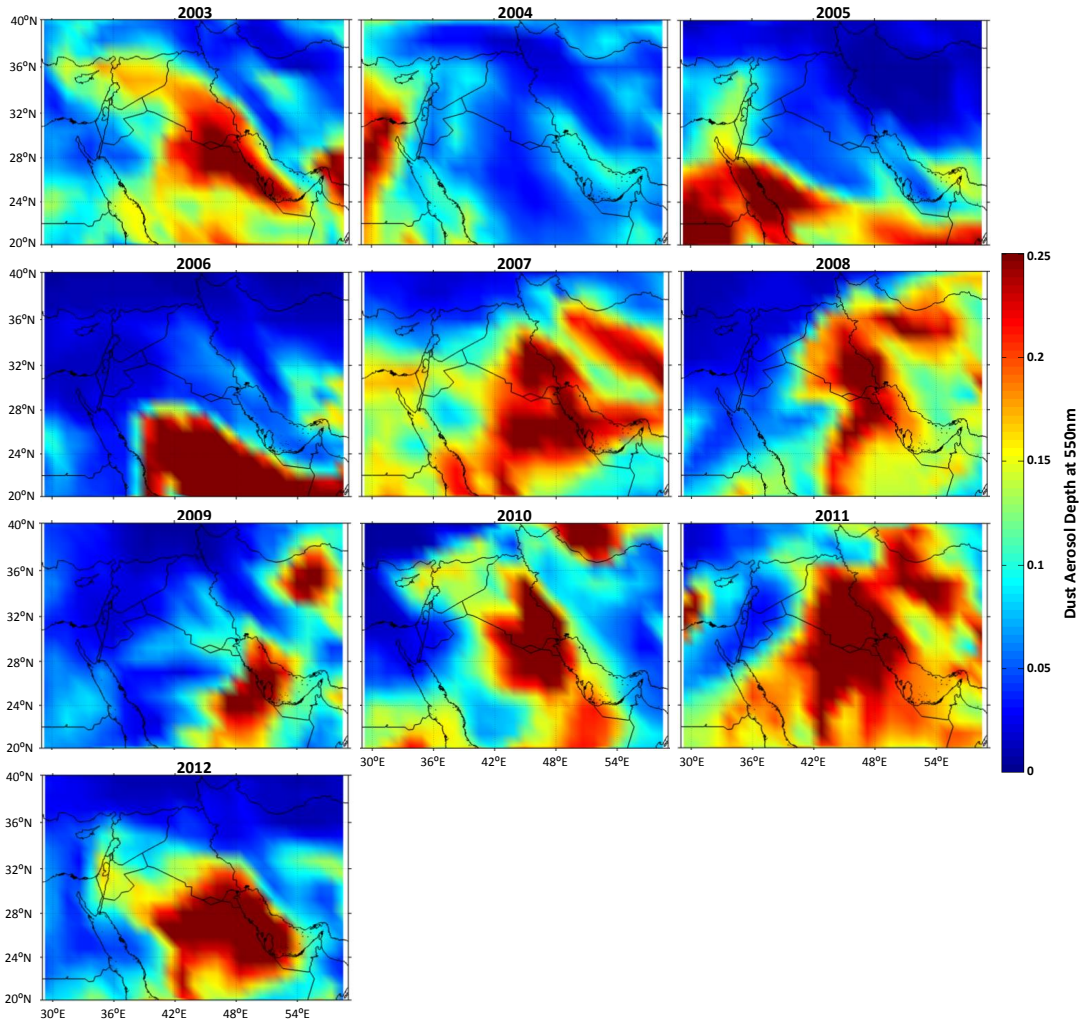

Figure 2.9: Yearly averaged (2003 - 2012) dust aerosols optical depth at 550nm (unitless; represents the fraction of light that is not scattered or absorbed; (Chin et al., 2002)).

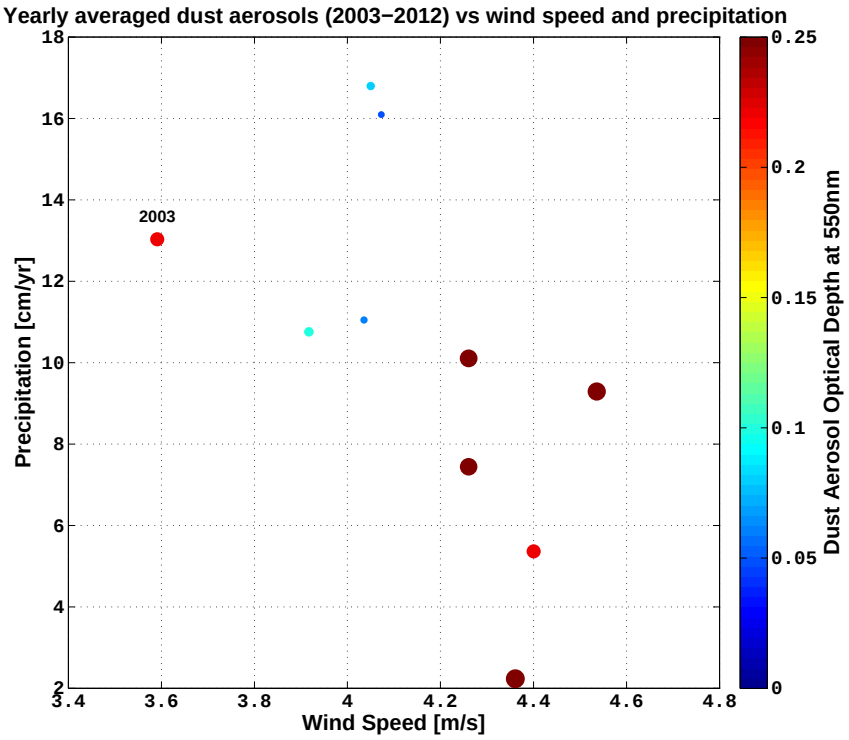

Figure 2.10: Yearly averaged (2003 - 2012) dust aerosols (colored circles) at Kuwait versus wind speed (horizontal coordinate) and precipitation (vertical coordinate). Colors and size of data points represents the quantitative measure of the dust aerosols optical depth at 550nm (unitless).

2.3.2 Shamals

2.3.2.1 Effects of Shamal events on meteorological parameters

Development of N-NW winds during Shamal events between 1973 - 2012 (Fig. 2.11) showed an average increase in wind speed of 2.7 m/s (Fig. 2.12A, Table 2.3). Average wind speeds of 11.5 m/s (7.2, 15.2) with maximum wind speeds up to 23 m/s were registered during these events. Similar observed wind speed averages have been reported by Rao et al. (2001), who used hourly wind speed/direction at Doha, Qatar between 1990 - 2000. However, these average wind speeds are lower than the reported wind speeds ($\geq$ 15.5 m/s) by Walters (1990) (Section 2.1.2).

Average wind speeds during Shamal events that were higher than the dust pick-up threshold speed (9.85 m/s) reduced visibility by an average of 1.7 km (Fig. 2.12B, Table 2.3), resulting in average visibilities of 4.3 km (0.6, 9.0) as dust was being suspended into the air from the Mesopotamian region (Fig. 2.1). Shamal winds brought drier air to the region while traveling over the continental land mass, reducing the relative humidity by 4.3% on average (Fig. 2.12C, Table 2.2).

Changes in barometric pressure during Shamal events (Fig. 2.12D) were dependent on the season. In the winter, a cold frontal system moving from the E Mediterranean and the development of a high pressure system over Iraq, Kuwait, and Saudi Arabia generates steep pressure gradients leading to winter Shamals (Thoppil & Hogan, 2010). The development of a high pressure system during winter Shamals causes an average increase in barometric pressure of 7.8 mb (Fig. 2.13D, Table 2.4). This increase in barometric pressure during winter Shamals is in agreement with Vishkaee et al. (2012) case study on 22 - 23 February 2010, which used 13 observational land sites (8 in Iraq and 5 in Iran) and ECMWF reanalysis for analysis. In summer, the stationary summer monsoon low pressure system over NW India, which

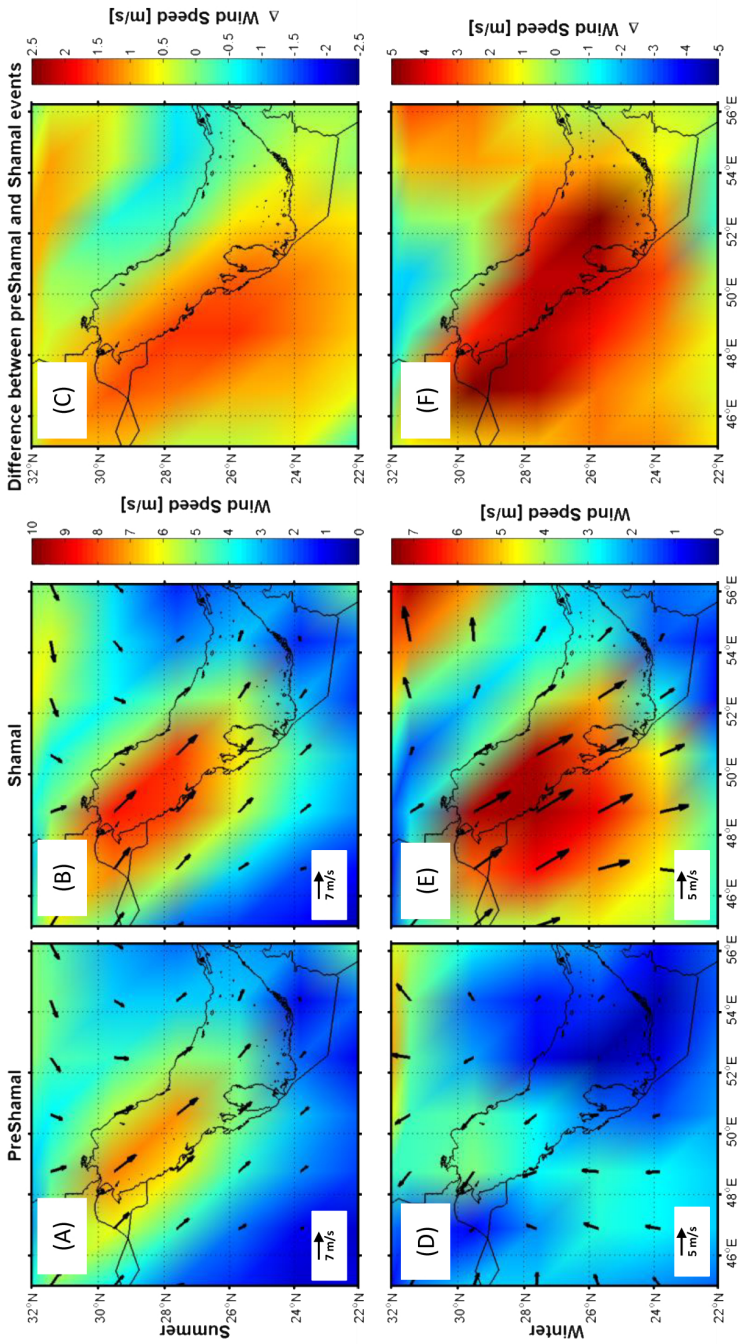

Figure 2.11: Differences in wind speeds (Eq. 2.6) between preShamal and Shamal events (1973 - 2012): (A) average wind speeds of all (281 events) summer preShamal days, (B) average wind speeds of all (281 events) summer Shamal days, (C) difference between average wind speeds during summer preShamals and Shamals for all 281 events, (D-F) same as (A-C) but for winter.

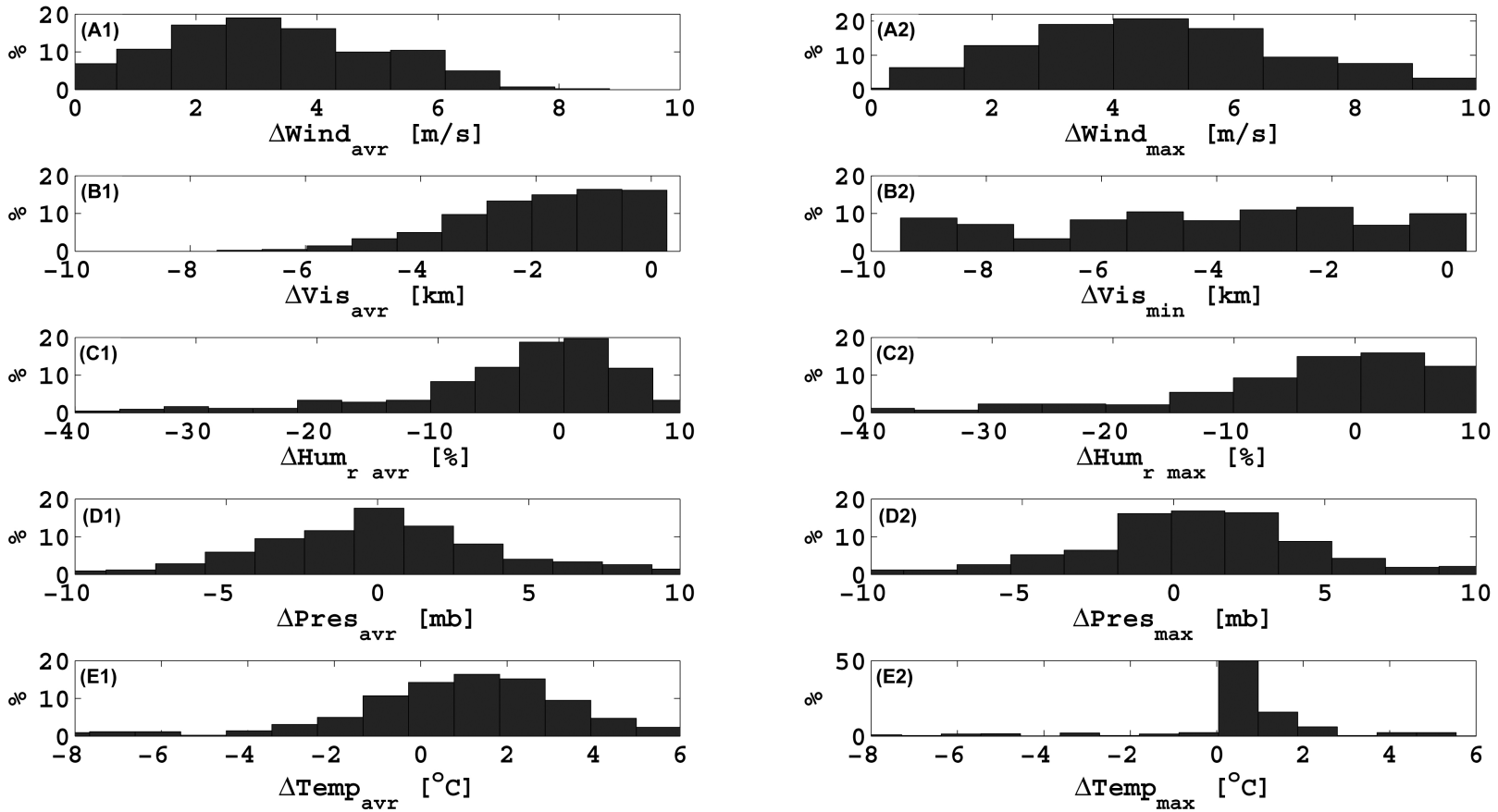

Figure 2.12: Histograms of differences in meteorological parameters between preShamal and Shamal events (421 events, 1973 - 2012): (A1) average wind speed (Eq. 2.6), (A2) max wind speed (Eq. 2.7), (B1) average visibility (Eq. 2.8), (B2) min visibility (Eq. 2.9), (C1) average relative humidity (Eq. 2.12), (C2) max relative humidity (Eq. 2.13), (D1) average barometric pressure (Eq. 2.14), (D2) max barometric pressure (Eq. 2.15), (E1) average air temperature (Eq. 2.10), and (E2) max air temperature (Eq. 2.11).

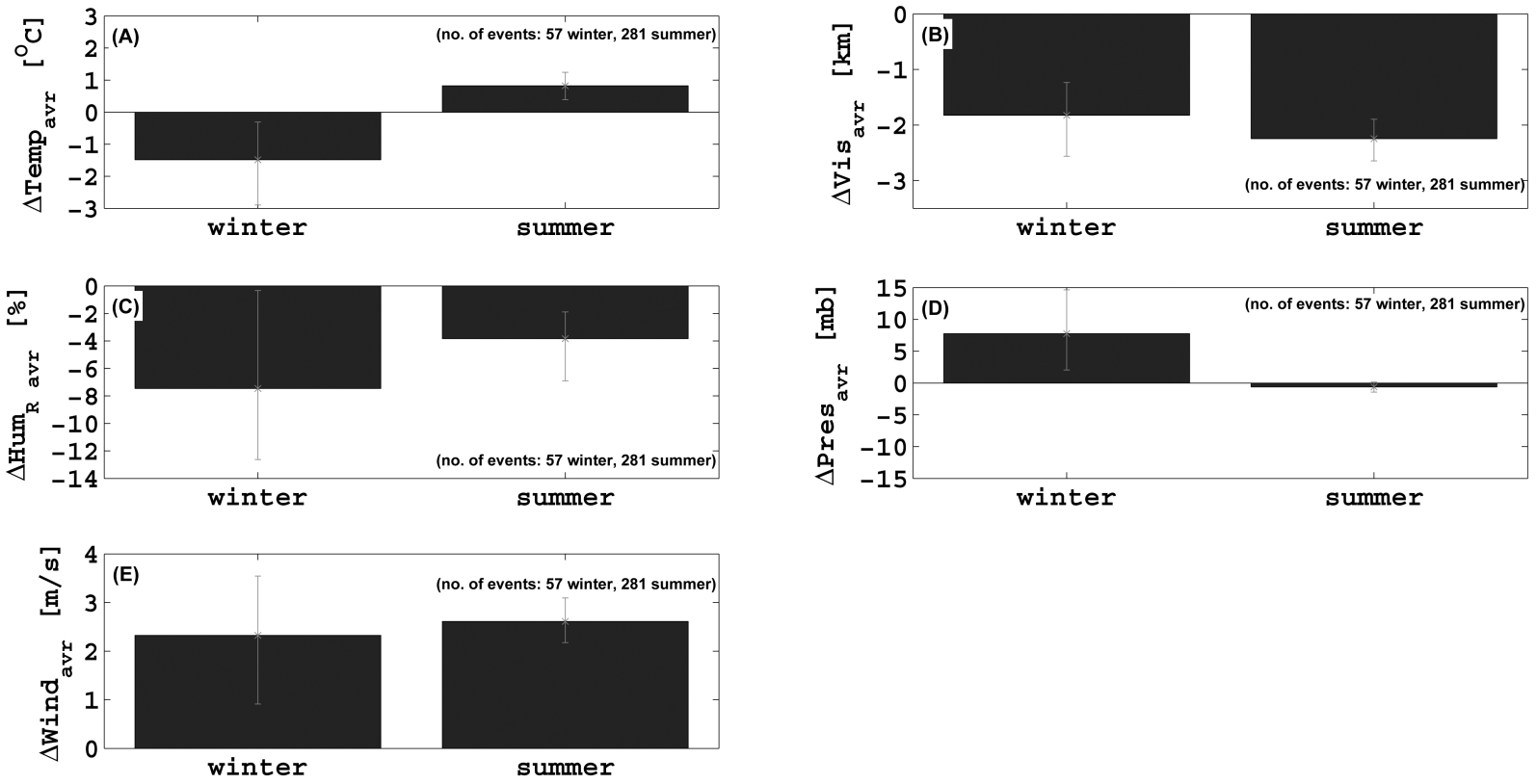

Figure 2.13: Average differences in meteorological parameters between preShamal and Shamal events for winter (57 events) and summer (281 events): (A) air temperature (Eq. 2.10), (B) visibility (Eq. 2.8), (C) relative humidity (Eq. 2.12), (D) barometric pressure (Eq. 2.14), and (E) wind speed (Eq. 2.6).

Table 2.3: Maximum, minimum and average differences in meteorological parameters between preShamal and Shamal events (421 events, 1973 - 2012). 95% bootstrap confidence intervals are given in parentheses.

Meteorological parameter	Average	Max	Min
$\Delta Wind_{avr}$ [m/s]	2.7	11.1	0.2
(Eq. 2.6)	(0.4,5.8)		
ΔVis_{avr} [km]	-1.7	-7.9	-0.2
(Eq. 2.8)	(-4.9,-1.1)		
$\Delta Temp_{avr}$ [^{0}C]	0.3	5.1	-7.5
(Eq. 2.10)	(-3.9,3.5)		
$\Delta Hum_{r\ avr}$ [%]	-4.3	29.8	-44.5
(Eq. 2.12)	(-25.0,6.9)		
$\Delta Pres_{avr}$ [mb]	-0.2	29.5	-19.6
(Eq. 2.14)	(-8.7,10.9)		

Table 2.4: Differences in meteorological parameters between preShamal and Shamal events (1973 - 2012) grouped into seasons. 95% bootstrap confidence intervals are given in parentheses.

	Average		Std deviation	
Meteorological parameter	Winter	Summer	Winter	Summer
$\Delta Wind_{avr}$ [m/s]	2.3	2.6	2.3	1.8
(Eq. 2.6)	(0.9,3.5)	(2.2,3.1)		
ΔVis_{avr} [km]	-1.8	-2.2	1.9	1.7
(Eq. 2.8)	(-1.2,-2.6)	(-2.6,-1.9)		
$\Delta Temp_{avr}$ [^{0}C]	-1.5	0.8	2.3	1.7
(Eq. 2.10)	(-2.8,-0.3)	(0.4,1.2)		
$\Delta Hum_{r\ avr}$ [%]	-7.5	-3.8	4.4	2.5
(Eq. 2.12)	(-13.1,-0.4)	(-7.1,-1.8)		
$\Delta Pres_{avr}$ [mb]	7.8	-0.6	5.5	2.7
(Eq. 2.14)	(2.1, 14.6)	(-1.5,-0.1)		

affects the N Gulf region, induces the summer Shamal and reduces the barometric pressure by an average of 0.6 mb (Fig. 2.13D, Table 2.4) during Shamal events.

The change in air temperature (Fig. 2.12E) during Shamal events was also dependent on the season. Winter Shamals resulted in a reduction of temperatures by 1.5 ^{0}C, while summer Shamals resulted in an increase of 0.8 ^{0}C (Fig. 2.13A, Table 2.4). Overall, with exception of air temperature and barometric pressure, there was no significant difference between summer and winter Shamals and average differences of visibility, humidity and wind speed were similar in both seasons (Fig. 2.13, Table 2.4). By comparing the differences in meteorological parameters due to Shamal events, it is apparent that winter Shamals exhibited larger variability than summer Shamals, as indicated by the larger standard deviation values of the differences in meteorological parameters (Table 2.4). The SE 'Kaus' wind that travels over the Gulf prior to winter Shamals (Fig. 2.11D) is suggested to be the main reason for the larger variability in relative humidity and air temperature, as the 'Kaus' wind brings humid and warmer conditions during preShamal.

2.3.2.2 Variability of Shamal events (1973 - 2012)

A total of 1165 days, comprised of 421 Shamal events (281 summer, 57 winter and 83 transition periods), occurred during the study period (1973 - 2012) with the number of Shamal days per year fluctuating throughout this period. The average number of Shamal days and events stands on 29 days/year and 10 events/year, respectively. 1973 had the highest number of Shamal days (72 days), while 1992 had the lowest (4 days) (Fig. 2.14A). The first quarter of the 1973 - 2012 period had the largest number of Shamal days (32% of the total) with the number of Shamal days declining by 46%, a change of -0.43 days/year, over the 40 year period. However, further analysis suggests that the decline in the number of Shamal days occurred

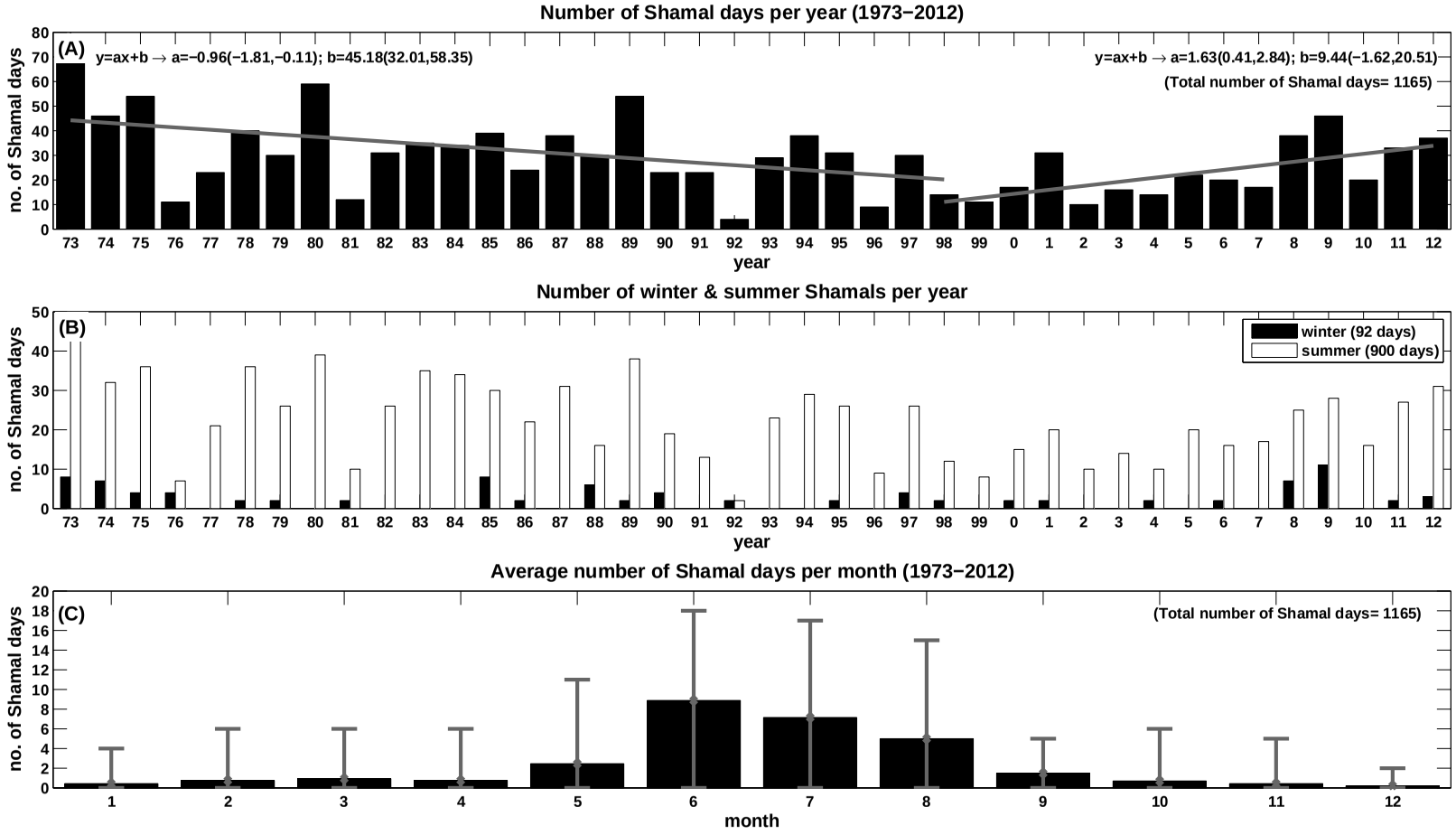

Figure 2.14: Number of Shamal days in 1973 - 2012: (A) number of Shamal days per year. A linear fit to the data, using robust regression is represented by the solid line (fit parameters are given in the top corners), (B) number of winter and summer Shamal days per year, and (C) average number of Shamal days per month with the data range indicated by red whiskers.

mainly between 1973 and 1998 with a decrease of 0.96 days/year. Afterwards, from 1998 to 2012, the number of Shamal days/year has increased by 1.63 days/year. This increase in the number of Shamal days between 1998 to 2012 is consistent with the observed reduction in the yearly average visibility (Fig. 2.4F).

There was a significant difference in the number of Shamal days as a function of the season, with 77% of Shamal days occurring in summer and only 8% in winter (Fig. 2.14B). 52% of Shamal days occurred during the first part of summer (Jun - Jul), commensurate with the stationary intense summer monsoon low pressure system over NW India that affects the N Gulf (Fig. 2.14C). For comparison, a study by Rao et al. (2001) observed an average number of 46 Shamal days/year between 1990 - 2000 in Qatar. That study suggested seasonal differences in the number of Shamal events as well, with 51% of the total Shamal days occurring during the first part of summer.

2.3.2.3 Dust storms and Shamal events

The average number of dust storms (visibility $\leq$ 1 km; Kutiel & Furman, 2003) since 1973 was 13 storms/year, with the first half of the period (1973 - 1991) accounting for 76% of the dust storms (Fig. 2.15). Furthermore, the number of dust storms has decreased by 93% since 1973. Moreover, between the years 1973 and 1998 a decrease of 0.93 dust storms/year was observed, with a more pronounced decrease of 2.04 dust storms/year from 1982 to 1998. This trend reversed between 1998 and 2010, and the number of dust storms has increased by 0.74 events/year (Fig. 2.15). This increase is consistent with the increase in the number of dust storms observed in Riyadh, Saudi Arabia, during 2000 to 2010 as reported by the World Meteorological Organization (WMO, 2010). Moreover, this trend is similar to that of the number of Shamal days, with a correlation of 0.42 (0.30, 0.62) between the number of Shamal

days/year and number of dust storms/year (Fig. 2.14A).

We note that dust storms in the region are not always associated with Shamal events. They may result also from local, short period, unstable weather systems that advect dust from the dry wash regions of Iraq or the eastern deserts of Saudi Arabia (Kutiel & Furman, 2003). Between 1973 - 2010, observations indicate that only 38% of the 495 dust storms formed during Shamal events. The observed dust storms during the study period exhibited wind speeds up to 13 m/s, caused abrupt drops in air temperature of 1.0 ^{0}C (0.4, 1.7) in an hour, and reduced visibility to an average of 0.78 km (0.69, 0.85).

Similar to Shamal events, there were seasonal differences in the frequency of dust storms, with the highest number of storms observed during summer with an average of 7 storms, compared to only 1 dust storm per winter (Fig. 2.15). The lower values during winters are a result of weaker average wind speeds (3.7 m/s) and the Mesopotamian floodplain being more resistant to wind erodibility due to relatively high (880 m^3/s) river discharge from the Euphrates, Tigris, and other streams. In the summer, average wind speed is higher (5.3 m/s), while river streams dry out due to lower fresh water discharge (350 m^3/s) (Iraq Foundation, 2003) resulting in a dry surface layer that is more susceptible to erosion by winds.

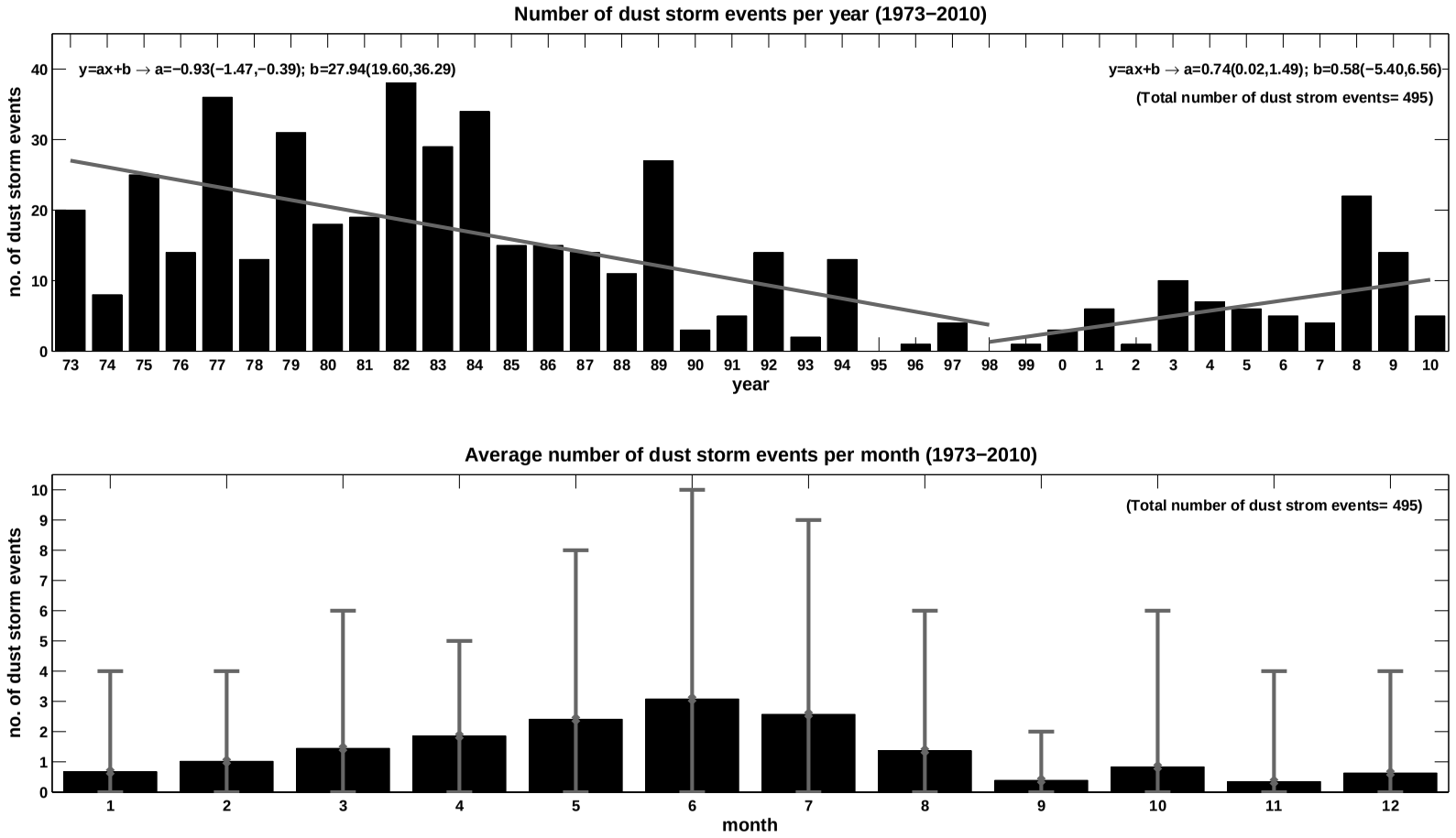

Figure 2.15: (Top) Number of dust storms per year. A linear fit to the data, using robust regression is represented by the solid line; (Bottom) average number of dust storms per month in 1973 - 2010 with their monthly maximum and minimum values indicated by whiskers.

2.4 Conclusions

The present study focused on climate variability over a period of 40 years (1973 - 2012) in the N Gulf, based on observations at Kuwait, Bahrain and NE Saudi Arabia, and the relation of Shamal events and teleconnection patterns to this variability. Results of our study indicate that over the last 40 years the climate in the region experienced a general trend of:

- increase in temperature of 0.8 ^{0}C (0.4, 1.6);
- decrease in barometric pressure of 0.8 mb (0.4, 1.6);
- reduction in humidity of 5.6% (1.2, 9.6);
- decrease in visibility of 0.8 km (0.4, 1.6).

Variability observed in air temperature, barometric pressure and precipitation throughout the study period is suggested to be in response to the three teleconnection patterns NAO, ENSO and IOD impacting the region. This conclusion is supported by significant ($p_{value} < 0.05$) correlations, as well as positive N_s coefficient of efficiency values between these three meteorological parameters and the teleconnection patterns indices.

Visibility variability was mainly in response to the wind speed and precipitation in the region. Furthermore, it is suggested that the result of anthropegnic activity disturbances to about a quarter of the pavement of desert areas, resulting from military activity during the 1990 - 1991 Gulf War and 'Operation Iraqi Freedom' in 2003 has further led to a decrease in visibility.

Relating Shamal events to climate variability necessitates an operational definition of such events, however, we could not find a standard and agreed upon definition

of a Shamal in the literature. Thus, we defined a Shamal event in the present study as a WNW-N (287^0 $<$ direction $<$ 360^0) wind with an hourly average speed $\geq$ 9.85 m/s blowing during at least 3 hours/day. Two consecutive Shamal days are required for a Shamal to be classified as a Shamal event. Based on this definition, and comparison to preShamal conditions, Shamal events were found to cause abrupt changes in meteorological parameters: an increase in wind speed of 2.7 m/s (0.4, 5.8), an increase in temperature during summer of 0.8 ^{0}C (0.4, 1.2), and a decrease of 1.5 ^{0}C (0.3, 2.8) during winter, a decrease in barometric pressure during summer of 0.6 mb (0.1, 1.5) and a increase of 7.8 mb (2.1, 14.6) during winter, a decrease in visibility of 1.7 km (1.1, 4.9), and reduction in humidity of 4.3 % (6.9, 25.0). A total of 421 Shamal events, compromised of 1165 days, occurred during the study period, with 77% of Shamal days occurring in the summer season. The overall number of Shamal event days has decreased by 46% between 1973 and 2012. However, further analysis suggests an increase of 1.63 Shamal days/year in the last 15 years of the study period. Similarly, the number of dust storms has also increased between 1998 and 2010 at a rate of 0.74 dust storm events/year. Results of the present study encourages future observational and numerical studies of the Gulf's response (physically and biologically) to local weather events, e.g. dust storms, as well as teleconnection patterns.

Furthermore, the significance of Shamal events through their effect on the momentum and surface heat exchange at the air-sea interface has motivated a detailed observational meteorological (surface shortwave/longwave radiation, air temperature, SST, humidity, barometric pressure and wind speed/direction) and oceanographic (currents, thermal, salinity and dissolved oxygen structures) study in the N Gulf. This study, which is currently in progress is focusing on the winter, fall and spring transition periods.

3. MIXING INDUCED BY WINTER SHAMALS IN THE NORTHWESTERN ARABIAN / PERSIAN GULF

3.1 Introduction

The Arabian/Persian Gulf (hereafter called Gulf) is a semi-enclosed shallow basin, extending from northwest to southeast (Fig. 3.1). The basin is 990 km long and 370 km wide at its widest and is connected to the Gulf of Oman through the Strait of Hormuz to the south. It has an estimated surface area and volume of 239,000 km^2 and 8,630 km^3 respectively (Emery, 1956). The basin has an average depth of 35 m with 100 m being the maximum near the Strait of Hormuz (Chao et al., 1992). The main sources of inflow in the Gulf are from the Euphrates, Tigris, and Karun rivers' discharge (average 703 m^3/s; Janabi, 2010) to the north and exchange with the Arabian Sea (annual mean 1-2 x 10^5 m^3/s; Swift & Bower, 2003) through the Strait of Hormuz to the south.

The Gulf is situated between 24-30 ^oN in the subtropical high pressure region, where the descending air commonly produces clear skies and arid conditions with high net evaporation (evaporation-precipitation) rates of 1.3 m/yr (Privett, 1959; Hartmann et al., 1971). The main winds in the Gulf are from the northwest, known as 'Shamal' (literally meaning north), and from the southeast (Fig. 3.2). Shamal winds can intensify well above their average and reach wind speeds up to 23 m/s becoming a Shamal event. The definition of a Shamal event used here follows that detailed in Chapter 2, namely a WNW-N (287^o <direction< 360^o) wind with an hourly average speed $\geq$9.85 m/s blowing during at least 3 hours/day. Shamal events occur mostly (85%) during the summer (Jun-Sep) and winter (Dec-Mar) seasons (Chapter 2). In summer, these events are more common due to the stationary monsoon low pressure

system located over Northwestern India and South Saudi Arabia during this time of the year (Rao et al., 2003). Winter Shamals are associated with mid-latitude disturbances that develop over the Eastern Mediterranean and move towards the region (Rao et al., 2001; Thoppil & Hogan, 2010). Durations of winter Shamals are commonly 2 to 5 days (Ali, 1994; Walters, 1990), depending on the speed of the frontal system passing the region. In relatively shallow environments such as the Northwestern Gulf (max depth 37 m), the dynamics and turbulence mixing are strongly controlled by surface forcing (surface buoyancy, heat, and momentum (wind stress) fluxes). Weather events such as Shamals are particularly likely to have a major impact on mixing dynamics, formation of dense water, sediment transport, fluxes of nutrients, and other waterborne constituents in the Gulf. It is expected that in these relatively shallow environments the cold, dry, and strong Shamal winds would result in convective forced mixing similar to that observed due to the Mistral (Schott et al., 1996) and Bora (Lee et al., 2005) wind events where deep convection and overturning have been observed. Thus it is also expected that the Shamal induced convection would penetrate down to the seabed and possible re-suspend nutrients from the seabed which eventually may induce algae blooms. A study by Nezlin et al. (2010) suggests that dust deposition, commonly associated with Shamal events (Fig. 3.3), may further regulate phytoplankton blooms in the Gulf waters.

Unfortunately, our present understanding of turbulence dynamics and mixing processes in the Gulf is lacking and to the best of our knowledge no such observations have been made to-date. Surprisingly, none of the previous documented comprehensive observational and numerical studies of the Gulf by Emery (1956), Brewer and Dyrssen (1985), Chao et al. (1992), Reynolds (1993), Swift and Bower (2003), or Thoppil and Hogan (2010) have focused on the mixing processes associated with the Shamal events. The present study aims to address these challenges and improve our

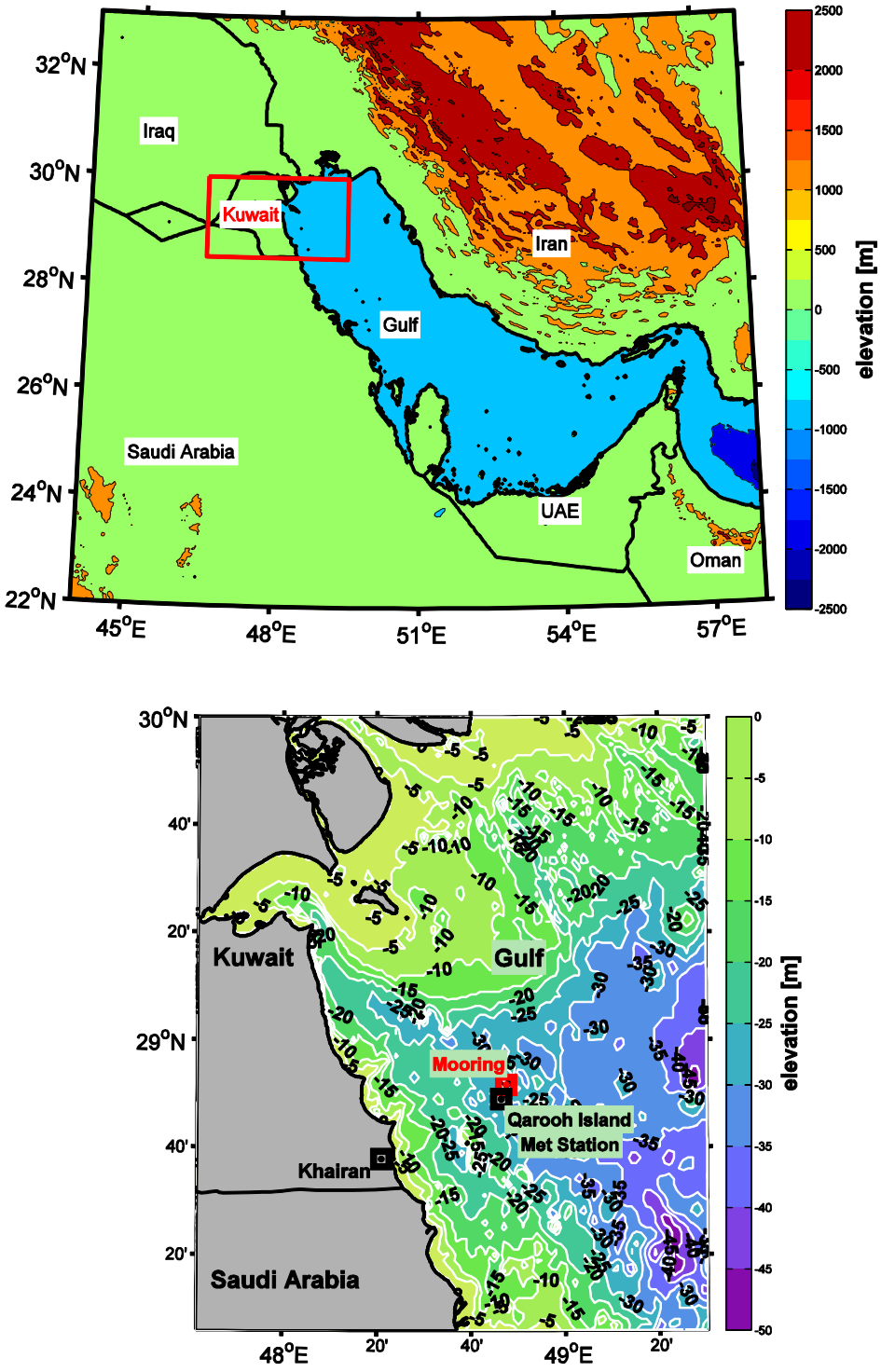

Figure 3.1: Gulf regional topographic and bathymetery map (top); Study region with locations of mooring station and meteorological station. Depth contour lines at 5 m contour intervals (bottom).

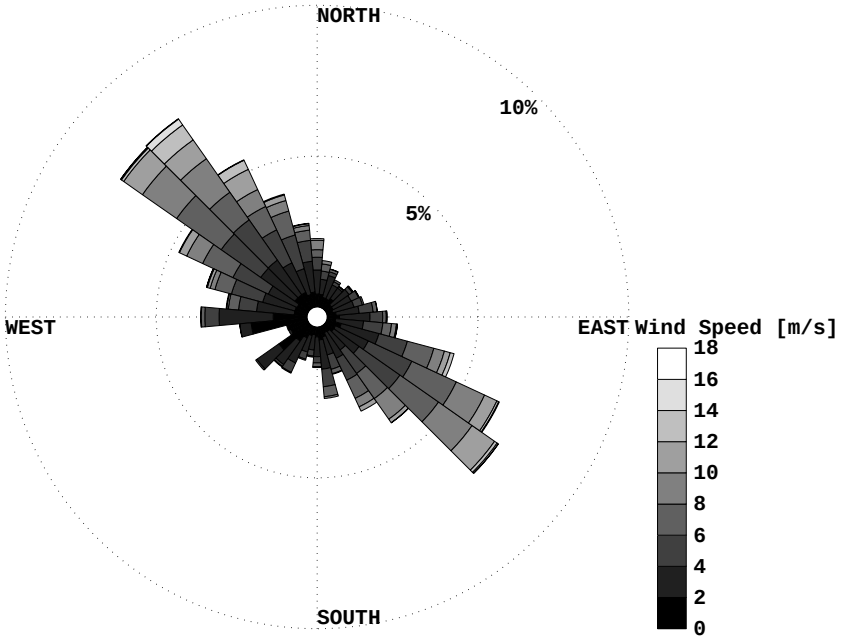

Figure 3.2: Hourly averaged wind speed, direction (from where wind blows), and frequency of occurrence (in %) during mid-Jan to mid-Apr 2013 at Qarooh Island, Kuwait.

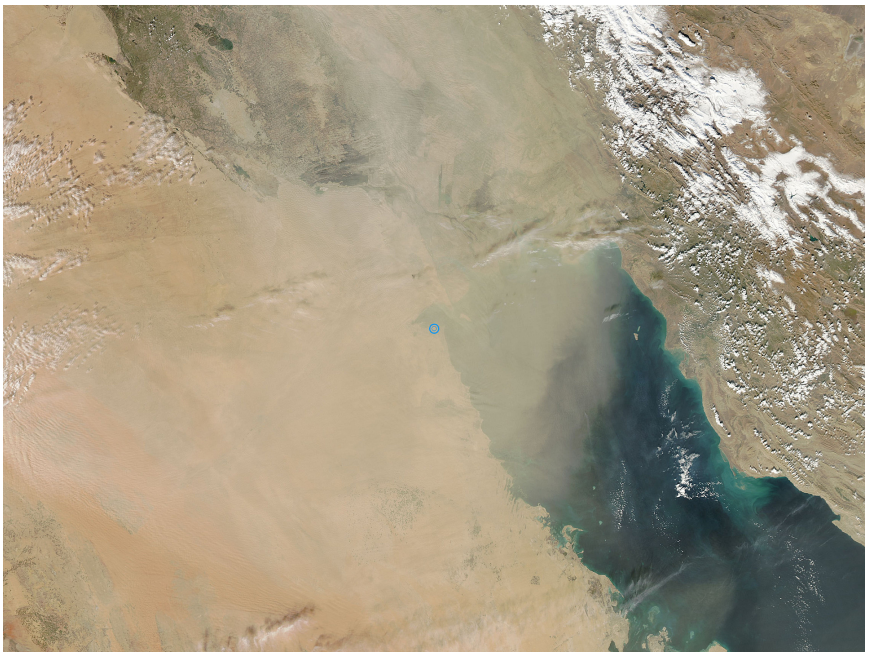

Figure 3.3: True color aqua satellite image of N Gulf rising dust during a Shamal event on Mar-6-2013. The blue circle shows the location of Kuwait City (NASA, 2013).

understanding and quantitative description, and thus predictive capabilities, of water column dynamics, mixing processes and the related fluxes of water borne substances in the northwestern Gulf and their relation to external forcing.

In this study we combined observational and modeling results of turbulence dynamics and mixing processes in the Northwestern Gulf in response to the extreme Shamal events. The main objective of the observations was to determine the magnitude and temporal variability of turbulence mixing intensities and relate them to external forcings and current velocities at the surface boundary layer (SBL) and bottom boundary layer (BBL). The excessive vertical mixing in the SBL resulting from the air-sea processes, which include wind stress (e.g. Tsagareli et al., 2010), buoyancy and heat fluxes (e.g. Anis & Moum, 1994), and surface waves (e.g. Bakhoday Paskyabi et al., 2012), commonly generates a homogeneous or near homogeneous density layer. The SBL extends from the sea surface to a depth where the water becomes stratified (Anis & Singhal, 2006) and its depth depends on the vertical mixing intensity (Sutherland et al., 2014). This depth may vary by tens of meters diurnally (e.g. Schneider & Muller, 1990) and can vary up to 100 m annually (e.g. Sprintall & Roemmich, 1999). Most biological activity and air-sea gas exchange occur in this layer. Other processes contributing to mixing intensities in the SBL and the deeper layers are currents (tidally, storm forced), which may enhance mixing through shear production. The BBL is a layer near the seabed, with typical vertical extents ranging between 4 m and 50 m (Trowbridge, 1991; Gloor et al., 2000), where the current profile is often assumed to be logarithmic if a constant stress layer exists (Doron et al., 2001). The mixing intensity in this layer is commonly high due to the interaction between the near bottom current and seabed friction producing shear. The high mixing levels are a main driving force for re-suspension and transport of nutrients, toxins, and sediments from the seabed (Dewey et al., 1986). The main

objective of the simulations was to evaluate the performance of a one dimensional numerical model in reproducing turbulence properties (Reynolds stresses, eddy diffusivities, turbulent kinetic energies, and its dissipation rates) in the BBL in response to the tidal currents and Shamal events. This will allow for predictions of present and future scenarios, such as those resulting from Shamals and other extreme events.

The study methodology (observations and numerical model details) are described in Section 3.2. Section 3.3.1 to 3.3.3 describe the meteorological conditions, hydrographic fields as well as the observed and simulated turbulence quantities during three Shamal events. Section 3.3.4 analyzes the effect of tidal induced shear on turbulence quantities. Finally, conclusions and summary are given in Section 3.4.

3.2 Methods

3.2.1 Observational details

A field experiment was conducted in the vicinity of Qarooh Island, Kuwait (about 40 km NE of Al Khairan; Fig. 3.1), in the northern tip of the Gulf (about 120 km South of the Euphrates-Tigris delta), from mid-Jan to mid-Apr 2013. The general axis of the coastline and bathymetery in the study region is in the NW-SE direction (315-135^o), with a maximum depth of 37 m. Data was collected at a meteorological station and an oceanographic mooring station.

3.2.1.1 Meteorology

A surface meteorological station (Fig. 3.4) was mounted on a pole at a nominal distance of 7 m above sea level (ASL) at the end of a pier at Qarooh Island (28^o 48.973$'$ N, 048^o 46.457$'$ E; Fig. 3.1). Measurements included wind speed and direction (Young marine wind monitor model 05106), air temperature and humidity (Onset S-THB housed in a Davis solar powered fan aspirated radiation shield), incoming solar radiation (Apogee VR1761-5), incoming infrared radiation (Kipp and Zonen CG 3

Pyrgeometer), barometric pressure (Onset S-BPA-CM10), and rain (Texas electronic tipping bucket model TE 525). Sensors were set to sample at 2 min intervals and then were averaged and logged at 10 min intervals and transmitted via Iridium satellite to a web server (Data Garrison). The radiometers were cleaned daily. Sea surface temperature (SST) was collected at 3.5 min intervals at a depth of 0.2 m with a HOBO onset temperature sensor mounted inside a small surface float.

Due to logger problems, wind speed/direction throughout the study period and relative humidity and air temperature from mid-Jan to the first of March had to be discarded. In lieu of these, we obtained and used 10 min interval wind speed/direction (Vaisala WS425 Ultrasonic), air temperature (Vaisala HMP45A), and relative humidity (Vaisala HMP45D) data from the Kuwait Meteorological Office (KMO) Qarooh Station located on the same pier at a distance of about 10 m from our meteorological station. All data was adjusted to a standard 10 m height ASL. Turbulent latent heat, J_q^L, sensible heat, J_q^S, momentum (wind stress), τ, net shortwave radiation, J_q^{sw}, and net longwave, J_q^{lw}, fluxes at the air-sea interface were computed using the Coupled Ocean-Atmosphere Response Experiment (COARE 3.0) software (for details see Fairall et al., 1996, 2003; Drennan, 2003). The net surface heat flux was calculated as

$$J_q^0 = J_q^{sw} + J_q^{lw} + J_q^L + J_q^S \quad . \tag{3.1}$$

From J_q^0 (Dorrestein, 1979) the surface buoyancy flux was computed

$$J_b^0 = \frac{g\alpha_T J_q^0}{\rho_o C_p} \quad , \tag{3.2}$$

where g is the gravitational acceleration, α_T is the thermal expansion coefficient, ρ_o is the sea water density near the surface, and C_p is the specific heat of sea water

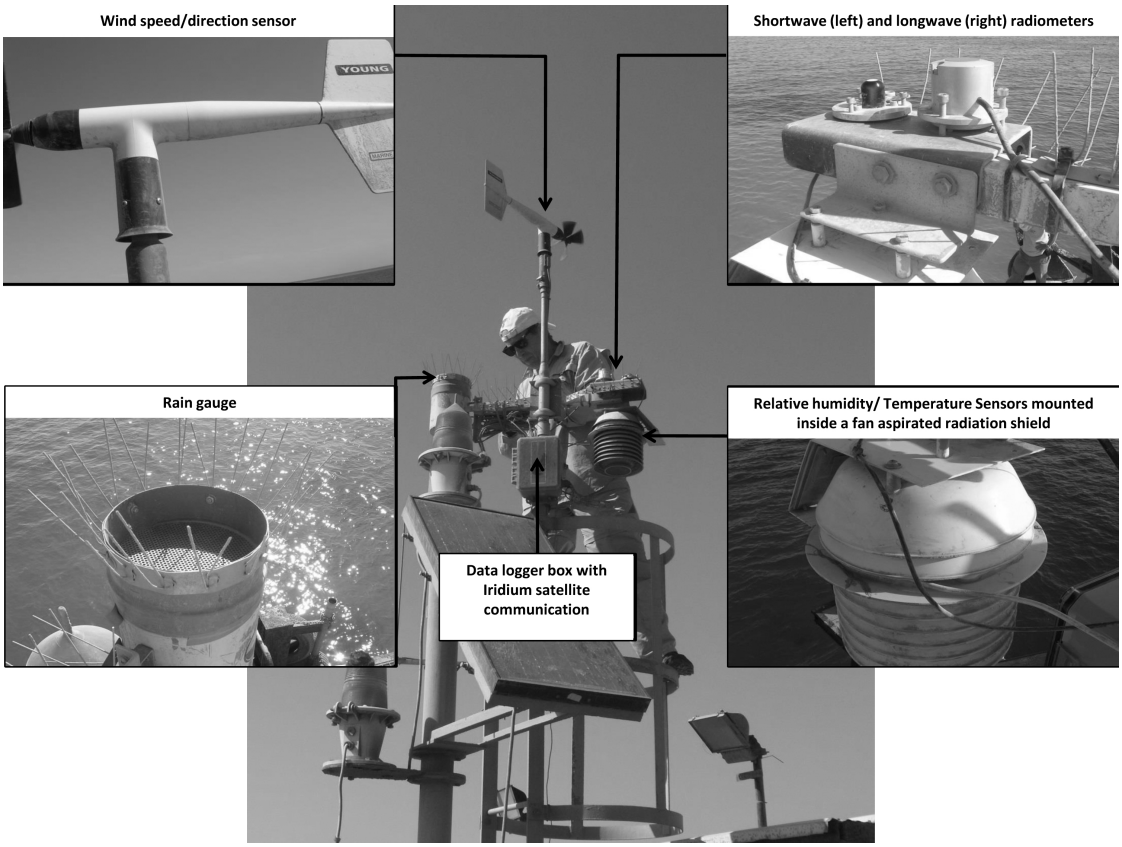

Figure 3.4: Meteorological station positioned on a pier at Qarooh Island, Kuwait (see Fig. 3.1).

(computation method of C_p see Fofonoff & Millard, 1983). A positive J_b^0 is a result of net cooling ($0 < J_q^0$) at the sea surface, which may enhance mixing and deepen the surface mixed layer. A negative J_b^0 is a result of net heating ($0 > J_q^0$) at the sea surface, which suppresses mixing by stabilizing stratification.

If the only sources for turbulence mixing in the SBL were wind stress and surface buoyancy flux, the Monin-Obukov scale determines the relative contribution of the two sources and is given by

$$L = \frac{-u_*^3}{\kappa J_b^0} \quad , \; u_* = (\tau/\rho_o)^{1/2} \quad , \tag{3.3}$$

where u_* is the water surface frictional velocity and κ=0.41 is the Von Karman constant. During convective favorable conditions L is negative ($0 < J_b^0$), and its value represents the depth at which wind and bouyant production of turbulence in the SBL are of similar importance (Thorpe, 2005).

3.2.1.2 Hydrography

Hydrographic data was collected from instruments moored 2 nm NE of Qarooh Island, Kuwait (28^o 50.938′ N, 048^o 47.534′ E; Fig. 3.1). The mooring consisted of two parts: a tight mooring and a bottom pod, separated by a distance of 21 m (Fig. 3.5). The tight mooring included 23 temperature sensors (ONSET water temp pro) sampling every 3.5 min, three fluorometers (PME Cyclop-7) sampling every 5 min, five dissolved oxygen sensors (PME MiniDOT) sampling every 1 min, four mini-Conductivity Temperature Depth sensors (mini-CTD, INW CT2X) sampling every 2 min, two CTD's (RBR XR-420 and XR-620) sampling every 20 s, ten light intensity sensors (ONSET light loggers) sampling every 5 min, and two Acoustic Doppler Velocimeters (ADV, Nortek) sampling in bursts. Each burst included 512 samples at 16 Hz sampling frequency, with an interval of 3.5 min between bursts.

Manufacture related problems in the three fluorometers limited data collection to 18-30 Jan. Conductivity measurements of the six CTD's were affected by biofouling although copper film and mesh were used for anti-fouling. Therefore, in this study we have assumed constant salinity profiles following a survey by Reynolds (1993), where the study suggested constant salinity profiles off the coast of Kuwait during the Feb-Mar period.

The bottom pod included one temperature sensor (ONSET water temp pro) sampling every 3.5 min, one mini-CTD(INW CT2X) sampling every 2 min, and two upwards looking Acoustic Doppler Current Profilers (ADCPs): a Nortek 1 MHz Aquadopp sampling every 3 min for 36 s with a vertical resolution of 0.5 m and a 0.2 m blanking distance; a 2 MHz Aquadopp with a high resolution firmware (ADCP-HR) sampling in bursts. Each burst included 512 samples at 8 Hz sampling frequency, with 6 min intervals between bursts. The ADCP-HR provided vertical current profiles in the BBL with a resolution of 75 mm and a blanking distance of 5 cm. The ADCP-HR measurements were then rotated from beam coordinates (u, v, and w; relative to the instrument) into Earth coordinated (North-South and East-West, Up-Down) using the tilt, roll and heading data following the manufacturer software (Lohrmann et al., 1990).

Using the vertical high resolution temperature profiles that included 25 sensors measurements (one on surface, 23 mooring, and one on pod), we estimated the mixed layer depth following Thomson and Fine (2003) approach that used the split-and-merge algorithm developed by Pavlidis and Horowitz (1974). This method divides the temperature profile into segments by defining their breaking points using piecewise polynomial function. The mixed layer is defined as the uppermost segment from which the mixed layer depth is estimated.

3.2.2 Estimating turbulence parameters

The notion that shear causes instability by generating turbulence and stratification causes stability by suppressing turbulence is fundamental. It is assumed that the ratio between the shear frequency squared, $S^2 = (\partial u/\partial z)^2 + (\partial v/\partial z)^2$, and the buoyancy frequency squared, $N^2 = -(g/\rho_o)(\partial \rho_o/\partial z)$, quantifies the stability of a flow. Various observational studies link this classical ratio known as the Richardson number, $Ri = (N^2)/(S^2)$, with an empirical critical value $Ri_c = 0.25$ (Miles, 1961) to turbulence quantities (Zaron & Moum, 2009). Generally, Ri_c values between 0.2 and 1 are accepted (Galperin et al., 2007). A flow where S^2 dominates ($Ri < Ri_c$) is a turbulent flow, while a flow where N^2 dominates ($Ri > Ri_c$) decays turbulence causing stable flow.

Our ability to measure turbulence will allow us to discern which physical mechanism and when surface forcing (wind stress, surface buoyancy flux, waves) or current shear are driving mixing and fluxes of water-borne constituents such as nutrients and sediments. Moreover, the estimated turbulence parameters (Turbulence kinetic energy (TKE) dissipation rates ,ε, TKE, k, vertical eddy diffusivity, K_z, and Reynolds stress τ_b) in the present study will also be used to compare with the numerical model simulations (details Section 3.2.3).

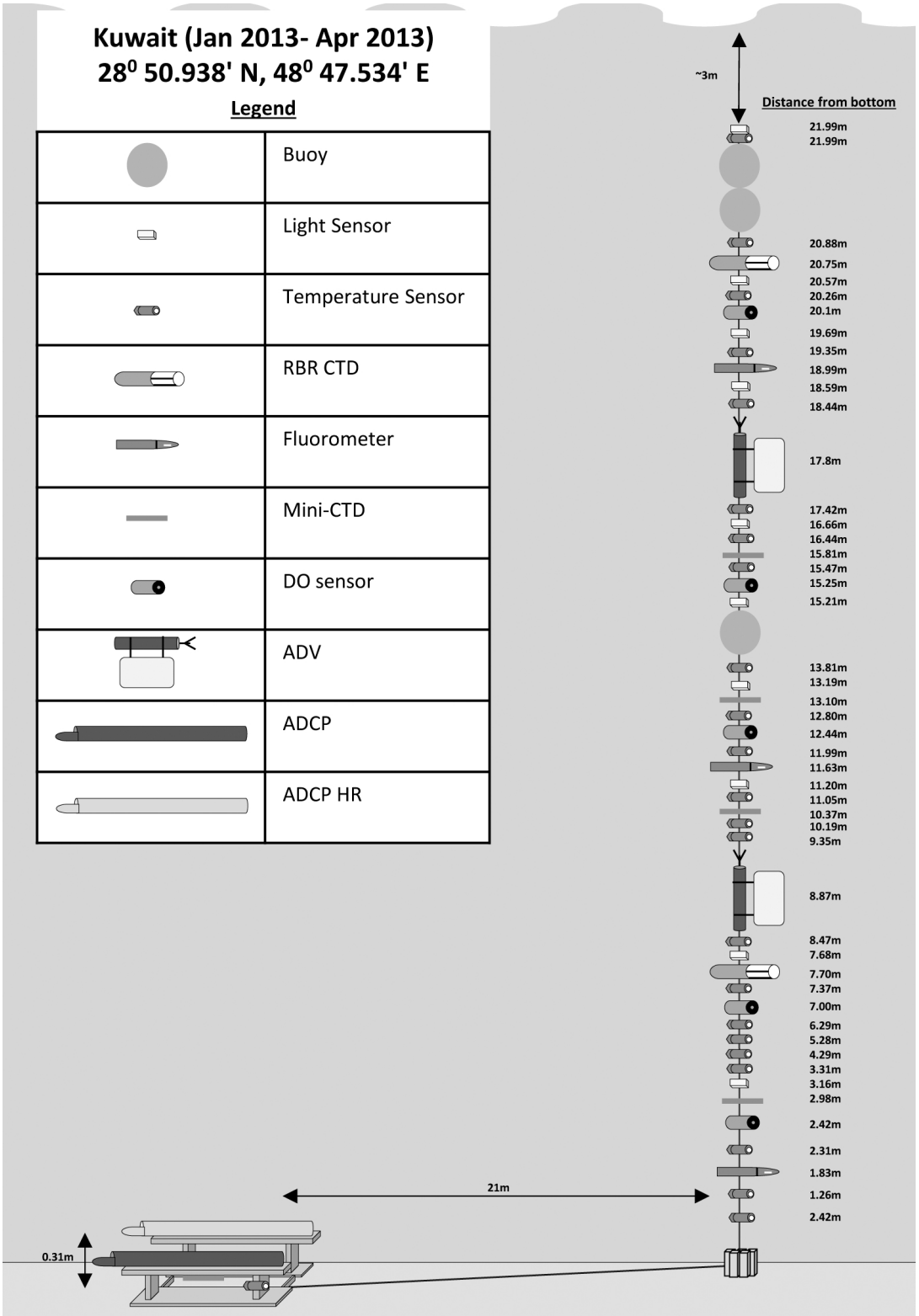

Figure 3.5: Instrumented cable mooring (right) and bottom pod (left).

Time series of vertical velocity fluctuations, w', measured by the bottom mounted ADCP-HR were used to estimate the power spectrum density (PSD) from which ε, and TKE were estimated. Using the vertical velocity component allows estimation of lower ε values due to the lower noise level (1.1 x 10^{-6} $\frac{m^2/s^2}{rad/m}$) of the vertical velocity component compared to the horizontal velocity component noise level (2.6 x 10^{-6} $\frac{m^2/s^2}{rad/m}$) as well as suffering less contamination from wave motions (Stapleton & Huntley, 1995; Gordon et al., 1999). The classical approach in estimating ε is by fitting the PSD with Kolmogorov's -5/3 slope in the inertial subrange (Kolmogorov, 1941; Davidson, 2004) following

$$E(K) = C_{Kol}\varepsilon^{2/3}K^{-5/3} \quad , \tag{3.4}$$

where $E(K)$ is the wavenumber, K, spectra, and $C_{Kol} = 1.5$ is the Kolmogorov constant for a transverse spectrum (where the velocity component is perpendicular to the wavenumber; Pope, 2000). Using this classical approach problems may arise in shallow or coastal regions where in the inertial subrange turbulence might be enhanced by the surface wind waves orbital velocities (Lumley & Terray, 1983). The effect of surface waves on the PSD can be seen in the frequency range of 0.125-0.25 Hz (period of 4-8 s) in Figure 3.6. Modification to the classical approach using the horizontal current speed, V (magnitude of the mean horizontal velocity in each burst), was applied by Trowbridge and Elgar (2001) to filter out the energy produced by the surface wind waves and reduce it to energy produced by turbulence alone

$$E(K) = \frac{12}{55}C_{Kol}V^{2/3}\varepsilon^{2/3}K^{-5/3} \quad . \tag{3.5}$$

To estimate ε we applied the Trowbridge and Elgar (2001) method to all bursts

after filtering out velocities with correlations (measure of similarity between two consecutive pulse echoes) <70% for data integrity (Rusello, 2009). This approach is similar to that taken by Moum et al. (2007), who estimated ε from an ADV in the BBL (124 m depth) off the Oregon Coast where swell waves were significant (periods of 12+ s). Figure 3.6 shows an example of a single burst collected by the ADCP-HR on Feb 13 where the wavenumber selected for fitting the -5/3 slope range was 25.8 - 38.6 rad/m. The -5/3 slope was fitted using the robust regression algorithm (Huber, 1964; Huber & Ronchetti, 2009). This fitting method reduces the error of the least square fit by the use of a bisquare weighting function that reduces the weight of possible outliers.

The second turbulence parameter estimated using the ADCP-HR is TKE. TKE was computed using the spectral integral of the PSD in the inertial subrange following

$$k = \frac{3}{2}(\int_{K_h}^{K_l} E(K)dK - \int_{K_h}^{K_l} NdK) \quad , \tag{3.6}$$

where K_l and K_h are the lower and higher limit wavenumbers, respectively, of the inertial subrange, and N is the instrument noise level (Fig. 3.6). Using these limits filters out the effect of surface waves (lower wavenumber $> K_l$) as well as instrument noise (higher wavenumber $< K_h$), thus, giving us TKE values produced by turbulence alone.

The third turbulence parameter computed using the ADCP-HR is the BBL Reynolds stress, τ_b. BBL stresses are of particular interest since the fluid will begin to resuspend/transport sediments and nutrients that are at rest on the bottom once a critical stress required for initiation of motion is exceeded (Kimn et al., 2000) and is computed using the velocity variance method proposed by Lohrmann et al. (1990)

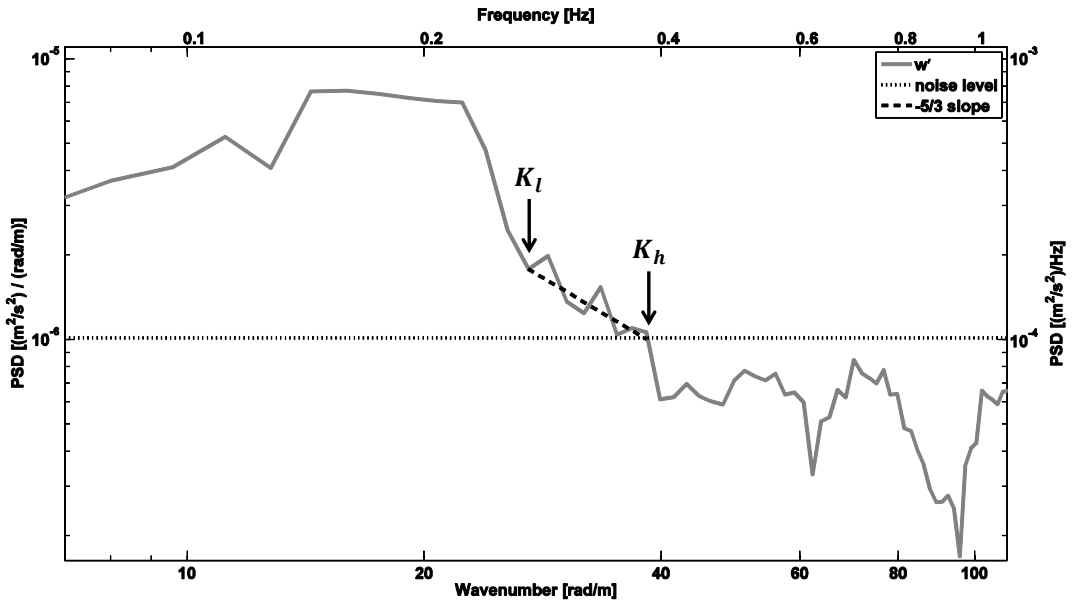

Figure 3.6: An example of energy spectra of the vertical velocity fluctuations (solid line) of a single burst measured by the ADCP-HR taken on Feb 13 2:55 (UTC) with the inertial subrange limits outlined (K_l and K_h). The -5/3 slope results in an estimate of $\varepsilon = 2.75$ x $10^{-5} m^2/s^3$.

following

$$\tau_b = \rho_b \overline{u'w'} \quad , \tag{3.7}$$

where ρ_b is the density in the BBL.

The fourth estimated turbulence parameter is the vertical eddy diffusivity. The vertical transport of nutrients and sea water properties throughout the water column is one of the controlling factors in primary production (MacIntyre, 1993) that may lead to harmful phytoplankton blooms and fish kill (e.g. Glibert et al., 2002). The vertical transport of constituents is dependent on the vertical eddy diffusivity (Osborn, 1980), which may be estimated using ε by

$$K_z = \Gamma \frac{\varepsilon}{N^2} \quad , \tag{3.8}$$

where mixing efficiency, Γ=0.2 (Oakey, 1985), however, other studies have reported values of Γ= 0.05 (Yamazaki & Osborn, 1993). Moreover, using the estimated K_z in the BBL we can estimate the BBL heat flux using

$$J_q^{bbl} = \rho_b C_p K_z \frac{\partial T}{\partial z} \quad . \tag{3.9}$$

J_q^{bbl} will be used to relate Shamal cool plumes that penetrate to the BBL.

3.2.3 Numerical model details

Observations of turbulence processes in aquatic systems are challenging due to their intermittent nature and requirement of specialized instruments. Numerical models, forced by basic hydrographic (temperature, salinity and velocity) observations, and surface forcings (heat and momentum fluxes) attempt to quantify these processes using suitable mathematical models of the flow field (Bolding et al., 2002). The present study evaluates the performances of the widely used second moment two equation models $k-\varepsilon$ (Launder & Spalding, 1972) and $k-kl$ (Mellor & Yamada, 1982). For this purpose, and for comparison to our observations, we use the one-dimensional (1-D) General Ocean Turbulence Model (GOTM; for details see Burchard & Bolding, 2001; Burchard, 2002). Using simplified 1-D models will not give perfect simulations of 3-D environments. One obvious draw back in using 1-D models are their limitations in accounting for the spatially non-uniform conditions (e.g. water temperatures, salinities, and current velocities). Processes that are treated prognostically in 3-D models have to be parameterized or neglected (e.g internal pressure gradient and horizontal advective processes). To parameterize for these processes we relax (nudge) the model to the hourly observed temperature and velocity profiles. Furthermore, the model was forced by the surface momentum and heat fluxes that were computed from the meteorological observations at Qarooh Island.

The two equation turbulence models are based on the two dynamical equations for k and ε derived from the Navier-Stokes equation with the Boussinesq approximation (Boussinesq, 1903). The flow is separated into a fluctuating part and a mean part using Reynolds (1895) decomposition (e.g. Kundu & Cohen, 2008). The k equation is computed similarly in both $k-\varepsilon$ and $k-kl$ turbulence models

$$\partial_t k = D_k + P + B - \varepsilon \quad , \tag{3.10}$$

where D_k is the sum of the viscous and turbulence transport terms, P and B are the shear production and buoyancy production terms, respectively.

The $k-\varepsilon$ model uses a similar approach as used for k above to obtain a closed form for ε

$$\partial_t \varepsilon = D_\varepsilon + (\frac{\varepsilon}{k})(c_{\varepsilon 1} P + c_{\varepsilon 3} B - c_{\varepsilon 2}\varepsilon) \quad , \tag{3.11}$$

where $c_{\varepsilon 1}$, $c_{\varepsilon 2}$, and $c_{\varepsilon 3}$ are empirical constants (Table 3.1).

The $k-kl$ model obtains a closed form for ε using a turbulence length scale, l,

$$l = (c_\mu^o)^3 \frac{k^{3/2}}{\varepsilon} \quad , \tag{3.12}$$

that is related to ε by

$$\partial_t (kl) = \frac{l}{2}(c_{l1} P + c_{l3} B - (1 + c_{l2}(l/l_z)^2)\varepsilon) \quad , \tag{3.13}$$

where c_μ^o, c_{l1}, c_{l2}, c_{l3} are empirical constants (Table 3.1), and l_z is the diagnostic length scale that follows the law of wall near boundaries (Burchard, 1999).

Solving the dynamical equations for k and ε is required for computing the eddy viscosity, K_M, and eddy diffusivity, K_H, which allow 'closure' of the second moment

Table 3.1: Empirical constants used in the two equation models, $k-\varepsilon$ and $k-kl$.

c_μ^o	$c_{\varepsilon 1}$	$c_{\varepsilon 2}$	$c_{\varepsilon 3}$	c_{l1}	c_{l2}	c_{l3}
0.55	1.44	1.92	computed	1.8	1.33	computed

equations (Burchard et al., 2008)

$$K_M = c_\mu \frac{k^2}{\varepsilon} \quad , \tag{3.14}$$

$$K_H = c'_\mu \frac{k^2}{\varepsilon} \quad , \tag{3.15}$$

where c_μ and c'_μ are non-dimensional stability functions proposed by Canuto et al., 2001 (hereafter CA). The CA equations are non-equilibrium stability functions that use formulation deduced from the original Mellor and Yamada (1974) and Kantha and Clayson (1994) stability functions, but with improved parameterization of the second order moments. CA suggested improvements to the Kantha and Clayson (1994) stability functions by modifying the Ri_c from 0.23 to 0.85, and by modifying pressure-temperature and pressure-velocity formulations to improve convective simulations. This stability function is dependent on the shear and buoyancy numbers and the ratio of k^2 and ε^2 (Canuto et al., 2001) and is given by

$$c_\mu = \frac{0.107 + 0.01741\alpha_N - 0.00012\alpha_S}{1 + 0.26\alpha_N + 0.029\alpha_S + 0.0087\alpha_N^2 + 0.005\alpha_N\alpha_S - 0.000034\alpha_S^2} \quad , \tag{3.16}$$

$$c'_\mu = \frac{0.1120 + 0.004519\alpha_N - 0.00088\alpha_S}{1 + 0.26\alpha_N + 0.029\alpha_S + 0.0087\alpha_N^2 + 0.005\alpha_N\alpha_S - 0.000034\alpha_S^2} \quad , \tag{3.17}$$

where

$$\alpha_S = \frac{k^2}{\varepsilon^2} S^2, \alpha_N = \frac{k^2}{\varepsilon^2} N^2 \quad . \tag{3.18}$$

The ability of these models to elucidate turbulence parameters (k, ε, K_z, and τ_R) is investigated here using four statistical tools. Two statistics (mean bias error, MBE, and root mean square error, RMSE) will evaluate the model accuracy by quantifying the mean difference between an observed, y, and simulated, x, turbulence parameter and are given by

$$MBE = \frac{1}{n}\sum_{i=1}^{n}(x_i - y_i) \quad , \tag{3.19}$$

$$RMSE = \sqrt{\frac{1}{n}\sum_{i=1}^{n}(x_i - y_i)^2} \quad . \tag{3.20}$$

where i is the time series data point, and n is the total number of data points.

The third statistic is the Nash-Sutcliffe coefficient efficiency, (N_s; Nash & Sutcliffe, 1970) which assess the models predictive power by its ability in fitting the observations

$$N_s = 1 - \frac{\sum_{i=1}^{n}(y_i - x_i)^2}{\sum_{i=1}^{n}(y_i - \overline{y})^2} \quad . \tag{3.21}$$

Negative N_s values indicate a poor relation between the simulation and observations, $N_s = 0$ indicates that simulations and observations are similar only in their mean values, $N_s = 1$ indicates that the simulated values perfectly match the observations. Positive N_s values are generally viewed as acceptable (Gupta & Kling, 2011). The fourth statistic is the commonly used Pearson correlation function, which quantifies the linear relation between two independent variables and is given by

$$r = \sum_{i=1}^{n}\frac{(x_i - \overline{x})(y_i - \overline{y})}{(n-1)\sigma_x\sigma_y} \quad , \tag{3.22}$$

where σ_y and σ_x are the observed and simulated turbulence parameter standard deviation, respectively (Press et al., 2007). Furthermore, the correlation values were tested for significance using the p-value, which quantifies the probability of no cor-

relation using the students t-test (for p-values < 0.05 correlations are significant; Rice, 1988). These statistic methods have been shown to be effective in evaluating hydrological and atmospheric models (e.g. Krause et al., 2005; Elsanabary & Gan, 2013; Jia et al., 2013; Pinker et al., 2014).

3.3 Shamal Events Observations

During the 94 days of field observations four Shamal events were observed. These lasted between 2-3 days each and occurred on Feb 3-5 (Shamal event #1), Feb 12-14 (Shamal event #2), Mar 6-8 (Shamal event # 3), and Mar 24-27 (Shamal event #4) (Table 3.2). In this section we describe events #1-3 only since the hydrographic data for Shamal event #4 was contaminated due to biofouling that built-up towards the last month of the study period.

3.3.1 Shamal event #1

3.3.1.1 Meteorological conditions

Shamal event #1 started on Feb 3 02:10 and ended on Feb 5 19:20 (Fig. 3.7). The wind conditions pre- (-1 day) Shamal event and post- (+1 day) Shamal event were weak and variable in magnitude (<7.5 m/s) and direction. Winds during the event peaked in strength over two periods: (1) on Feb 3 17:30 to Feb 4 09:40 with a maximum wind speed of 14 m/s and surface stress of 0.58 N/m^2 and (2) on Feb 4 22:10 to Feb 5 08:20 with a maximum wind speed of 9.95 m/s and surface stress of 0.21 N/m^2 from the NW, i.e. directed along the coast (Fig. 3.7A and B). Air and SST temperatures followed a diurnal cycle with maximum drops (4 ^{o}C and 1 ^{o}C, respectively) during the first peak period (Fig. 3.7C). Also during that peak event period, the dry NW wind traveling over the continental land mass resulted in a decrease in relative humidity of 35% (Fig. 3.7D). Furthermore, during the event increase in atmospheric pressure of 11.4 mb was observed (Fig. 3.7E) as the frontal

system generating the Shamal passed through the region.

Commonly associated with Shamal events is rising dust from the Mesopotamian region which reduces solar radiation reaching the surface (Fig. 3.3) (details in Chapter 2). The rising dust during Shamal event #1 as reported by the Kuwait Meteorological Office observations has decreased the net solar radiation to 642 W/m^2 on the first day of the Shamal event (Feb 3) compared to 707 W/m^2 on Feb 6 (post-Shamal; Fig. 3.7F). Net longwave radiation responded to cloud cover, humidity, and sea surface temperature, and was a loss during this period. The largest loss of 103 W/m^2 occurred during the first peak period, while the lowest loss of 26 W/m^2 was observed during cloudy skies on the afternoon of Feb 2 (pre-Shamal; Fig. 3.7G). Similar to longwave radiation, the maximum loss of sensible heat flux (40 W/m^2; Fig. 3.7H) occurred during the first peak period. The most significant contributor to the surface heat flux was the latent heat flux. High evaporation rates, resulting from the relatively low humidity and strong winds during the first peak period generated latent heat flux losses up to 334 W/m^2 (Fig. 3.7I). The maximum net surface heat flux loss was 420 W/m^2 (Fig. 3.7J). Overall, the net surface heat flux followed a diurnal cycle with a maximum net heat gain of 603 W/m^2 during the post-Shamal afternoon when solar radiation peaked.

Table 3.2: Shamal events statistics

Shamal event #	*duration* [hr]	*average wind speed* m/s	*max wind speed* m/s	*max* J_q^0 W/m^2
1	65	8.64	13.97	420
2	53	8.36	12.13	479
3	61	9.11	15.12	511

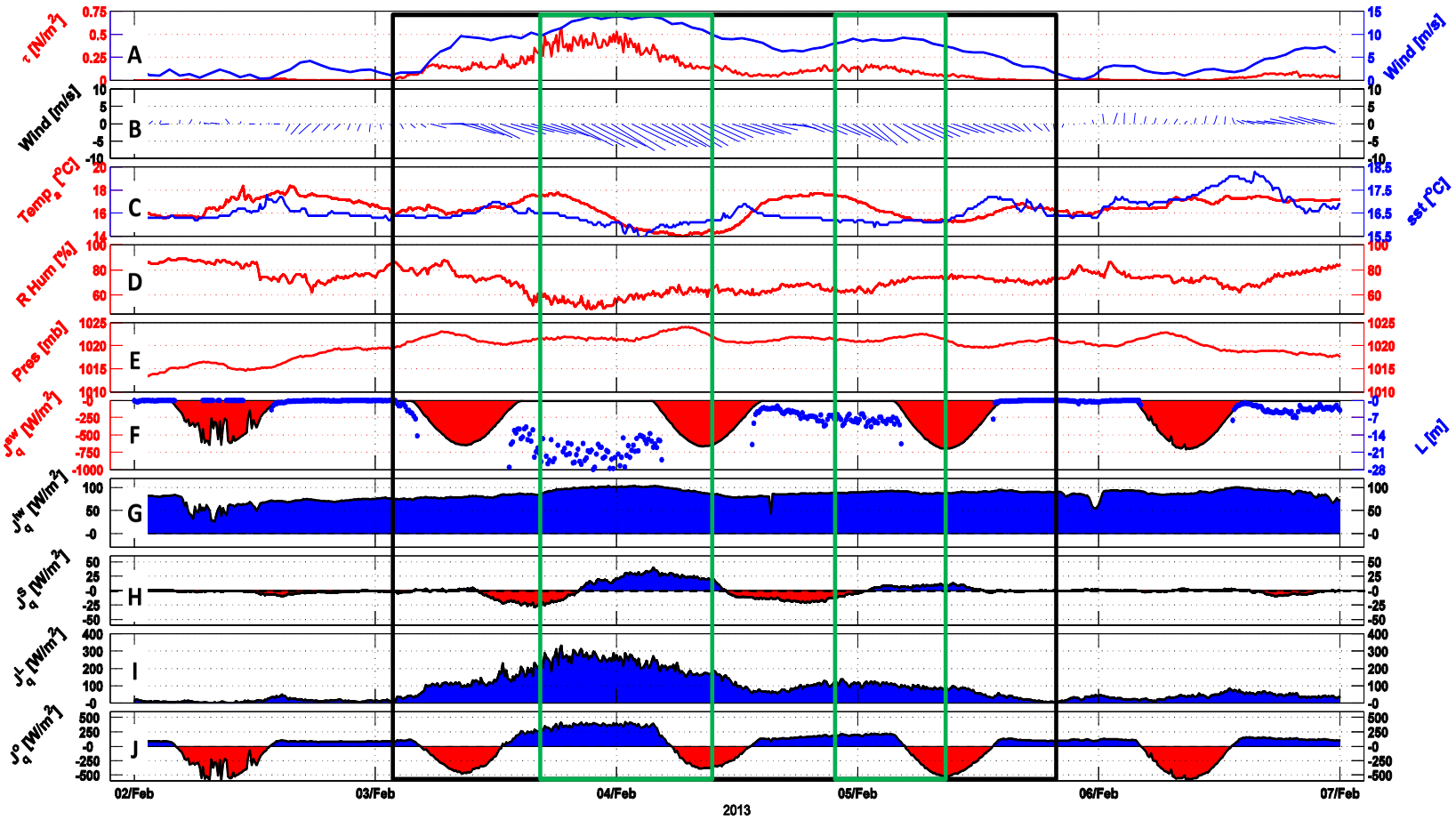

Figure 3.7: Meteorological data during Shamal event #1 (black box) and two wind peak periods (green boxes): (A) wind speed (blue) and wind stress (red), (B) wind speed vectors (to where wind blows), (C) air (red) and sea surface temperatures (blue), (D) relative humidity, (E) atmospheric pressure, (F) net shortwave radiation (shaded red) and Monin-Obukov length scale (blue dots), (G) net longwave radiation, (H) sensible heat, (I) latent heat, and (J) net surface heat flux. Time axis is in UTC and all are 10 min averages except wind data which is 1 hour averages.

3.3.1.2 Hydrographical conditions

Light intensity throughout the water column was dependent on the amount of solar radiation reaching the sea surface and decayed as a function of depth. Maximum values of 101 W/m^2 at 2.2 m depth and 11 W/m^2 at 22.0 m depth were observed on the afternoon of the post-Shamal day (Fig. 3.8B). The thermal structure followed three distinct patterns throughout the event.

The first pattern is the diurnal heating, consistent with the net surface heat flux (Fig. 3.8A), with relative warmer temperatures during day and relative cooler temperatures during night (Fig. 3.8C). The second distinct pattern of temperature is the gradual cooling of the water column in response to the Shamal event and warming during the post-Shamal event. Daily average temperatures for the whole water column during pre-Shamal (Feb 2), Shamal (Feb mid-3 to mid-5), and post-Shamal (Feb 6) were 16.37 ^{o}C, 16.35 ^{o}C, and 16.67 ^{o}C, respectively. The third temperature pattern is the change in water column temperature associated with horizontal advection (along and cross shore) (Fig. 3.8 E and F). To emphasize the connection between the horizontal currents and temperatures, a scatter plot was constructed (Fig. 3.9A1). This plot represents temperature versus the currents (along and cross shore) at a depth of 22 m for Feb 1-3. This depth and during the selected days minimizes the influence of surface forcing on temperature due to the depth being below the surface mixed layer and the relatively calmer surface conditions during those days. The figure suggests an average difference of 0.24 ^{o}C between the western component currents (NW 16.23 ^{o}C and SW 16.08 ^{o}C) and the eastern component currents (NE 16.49 ^{o}C and SE 16.29 ^{o}C), with the largest difference of 0.41 ^{o}C between the SW and the opposite NE currents. Based on the scatter plot results we are led to suggest that during the flooding tide phase (currents

flowing towards the NW) warmer waters were advected from the SE regions. While during the ebbing tide phase (currents flowing towards the SE) cooler waters were advected from the NE regions.

Similarly, the DO (Fig. 3.8D) followed two distinctive patterns. The first pattern is the response to the horizontal currents (Fig. 3.9A2), where eastern component currents increased (6.78 mg/L) the amount of DO and the western component currents decreased (6.74 mg/L) DO. Similar to temperature, the flooding tide phase advected more DO from the SE regions. While the ebbing tide phase advected less DO from the NW regions. The second pattern is the response of DO to the Shamal event. The daily average of DO in the water column increased on the progression of the Shamal event from 6.95 mg/L pre-Shamal to become 7.02 mg/L post-Shamal.

The along and cross shore currents followed the dominant semi-diurnal tide (Fig. 3.8E and F). During the flooding phase, the current throughout the water column flowed in the NW direction, while during ebbing phase the flow was to the SE. The current velocity ranged from -0.19 m/s to 0.28 m/s cross shore and -0.51 m/s to 0.53 m/s along shore. The amount of suspended particulate matter in the water column, as reflected by the ADCP (echo level), varied in the water column with most matter in suspension at depths of 20 - 25 m (Fig. 3.8G) during this period. The beginning 4 hours of the first and second peak of the Shamal period was when the strongest (69 dB) echo levels were recorded.

The buoyancy frequency in the water column was strongest ($> 3.2 \times 10^{-5}$ $1/s^2$) near the mixed layer depth, which is where the depth of the thermocline starts, indicating the presence of a strong stratified layer (Fig. 3.8H). The build-up of the warmer layer between 5 and 17 m depths during pre-Shamal increased stratification and thus the buoyancy frequency up to 1.7×10^{-3} $1/s^2$. On the beginning of the first peak period, wind induced vertical mixing, as indicated by the increase in depth of

the Monin-Obukov length scale (Fig. 3.7F), deepened the mixed layer, and weakened the buoyancy frequency. Unlike the first peak period, the weakening of the buoyancy frequency during the second peak period was induced by convective forcing, as indicated by the near zero Monin-Obukov length scale (Fig. 3.7F). The shear frequency in the water column was largest ($> 1.6 \times 10^{-3}$ $1/s^2$) around the mixed layer depth (Fig. 3.8I) as well as near the seabed (Fig. 3.10C), where the changes in along shore velocity with depth were relatively high (Fig. 3.8E and F). At depths of 23 - 26 m the shear frequency (Fig. 3.10C) followed a similar pattern to the along shore current velocity and increased up to 0.1 $1/s^2$ following the increase of the along shore current velocity eventually resulting in instability (Ri < 0.25; Fig. 3.8J). The shear frequencies during the two peak periods were low ($< 3.2 \times 10^{-3}$ $1/s^2$) relative to the other periods as the velocities were near homogeneous during these two periods.

3.3.1.3 Observed and simulated turbulence parameters

The turbulence parameters (TKE, TKE dissipation rate, Reynolds stress and eddy diffusivity; Fig. 3.10G-J) in the BBL ($\sim$23-27 m) mainly followed a consistent pattern in response to the instability (Ri < 0.25; Fig. 3.10F) due to shear (Fig. 3.10C) associated with the semi-diurnal tide. The maximum estimated TKE of 2.5 x 10^{-3} m^2/s^2 (Fig. 3.10G) was during the maximum recorded current speed of 0.25 m/s in the BBL on Feb 2 08:37 (pre-Shamal). The average observed TKE during the two peak phases of the Shamal event were lower (5.65 x 10^{-4} m^2/s^2) than the period average (6.92 x 10^{-4} m^2/s^2) and was less consistent with the tidal cycle. The model simulations were consistent with observations during the two Shamal peak phases and also simulated lower average TKE values (5.35 x 10^{-4} m^2/s^2) during the peak phases of the Shamal event. Overall, the results of TKE simulations by both models during this five day period were significantly (p-values < 0.05) correlated (≥ 0.66)

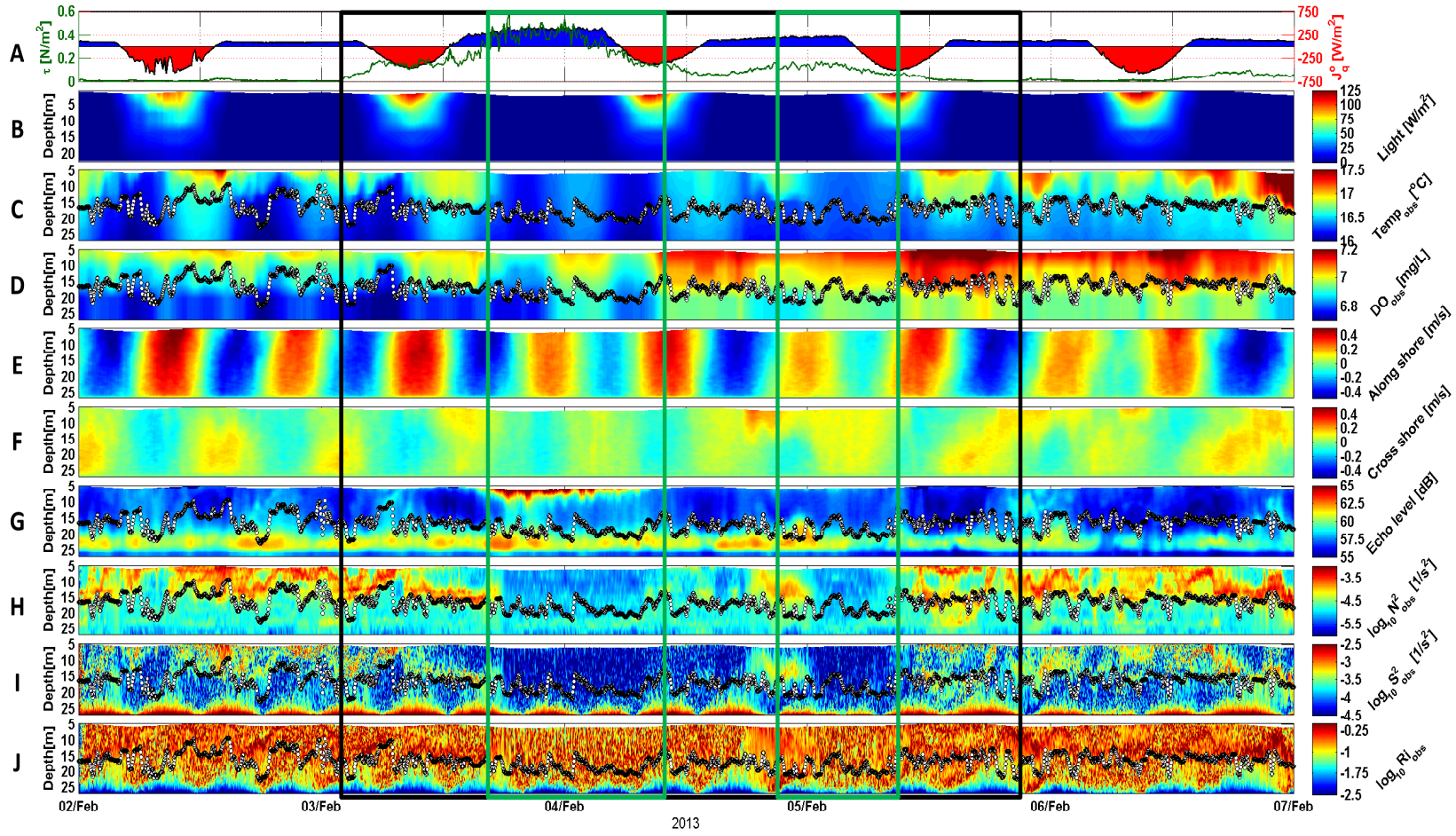

Figure 3.8: Hyrdographic observations during Shamal event #1 (black box) and two wind peak periods (green boxes) with the mixed layer depth marked by black dots: (A) wind stress (green) and net heat flux (shaded), (B) light intensity, (C) potential temperature, (D) dissolved oxygen, (E) along shore (315^o) current, (F) cross shore (45^o) current, (G) ADCP echo level, (H) N^2, (I) S^2, and (J) Ri number. Time axis is in UTC.

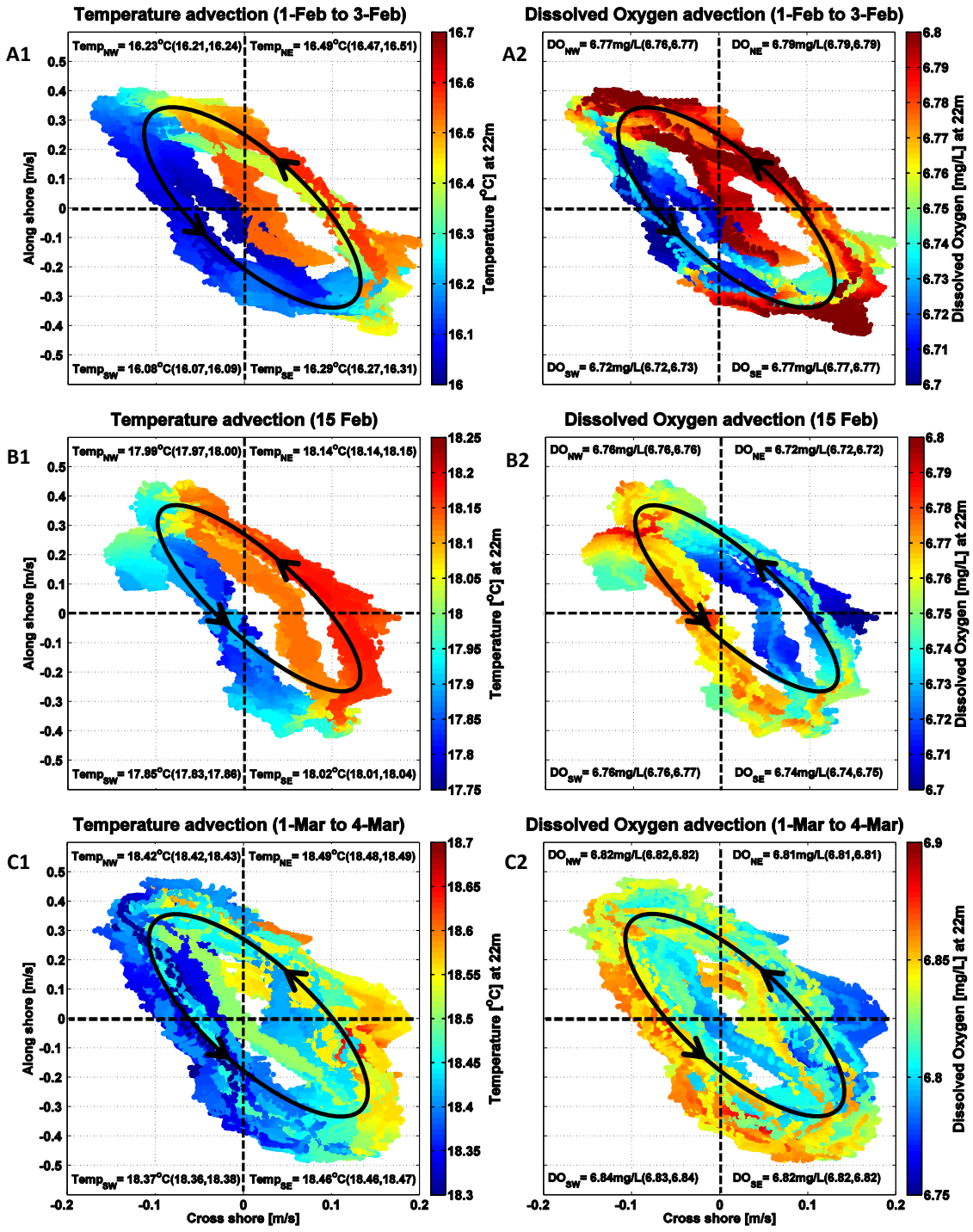

Figure 3.9: Scatter plots of temperature (left) and dissolved oxygen (right) versus currents at a depth of 22 m on: (A) Feb 1-3, (B) Feb 15, and (C) Mar 1-4. Average temperature and DO values for each quarter (NW, NE, SW and SE) and their 95% bootstrap confidence interval are presented in the respective quarters. Current ellipse are indicated in solid black.

with the observations as well as having low MBE ($\leq$ 3.8 x 10^{-4} m^2/s^2) and RMSE ($\leq$ 6.06 x 10^{-4} m^2/s^2) values (Table 3.3).

The TKE dissipation rates (Fig. 3.10H) and Reynolds stresses (Fig. 3.10I) followed a similar pattern to TKE. The average estimated TKE dissipation rates and Reynolds stresses during the five day period were 1.35 x 10^{-5} m^2/s^3 and 0.27 Pa, respectively. A cool plume generated by the Shamal winds on Feb 4 2:07 indicated by the vertical heat flux of -14.73 W/m^2 (Fig. 3.10B) in the BBL homogenized the water column and reduced the shear frequency (Fig. 3.10C). Although the shear frequency was relatively low during the cool plume, mixing was high, resulting in peak TKE dissipation rate and Reynolds stress values of 6.07 x 10^{-5} m^2/s^3 and 0.82 Pa, respectively. Both models k-kl and k-ε underestimated the mixing intensity during the cool plume with low TKE dissipation rates of 1.17 and 1.21 x 10^{-5} m^2/s^3 and Reynold stresses of 0.28 and 0.29, respectively. Similarly, during the second peak phase the Shamal induced convective forcing homogenized the water column and reduced the shear frequency at the BBL. However, unlike the first peak phase, the second peak phase mixing was lower than the five day average with a TKE dissipation rate of 7.43 x 10^{-6} m^2/s^3. Overall, the dominance of the tidal shear and the cool plume enhancing mixing, thus causing an increase in TKE dissipation rates and Reynolds stresses throughout the period were captured by both models with significant (p-values < 0.05) correlations ($\leq$ 0.63), positive Nash-Sutcliffe coefficients ($\leq$ 0.32), as well as low MBE and RMSE values (Table 3.3).

The observed vertical eddy diffusivity (Fig. 3.10J) followed a similar pattern to the other turbulence quantities. The observed eddy diffusivity average during the five day period was 0.06 m^2/s, which is similar to the k-kl models average. The observed and simulated eddy diffusivity values ranged between 7 x 10^{-4} and 0.48 m^2/s, with maximum values occurring during the first Shamal peak phase and

minimum values occurring before the first Shamal peak on Feb 3 12:55. Both models were consistent with the observations throughout the period with significant (p-values < 0.05) correlations (0.79), positive Nash-Sutcliffe coefficients (0.6), as well as low MBE (< 0.58 x 10^{-2} m^2/s) and RMSE (< 5.11 x 10^{-2} m^2/s) values (Table 3.3).

Simulations of the turbulence parameters by both models (k-kl and k-ε) during this period were similar to one another (r=1 and $N_s \geq 0.98$). Moreover, the satisfactory agreement between the observed and simulated turbulence parameters has led us to suggest that the tidal current shear and convection driven turbulence were reproduced by two equation turbulence models (k-kl and k-ε).

3.3.2 Shamal event #2

3.3.2.1 Meteorological conditions

Shamal event #2 started on Feb 12 12:30 and ended on Feb 14 17:30 (Fig. 3.11). The winds pre-Shamal were strong in magnitude (up to 11.15 m/s) from the SE, which are common during winter pre-Shamals (details in Chapter 2) (Fig. 3.11 A and B). Similar to event #1, winds during the event peaked in strength over two periods: (1) on Feb 12 23:30 to Feb 13 12:40 with a maximum wind speed of 12.13 m/s and surface stress of 0.35 N/m^2 and (2) on Feb 13 21:00 to Feb 14 13:30 with a maximum wind speed of 11.69 m/s and surface stress of 0.26 N/m^2 from the NW, i.e. directed along the coast (Fig. 3.11A and B). This event is the shortest in duration (53 hours) and had the weakest wind speeds (average 8.36 m/s) compared to the other three recorded events. The air temperature followed a diurnal cycle with maximum drops of 2.9 ^oC and 3.0 ^oC occurring during the two peak periods, respectively (Fig. 3.11C). Similarly, the SST followed a diurnal pattern with a minimum recorded temperatures as low as 17.5 ^oC occurring during the pre-Shamal SE winds. The dry Shamal winds have decreased humidity from 95% to 57% (Fig. 3.11D). Furthermore, an increase

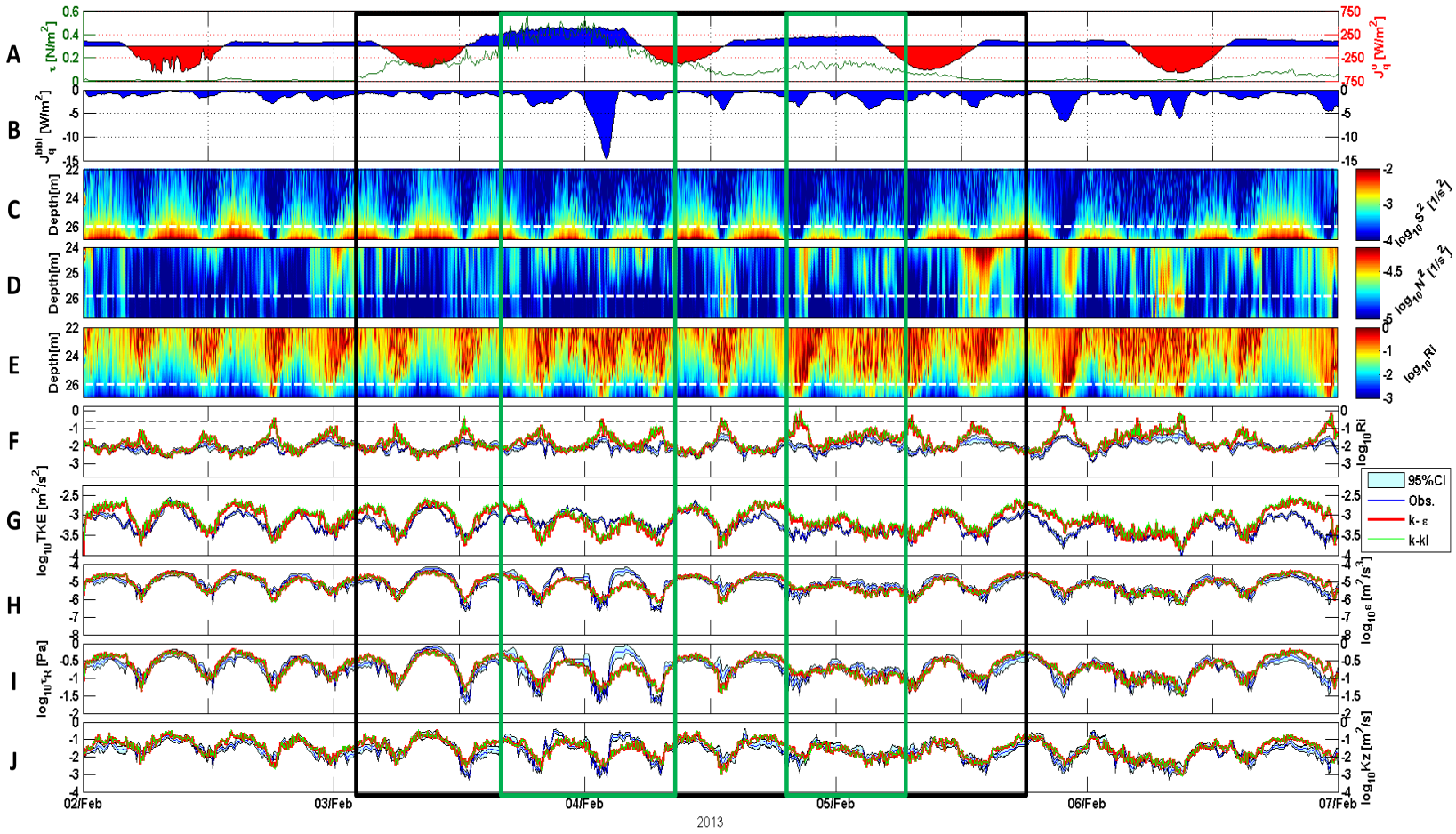

Figure 3.10: Comparisons of turbulence parameters computed from observations (blue) to those from k-ε (red) and k-kl (green) model simulations in the BBL at a depth of 25.8 m (white broken line) during Shamal event #1 (black box) and two wind peak periods (green boxes): (A) wind stress (green) and net heat flux (shaded), (B) vertical heat flux, (C) BBL S^2, (D) BBL N^2, (E) BBL Ri number, (F) Ri number, (G) TKE, (H) TKE dissipation rate, (I) Reynolds stress, and (J) vertical eddy diffusivity. Time axis in UTC.

Table 3.3: Statistics and their 95% CI (in parenthesis) for the observed and simulated turbulence parameters during Shamal event #1.

		min	max	average	MBE	RMSE	N_s	r
	Obs.	0.81	25	6.92	-	-	-	-
				(6.7,7.1)				
TKE	k-ε	1.51	29	9.68	2.76	4.99	0.08	0.68
10^4 $[m^2/s^2]$				(9.39,10.02)	(2.55,3.01)	(4.76,5.26)	(0.01,0.17)	(0.64,0.71)
	k-kl	1.49	32	10.74	3.80	6.06	0.37	0.66
				(10.35,11.10)	(3.52,4.11)	(5.75,6.36)	(0.26,0.48)	(0.63,0.69)
	Obs.	0.01	6.07	1.35	-	-	-	-
				(1.28,1.41)				
ε	k-ε	0.05	4.63	1.23	-0.12	0.95	0.33	0.63
10^5 $[m^2/s^3]$				(1.18,1.29)	(-0.17,-0.06)	(0.87,1.04)	(0.26,0.40)	(0.59,0.68)
	k-kl	0.04	4.72	1.28	-0.11	0.95	0.32	0.63
				(1.18,1.29)	(-0.16,0.06)	(0.87,1.04)	(0.27,0.39)	(0.58,0.68)
	Obs.	0.02	0.82	0.27	-	-	-	-
				(0.26,0.28)				
τ_b	k-ε	0.04	0.71	0.26	0.00	0.13	0.37	0.67
$[Pa]$				(0.25,0.27)	(-0.01,0.00)	(0.12,0.14)	(0.32,0.43)	(0.63,0.71)
	k-kl	0.04	0.71	0.26	0.00	0.13	0.37	0.67
				(0.26,0.27)	(-0.01,0.00)	(0.12,0.14)	(0.31,0.43)	(0.63,0.71)
	Obs.	0.07	48.7	5.74	-	-	-	-
				(5.44,6.12)				
K_z	k-ε	0.08	28.5	5.15	-0.58	4.97	0.60	0.79
10^2 $[m^2/s]$				(4.87,5.43)	(-0.88,-0.31)	(4.55,5.54)	(0.55,0.65)	(0.75,0.82)
	k-kl	0.08	34.2	5.55	-0.19	5.11	0.60	0.78
				(5.22,5.85)	(-0.99,-0.05)	(4.72,5.68)	(0.55,0.64)	(0.75,0.81)

in atmospheric pressure of 13.1 mb was observed (Fig. 3.11E) as the frontal system generating the Shamal advanced towards the region.

The net shortwave radiation followed a diurnal pattern with recorded values up to 738 W/m^2 occurring post-Shamal (Fig. 3.11F). The well defined net shortwave radiation bell shaped was broken on Feb 11 and 12 daytime due to cloud clover. Furthermore, the cloud cover and humid conditions occurring pre-Shamal resulted in minimum net longwave radiation losses of 8 W/m^2, while maximum losses of 108 W/m^2 occurred during the second peak period (Fig. 3.11G). The sensible heat flux followed a pattern in response to the difference between air temperature and SST. The sensible heat flux was negative (gain) during the periods when the air temperature was warmer than SST and was positive (loss) when air temperature was cooler. Moreover, the maximum computed sensible heat flux of 34 W/m^2 occurred during the largest difference between air temperature and SST of 2.4 ^{o}C during pre-Shamal. Similarly, the minimum computed sensible heat flux of -40 W/m^2 occurred during the minimum temperature differences between air temperature and SST of -2.1 ^{o}C during second peak period (Fig. 3.11H). The latent heat flux responded to the evaporation rate with maximum losses of 266 W/m^2 occurring during the second peak (Fig. 3.11I). The net heat flux followed a diurnal cycle with values ranging between -677 W/m^2 (post-Shamal afternoon) and 479 W/m^2 (second peak period) (Table 3.2).

3.3.2.2 Hydrographical conditions

The hydrographic observations during this period responded to two types of wind events: SE event and Shamal event (Fig. 3.12). The cloudy conditions during the SE event reduced the light intensity throughout the water column to an average of 21 W/m^2 during the afternoon of Feb 11. This is lower compared to the Shamal

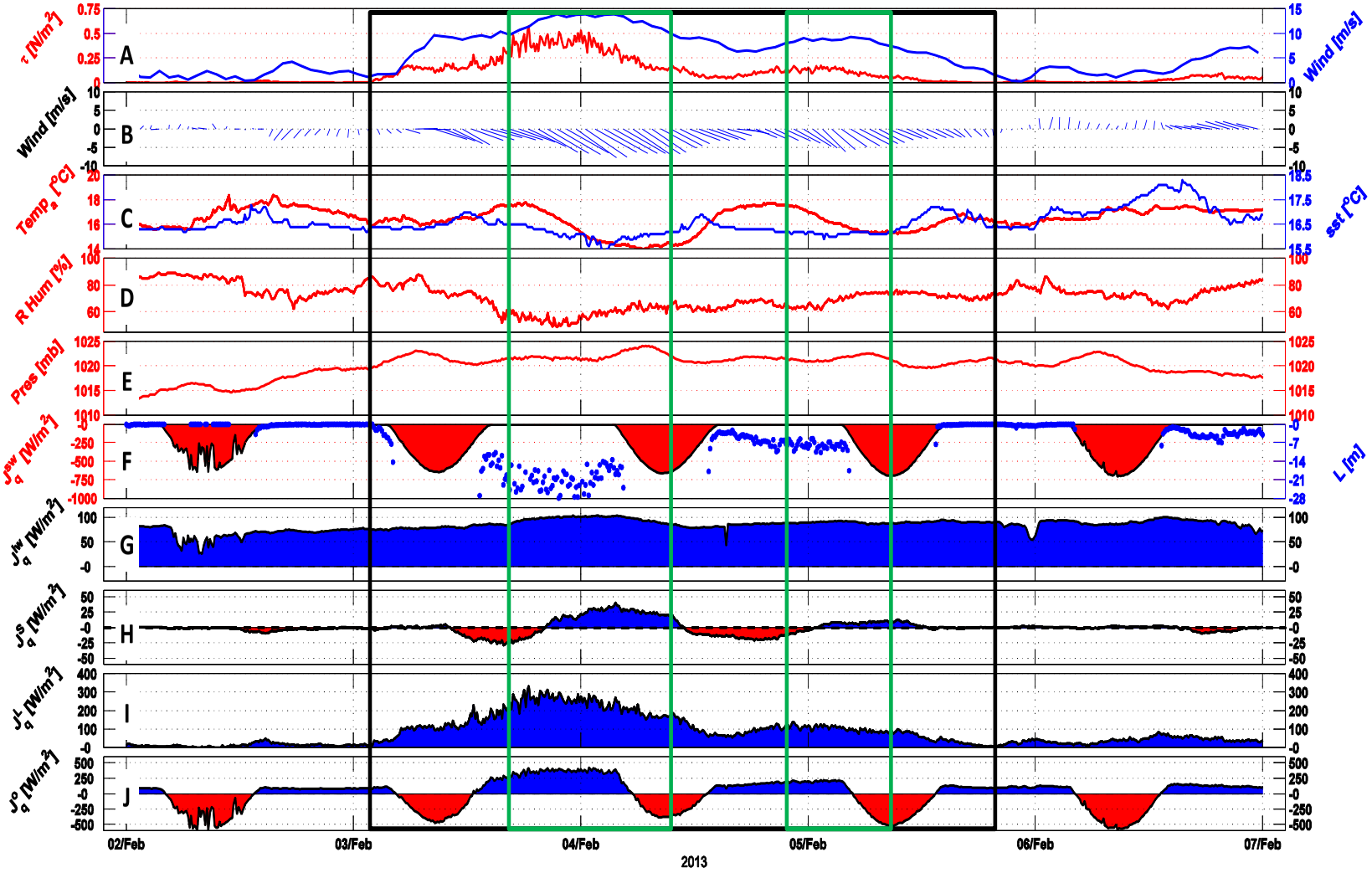

Figure 3.11: Same as Figure 3.7 but for Shamal event #2.

event afternoons of 35 W/m^2 and post-Shamal afternoon of 36 W/m^2 (Fig. 3.11B).

Similar to event #1, the temperature structure throughout the five days followed three patterns (Fig. 3.11C). The first pattern is the diurnal heating, which is consistent with the net heat flux. The second is the water column temperature response to the SE and Shamal events. The daily water column average temperature cooled between the start and end of the SE event (Feb 10 to 12) from 17.81 ^{o}C to 17.67 ^{o}C (Feb 11 to 12). Moreover, at the end of the SE event (Feb 12 02:30) and before the Shamals first peak phase (Feb 12 23:30) the surface mixed layer (0-15 m) gradually warmed to become 18.23 ^{o}C. As the event strengthened during the first peak phase, the wind induced vertical mixing increased, as indicated by the increase in depth of the Monin-Obukov length scale (Fig. 3.11F). This deepened the mixed layer depth (up to 21.9 m) causing the deeper waters (below the mixed layer) to warm to 18.01 ^{o}C and the mixed layer waters to cool to 18.31 ^{o}C. This was followed by a gradual cooling in temperatures as the second peak phase progressed to reach a daily average water column temperature of 18.05 ^{o}C by the end of the Shamal event. The third temperature pattern is the change in temperature due to horizontal advection. Similar to Figure 3.9A, a depth of 22 m and the calm post-Shamal conditions period was chosen to minimize the surface forcing effects. Figure 3.9B1 suggests that eastern current component (NE and SE) resulted in warmer temperatures (18.08 ^{o}C), compared to the cooler (17.92 ^{o}C) western component currents. Moreover, during the flooding tide phase warmer waters were advected from the SE regions. While during the ebbing tide phase cooler waters were advected from the NE regions.

Similar to event #1, the DO followed two patterns. The first pattern is the response of DO to the events of this period. The average water column DO ranged between 6.65 mg/L and 6.92 mg/L throughout the five day period (Fig. 3.12D). The maximum DO was on Feb 11 19:18 during the SE event and the minimum DO was

during the surface calm conditions on Feb 12 03:24 pre-Shamal. The average water column DO dropped from 6.87 mg/L during pre-Shamal to 6.86 mg/L by the end of the Shamal period. The second pattern is the response of DO to horizontal advection (Fig. 3.9B2). Unlike event #1, during this period the western component currents resulted in lower DO (6.73 mg/L) than the eastern component currents (6.76 mg/L). The flooding phase advected less DO from the SE regions. While the ebbing phase advected more DO from the NW regions.

The along and cross shore currents followed the dominant semi-diurnal tide (Fig. 3.12E and F) as observed in event #1. During the flooding phase, the current throughout the water column flowed in the NW direction, while during ebbing phase the flow was to the SE. The maximum (0.37 m/s) and minimum (-0.23 m/s) recorded cross shore current occurred during the first peak phase. The maximum (0.67 m/s) recorded along shore current occurred during the beginning of the SE event on Feb 11 06:03, while the minimum (-0.75 m/s) recorded along shore current occurred at the end of the SE event on Feb 12 00:21.

The maximum water column suspended particulate was observed during the SE event (average 58.95 dB). The suspended particulate matter decreased to 57.68 dB during the Shamal event (Fig. 3.12G) and remained more-or-less similar during the post-Shamal (57.73 dB).

The buoyancy frequency in the water column was largest ($> 3.1 \times 10^{-5}$ $1/s^2$) around the mixed layer depth (Fig. 3.12H). The warming of the mixed layer and a decreased in its depth from 21 to 11 m prior to the SE event (Feb 11 mid-night to 10:30) enhanced the buoyancy frequency (0.002 $1/s^2$) near the surface. This warm and stratified layer was cooled and weakened by the SE event, which resulted in a deepening of the mixed layer depth to 22 m and a weakening of the buoyancy frequency around the mixed layer depth to 6.32×10^{-5} $1/s^2$. After the SE event and

before the first Shamal peak phase, the mixed layer warmed again. This enhanced stratification and resulted in a shallower mixed layer depth of 12 m and higher buoyancy frequency of 7.63 x 10^{-4} $1/s^2$. The strengthening of the Shamal event gradually deepened the mixed layer depth to 21.2 m and decreased the buoyancy frequency to the minimum computed value of 2.52 x 10^{-6} $1/s^2$ towards the end of the second peak phase.

The shear frequency in the water column was largest (> 2.6 x 10^{-3} $1/s^2$) around the mixed layer depth (Fig. 3.12I) and the seabed (Fig. 3.13C), where the changes in along shore velocity with depth were the highest (Fig. 3.12E). At the depths of 23 - 27 m the shear frequency followed a similar pattern to the along shore current velocity (Fig. 3.13C) and increased up to 0.05 $1/s^2$ following the increase of the along shore current velocity eventually resulting in instability (Ri < 0.25; Fig. 3.12J). The water column average shear frequency decreased from 9.96 x 10^{-4} $1/s^2$ at the start of the Shamal event towards the end of the second peak phase to become 7.51 x 10^{-4} $1/s^2$.

3.3.2.3 Observed and simulated turbulence parameters

Similar to Shamal event #1 the turbulence parameters (TKE, TKE dissipation rate, Reynolds stress, and eddy diffusivity; Fig. 3.13 G-J) in the BBL ($\sim$23-27 m) followed a consistent pattern in response to the instability (Ri < 0.25; Fig. 3.13F) due to the shear (Fig. 3.13C) associated with the semi-diurnal tide. However, unlike Shamal event #1, the shear frequency in the BBL did not decrease during the Shamal. Furthermore, the vertical heat flux in the BBL (Fig. 3.13B) during this relatively weaker event is lower (-6.05 W/m^2) compared to event #1. The TKE peaked during the SE event on Feb 11 06:03 with a value of 3.8 x 10^{-3} m^2/s^2 (Fig. 3.13G) following the peak along shore current speed of 0.67 m/s. Similar to Shamal event #1, the

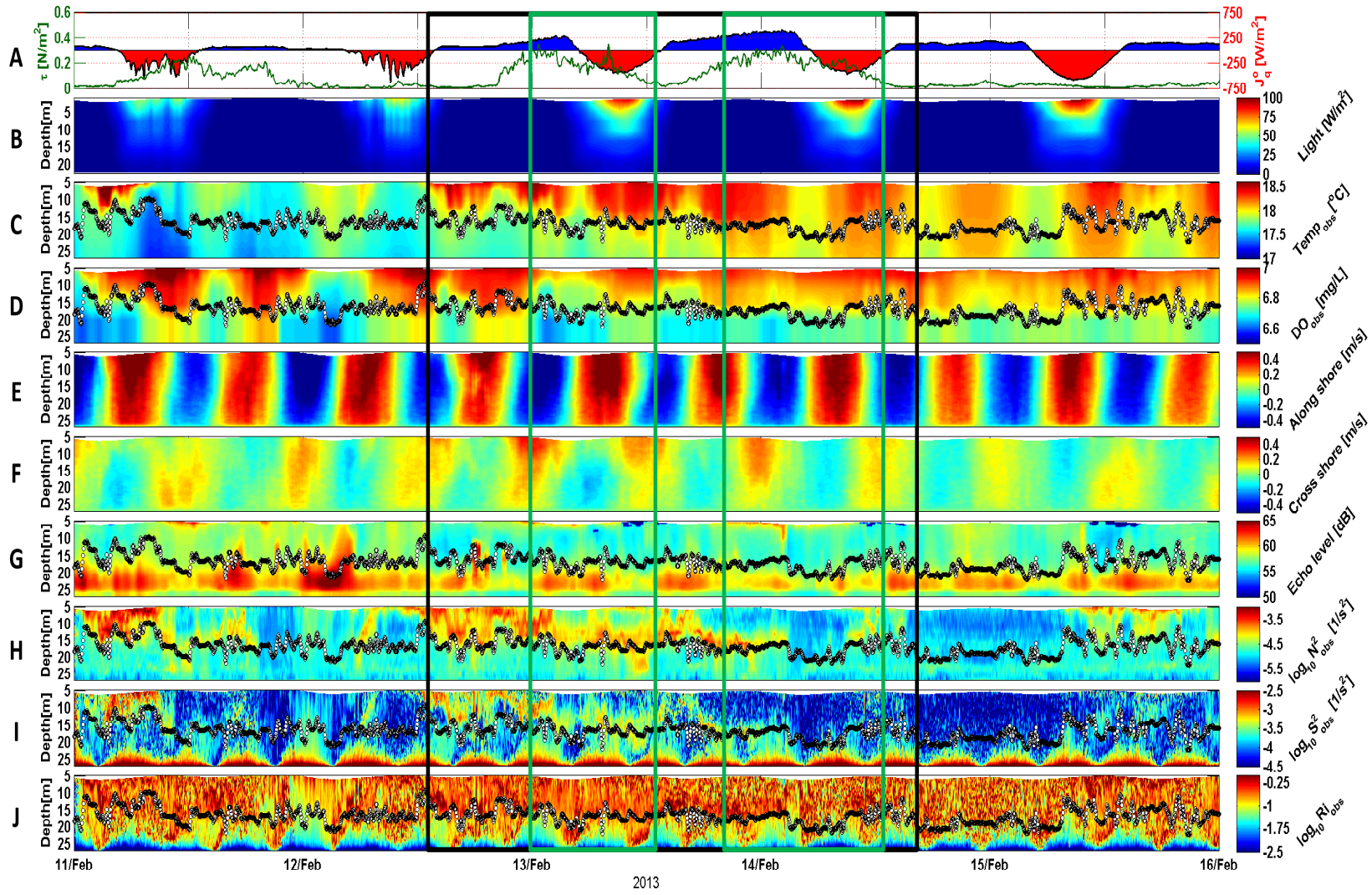

Figure 3.12: Same as Figure 3.8 but for Shamal event #2.

average TKE during the two peak phases of the Shamal event was lower (9.21 x 10^{-4} m^2/s^2) than the period average (9.33 x 10^{-4} m^2/s^2). Moreover, TKE was above (9.9 x 10^{-4} m^2/s^2) average during the SE wind event. The results of TKE simulations by both models during this five day period were significantly (p-values <0.05) correlated ($\geq$ 0.64) with the observations as well as having low MBE ($\leq$ 6.48 x 10^{-4} m^2/s^2) and RMSE ($\leq$ 9.57 x 10^{-4} m^2/s^2) values (Table 3.4).

The TKE dissipation rates (Fig. 3.13H) and Reynolds stresses (Fig. 3.13I) followed a similar pattern to TKE. The five day period averages for TKE dissipation rates and Reynolds stresses were 2.48 x 10^{-5} m^2/s^3 and 0.44 Pa, respectively. These two parameters were higher than the period average during the Shamal event with values of 3.10 x 10^{-5} m^2/s^3 and 0.48 Pa. Moreover, the two parameters peaked during the end of the second peak phase at Feb 14 8:07 with values of 9.83 x 10^{-5} m^2/s^3 and 1.18 Pa. The peak of both parameters followed the mixing layer depth deepening to 21.3 m, higher shear frequency, and a decrease in the water column buoyancy frequency to 2.52 x 10^{-6} $1/s^2$ (Fig. 3.12G). The dominance of the tidal shear enhancing mixing on the TKE dissipation rates and Reynolds stresses throughout the period were also captured by both models with significant (p-values <0.05) correlations ($\leq$ 0.73), positive Nash-Sutcliffe coefficients ($\leq$ 0.5), as well as low MBE and RMSE values (Table 3.4).

The observed vertical eddy diffusivity (Fig. 3.13J) followed a similar trend to the other turbulence quantities. The observed eddy diffusivity average during the five day period was 0.01 m^2/s, which is similar to both model averages. The observed and simulated eddy diffusivity values peaked during pre-Shamal following the maximum recorded TKE and along shore current velocity on Feb 11 06:03. Both models were consistent with the observations throughout the period with significant (p-values < 0.05) correlations (0.73), positive Nash-Sutcliffe coefficients (0.52), as well as low

MBE (< 1 x 10^{-4} m^2/s) and RMSE (< 0.01 m^2/s) values (Table 3.4).

As in Shamal event #1 the simulations of the turbulence parameters by both models (k-kl and k-ε) during this period were similar to one another (r=1 and $N_s \geq 0.98$) and have been consistent in following the dominant semi-diurnal tide effect.

3.3.3 Shamal event #3

3.3.3.1 Meteorological conditions

Shamal event #3 started on Mar 6 01:30 and ended on Mar 8 15:10 (Fig. 3.14). The winds pre-Shamal during this event were similar to event #2 a strong in magnitude winds (up to 10.14 m/s) from the SE (Fig. 3.14A and B) were measured. Similar to the previous two events, this event peaked in strength over two periods: (1) on Mar 6 4:40 to 9:10 with a maximum hourly wind speed of 11.38 m/s and surface stress of 0.2 N/m^2 and (2) on Mar 6 21:40 to Mar 7 23:40 with a maximum hourly wind speed of 15.12 m/s and surface stress of 0.67 N/m^2 from the NW (Fig. 3.14A and B). This event was the strongest in wind magnitude (average 9.11 m/s) compared to the other three events. The air temperature ranging between 22.4 ^oC and 14.3 ^oC and followed a diurnal cycle (Fig. 3.14C); the latter temperature occurred during the mid-second peak phase. The daily average air temperatures dropped from 20.9 ^oC to 18.9 ^oC as the Shamal intensified. The minimum recorded SST of 17.6 ^oC occurred during the mid-second peak phase and the maximum SST of 19.6 ^oC occurred during the beginning of the pre-Shamal SE event. The dry Shamal winds have resulted in a decrease of humidity from 94% to 33% (Fig. 3.14D). Furthermore, the event resulted in an increase in the daily average atmospheric pressure from 1007 mb to 1017 (Fig. 3.14E) as the frontal system generating the Shamal passed through the region.

The net solar radiation followed a diurnal pattern with a minimum day average

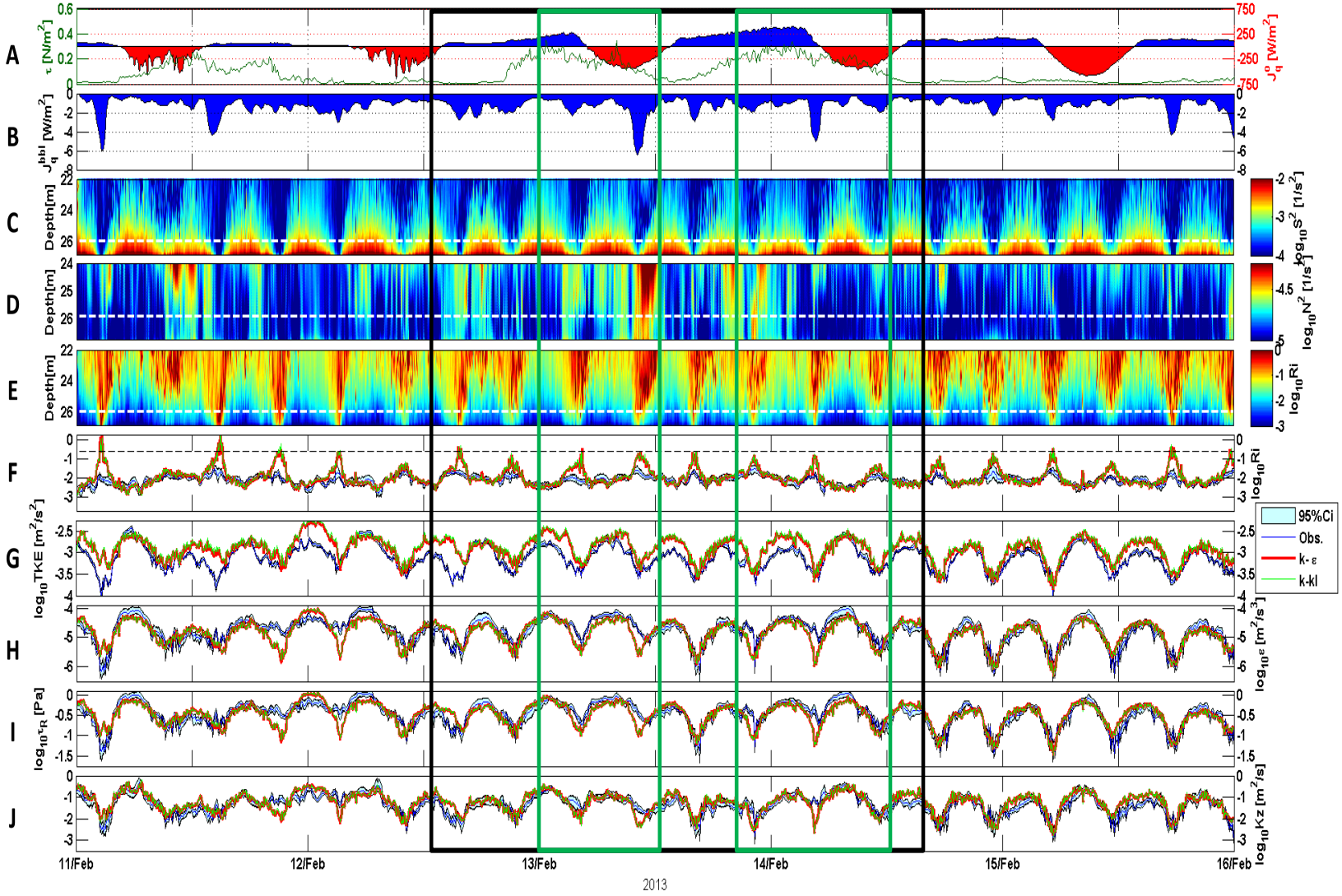

Figure 3.13: Same as Figure 3.10 but for Shamal event #2.

Table 3.4: Same as Table 3.3 but for Shamal event #2.

		min	max	average	MBE	RMSE	N_s	r
	Obs.	1.02	37.81	9.33	-	-	-	-
				(8.99,9.67)				
TKE	k-ε	1.63	55.83	14.53	5.18	8.03	0.07	0.67
10^4 $[m^2/s^2]$				(14.09,15.01)	(4.83,5.50)	(7.54,8.64)	(0.01,0.13)	(0.64,0.69)
	k-kl	1.75	63.40	15.82	6.48	9.57	0.17	0.64
				(15.34,16.34)	(6.12,6.89)	(8.97,10.25)	(0.08,0.26)	(0.61,0.67)
	Obs.	0.05	9.83	2.48	-	-	-	-
				(2.36,2.59)				
ε	k-ε	0.06	9.23	2.06	-0.42	1.14	0.50	0.74
10^5 $[m^2/s^3]$				(1.98,2.15)	(-0.51,-0.34)	(1.32,1.49)	(0.47,0.53)	(0.71,0.76)
	k-kl	0.06	9.81	2.08	-0.39	1.44	0.48	0.72
				(2.00,2.18)	(-0.47,-0.31)	(1.36,1.53)	(0.45,0.52)	(0.70,0.75)
	Obs.	0.04	1.18	0.44	-	-	-	-
				(0.42,0.45)				
τ_b	k-ε	0.04	1.16	0.40	-0.04	0.16	0.57	0.78
$[Pa]$				(0.38,0.41)	(-0.05,-0.03)	(0.15,0.17)	(0.54,0.59)	(0.76,0.80)
	k-kl	0.04	1.16	0.40	-0.04	0.16	0.57	0.78
				(0.39,0.41)	(-0.05,-0.03)	(0.15,0.17)	(0.54,0.59)	(0.76,0.80)
	Obs.	0.01	85.6	0.94	-	-	-	-
				(0.89,1.11)				
K_z	k-ε	0.02	51.2	0.86	-0.08	0.69	0.60	0.79
10^2 $[m^2/s]$				(0.81,0.91)	(-0.12,-0.4)	(0.58,0.77)	(0.55,0.65)	(0.75,0.82)
	k-kl	0.02	64.3	0.92	-0.02	0.66	0.60	0.78
				(0.87,0.96)	(-0.06,-0.01)	(0.60,0.76)	(0.55,0.64)	(0.75,0.81)

of 299 W/m^2 occurring during a dust storm accompanying the Shamal on Mar 6 (Figs. 3.3 and 3.14F). Furthermore, the peak net solar radiation was 817 W/m^2 occurred during the post-Shamal afternoon. Similar to Shamal event #2, the cloud cover as well as moisture associated with the SE wind event during pre-Shamal resulted in minimum longwave radiation losses of 4 W/m^2, while maximum losses of 111 W/m^2 occurred during the second peak period (Fig. 3.14G). The sensible heat flux responded to the difference between air temperature and SST. The sensible heat flux peaked (43 W/m^2) during the largest difference between air temperature and SST of 3.3 ^{o}C occurring during the pre-Shamal SE event. Similarly, maximum losses of sensible heat flux of 69 W/m^2 occurred at the lowest difference between air temperature and SST of -4.3 ^{o}C during the second peak period (Fig. 3.14H). The latent heat flux responded to the evaporation rate with a maximum loss of 406 W/m^2 computed during the second peak (Fig. 3.14I). The net heat flux followed a diurnal cycle with values ranging between -511 W/m^2 (post-Shamal afternoon) and 701 W/m^2 (second peak period).

3.3.3.2 Hydrographical conditions

The hydrographic observations (Fig. 3.15) during this period responded to convective forcing during the night, as indicated by the near zero Monin-Obukov length scale (Mar 3, 7 and 8 nights) and two wind events (SE event and Shamal event). The cloudy conditions during the SE event reduced the light intensity throughout the water column from an average of 52 W/m^2 on Mar 4 to 36 W/m^2 during the afternoon of Mar 5 (Fig. 3.15B). The light intensity measurements during the daytime of the first Shamal event day is lower (max recorded value of 43 W/m^2) compared to the other days due to the rising dust conditions during that day (Fig. 3.3).

Similar to the previous two Shamal events, the temperature structure (Fig. 3.15C)

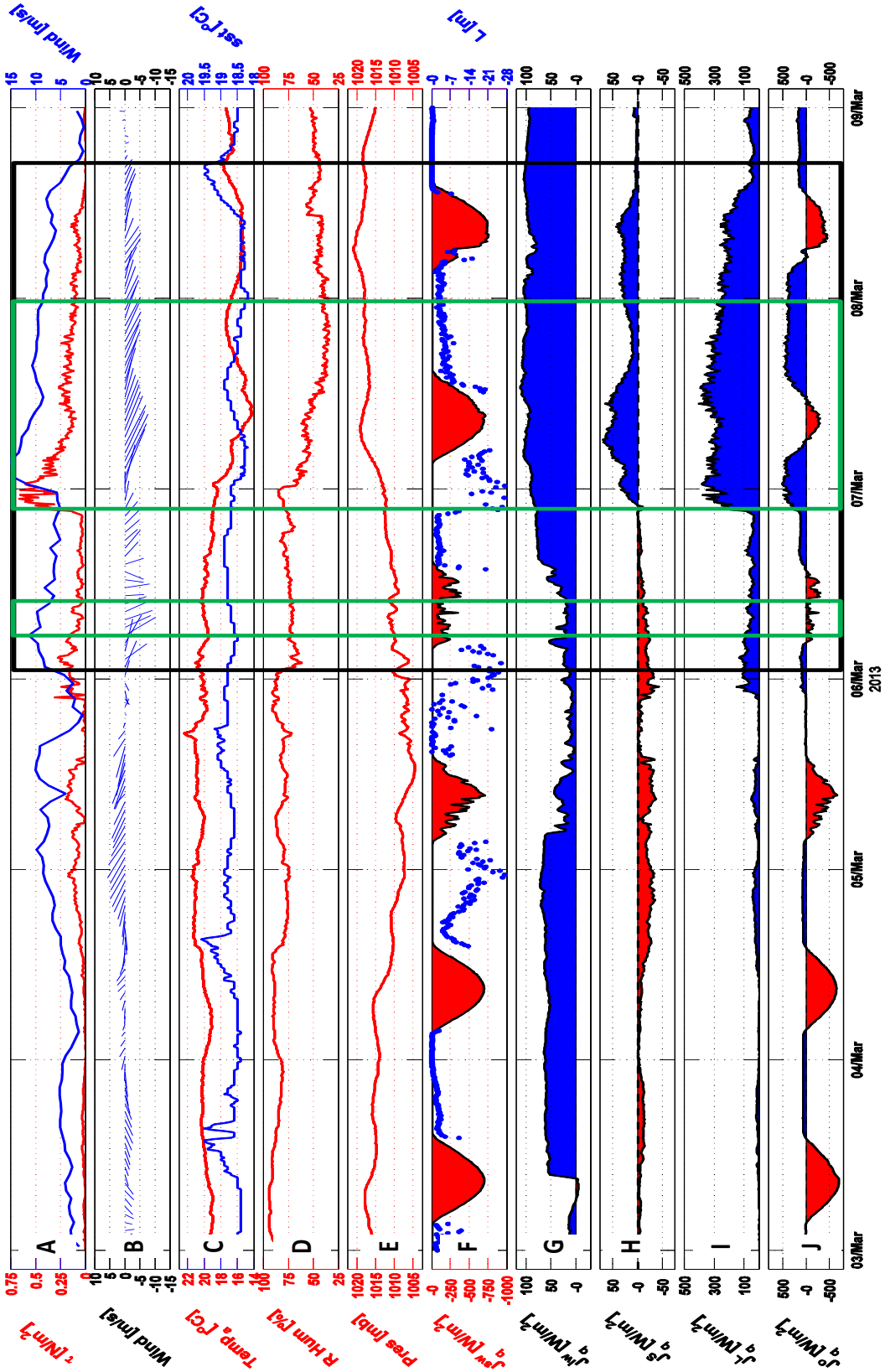

Figure 3.14: Same as Figure 3.7 but for Shamal event #3.

throughout this six days followed three patterns. The first is the diurnal heating, consistent with the net heat flux. During the calm wind (<5 m/s) evening of Mar 3, night convection indicated by near zero Monin-Obukov (Fig. 3.14F) prior to the SE event caused the mixed layer depth to deepen to the seabed and cooling of the water column. Next, the daytime heating and calm winds on Mar 4 prior to the SE event resulted in the warming of the surface waters to reach a maximum measured value of 19.23 ^{o}C in the afternoon. This daytime heating also reduced the depth of the mixed layer from 26.8 m to 17.2 m. The second temperature pattern is the temperature response to the SE and Shamal events. The SE events resulted in the deepening of the mixed layer (16.5 m to 17.5 m) and warming (18.63 ^{o}C to 18.73 ^{o}C) of the water column temperature between Mar 4 and 5 as the warmer surface waters penetrated deeper in the water column. This warming was followed by a period of cooling along the progression of the Shamal event to become 18.58 ^{o}C by the end of the Shamal period. The third temperature pattern is the response of the temperature to horizontal advection. Similar to Figures 3.9A and B, a depth of 22 m and the calm conditions prior the SE events period were chosen to reduce the surface forcings influence. Figure 3.9C1 suggests that eastern current component (NE and SE) resulted in warmer temperatures (18.48 ^{o}C), compared to the cooler (18.39 ^{o}C) western component currents (NW SW), which is similar to the previous two periods. Moreover, during the flooding tide phase warmer waters were advected from the SE regions. While during the ebbing tide phase cooler waters were advected from the NE regions.

The average water column DO ranged between 6.58 mg/L and 7.04 mg/L between Mar 3 and 5 (Fig. 3.15D). We have excluded the DO data post Mar 5 due to the degradation of the DO data from biofouling. Similar to the thermal structure, the deepening of the mixed layer depth to the seabed on the evenings of Mar 3 and

4 has led to an increase in DO near the seabed from 6.71 mg/L to 6.87 mg/L. Furthermore, the DO during this period also responded to horizontal advection (Fig. 3.9C2), where eastern component currents (NE and SE) resulted in lower DO (8.81 mg/L) compared to the DO rich (6.83 mg/L) western component currents (NW SW), which is similar to the Shamal event #2 period. The flooding tide phase advected less DO from the SE regions. While the ebbing tide phase advected more DO from the NW regions.

The along and cross shore currents followed the dominant semi-diurnal tide (Fig. 3.15E and F) as observed during the previous two Shamal events. During the flooding phase, the current throughout the water column flowed in the NW direction, while during ebbing phase the flow was to the SE. The maximum (0.21 m/s) and minimum (-0.20 m/s) recorded cross shore current occurred on the afternoon of Mar 3. During this same period, the maximum (0.56 m/s) and minimum (-0.53 m/s) along shore currents were recorded.

The water column average suspended particulate matter throughout this period peaked during two periods. The first was post SE event on the evening of Mar 5 and the second was during the second peak phase of the Shamal event with a water column average of 69.65 dB.

The buoyancy frequency in the water column was largest ($> 3.2 \times 10^{-5}$ $1/s^2$) around the mixed layer depth (Fig. 3.15H). The daytime warming of the sea surface prior the SE event (on Mar 3 and 4) enhanced the buoyancy frequency to a maximum value of 1.1×10^{-3} $1/s^2$ near the surface and decreased the mixed layer depth to 16.5 m. This warm layer was cooled during the SE event, which resulted in a deepening of the mixed layer to 17.5 m, and a weakened buoyancy frequency around mixed layer depth of 3.98×10^{-5} $1/s^2$. With the progression of the Shamal event, the water column buoyancy frequency decreased during the two peak phases to values < 7.94 x

10^{-6} $1/s^2$ and started to increase post-Shamal to an average water column buoyancy frequency of 1.65 x 10^{-5} $1/s^2$.

The shear frequency in the water column (Fig. 3.15I) was strongest near the seabed (Fig. 3.16C) with an average of 1.3 x 10^{-3} $1/s^2$ at the lower 3 m where the changes in velocity with depth were relatively high. Moreover, shear frequency followed a similar pattern to the along shore current velocity and increased up to 5 x 10^{-3} $1/s^2$ following the increase of the along shore current velocity eventually leading to instability (Ri $<$ 0.25; Fig. 3.15J). The water column average shear frequency decreased from 5.91 x 10^{-4} $1/s^2$ pre-Shamal to become 3.29 x 10^{-4} $1/s^2$ during the second peak phase as the velocities became near homogeneous.

3.3.3.3 Observed and simulated turbulence parameters

Similar to the previous two Shamal events, the turbulence parameters (TKE, TKE dissipation rate, Reynolds stress, and eddy diffusivity; Fig. 3.16 G-J) in the BBL ($\sim$23-27 m) followed a consistent pattern in response to the instability (Ri $<$ 0.25; Fig. 3.16F) due to the shear (Fig. 3.16C) associated with the semi-diurnal tide. The estimated observations of TKE ranged between 1.14 - 25.01 x 10^{-4} m^2/s^2 (Fig. 3.16G). Similar with the previous two events the maximum recorded TKE was during the highest recorded along shore current speed of 0.56 m/s on Mar 3 afternoon. Moreover, TKE was lower during the Shamal event (5.22 x 10^{-4} m^2/s^2) compared to the period average (7.14 x 10^{-4} m^2/s^2). The results of TKE simulations by both models during this five day period were significantly (p-values $<$0.05) correlated ($\geq$0.71) with the observations as well as having low MBE ($\leq$ 2.36 x 10^{-4} m^2/s^2) and RMSE ($\leq$ 4.88 x 10^{-4} m^2/s^2) values (Table 3.5).

The TKE dissipation rates (Fig. 3.16H) and Reynolds stresses (Fig. 3.16I) followed a similar pattern to TKE in response to the tidal cycle with six day period

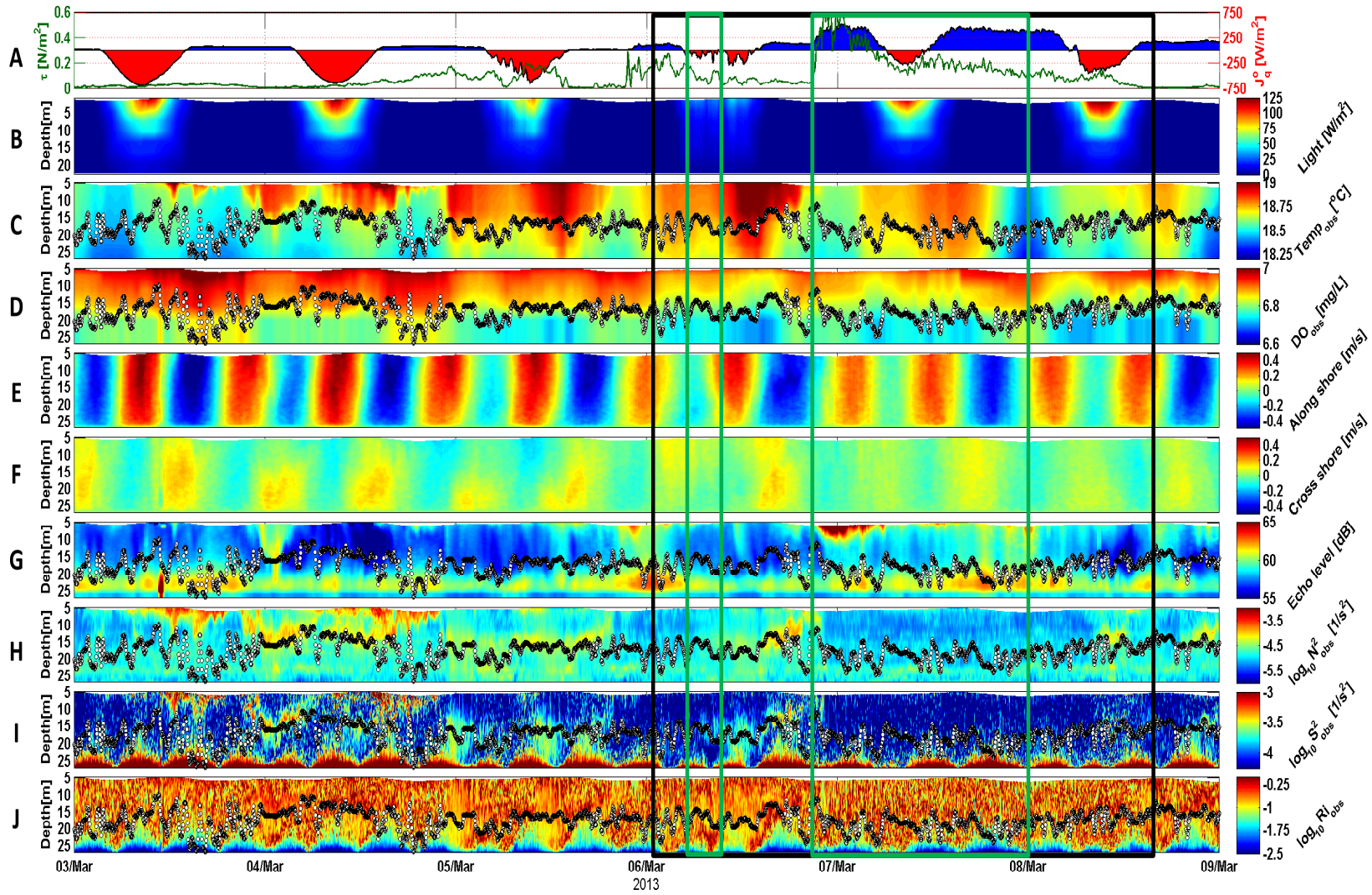

Figure 3.15: Same as Figure 3.8 but for Shamal event #3.

averages of 1.30 x 10^{-5} m^2/s^3 and 0.26 Pa, respectively. Similar to Shamal event #2 , both parameters peaked towards the end of the second peak phase with values of 6.45 x 10^{-5} m^2/s^3 and 0.88 Pa, respectively. The Shamal winds during the two peak phases generated cool plumes, as indicated by vertical heat fluxes > 20 W/m^2 (Fig. 3.16B). These plumes homogenized the water column and reduced the shear frequency (Fig. 3.16C). The reduction in shear frequency suppressed mixing, thus resulting in lower TKE dissipation rates and Reynold stresses during the cool plumes. Both models captured the influences of the cool plume suppressing mixing and the effects of the tidal induced shear generating turbulence with significant (p-values $<$ 0.05) correlations ($\leq$ 0.84), positive Nash-Sutcliffe coefficients ($\leq$ 0.67), as well as low MBE and RMSE values (Table 3.5).

The observed vertical eddy diffusivity (Fig. 3.16J) followed a similar pattern to the other turbulence quantities. The observed eddy diffusivity average during the five day period was 0.03 m^2/s, which is similar to both model averages. Similar to the previous two Shamal events, the eddy diffusivity peaked following the maximum recorded TKE and along shore current velocity on the afternoon of Mar 3. Both models were consistent with the observations throughout the period with significant (p-values $<$ 0.05) correlations (0.78), positive Nash-Sutcliffe coefficients (0.60), as well as low MBE ($<$ 0.32 x 10^{-2} m^2/s) and RMSE ($<$ 0.01 m^2/s) values (Table 3.5).

As in the previous two events, the model simulations of turbulence parameters by both k-kl and k-ε during this period were similar to one another (r=1 and $N_s \geq$ 0.98) and were consistent in following the semi-diurnal tide effect and Shamal effects.

3.3.4 Tidal shear influence in the BBL

The hydrographic analysis of the three Shamal periods suggests a dominant role of tidal currents on the thermal structure, dissolved oxygen profiles, and the tur-

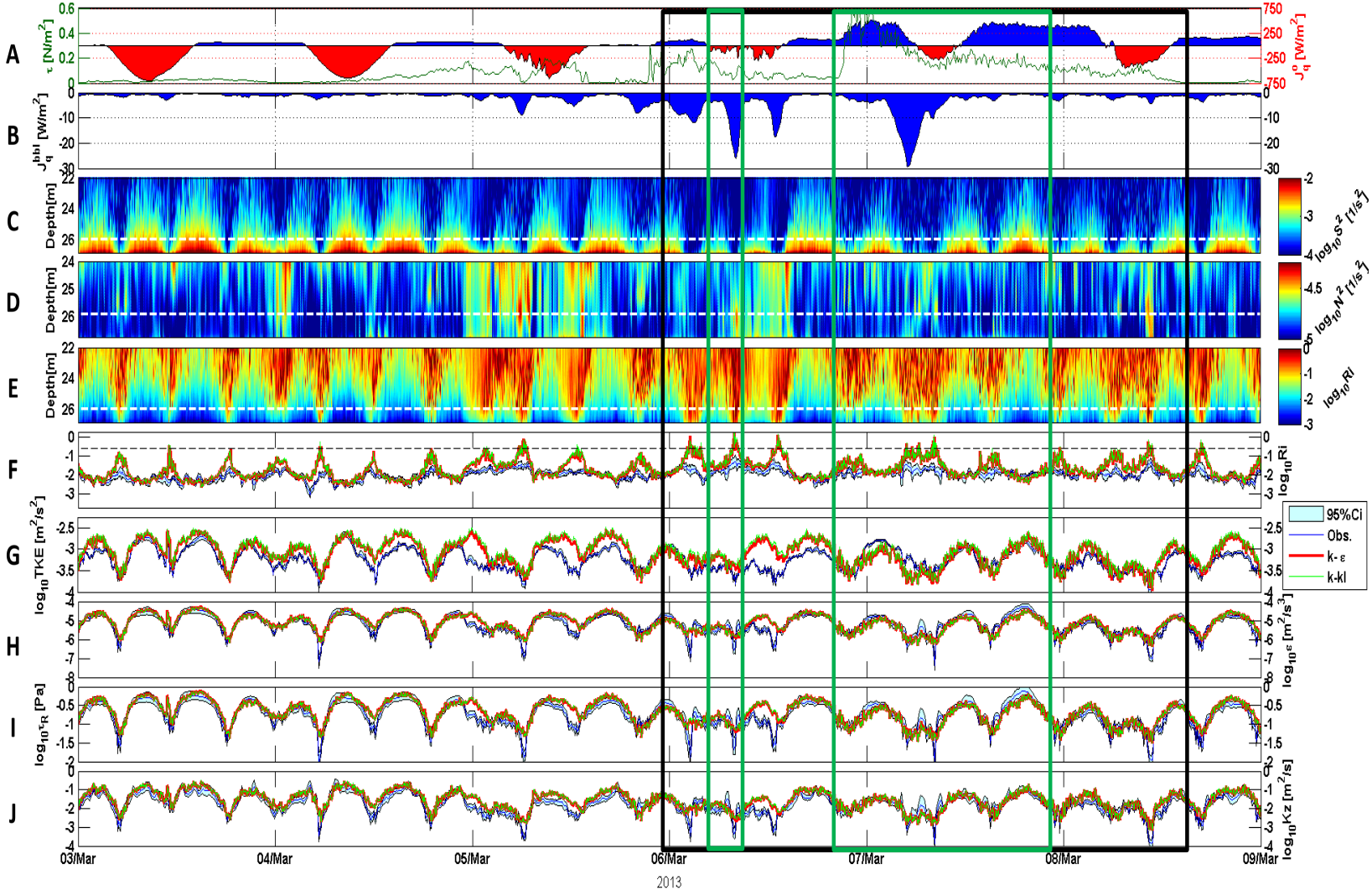

Figure 3.16: Same as Figure 3.10 but for Shamal event #3.

Table 3.5: Same as Table 3.3 but for Shamal event #3.

		min	max	average	MBE	RMSE	N_s	r
	Obs.	1.14	25.01	7.14	-	-	-	-
				(6.83,7.51)				
TKE	k-ε	1.40	33.00	8.57	1.42	4.06	0.19	0.73
10^4 $[m^2/s^2]$				(8.17,8.98)	(1.15,1.72)	(3.81,4.36)	(0.07,0.30)	(0.69,0.76)
	k-kl	1.52	38.24	9.53	2.36	4.88	0.17	0.71
				(9.09,9.98)	(2.08,2.71)	(4.57,5.25)	(0.01,0.38)	(0.67,0.75)
	Obs.	0.01	6.45	1.30	-	-	-	-
				(1.20,1.30)				
ε	k-ε	0.04	5.16	1.08	-0.22	0.77	0.68	0.85
10^5 $[m^2/s^3]$				(1.01,1.16)	(-0.23,-0.21)	(0.71,0.85)	(0.65,0.71)	(0.82,0.87)
	k-kl	0.05	5.48	1.09	-0.21	0.78	0.67	0.84
				(1.02,1.17)	(-0.26,-0.15)	(0.71,0.87)	(0.64,0.70)	(0.82,0.86)
	Obs.	0.01	0.88	0.26	-	-	-	-
				(0.25,0.27)				
τ_b	k-ε	0.03	0.72	0.24	-0.02	0.10	0.72	0.86
$[Pa]$				(0.23,0.25)	(-0.03,-0.02)	(0.09,0.11)	(0.70,0.75)	(0.84,0.88)
	k-kl	0.04	0.71	0.24	-0.02	0.10	0.73	0.86
				(0.23,0.25)	(-0.03,-0.02)	(0.09,0.10)	(0.70,0.75)	(0.85,0.88)
	Obs.	0.04	86.1	2.63	-	-	-	-
				(2.41,2.95)				
K_z	k-ε	0.08	28.0	2.31	-0.32	1.02	0.60	0.79
10^2 $[m^2/s]$				(2.22,2.54)	(-0.38,-0.19)	(0.36,1.44)	(0.55,0.65)	(0.75,0.82)
	k-kl	0.08	28.2	2.43	-0.20	0.41	0.60	0.78
				(2.22,2.60)	(-0.35,-0.19)	(0.36,1.25)	(0.55,0.64)	(0.75,0.81)

bulence parameters in the BBL due to current shear. In this section we used the harmonic analysis by Pawlowicz et al. (2002), which uses the current structure (Fig. 3.17C and F) to deduce tidal currents (Fig. 3.17D and G) and non-tidal currents (residual) (Fig. 3.17E and H) from a flow. The simulations in this section were run using both turbulence models (k-kl and k-ε) forced by temperature profiles and tidal currents. The surface forcings (heat and momentum fluxes; Fig. 3.18A) during these simulations were turned off. This approach will emphasize the effects of tidal induced shear on generating turbulence and causing instability. Furthermore, these simulations will indicate if the tidal currents are more dominant than the Shamals in generating turbulence by comparing the simulations with surface forcings 'on' (Fig. 3.16) and 'off' (Fig. 3.18).

We focus here on the strongest Shamal event #3 period and specifically on the ~24 hours of the 2nd peak Shamal phase (Mar 7) when the event was at its strongest. The simulated shear frequency during the 2nd peak phase with the surfacing forcings 'on' was lower (5.12 x 10^{-5} $1/s^2$; Fig. 3.16C) than the simulations with the surface forcings 'off' (5.83 x 10^{-5} $1/s^2$; Fig. 3.18B). These simulation results, as well as results from the analysis of the three events, have led us to suggest that Shamals caused a reduction in the BBL shear frequency by homogenizing the water column.

The higher shear frequency simulations with surface forcings 'off' have led to unstable flows, indicated by lower average Ri number (0.07; Fig. 3.18C and E) compared to the higher Ri number with surface forcings 'on' (0.12; Fig. 3.16E). This higher instability with surface forcing 'off' have led to higher TKE values by a factor of two, and higher TKE dissipation rates by 3.20 x 10^{-6} m^2/s^3 (Tables 3.5 and 3.6). However, the Reynold stresses during these simulations remained similar in both simulations, while the vertical eddy diffusivity was lower with surface forcings 'off' by 0.01 m^2/s .

Although the simulations of turbulence parameters with surface forcings 'off' during the Shamal event were inconsistent with the observations, they were consistent during the period of relatively low winds (Mar 3; Fig. 3.18F-I) with positive Nash-Sutcliffe coefficients (> 0.1) and significant (p-values < 0.05) correlation values (> 0.6). This suggests the significance of tidal forcing in controlling the turbulence parameters in the BBL during weak wind periods. During wind event periods, the influence of tidal current is reduced following the reduction in the tidal induced shear.

3.4 Conclusion

The regional hydrodynamics and mixing in the BBL of northwestern part of the Gulf have been studied using observations and numerical model simulations. We extensively investigated the meteorological, hydrodynamics, and mixing responses to three winter Shamal events that lasted between 53 to 65 hours. All three Shamal events were consistent in their abrupt changes in the meteorological parameters. As a Shamal progressed to the region, the wind speed averages increased up to 9.11 m/s with maximum speeds of 15.12 m/s. These winds resulted in lower humidities (61%) and air (4 ^{o}C) and sea surface temperatures (2 ^{o}C) as they traveled over the continental land mass and northern regions. Moreover, the build-up of a high pressure following the cold front has led to barometric pressure increases up to 13.1 mb, thus steeper pressure gradient and the strong Shamal winds. The combination of cooler temperatures, drier conditions, reduction in visibility due to dust, and higher wind speeds during the Shamal have generated more surface heat flux losses (622 W/m^2) and mostly in the form of latent heat. These conditions have led to convection that penetrated to the BBL resulting from either the increase in surface buoyancy or by the surface wind stress.

The thermal structure during the studied period followed three distinct patterns.

Table 3.6: Statistics and their 95% CI (in parenthesis) for simulated turbulence parameters during Shamal event #3 with surface forcings 'off'.

		average	MBE	N_s	r
TKE	k-ε	14.01	-8.48	0.12	0.63
10^4 $[m^2/s^2]$		(13.2,15.3)	(-9.44,-7.45)	(0.05,0.19)	(0.56,0.69)
	k-kl	16.02	-13.12	0.16	0.60
		(14.19,17.08)	(-12.01,-9.51)	(0.08,0.22)	(0.52,0.66)
ε	k-ε	1.39	-1.18	0.36	0.73
10^5 $[m^2/s^3]$		(1.26,1.54)	(-1.32,-1.07)	(0.31,0.40)	(0.68,0.78)
	k-kl	1.44	-1.23	0.34	0.72
		(1.31,1.61)	(-1.38,-1.09)	(0.29,0.38)	(0.67,0.77)
τ_b	k-ε	0.27	-0.01	0.37	0.76
$[Pa]$		(0.25,0.29)	(-0.02,-0.01)	(0.33,0.41)	(0.71,0.79)
	k-kl	0.28	-0.01	0.34	0.74
		(0.26,0.30)	(-0.03,-0.01)	(0.30,0.38)	(0.69,0.77)
K_z	k-ε	0.07	-0.04	0.61	0.68
$[m^2/s]$		(0.06,0.08)	(-0.05,-0.03)	(0.57,0.71)	(0.63,0.73)
	k-kl	0.08	-0.05	0.61	0.67
		(0.07,0.09)	(-0.05,-0.04)	(0.55,0.71)	(0.61,0.72)

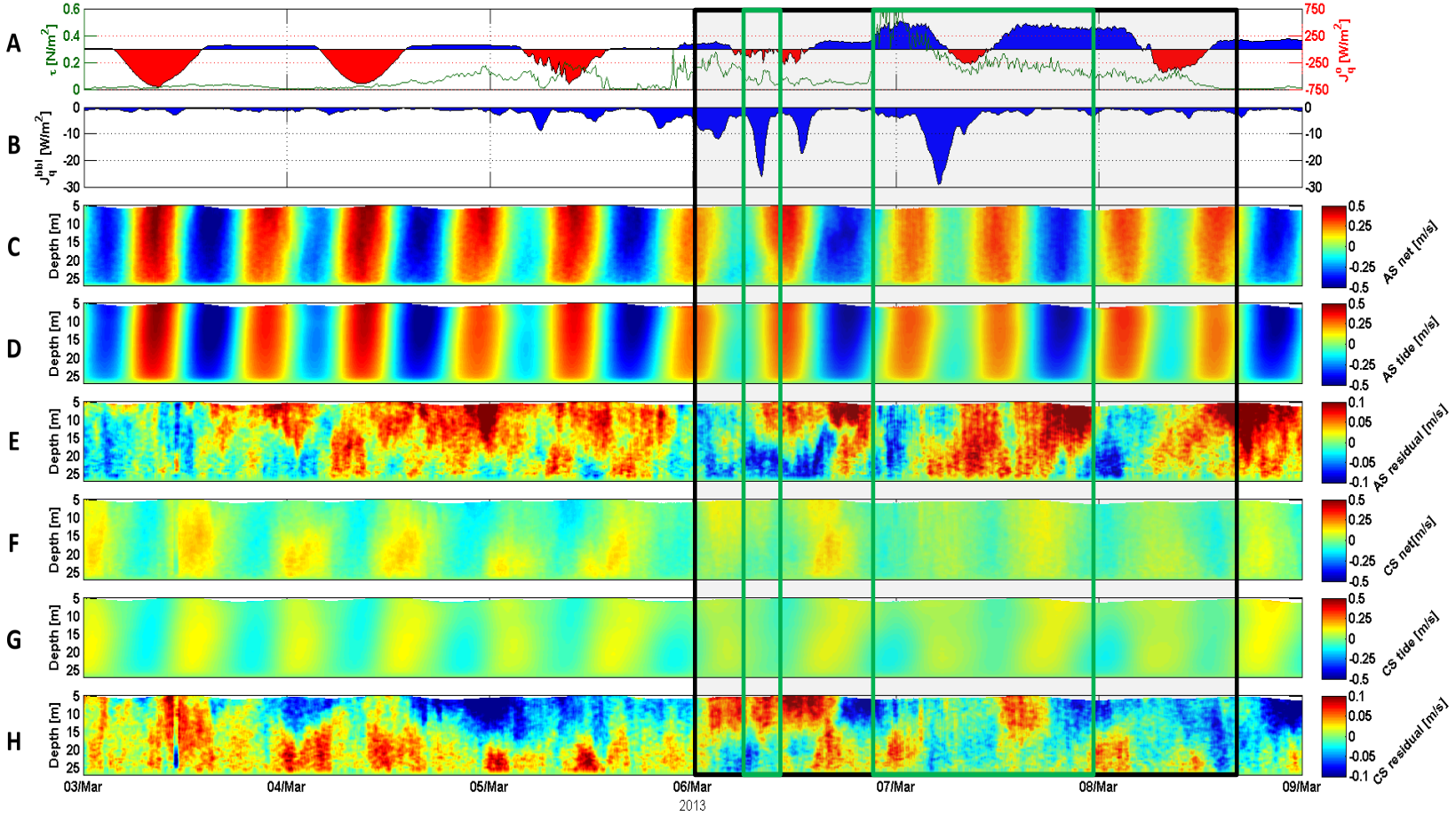

Figure 3.17: The effect of tide on the along shore (AS) and cross shore (CS) current during Shamal event #3 (black box) and two wind peak periods (green boxes): (A) wind stress (green) and net heat flux (shaded), (B) vertical heat flux in the BBL, (C) net (tide+residual) AS current, (D) filtered AS tidal current, (E) residual of non-tidal AS current, (F) net (tide+residual) CS current, (G) filtered CS tidal current, and (H) residual of non-tidal CS current. Time axis in UTC.

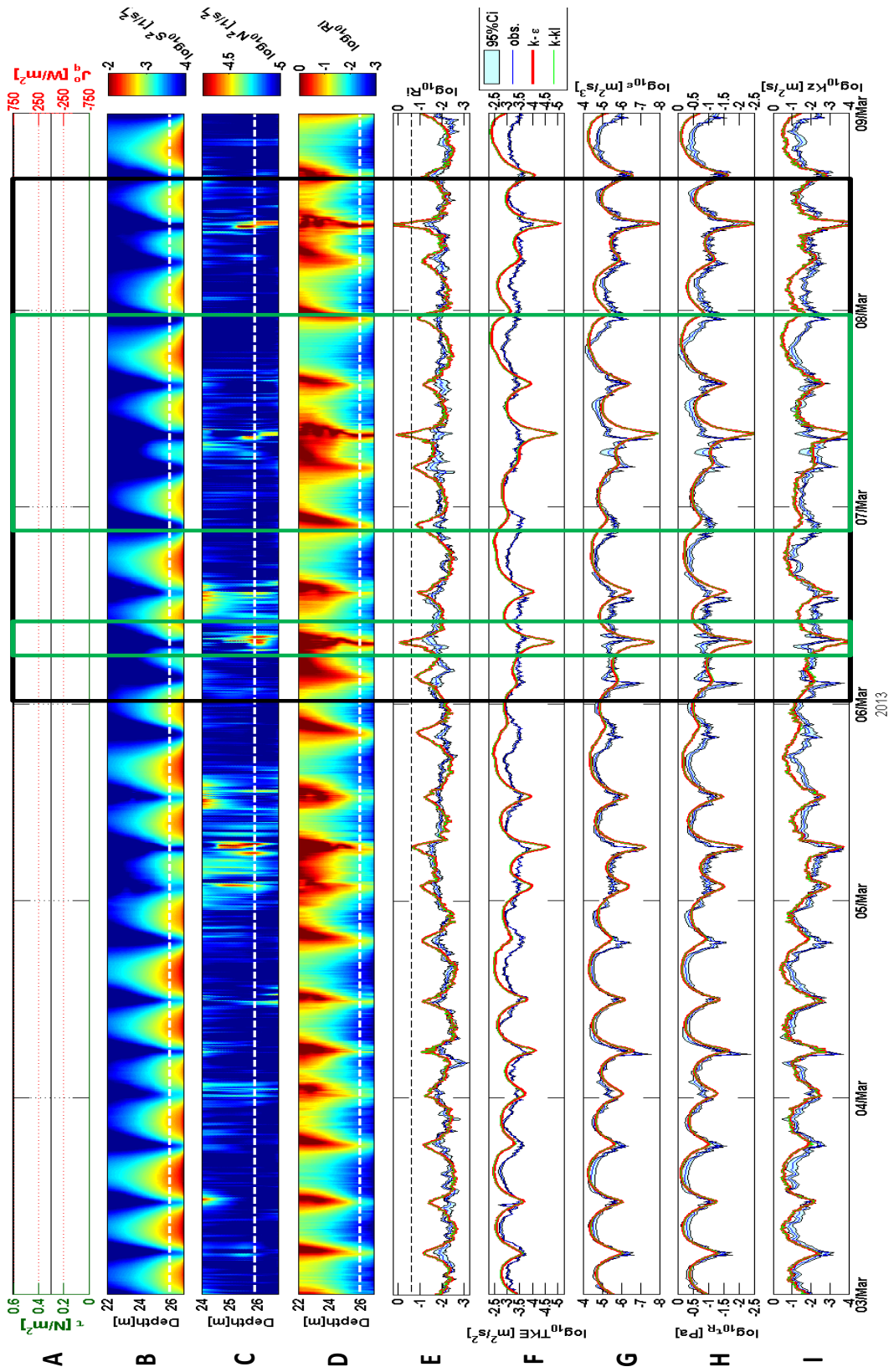

Figure 3.18: Same as Figure 3.10 but for Shamal event #3 and no surface forcing.

The first was a diurnal cycle in response to the surface net heat flux. The second pattern was the gradual cooling during the progression of the Shamal. The third pattern was a result of horizontal advection that was controlled by the dominate semi-diurnal tide. The tides flooding phase resulted in warmer conditions advecting warmer SE waters to the region. The tides ebbing phase resulted in cooler conditions advecting cooler NW waters to the region. The currents throughout the water column also followed the semi-diurnal tide pattern with velocities in the along shore direction up to 0.67 m/s and the cross shore direction up to 0.37 m/s.

The comparison of the measured and simulated turbulence parameters (Reynolds stresses, eddy diffusivities, TKE, and its dissipation rates) demonstrated satisfactory agreement between the two. Mixing in the BBL was mainly controlled by two main forcings. The first forcing was the increase in mixing resulting from the current shear generated by tides. The second was by the Shamal induced convection. The highest averages of the estimated turbulence parameters from the observations during the three studied periods were TKE 9.33 x 10^4 m^2/s^2, TKE dissipation rate 2.48 x 10^{-5} m^2/s^3, Reynold stress 0.44 Pa, and vertical eddy diffusivity 5.47 x 10^{-2} m^2/s. The satisfactory agreement between the observed and simulated turbulence parameters has led us to suggest that tidal current shear and convection driven turbulence are reproduced by two equation turbulence models (k-kl and k-ε). This conclusion was further supported by the significant correlations, low MBE, low RMSE, and positive N_s values.

Finally, the present study focuses on the winter Shamals. Further observations during the summer Shamal are needed to investigate the seasonal variability as well as extending the study region to other regions of the Gulf to outline any spatial variability. Furthermore, the significance of Shamals on the meteorological conditions as well as the Gulfs' hydrodynamics motivates the use of 3-D models for simulating

the Gulfs' response to the Shamal.

4. WIND DRIVEN FLOW DYNAMICS OFF THE COAST OF KUWAIT

4.1 Introduction

Coastal zone ecosystems are generally considered to be the most ecologically productive areas of all marine environments, accounting for 59% of the global primary production from which 30 - 40% is consumed by humans (Pauly & Christensen, 1995). The dynamics in coastal zones have considerable implications on the transport of sediments, nutrients, sewage, hydrocarbons, metals, and other pollutants along/cross shore that may lead to the undesired development of Hypoxia (e.g. Booth et al., 2012) and Algea blooms (e.g. Glibert et al., 2002). No observational study to date has quantified the advectional processes, which are the main drivers of transport of these contaminants (e.g. Boehm et al., 2002), nutrients (e.g. Leichter et al., 2003), and other sea water properties (e.g. temperature and salinity; García-Reyes & Largier, 2012) in the study region. Furthermore, none of the previously documented comprehensive observational studies by Emery (1956), Brewer and Dyrssen (1985), Reynolds (1993), and Swift and Bower (2003) of the Arabian/Persian Gulf (hereafter called Gulf) have focused on the hydrodynamics off the coast of Kuwait. The goal of the present study is to improve our understanding of the horizontal and vertical advectional processes off the coast of Kuwait and their response to wind events using two different 3 month long detailed hydrographic and meteorological observational datasets.

4.1.1 Meteorological background

The Gulf is located between latitudes 24 - 30 ^{o}N which is where most of the deserts are located. This region marks the boundary between tropical circulations (Hadley Cell) and the synoptic weather systems of mid-latitudes. Descending dry air in these

latitudes produces clear skies and arid conditions. The Gulf is characterized by extra-tropical weather systems from the northwest and the most well-known weather phenomenon in the Gulf is the Shamal. Shamal in Arabic literally means 'north' and designates the strong northwesterly winds that blow in the Gulf in summer (June - August; associated with the relative strengths of the Indian and Arabian thermal lows; Rao et al., 2003) and in winter (November - March; related to synoptic weather systems to the northwest; Rao et al., 2001). Winter Shamals are associated with mid-latitude disturbances that progress from the west to east and occur following southeast moving cold fronts producing average wind speeds of 11.5 m/s (details in Chapter 2). Ahead of a progressing cold front are typically southeast winds, locally called Kous (Reynolds, 1993; Vishkaee et al., 2012). The Shamal and Kous winds are the dominant winds in the Northwestern Gulf region (Fig. 4.1).

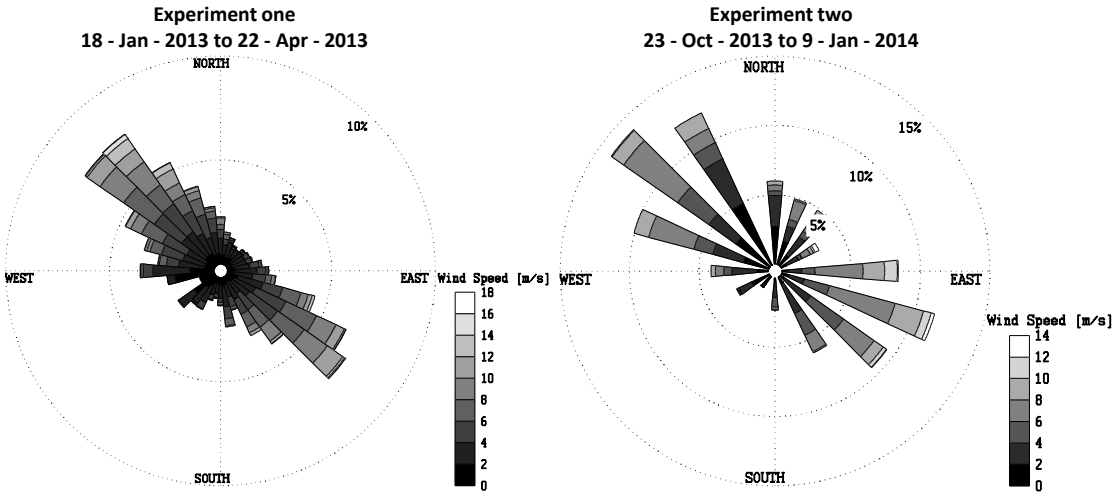

Figure 4.1: Hourly averaged wind speed, direction (from where wind blows), and frequency of occurrence (in %) during experiment one (left) and experiment two (right) at Qarooh Island, Kuwait.

4.1.2 General circulation

The Gulf is 990 km long, has a maximum width of 370 km, and a surface area of 239,000 km^2 with an average depth of 36 m (Nezlin et al., 2010). The general circulation in the Gulf, like in other semi-enclosed, marginal seas, such as the Red Sea and the Mediterranean Sea, is a coupled result of the wind driven and thermohaline-driven flows, complex mesoscale eddy fields and constricted water exchange through the Strait of Hormuz (annual mean 1 - 2 $*10^5$ m^3/s; Swift & Bower, 2003) with the Arabian Sea (Fig. 4.2) (Johns et al., 1999). Surface circulation in the Gulf can be divided into northern and southern flow regimes separated by a front, typically found off Qatar (Yao & Johns, 2010). The northern regime (where the study region is located) is dominated by wind forcing along the axis of the Gulf and riverine input from the Euphrates, Tigris, and Karun rivers (average 703 m^3/s; Iraq Foundation, 2003) at the Gulf's head. The wind-driven response of the Gulf appears to be through an adjustment of the pressure field that produces a general downwind flow. Furthermore, there are two southern coastal currents on both the Arabian and Iranian Coasts. The flow along the Iranian coast appears to continue into the southeastern basin as a tightly trapped coastal current extending perhaps as far as the Strait of Hormuz. The flow along the Kuwaiti and Saudi coast is augmented by freshwater input from the north forming the Euphrates River plume (Reynolds, 1993).

Fresh riverine discharge off coastal zones forms an offshore pressure gradient that is balanced by the Coriolis force and results in a transport alongside the coast to the right (Northern Hemisphere) of the pressure gradient (Blanton et al., 1989) (e.g. Columbia River plume, USA; Thomas & Weatherbee, 2006, Danshuei River plume, Taiwan; Liu et al., 2008, and Euphrates River plume, Iraq; Johns et al., 1999). A

flow opposite to the pressure gradient may evolve if the wind stress is significant. Previous studies (e.g. Hickey et al., 1998; García Berdeal, 2002) show that river plumes respond to wind events as short as three hours in duration causing changes in their position and depth due to vertical mixing. The location of the Euphrates River plume is important, as fronts dividing sea water and rivereine discharge often generate high primary and secondary production (Grimes & Kingsfrod, 1996). To date, understanding the currents climate off the Kuwaiti Coast driven by the Euphrates River plume has been hampered due to lack of observational data. Moreover, wind events aligned along direction of the coast (e.g. Kous and Shamal) can generate upwelling / downwelling (e.g. Hickey et al., 2005).

In coastal upwelling / downwelling regions the transport of nutrients and sea water constituents is driven by both horizontal and vertical advection (Klein & Coste, 1984) as response to the offshore Ekman transport of the subsurface waters (Huyer, 1983). To our best knowledge there exists no published observational nor numerical study of upwelling / downwelling off the coast of Kuwait.

The main objectives of this study are to assess the main forcings and the resulting flow dynamics, with a focus on upwelling / downwelling dynamics, off the Kuwaiti Coast. Additionally, we examine how these processes contribute to changes in temperature and salinity. Finally, we evaluate the ability of a one dimensional numerical model to account for the advective effects forced by surface forcings (momentum and heat fluxes) and horizontal temperature gradients (details in Section 4.2.2).

The observational dataset and numerical model details are described in Section 4.2. The results (Section 4.3) are divided into two main parts with each describing the general meteorology and hyrdrographic conditions, and the net volume transport in relation to different wind events during the two observational periods. Model simulation results are described in each part as well. A summary and conclusions

are given in Section 4.4.

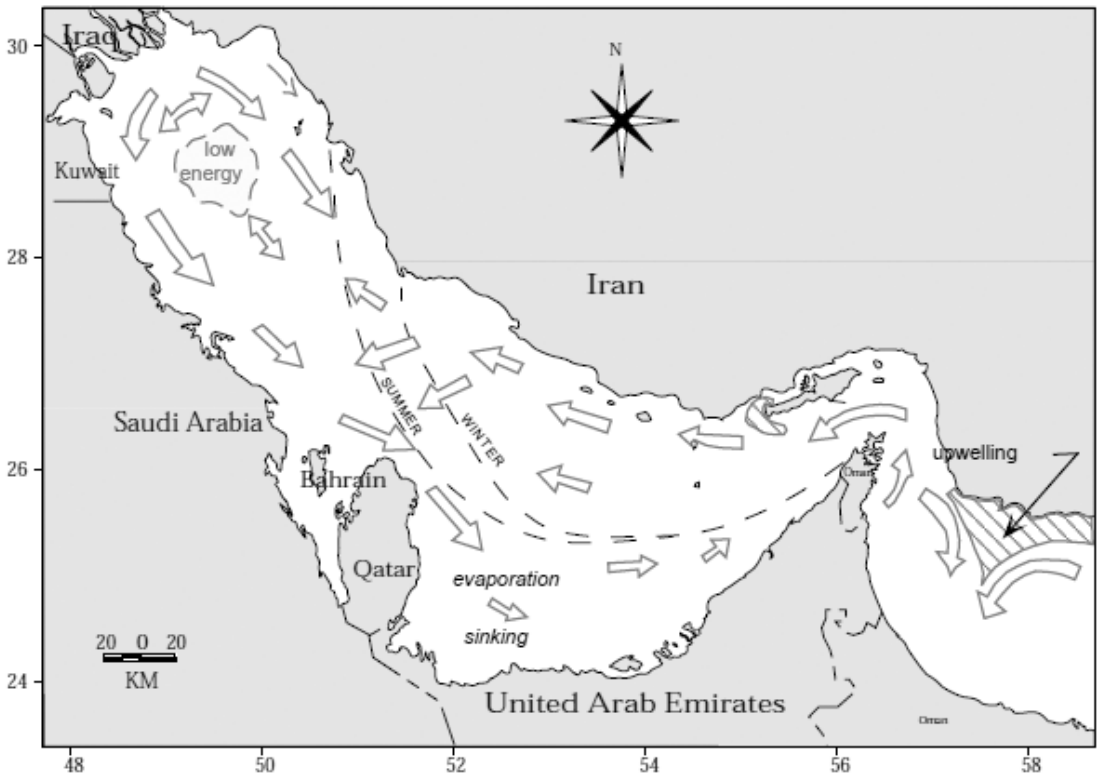

Figure 4.2: Map of the Gulf with schematic of the surface circulation (arrows). Dashed lines in the central part of the Gulf indicate the appoximate seasonal location of the salinity front between the inflowing fresher Indian Ocean Surface Water (IOSW) entering through the strait of Hurmoz and the more saline waters of the Gulf (Reynolds, 1993).

4.2 Methods

4.2.1 Observations details

Observations were conducted in the vicinity of Qarooh Island, Kuwait (28^o 48.973' N, 048^o 46.457' E; Fig 4.3), 44 km east of Khairan city and 120 km south of the Euphrates-Tigris delta during two different 3 months experiment periods. The first experiment was between mid-January to mid-April 2013 and the second experiment was between mid-October 2013 to mid-January 2014. Both experiments included a meteorological station mounted at a pier on Qarooh Island at a nominal distance of 7 m above sea level (ASL) and an oceanographic mooring ~4 km northeast of Qarooh Island.

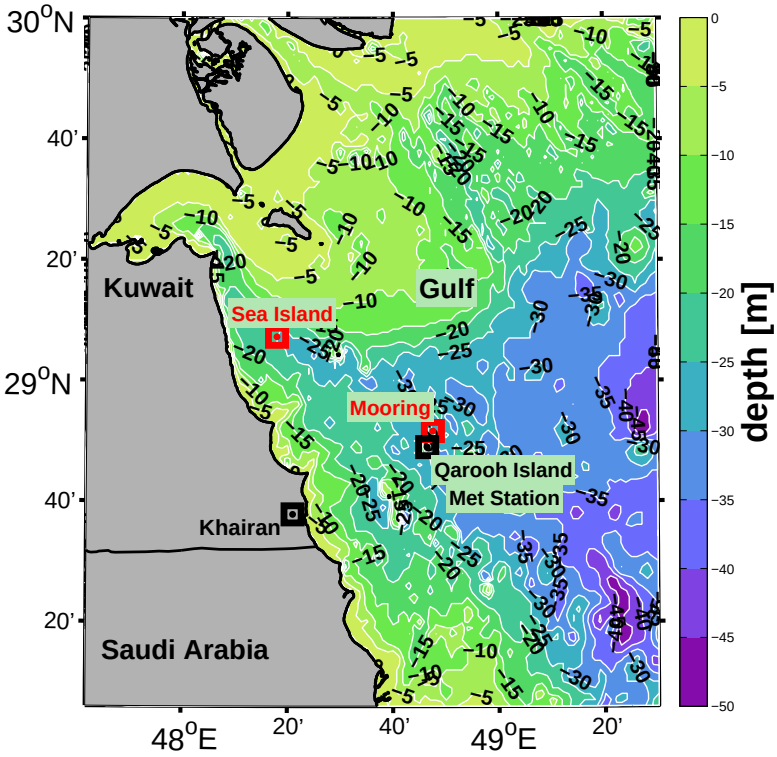

Figure 4.3: Study region with locations of mooring stations (red) and meteorological station. Depth contour lines are in 5 m intervals.

4.2.1.1 Meteorology

Surface meteorological data station for both 3 month experiments included air temperature and humidity (Onset S-THB; mounted in a fan aspirated radiation shield), downward shortwave (Apogee VR1761-5) and downward longwave (Kipp and Zonen CG 3 Pyrgeometer) radiations, barometric pressure (Onset S-BPA-CM10), and rain (Texas electronic TE 525). Sensors were set to measure every 2 minutes and datasets were then averaged and logged every 10 minutes. Sea surface temperature (SST) measurements were collected using a Onset Hobo Pro v2 temperature sensor attached to a surface float and sampling at 3 minutes intervals. Wind measurements (Vaisala WS425 Ultrasonic) were collected at 10 minute intervals by the Kuwait Meteorological Office (KMO) station located ∼10 m from our station. Wind velocity measurements were rotated into along-shore (AS 314^o; v_w) and cross-shore (CS 44^o; u_w) components to emphasize upwelling / downwelling favorable winds conditions in a similar approach used by Woodson et al. (2009).

From the meteorological measurements, the surface wind stress (τ) and net heat flux (J_q^o), were computed using the Coupled Ocean-Atmosphere Response Experiment software (COARE 3.0; Fairall et al., 1996, 2003; Brunke et al., 2003):

$$\vec{\tau} = \rho_a C_D \vec{U} |\vec{U}| \quad , \tag{4.1}$$

where ρ_a is the air density, C_D is the drag coefficient (function of air density, wind speed, and sea surface waves), $\vec{U}$ is the wind velocity.

$$J_q^0 = J_q^{sw} + J_q^{lw} + J_q^L + J_q^S \quad , \tag{4.2}$$

where J_q^{sw} is the net (corrected for albedo) solar radiation (shortwave), J_q^{lw} is the

net (sum of downward and upward) infrared radiation (longwave), J_q^L is the latent heat flux and J_q^S is the sensible heat flux. The net heat flux and wind stress values (surface forcings) are those used to force the model simulations.

4.2.1.2 Hydrography

The mooring station for both experiments included a bottom pod and a tight mooring at a distance of 21 m apart (Fig. 4.4).

During the first experiment, the tight mooring (water depth of 26.2 m) was instrumented with 23 temperature sensors (Onset HOBO Pro v2) sampling at 3.5 minute intervals, four mini-Conductivity Temperature Depth sensors (mini-CTD, INWUSA CT2X) sampling at 2 minute intervals and two CTDs (RBR XR-420 and XR-620) sampling every 0.3 minutes and ten light intensity sensors (Onset HOBO pendant light) sampling every 5 minutes. The bottom pod carried an upward facing 1 MHz Acoustic Doppler Current Profiler (ADCP; Nortek), which collected 0.5 minute averaged current profiles of the water column at 3 minute intervals and 0.5 m vertical resolution. Additionally, a mini-CTD and a HOBO temperature sensor were attached to the pod. The conductivity data measurements by the CTDs during experiment one were contaminated due to rapid biofouling, although copper was used to prevent fouling, and therefore was not used for analysis.

During the second experiment, the tight mooring line (water depth of 23.7 m) was instrumented with five temperature sensors (HOBO Pro v2) sampling every 3 minutes, four high resolution temperature sensors (RBR SOLO) sampling at 2 Hz, two CTDs (RBR XR-420 and Infinity-CTW) sampling every 3 minutes, and four light intensity sensors sampling every 5 minutes. Unfortunately, the mooring cable during this experiment was cut off around the center on 11 December. This led to loss of instruments between depths 3.9 m to 13.75 m, and 17.67 m to 20.08 m (distance from

seabed) (Fig. 4.4). The lost sensors are not included in the previous description. The bottom pod carried an upward facing 1 MHz ADCP (Nortek), which collected 0.5 minute current profile averages of the water column at 1.8 minute intervals with 0.5 m vertical resolution. Additionally, a RBR CTD and a HOBO temperature sensor were attached to the pod.

To capture the extent of the river plume in the region, additional data was acquired from the KMO at the Sea Island location, depth 28.5 m (Fig. 4.3). We note that this is the only other hydrographic data available and covers both experiment periods. The KMO data included hourly salinity and temperature measurements (Sea-bird SBE 37-IMP) at 4 m depth and currents from an upward facing 600 kHz ADCP (Nortek) of 1 minute averages at 10 minute intervals. The 10 minute measurements were then averaged into hourly data. 4 m cells were also averaged over three depth levels. KMO currents were provided to us at three depth levels: the first depth level extended from the surface to 8 m, the second depth level from 8 m to 20 m, and the third depth level from 20 m to 28 m.

The velocity measurements of all stations were detided using the T_TIDE matlab harmonic analysis toolbox (Pawlowicz et al., 2002) to emphasize none-tidal responses. Current velocities were rotated into AS (positive is parallel to coast northwestward) and CS (positive is away from the coast), similar to the approach we used to rotate the wind velocity components. The current components were used to compute the volume transport (units of m^3/ms) in the upper layer ($upper_{cs}$, $upper_{as}$; surface to 8 m), lower layer ($lower_{cs}$, $lower_{as}$; 8 m to seabed) and water column (M_{cs}, M_{as}; surface to seabed) by direct integration of the current profiles using:

$$M_{cs} = \int_{h_2}^{h_1} u \, dz \quad , \quad M_{as} = \int_{h_2}^{h_1} v \, dz \quad , \tag{4.3}$$

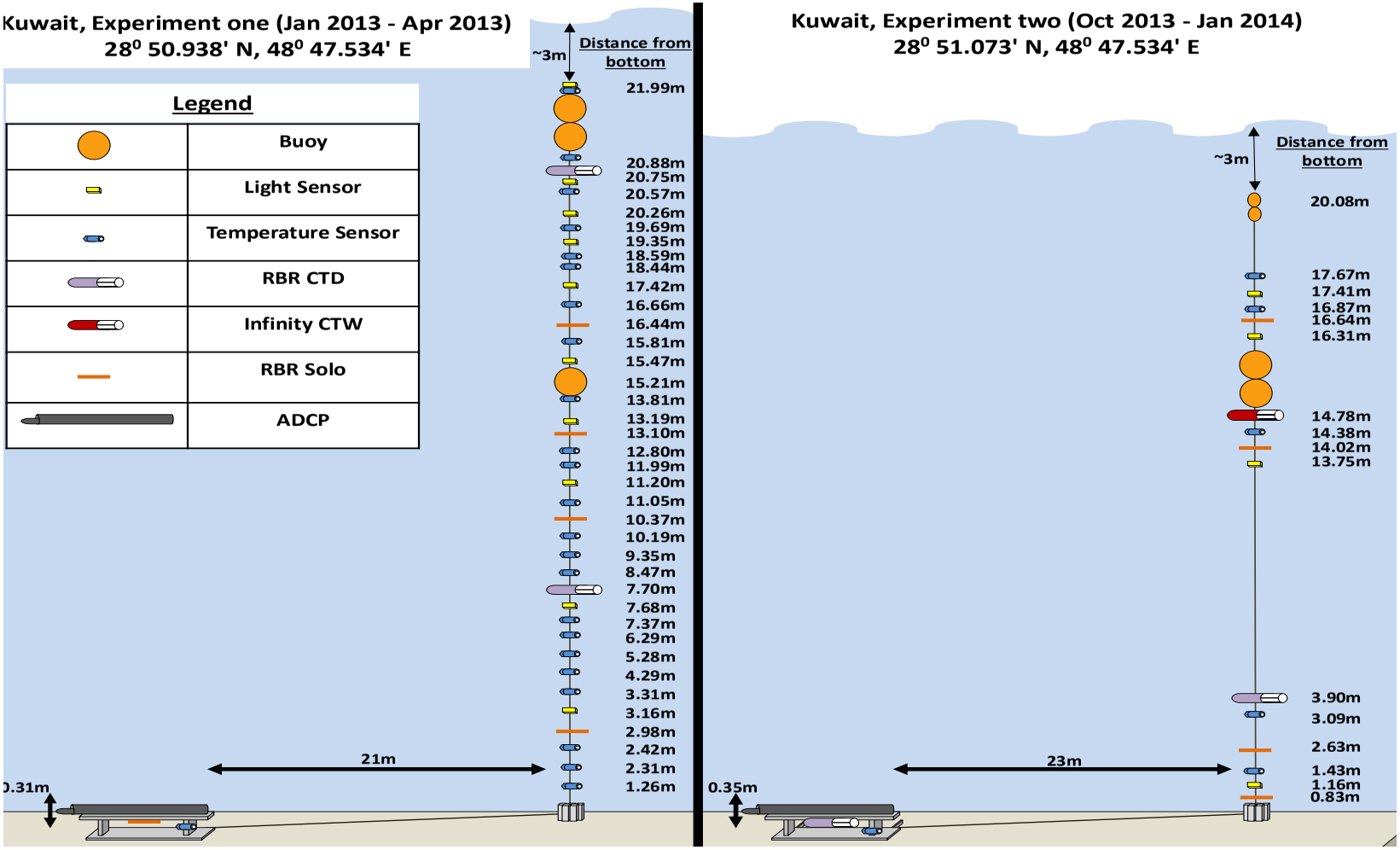

Figure 4.4: Schematic of mooring station during experiment one (left) and experiment two (right). Each experiment included an instrumented cable mooring (right) and bottom pod (left).

where h_1 and h_2 are the layers top and bottom depths, respectively. The volume transport can be an indicator of upwelling / downwelling if the surface waters flow away / toward the coast while waters below the surface flow in the opposite direction (Huyer, 1983).

The temperature and salinity time series are 36 hour low-pass filtered (Butterworth; Roberts & Roberts, 1978) to emphasize non-tidal, non-diurnal, and other low frequency responses in a approach similar to that taken by Ullman & Codiga, 2004. Using the low-pass filtered temperatures we generated hourly temperature profiles from which the mixed layer (ML) depths were estimated by manually selecting the shallowest breaking point where the change in temperature was $\geq 0.1^{o}$C.

Additionally, spatial gap-free SST data were obtained from the Level 4-Group for High Resolution Sea Surface Temperature (L4-GHRSST; http://www.ghrsst.org). This high resolution (1 km) daily data is a blend of eight satellite (AATSR / Envisat, AVHRR / NOAA, MODIS / Aqua, AMSR-E / Aqua, TMI / TRMM, SEVIRI / MSG, GOES / NASA, and MTSAT-2 / JMA) observations and includes various sensors (infrared wide swath radiometer, infrared dual-view radiometer, infrared Earth disc radiometer and microwave radiometer) and in-situ data with an accuracy of 0.1 K (Martin et al., 2012; Dash et al., 2012). This data was used to construct SST images for analysis of variability of spatial SST and to track water sources.

4.2.2 Numerical model details

The one-dimensional numerical model used in the present study is the General Ocean Turbulence Model (GOTM; Burchard, 2002). The model is based on the six dynamical equations of which two are derived from the Reynolds averaged Navier-Stokes equation for turbulent kinetic energy (TKE; k), and TKE dissipation rate (ε), and four derived from the Reynolds-averaged transport equations (hydrostatic primitive equations) for potential temperature (T), salinity (s), and velocity (u and v):

$$\partial_t u - \partial_z[(\nu_t + \nu)\partial_z u] = fv \quad , \tag{4.4}$$

$$\partial_t v - \partial_z[(\nu_t + \nu)\partial_z v] = -fu \quad , \tag{4.5}$$

$$\partial_t T - \partial_z[(\nu'_t + \nu')\partial_z T] = \frac{1}{C_p \rho_o}\partial_z I \quad , \tag{4.6}$$

$$\partial_t s - \partial_z[(\nu'_t + \nu')\partial_z s] = 0 \quad , \tag{4.7}$$

$$\partial_t k - \partial_z(\frac{\nu_t}{\sigma_k}\partial_z k) = \nu_t[(\partial_z u)^2 + (\partial_z v)^2] + \nu'_t \frac{g}{\rho_o}\partial_z \rho - \varepsilon \quad , \tag{4.8}$$

$$\partial_t \varepsilon - \partial_z(\frac{\nu_t}{\sigma_\varepsilon}\partial_z \varepsilon) = \frac{\varepsilon}{k}[c_1 \nu_t(\partial_z u)^2 + (\partial_z v)^2] + c_3 \nu'_t \frac{g}{\rho_o}\partial_z \rho - c_2 \varepsilon \quad , \tag{4.9}$$

where f is the Coriolis frequency, g is the gravitation acceleration, C_p is the specific heat capacity of seawater, ρ_o is the mean water density, I is the shortwave radiation in the water column (function of depth; in the present study the observed light intensity profiles were used to estimate the shortwave radiation decay with depth), ρ is seawater density, ν is the eddy viscosity, ν' is the eddy diffusivity, and $c_{1,2,3}$ and $\sigma_{k,\varepsilon}$ are empirical constants (Table 4.1). GOTM provides a unique set of well tested two equation statistical closure models (e.g. k-ε, k-kl and k-ω) for selection (e.g. Stips et al., 2002; Bolding et al., 2002; Anis & Singhal, 2006). The use of

Table 4.1: Empirical constants used in the two equation models ($k-\varepsilon$)

c_1	c_2	c_3 (stable stratification)	c_3 (instable stratification)	σ_k	σ_ε
1.44	1.92	-0.63	1.0	1.0	1.2

these two equation turbulence closure models allows computation of ε and 'closure' of the second moments using the Kolmogorov-Prandtl relation where both ν and ν' are proportional to the turbulent macro length scale (k^2/ε):

$$\nu_t = c_\mu \frac{k^2}{\varepsilon} \quad , \nu'_t = c'_\mu \frac{k^2}{\varepsilon} \quad , \tag{4.10}$$

where c_μ and c'_μ are non-dimensional stability functions (Canuto et al., 2001):

$$c_\mu = \frac{0.107 + 0.01741\alpha_N - 0.00012\alpha_S}{1 + 0.26\alpha_N + 0.029\alpha_S + 0.0087\alpha_N^2 + 0.005\alpha_N\alpha_S - 0.000034\alpha_S^2} \quad , \tag{4.11}$$

$$c'_\mu = \frac{0.1120 + 0.004519\alpha_N - 0.00088\alpha_S}{1 + 0.26\alpha_N + 0.029\alpha_S + 0.0087\alpha_N^2 + 0.005\alpha_N\alpha_S - 0.000034\alpha_S^2} \quad , \tag{4.12}$$

with the non-dimensional buoyancy number (α_N) and non-dimensional shear number (α_S):

$$\alpha_N = \frac{k^2}{\varepsilon^2} N^2 \quad , \alpha_S = \frac{k^2}{\varepsilon^2} S^2 \quad , \tag{4.13}$$

where $N^2 = -(g/\rho_o)(\partial\rho_o/\partial z)$ and $S^2 = (\partial u/\partial z)^2 + (\partial v/\partial z)^2$ are the squared buoyancy and shear frequencies , respectively.

To simulate the regional thermal structure dynamics we employ the widely used (e.g. Rodi, 1987; Burchard et al., 1998) state-of-the-art k-ε two equation turbulence closure model (Eqn. 4.8 and 4.9). Using this model approach necessitates an assumption of horizontal homogeneity where horizontal gradients (e.g of pressure and

velocity) and turbulent transport are negligible in one-dimensional models (Simpson et al., 2002; Burchard et al., 2006). The present study tries to assess these one-dimensional model limitations by comparing the thermal structure simulations with the observed thermal structure using multiple statistical tools. Two statistics (Mean Bias Error, MBE; Root Mean Square Error, $RMSE$) assess the accuracy of the model by evaluating the mean difference between the observed, x, and simulated, y, temperatures

$$MBE = \frac{1}{n}\sum_{i=1}^{n}(x_i - y_i) \quad , \tag{4.14}$$

$$RMSE = \sqrt{\frac{1}{n}\sum_{i=1}^{n}(x_i - y_i)^2} \quad . \tag{4.15}$$

where i is a time series data point, and n is the total number of data points. The goodness of fit statistics (Nash-Sutcliffe coefficient efficiency, N_s, and Pearsons correlation, r) are used to measure the models predictive power by its ability in fitting the observations,

$$N_s = 1 - \frac{\sum_{i=1}^{n}(y_i - x_i)^2}{\sum_{i=1}^{n}(y_i - \overline{y})^2} \quad , \tag{4.16}$$

where $\overline{y}$ is the simulated temperature mean value. $N_s < 0$ values indicate poor model simulations, $N_s = 0$ indicates that the model simulations are only as accurate as the observations' mean value, $N_s = 1$ indicates perfect model simulations (Nash & Sutcliffe, 1970). Positive N_s values are generally viewed as acceptable (Gupta & Kling, 2011).

$$r = \sum_{i=1}^{n}\frac{(x_i - \overline{x})(y_i - \overline{y})}{(n-1)\sigma_x\sigma_y} \quad , \tag{4.17}$$

where σ_x and σ_y are the simulated and observed temperature standard deviations, respectively. r values range between -1 and 1 with -1 and 1 indicating perfect model simulations (Press et al., 2007). The r values were further tested for significance

using the p-value resulting from the student t-test to quantify the probability of no correlation. When p-values are <0.05 the correlations are considered significant (Rice, 1988). The use of these multiple statistical tools have been shown to be successful in evaluating hydrological and atmospheric models (e.g. Krause et al., 2005; Elsanabary & Gan, 2013; Jia et al., 2013; Pinker et al., 2014).

4.3 Results & Discussion

In this section we focus on a period during which three upwelling / downwelling favorable wind events were observed. Analysis of the events suggests that upwelling and downwelling conditions did exist in regions near the coast (16 km offshore) but did not extend to the Qarooh region, located 44 km offshore. However, during the strongest recorded southeasterly wind event (Event #3) effects of upwelling near the coast appears to have extended to the Qarooh region. Next, analysis results for each of the three events, including simulation results, are presented.

4.3.1 Event #1- upwelling favorable wind

4.3.1.1 Meteorological conditions

The first event was a relatively strong southeasterly (Kous) lasting for 3 days (8 - 11 Nov), with wind speed average of 6.71 m/s (6.57, 6.83) (Fig. 4.5A and B). These winds increased the average relative humidity and air temperature by 24.62 % (24.43, 24.98) and 1.16 ^{o}C (1.13, 1.20), respectively, as they traveled over the Gulf approaching from the south (Fig. 4.5C and D). This event was a result of a low pressure system that progressed across the region prior to a winter Shamal (Event #2), thus, decreasing the average barometric pressure by 3.11 mb (3.00, 3.21) (Fig. 4.5E). The net shortwave radiation followed a diurnal cycle (Fig. 4.5F) with cloudy conditions setting in during the event and reducing the average solar radiation from 182 W/m^2 (pre-event; -1 day of event) to 167 W/m^2 (event). The cloudy conditions

also reduced the net longwave radiation (loss) from the sea surface from 101 W/m^2 (pre-event) to 42 W/m^2 (event), due to an increase in downward longwave radiation associated with the cloud cover (Fig. 4.5G). The sensible heat flux reversed from a loss to a gain term by the sea surface at about mid-Event #1 (Fig. 4.5H) due to increase in air temperature. Maximum sensible heat flux gain during Event #1 was 11 W/m^2 commensurate with the time of maximum difference between air temperature and SST (1 ^{o}C). The second largest contributor to the net surface heat flux, after shortwave radiation, was latent heat flux. The highest loss of latent heat flux during Event #1 of 233 W/m^2 occurred when winds were the highest (9.76 m/s) (Fig. 4.5I). Consequently, the highest loss net heat flux (314 W/m^2) occurred during this time (Fig. 4.5J).

4.3.1.2 Hydrographic conditions

The thermal structure of the water column during Event #1 followed a diurnal heating pattern, consistent with the net surface heat flux, superposed on a semi-diurnal tidal cycle with temperatures ranging between 25.80 ^{o}C and 26.36 ^{o}C (Fig. 4.6B, F and G). To filter out tides and diurnal cycles a 36 hours low-pass filter was used (details in Section 4.2.1.2) to emphasize the low frequency temperature response. Results, after low-pass filtering, are presented in Figure 4.7G.

The AS residual currents (after removing tides; details in Section 4.2.1.2) throughout the water column in the Qarooh region followed in general the AS wind direction (Fig. 4.7B) during this event, with currents weakening toward the seabed, likely the result of diminishing wind influence (Fig. 4.7C). The maximum observed net AS volume transport of 3.68 m^2/s on 9 Nov 1:40 (Fig. 4.7D) occurred about 3 hours after the maximum recorded wind speed (9.76 m^2/s). The net CS volume transport shifted toward the coast between 8 Nov 22:14 and 9 Nov 11:20 with a maximum

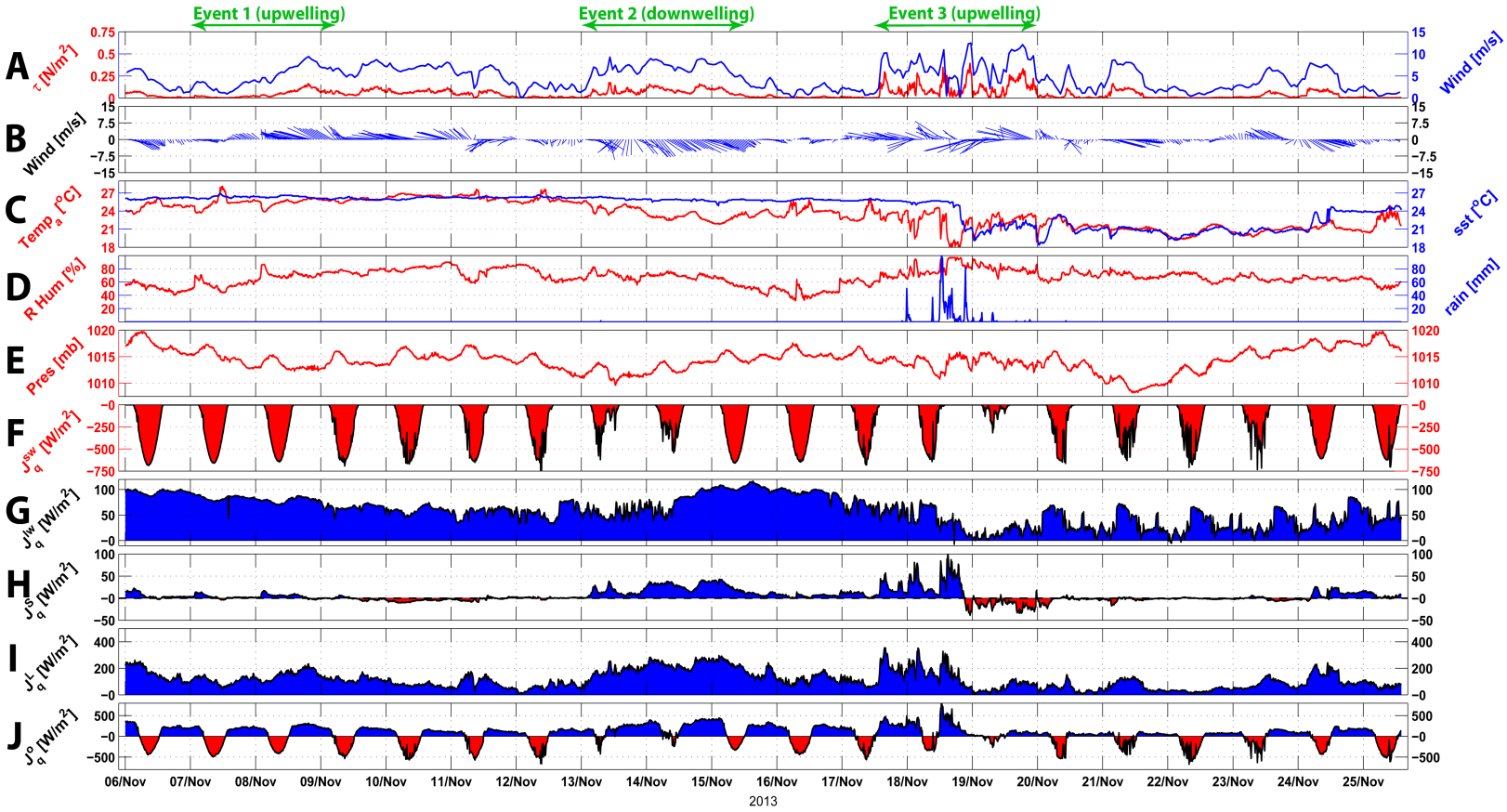

Figure 4.5: Surface meteorological data during the November 2013 period at Qarooh. The green arrows on top represent the durations of three upwelling / downwelling favorable wind events. (A) wind speed (blue) and wind stress (red), (B) wind velocity vectors, (C) air (red) and sea surface temperatures (blue), (D) relative humidity, (E) barometric pressure, (F) net shortwave radiation, (G) net longwave radiation, (H) sensible heat, (I) latent heat, and (J) net surface heat flux. Time is UTC and all measurements are 10 minute averages except wind data which are 1 hour averages. Positive (blue shading) heat flux values indicate heat loss and negative (red shading) indicate heat gain.

transport of 2.07 m^2/s on Nov 9 2:13. Consequently, the maximum observed temperature of 26.36 ^oC on 9 Nov 5:24 (Fig. 4.7G) suggests that water transported from the south and the east are warmer than the local waters in the Qarooh region. This appears to be consistent with the spatial GHRSST data (Fig. 4.8) for 9 Nov when a warm 'tongue' parallel to the coastline extended from the southeast. This 'tongue' progressed northwestward following the general direction of the wind and currents observed at Qarooh. After 9 Nov 11:20 the net CS volume transport direction reverted to away from shore. During this time, the water column average temperature cooled reaching a minimum temperature of 25.80 ^oC. This suggests that cooler waters, advected from regions closer to the shore, forced the warm 'tongue' to regress southeastward as indicated in Figure 4.8 for 10 Nov.

4.3.1.3 Examining upwelling conditions

To examine if upwelling conditions did exist during Event #1 at the Qarooh mooring location we divided the volume transport into two layers, an upper layer from the sea surface to a depth of 8 m, and a lower layer from 8 m to the seabed. The 8 m depth is roughly positioned at the center of the ML depth range (5 - 11 m; Fig. 4.6C). Furthermore, these depth layers were consistent with KMO Sea Island dataset, where only three levels were available (0 - 8 m, 8 - 20 m, and 20 - 28 m; details in Section 4.2.1.2). The results, presented in Figure 4.9, show that the volume transport in these upper and lower layers are consistent in their direction. During upwelling conditions the CS Ekman transport in the surface layer is expected to flow away from the coast, while it is expected to flow in the opposite direction in deeper waters (Huyer, 1983). However, such a flow structure was not observed in the Qarooh region, where the CS transport in the upper and lower layers were similar in direction (Fig. 4.9E and F). During upwelling conditions surface waters are expected also to

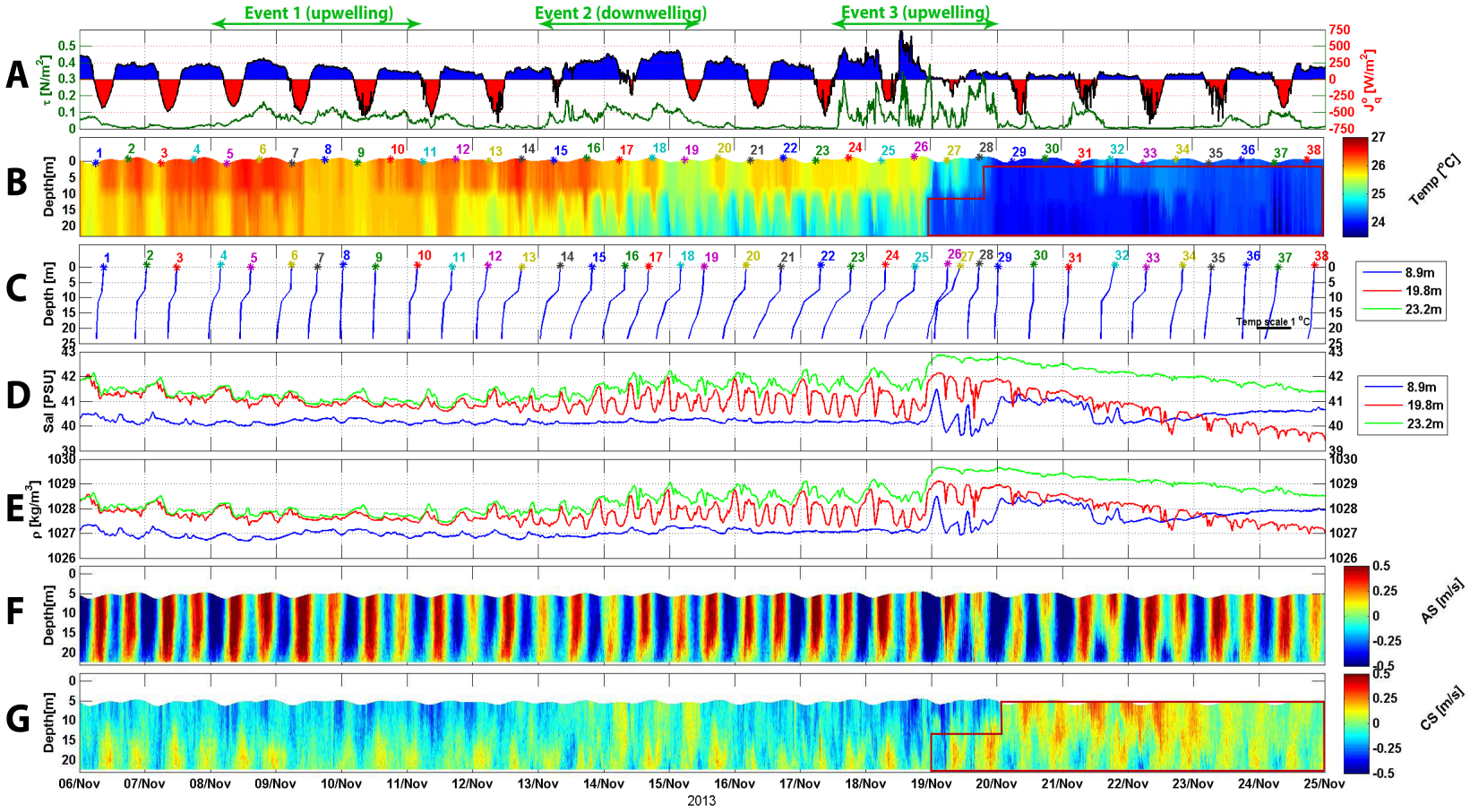

Figure 4.6: Raw hydrographic observations during the November 2013 period at Qarooh. The green arrows on top represent the durations of three upwelling / downwelling favorable wind events. (A) wind stress (green) and net surface heat flux (shaded), (B) potential temperature, (C) 3 hour average potential temperature profiles, (D) salinity at 3 depth levels, (E) potential density at 3 depth levels, (F) along-shore (AS, 315^o), and (G) cross-shore (CS, 45^o) currents. A strong offshore current period is indicated in a red box. Time is UTC.

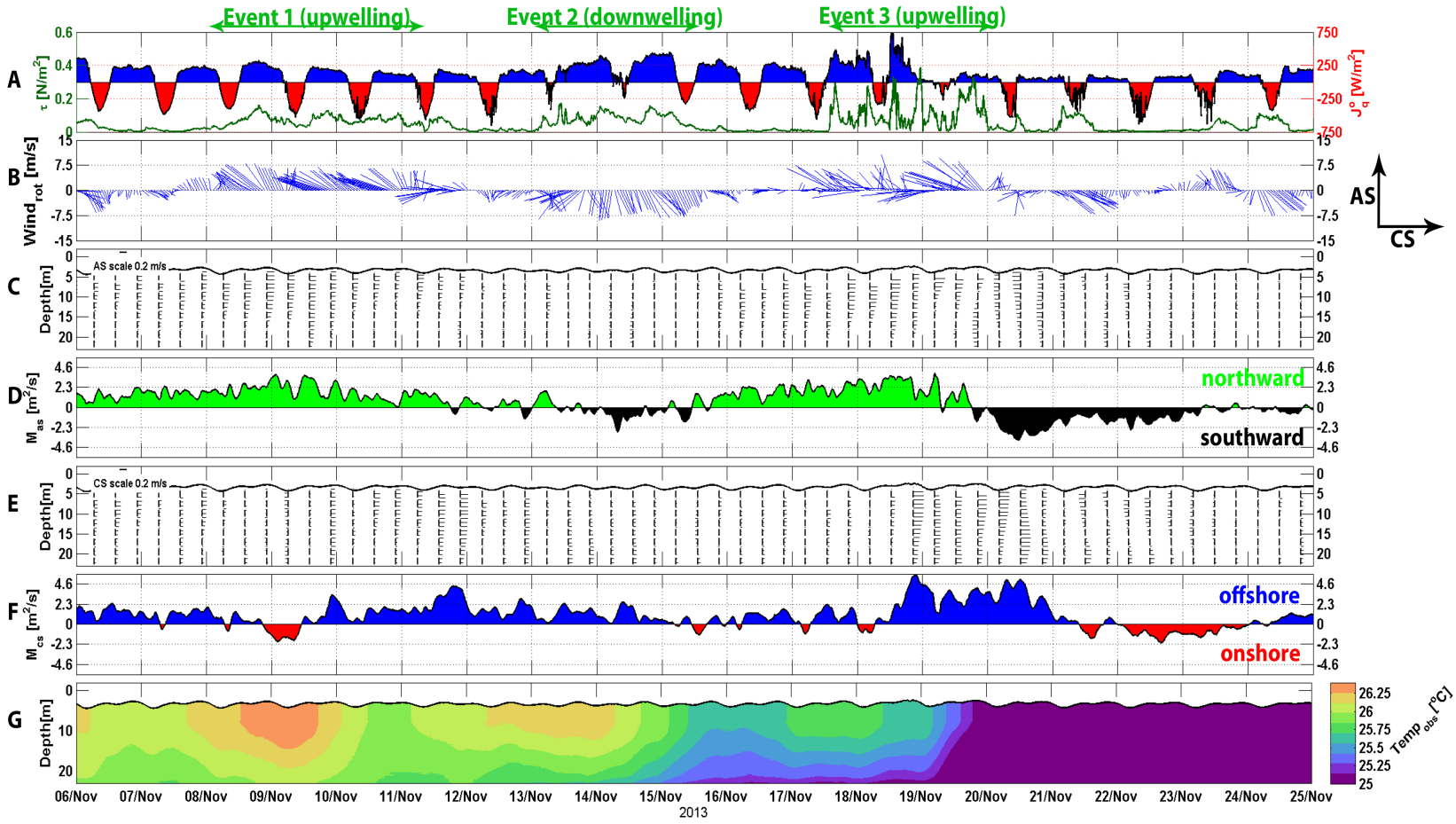

Figure 4.7: Hydrographic observations during the November 2013 period at Qarooh. The green arrows on top represent the durations of three upwelling / downwelling favorable wind events. (A) wind stress (green) and net surface heat flux (shaded), (B) rotated (315^o) wind velocity vectors, (C) AS residual current vectors, (D) AS net volume transport (Eqn. 4.3), (E) CS residual current vectors, (F) CS net volume transport (Eqn. 4.3), and (G) low-pass filtered potential temperature. Time is UTC.

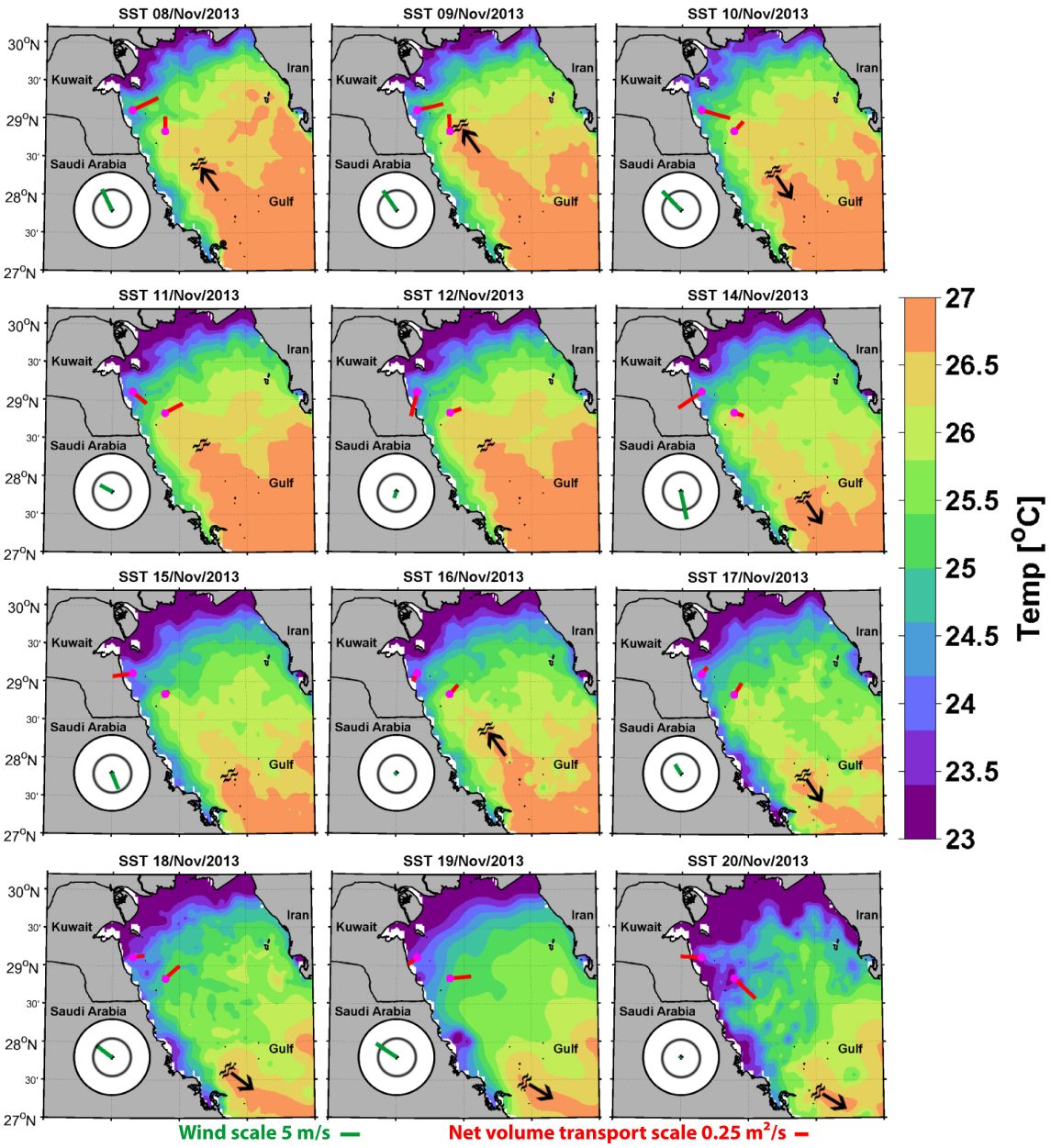

Figure 4.8: Daily SST images (L4-GHRSST) from November 8 and 20 with locations of Sea Island station and Qarooh mooring. Daily net volume transports are represented in red vector at both stations. Daily wind speed and direction are indicated by the green vector inside a circle (bottom left). Rings represent wind speeds at 5 m/s interval. Location of the warm 'tongue' tip is represented with a ≈ symbol and the propagation direction with a black arrow. No data was available on 13 Nov 2013.

cool, however, such cooling was not observed in the Qarooh region (Fig. 4.9B).

Unlike the Qarooh region, the net volume transport at the Sea Island mooring was offshore, roughly perpendicular to the wind direction and coastline during the three days of this event (Fig. 4.8). To further investigate if upwelling occurred in the near coast region (16 km offshore) we focus on the hydrographic conditions at the Sea Island mooring. Similar to the Qarooh mooring, we divided the AS/CS volume transport into upper and lower layers (Fig. 4.10C - F). During Event #1 a significant CS transport (Fig. 4.10D; $\geq$ 2.01 m^2/s) in the offshore direction was observed while the lower layer transport was 0.48 m^2/s (0.32, 0.64) in the opposite direction, onshore, (Fig. 4.10F). Moreover, the average water temperature at 4 m (Fig. 4.10B) was cooler 24.34 ^oC (24.30, 24.38) during Event #1 compared to the post-event (+ 1 days of event) average of 24.74 ^oC (24.71, 24.79). The cooler surface waters during this event were confined near the coast and did not extend to the Qarooh region (Figs. 4.8).

Based on the above hydrographic observations of flow structures, the upper layer temperatures from both moorings (Sea Island and Qarooh), and the SST from the GHRSST images, we are led to conclude that upwelling conditions did develop in the region near the coast but did not extend further offshore (44 km offshore) to the Qarooh region during this event.

4.3.2 Event #2- downwelling favorable wind

4.3.2.1 Meteorological conditions

The second event was a northwesterly wind (Shamal) lasting about 2.5 days (13 Nov 3:00 to 15 Nov 19:00) with a wind speed average of 6.24 m/s (6.03, 6.43) (Fig 4.5A and B). These winds reduced the average humidity by 6.02% (5.51, 7.21) and air temperature by 2.25 ^oC (2.24, 2.26) as they traveled over the continental land mass

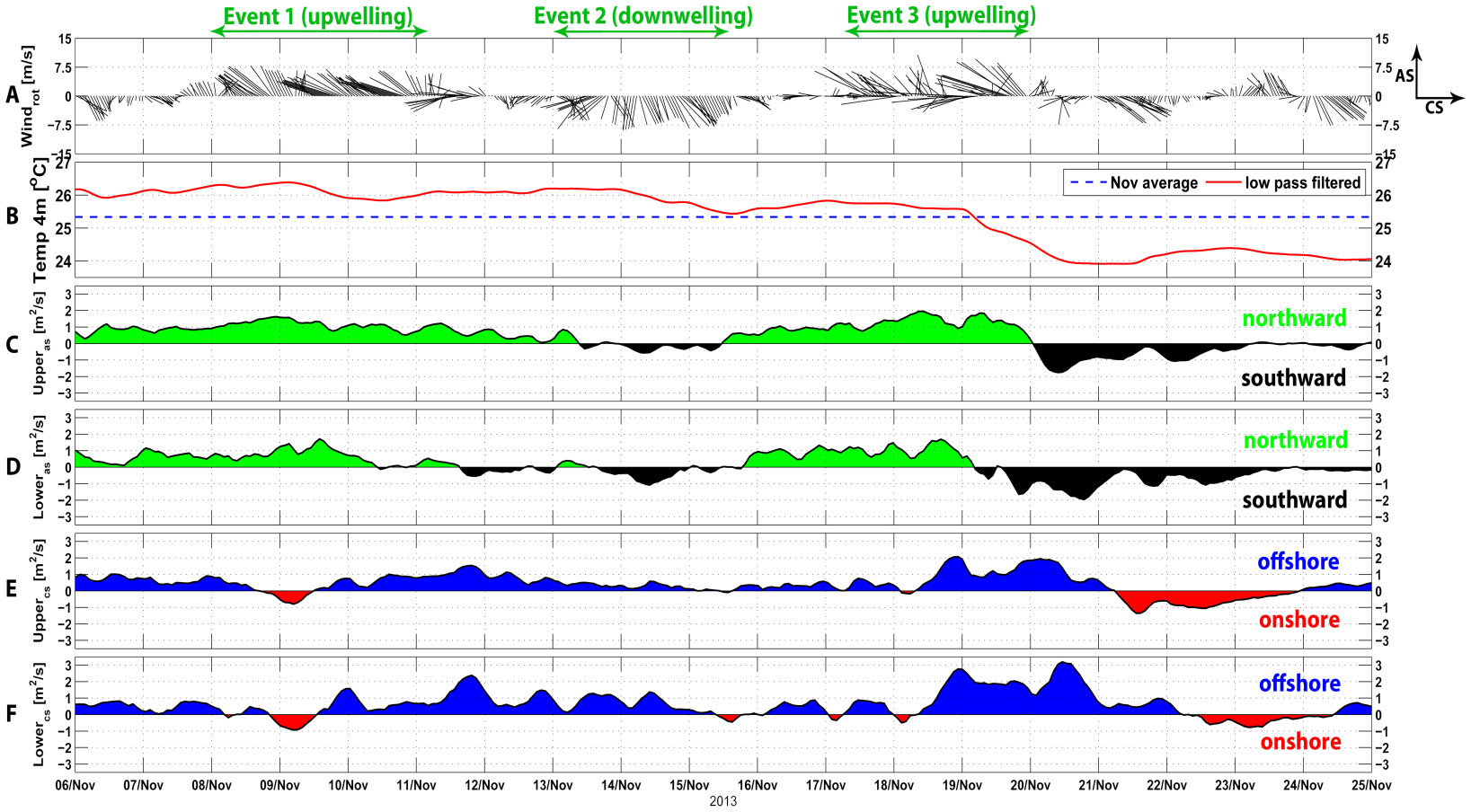

Figure 4.9: Along-shore (AS) and cross-shore (CS) volume transport in the upper (0 - 8 m) and lower (8 - 23 m) layers during November 2013 period at Qarooh mooring during three upwelling/downwelling favorable events (green arrow). (A) rotated (315°) wind velocity vectors, (B) hourly potential temperature at 4 m (blue is November average and red is low-pass filtered), (C) upper layer AS volume transport, (D) lower layer AS volume transport, (E) upper layer CS volume transport, and (F) lower layer CS volume transport. Time is UTC.

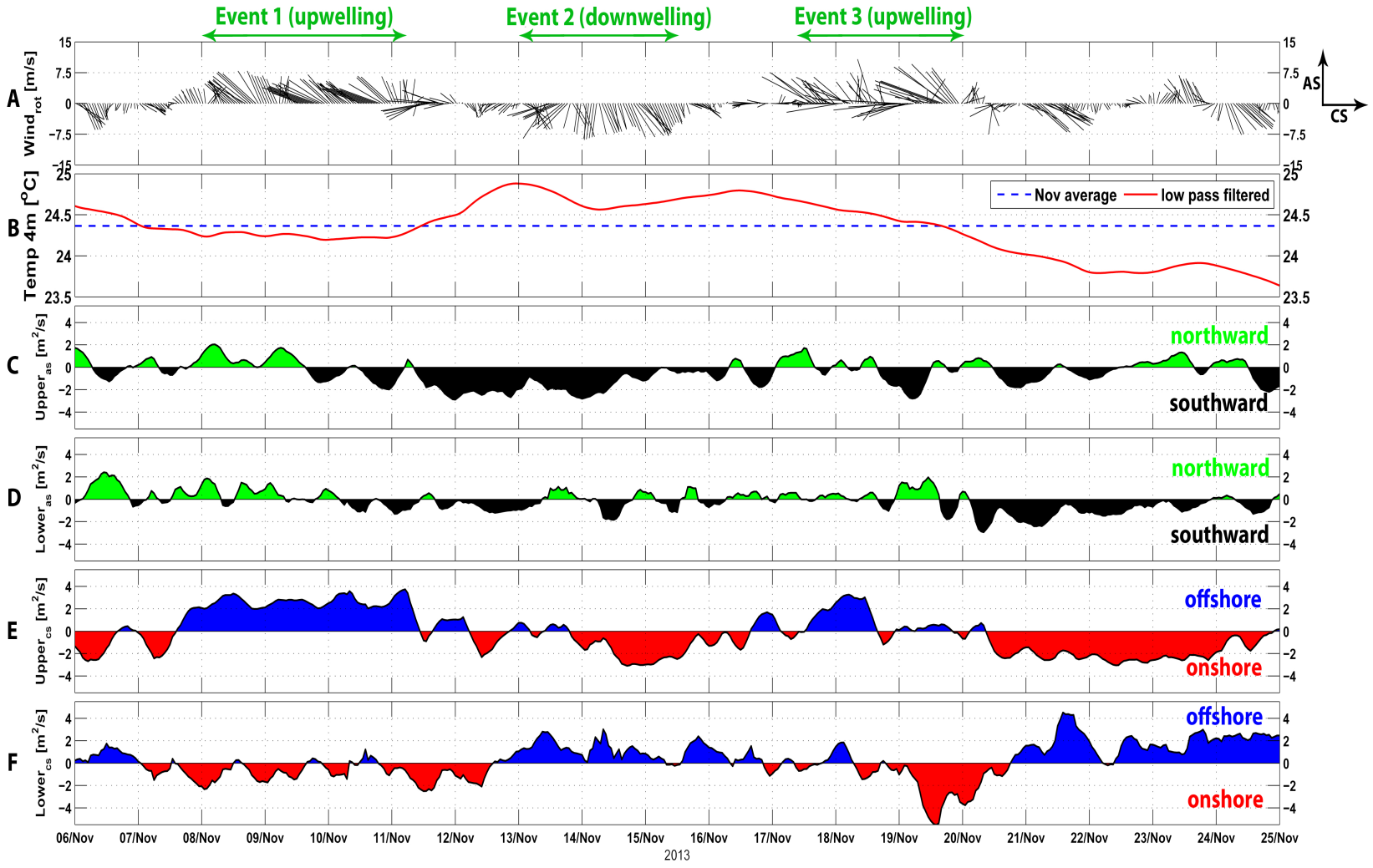

Figure 4.10: Same as Figure 4.9 but for the Sea Island region.

and the northerly regions (Fig 4.5C and D). Winter Shamals are a result of a high pressure system that develop behind a progressing cold front that causes an increase in barometric pressure gradient (Thoppil & Hogan, 2010). Development of the high pressure system led to an increase in barometric pressure to a maximum value of 1016.3 mb toward the end of the event (Fig 4.5E). Cloudy conditions during the first two days of this event, as indicated by the net shortwave (Fig. 4.5F), reduced net longwave radiation (loss) to 66.18 W/m^2 compared to the last day of the event (105.46 W/m^2; Fig. 4.5G). The reduction in air temperature and humidity, and the increase in wind speed during this event led to an increase in both sensible (Fig 4.5H) and latent heat (Fig 4.5I) losses from the sea surface resulting in a maximum net surface heat flux loss of 442.16 W/m^2.

4.3.2.2 Hydrographic conditions

Similar to Event #1, the thermal structure of the water column during Event #2 followed a diurnal heating pattern, consistent with the net surface heat flux, superposed on a semi-diurnal tidal cycle (Fig. 4.6B, F and G). The net CS volume transport during Event #2 was mostly (88%) offshore (Fig. 4.7F) while the net AS transport changed from northward to southward responding within about 3.5 hours to the change in wind direction to northwesterly (Fig. 4.7D). Consequently, during the change in net AS volume transport direction, the average water column temperature cooled from 25.98 ^{o}C (25.95, 26.00) to a minimum value of 25.43 ^{o}C (25.41, 25.45) toward the end of the event (Fig. 4.7G), suggesting that cooler waters were advected from the north. This is consistent with the GHRSST images (Fig. 4.8) showing the retreat of the warm 'tongue' southeastward from Qarooh and advance of cooler waters at the Gulf's head toward Qarooh between 12 Nov (pre-event) to 15 Nov (Fig. 4.8) in response to the northwesterly wind event.

4.3.2.3 Examining downwelling conditions

The AS and CS volume transport in both layers (upper and lower) at Qarooh (Fig. 4.9) during this event were similar to those during Event #1, where the upper and lower layer flows were similar in direction with no indication of downwelling. Conditions at the Sea Island mooring were different than those in the Qarooh region. Similar to Event #1 at the Sea Island region, the winds during Event #2 generated a net onshore flow, perpendicular to the coast and wind direction (Fig. 4.8). The upper CS volume transport (Fig. 4.10 E) reversed direction from offshore to onshore to become 2.08 m^2/s (1.84, 2.24) responding to the wind direction change to northwesterly within 2.75 hours from the start of the event. The lower layer CS transport flowed in the opposite direction (away from the coast) at a rate of 1.12 m^2/s (0.81, 1.28) (Fig. 4.10F). Moreover, the surface temperatures at the Sea Island mooring were relatively higher during this event (maximum 24.90 ^oC) compared to the November period average (24.38 ^oC) (Fig. 4.10B).

Based on the above observations at both moorings (Qarooh and Sea Island) and the GHRSST images, we suggest that as in Event #1 downwelling occurred near the coast but did not extend to the Qarooh region. The flow at Qarooh followed the general wind direction, with the AS volume transport advecting the warm 'tongue' in the same direction. During Event #1 (southeasterly wind event) the 'tongue' progressed in a northwesterly direction causing warmer conditions at Qarooh, while during Event #2 (northwesterly wind event) the 'tongue' regressed to the southeast following the advance of cooler waters from the Gulf head.

4.3.3 Event #3- upwelling favorable wind

4.3.3.1 Meteorological conditions

The third event was a southeasterly wind event (Kous) that started on 17 Nov 20:00 and ended on Nov 20 02:00. Average wind speed was 7.76 m/s (7.46, 8.06) with a maximum speed of 13.70 m/s (7.46, 8.06). Both the average and maximum winds speeds were higher than during the previous two events (Fig 4.5A and B). Associated with this event was a unique burst of rain (total of 29.2 cm in 24 hours) on 18 Nov (Fig 4.5D) that caused flooding in the coastal regions of Kuwait as reported by the KMO. Similar to the rain amount measured by us at Qarooh, a total of 25 cm was reported by the KMO at Um Al Maradim Island, Kuwait (19 km southwest of Qarooh Island). The lowest air temperature of 18 ^{o}C and highest humidity of 96% during November were recorded during this event (Fig 4.5C and D). The unique weather conditions during this event resulted in maximum sensible (105 W/m^2) and latent (352 W/m^2) heat flux losses, and a maximum net heat flux loss of 707 W/m^2.

4.3.3.2 Hydrographic conditions

On Nov 18 19:00 (mid-event), an abrupt drop in water column temperature (0.9 ^{o}C in 1.8 hrs; Fig 4.6B), increase in salinity (1.4 psu in 3.75 hrs; Fig 4.6D), and thus, increase in density (1.4 kg/m^3 in 3.75 hrs; Fig 4.6E), was observed. The abrupt rise in salinity was followed by a gradual decrease to a minimum value of 40.6 psu at 8.9 m depth toward the end of the event. On Nov 19 01:00, 6 hrs after the previous abrupt changes, the CS velocity component average velocity of 0.07 m/s (0.06, 0.07) changed to an offshore direction until 25 Nov (red box in Figure 4.6G). Two scatter plots (Fig. 4.11 A and B) were used to further investigate the relation between the observed changes in salinity and temperature, and the CS volume transport. The scatter plots suggest that the offshore transport, between 19 - 23 Nov, reduced

both the temperature and salinity by 0.14 ^{o}C and 0.40 psu, respectively as can be seen from the lower salinity and temperature values (cooler colors) in the eastern quadrants of Figures 4.11A and B.

A T-S diagram was used (Fig. 4.11 C) to further investigate the possible origin of the advected waters. The TS diagram indicates that prior to the strengthening of the offshore velocity component on 16 - 19 Nov, the Sea Island region (blue star) and Qarooh region (red cross) water properties (temperature and salinity) were significantly different. As the offshore velocity component strengthened (19 - 25 Nov; red box in Figure 4.6G), the temperature and salinity values in the Qarooh region became similar (green circle) to those at Sea Island (Fig. 4.11 C). This is also observed in the GHRSST images, where cooler water closer to shore extended to Qarooh Island toward the end of the event (20 Nov).

The differences between this event and the previous two events is the strength of the winds that appear to have lead to a significant offshore flow. Based on the above, we are led to conclude that unlike the previous two events, the extent of the cooler and fresher water close to shore did extend and reach the Qarooh region during this event.

4.3.3.3 Examining upwelling conditions

Although the CS volume transport at Qarooh appears to have altered the water properties (temperature and salinity), the AS flow component responded by flowing in the direction of the wind as in the previous events (Fig. 4.7D) i.e. the southeasterly wind generated a northerly AS flow. After Event #3, the AS current direction changed to become southerly following the change of the wind direction to northwesterly. In the Sea Island region, the CS currents followed a similar pattern to those during Event #1, when a southeasterly wind generated an offshore flow per-

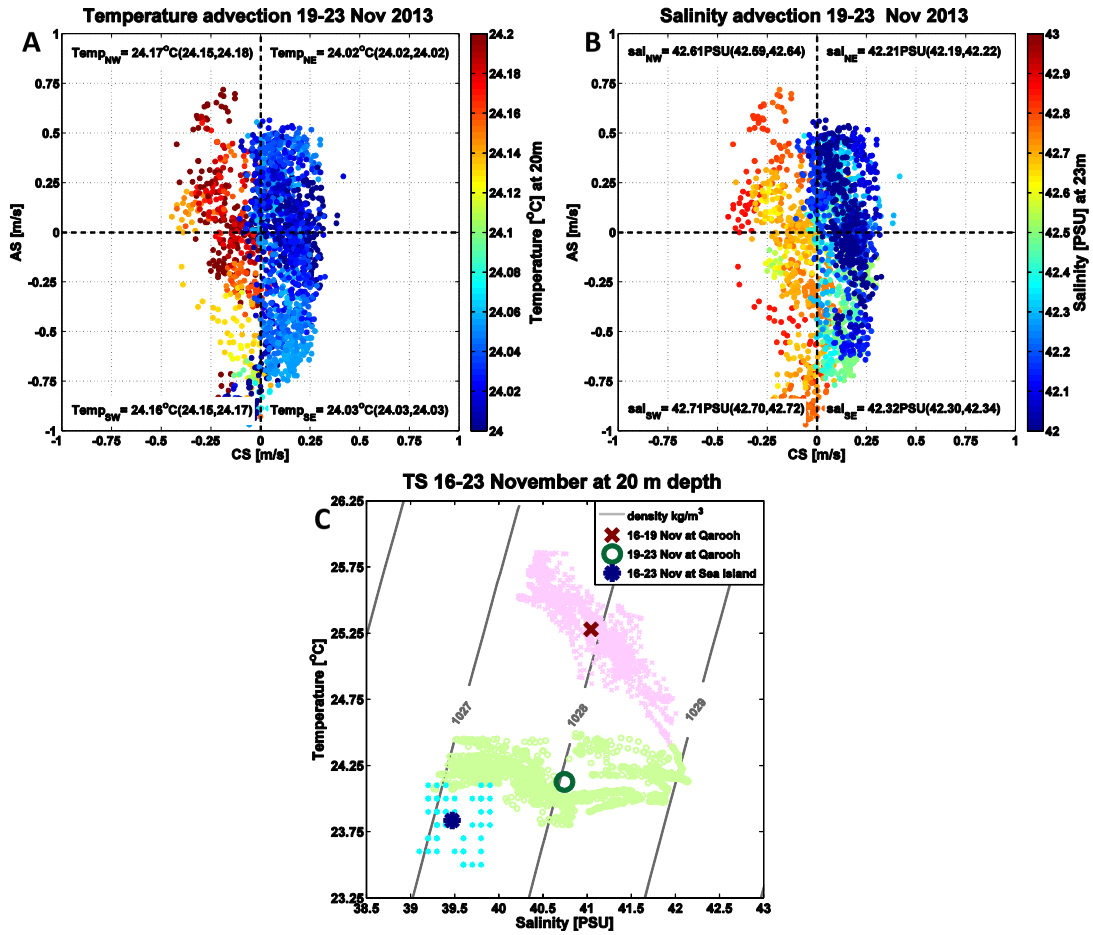

Figure 4.11: Scatter plots of (A) water temperature and (B) salinity versus currents at 20 m depth from 19 to 23 Nov as observed at Qarooh. Average potential temperature and salinity values (NW, NE, SW, SE) and their 95% confidence intervals are shown for each quadrant. (C) TS diagram showing temperature and salinity properties at Qarooh during 16 - 19 Nov (red cross) and 19 - 23 Nov (green circle), and at Sea Island between 16 - 23 Nov (blue star) at depths of 20 m. The global averages of temperature and salinity properties for each location are indicated by a bigger symbol.

pendicular to both the wind and the coast in the upper layer (Fig. 4.8 17 and 18 Nov). The flow in the lower layer was opposite in direction; i.e. toward the coast (Fig. 4.10F), thus suggesting upwelling conditions. This is further supported by the observed cooling of the upper layer water temperature from 24.75 ^{o}C to 23.52 ^{o}C in the Sea Island region (Fig. 4.10B).

Two scatter plots (Fig. 4.12) further clarify the relation between the wind direction and the upper layer AS volume transport at Qarooh, and between the wind direction and the upper layer CS volume transport at Sea Island during November. Inspection of Figure 4.12 indicates that in the Sea Island region the southeasterly winds were closely associated with an average offshore transport of 1.47 m^2/s (1.16, 1.74), suggesting upwelling favorable conditions. While the northwesterly winds were closely associated with an onshore transport of 1.80 m^2/s (1.62, 1.97), suggesting downwelling favorable conditions. The southeasterly wind in the Qarooh region was followed by an average AS transport of 0.88 m^2/s (0.75, 1.01), while a northwesterly wind by a -0.37 m^2/s (-0.50, -0.25) AS transport, suggesting that the upper layer transport in the Qarooh region generally follows the wind direction.

In summary, the previous three events suggest that upwelling / downwelling was confined near coast and did not extend to the Qarooh region (44 km offshore). This conclusion was supported by hydrographic observations of flow structures in the upper and lower layers, the upper layer temperatures from both moorings (Sea Island and Qarooh), and the SST from the GHRSST images. However, the significant wind forcing associated with Event #3 appears to have resulted in a relatively stronger offshore flow that did extend to Qarooh. This lead us to suggest that during this event the effects of upwelling did extend to Qarooh region.

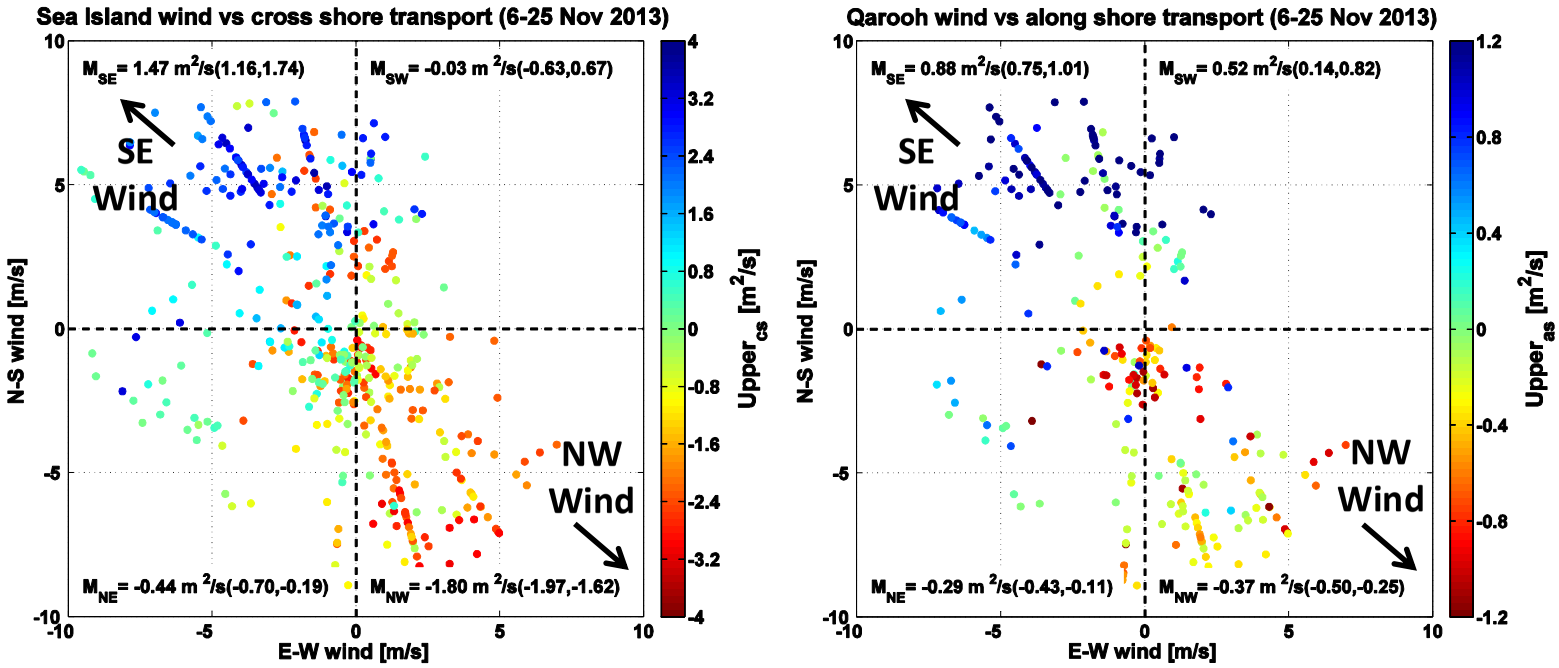

Figure 4.12: Scatter plot of wind versus the upper layer (0 - 8 m) CS volume transport at Sea Island mooring (left) and scatter plot of wind versus the upper layer AS volume transport at Qarooh mooring (right) from 6 to 25 Nov. Average volume transport values and their 95% confidence intervals are shown in their respective quadrant (NW, NE, SW, SE). The two main wind directions northwesterly (NW) and southeasterly (SE), are labeled with black arrows.

4.3.4 November period model simulations

4.3.4.1 Numerical simulation details

Numerical simulations (Section 4.2.2) for the Qarooh region were carried out with the two equation k-ε model using the Canuto et al. (2001) stability function. Simulations were forced with 10 minutes surface momentum, net non penetrative heat fluxes and solar radiation at the air-sea interface. To accurately simulate the hydrodynamics region necessitates information on the spatially non-uniform seawater properties (e.g. temperature and salinity). In general, this can only be achieved using 3D models but not with 1D models like the GOTM model used here (Simpson et al., 2002; Burchard et al., 2006). To partially account for this limitation, hourly spatial gradients of temperature ($\partial_x T$ and $\partial_y T$) were computed from the 4 m depth water temperature observations available to us at three locations. We used two locations (Sea Island mooring and Qarooh mooring) to compute $\partial_x T$, and two locations (Qarooh mooring and Jabriya mooring located 75 km north of Qarooh) for $\partial_y T$. Of interest to note that the daily gradients for $\partial_x T$ and $\partial_y T$ during this period ranged between 0.0029 ^{o}C/km to 0.043 ^{o}C/km, and 0.022 ^{o}C/km to 0.054 ^{o}C/km, respectively. The model was given initial and final temperature profiles at the start date of Nov 6 0:00 and end date of Nov 25 0:00, respectively. Next, simulation results of the water column temperature, net AS and CS volume transports, as well as ε are presented.

4.3.4.2 Numerical simulation results at Qarooh

As described from the observations for Events #1-3, the thermal fields at Qarooh were dominated by horizontal advection processes responding to the wind events. The net AS volume transports were in the general direction of the wind; i.e. northwesterly winds resulted in a southerly net AS volume transport and southeasterly

winds resulted in a northerly net AS volume transport (Fig. 4.13A and B). Model simulation results of the net AS volume transport (M_{as}^{mod}) were consistent with the net AS volume transport estimated from the observations (M_{as}) during the three events, simulating volume transport up to 2.84 m^2/s during a southeasterly wind and up to -1.42 m^2/s during a northwesterly wind (Fig. 4.13B; Table 4.2). Moreover, the general warming of the water column following the northwestward progression of the warm 'tongue' (Event #1) and cooling following the southeastward regression of the warm 'tongue' (Event #2) appears to be captured well by the model (Fig. 4.13D and E; Table 4.2). Although the general warming and cooling trends were captured well by the model during the November period, further analysis of the model results revealed cooler temperatures than observed in the ML during the three events (Fig. 4.13F). Next, we describe the possible reasons for these simulated cooler temperatures in each event.

During Event #1 model simulations underestimated the warming resulting from the net AS transport (northward) advecting the warm 'tongue' northward (Fig. 4.13D - F profiles 5 - 8) by MBE of -0.05 ^oC (-0.05, -0.04) and RMSE of 0.07 ^oC (0.07, 0.08). The weaker winds between Events #1 and #2 (Fig. 4.13A) enhanced stratification indicated by a shallower ML depth (Fig. 4.13D profiles 11 - 14). The model results followed well the observations showing a decrease in the ML depth in response to the relatively weaker mixing in the ML, as suggested by lower ε values (Fig. 4.13G).

On the progression of Event #2 the model overestimated the cooling near the surface and underestimated the cooling in deeper waters with a MBE of 0.08 ^oC (0.08, 0.09) (Fig. 4.13D - F profiles 15 - 20). At the beginning of Event #2, both simulated and observed ML depths were about 8 m (Fig. 4.13E and F profile 14). As the event progressed, the simulated ML depth deepened faster than the observed

following the relatively increase in vertical mixing indicated by higher ε values (Fig. 4.13G). By the end of Event #2 the simulated ML depth reached 22 m, while the observed ML depth was 13 m (Fig. 4.13E and F number 19). The simulated cooler surface waters in the ML and warmer deeper water than the observations is possibly due to the mixing of warmer surface waters with the deeper cooler waters, thus resulting in cooler surface waters and warmer deeper waters (Fig. 4.13F number 19 and 20).

Similarly, during the Event #3 (Fig. 4.13D - F profiles 23 - 27), the model also overestimated the ML depth following a consistent pattern to ε values (Fig. 4.13G). This resulted in the warmer surface waters to be mixed with deeper layers causing cooler waters in the ML to be cooler than the observations with a MBE of 0.09 ^{o}C (0.08, 0.09) and RMSE of 0.1 ^{o}C (0.10, 0.11).

Overall, during the three events, the model simulations displayed good results indicated by a significant (p-values <0.05) correlations between the observed and simulated water column temperatures of 0.77 (0.76, 0.78) and positive Nash-Sutcliffe values of 0.74 (0.73, 0.74). However, between events the model simulations of the net AS/CS transports were poor with insignificant (p-values >0.05) weak correlations of -0.11 (-0.14, -0.09) and negative Nash-Sutcliffe values of -0.19 (-0.20, -0.19). This is possibly due to the model simulating volume transports (AS and CS) near zero during the weak wind stress between events (Fig. 4.13B and C).

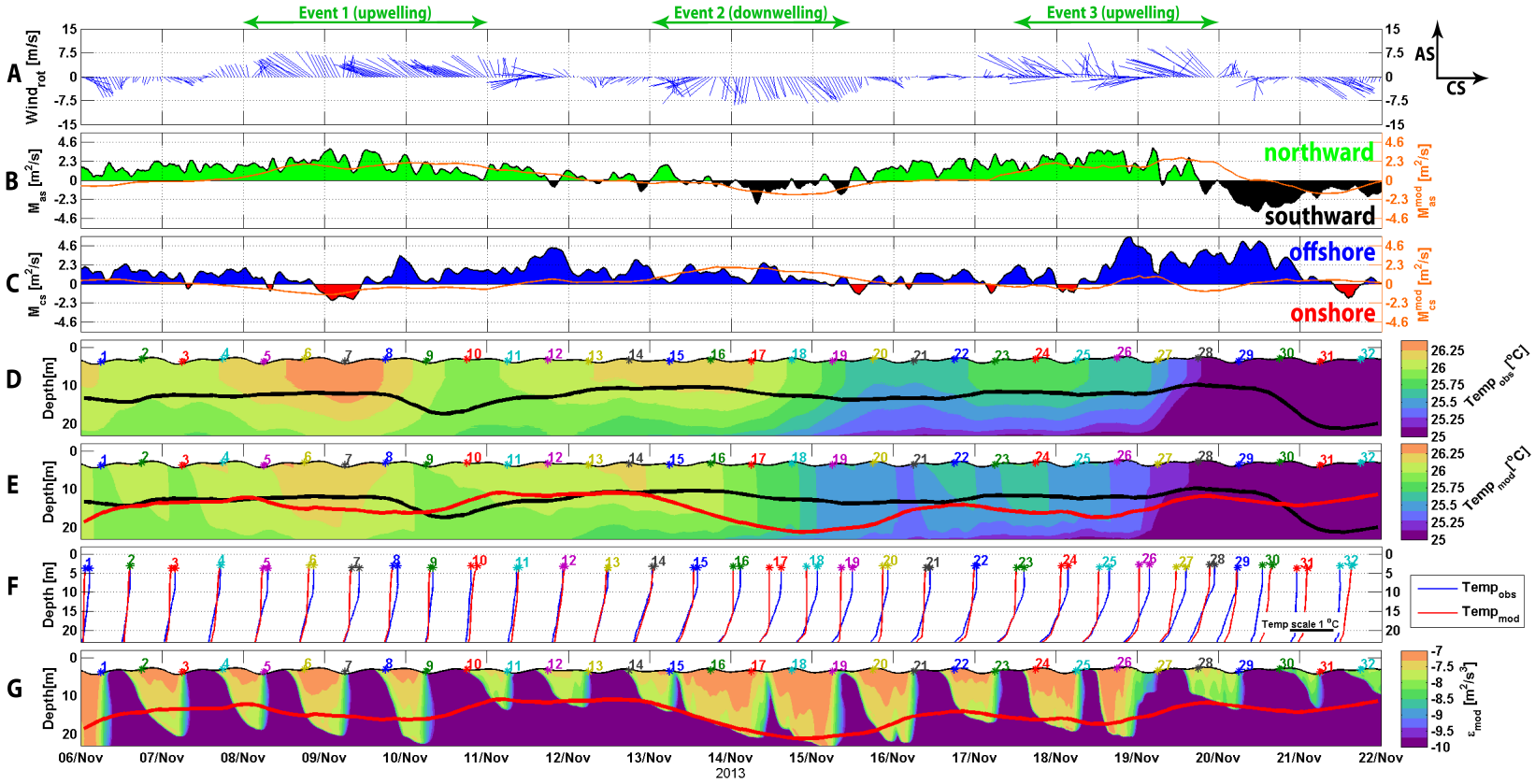

Figure 4.13: Hydrographic observations and model simulations during 6 - 22 November 2013 at Qarooh. The green arrows on top represent the durations of the three upwelling/downwelling favorable wind events. (A) rotated (315^o) wind velocity vectors, (B) observed (M_{as}; shaded) and simulated (M_{as}^{mod}; orange) AS net volume transport (Eqn. 4.3), (C) observed (M_{cs}; shaded) and simulated (M_{cs}^{mod}; orange) CS net volume transport (Eqn. 4.3), (D) low-pass filtered potential temperature estimated from observations with ML depth in black line, (E) simulated potential temperature with ML depth in black line, (F) computed from observations (blue) and simulated (red) potential temperature profiles, and (G) simulated turbulence kinetic energy dissipation rates (ε) with simulated ML depth in red line. Time is UTC.

4.3.5 Event #4- downwelling favorable wind

4.3.5.1 Meteorological conditions

The fourth event was during the February period and was a northwesterly event (Shamal) that lasted for 2.5 days (Feb 3 2:00 to Feb 5 13:00). The event resulted in wind speeds up to 14 m/s and wind stress of 0.58 N/m^2 (Fig. 4.14A and B). Similar to the previous northwesterly event (Event #2), the air was cooler (4^{o}C) and drier (35%) during this event as the wind traveled over the continental land mass and northern regions (Fig. 4.14C and D). Furthermore, the build-up of the high pressure that followed the passage of the cold front generated the northwesterly winds and increased the barometric pressure by 11.4 mb (Fig. 4.14E). The sky was clear of clouds during the event as indicated by the net shortwave radiation observations well defined 'bell-shape' (Fig. 4.14F). Maximum losses of longwave of 103 W/m^2, sensible of 40 W/m^2, and latent of 334 W/m^2 heat fluxes, and thus, maximum net heat flux loss of 420 W/m^2 were observed during this event (Fig. 4.14F - J).

4.3.5.2 Hydrographic conditions

Similar to Event #1-3, the thermal structure of the water column during Event #4 followed a diurnal heating pattern that was consistent with the net surface heat flux superposed on a semi-diurnal tidal cycle (Fig. 4.15B, F and G) with temperatures ranging between 16.02 ^{o}C and 17.21 ^{o}C. As in the November period, these cycles have been filtered out from the thermal structure observations using a 36 hour low-pass filter. Results, after filtering, are presented in Figure 4.16G. Additionally, tidal currents were filtered from the current observations, from which the AS/CS current vectors (Fig. 4.16C and E) and AS/CS volume transport were computed (Fig. 4.16D and F) (details in Section 4.2.1.2).

As in the previous northwesterly wind event (Event #2), the net AS volume

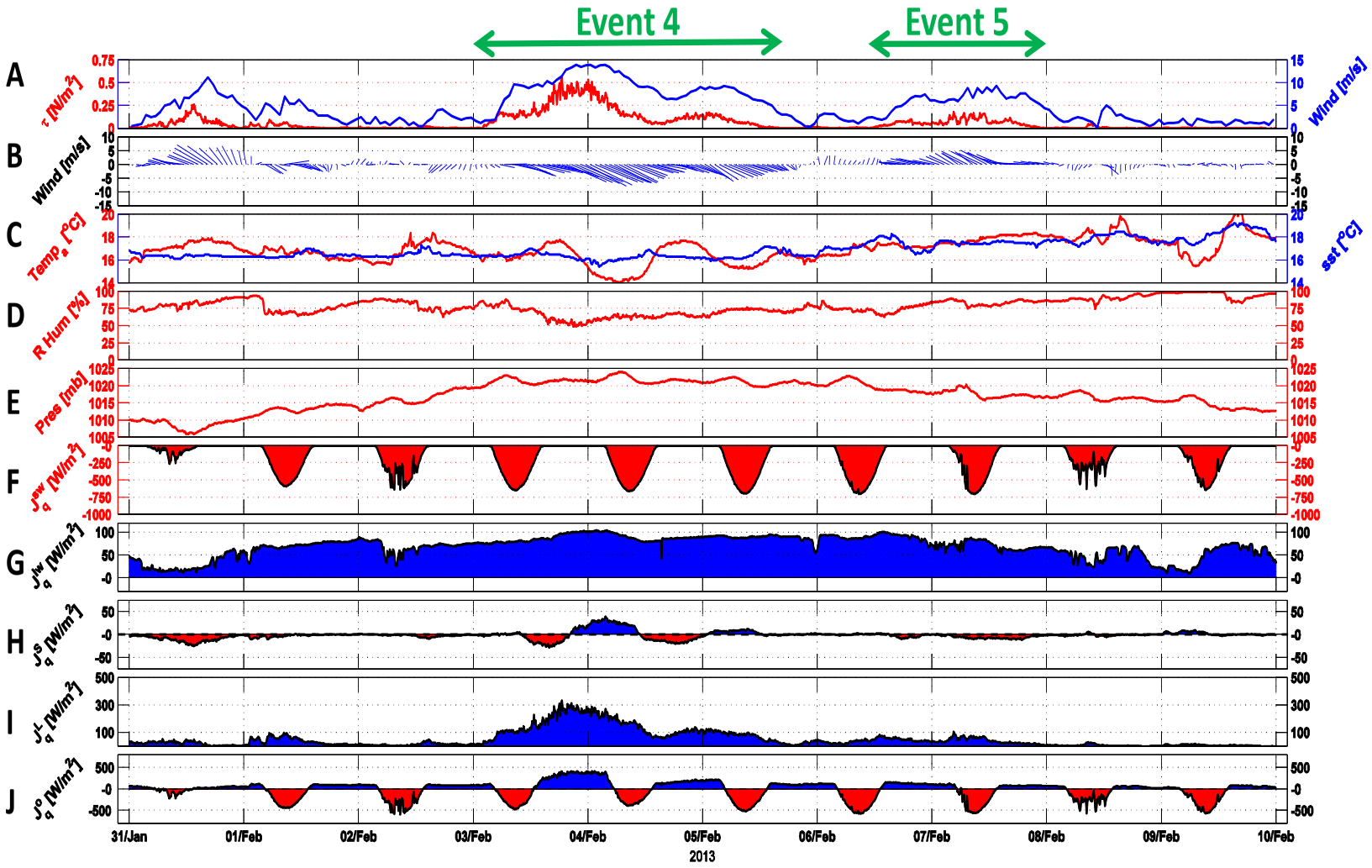

Figure 4.14: Same as Figure 4.5 but for February.

transport was similar to the wind direction at Qarooh (Fig. 4.16D). The AS current throughout the water column flowed in the general direction of the wind with currents weakening toward the seabed likely the result of diminishing wind influence (Fig. 4.16C). Moreover, during the events peak hour (Feb 4 mid-night) the CS volume transport reverted to offshore (Fig. 4.16F). As the CS volume transport changed direction, the water column cooled to reach the minimum average temperature of 16.35 ^{o}C (16.34, 16.37) on Feb 4 14:45, suggesting cooler waters were transported from regions closer to shore. This appears to be consistent with the GHRSST images (Fig. 4.17), where the SST images show the push-back of the warm 'tongue' to the southeast and advance of the cooler waters at the Gulf head between the Feb 4 and 5. These conditions were similar to the previous northwesterly event (Event #2).

4.3.5.3 Examining downwelling conditions

In a similar approach to the November period, the volume transport for both components (AS and CS) were divided into two layers (upper and lower), an upper layer spanning from the sea surface to a depth of 8 m, and a lower layer from 8 m to the seabed. Consistent with the previous three events, the upper and lower layers volume transport were similar in direction for both components (AS and CS) (Fig. 4.18), suggesting no downwelling in the Qarooh region.

At the Sea Island region, both volume transport components (AS and CS) at the two layers (upper and lower) responded to the northwesterly wind event within 2 hours (Fig. 4.19). Unlike the November period where it was only the CS component that responded to the wind event; during this event, a strong (maximum of 3.76 m^2/s) onshore volume transport developed at the upper layer (Fig. 4.19D), while a flow in the opposite direction (offshore) developed at the lower layer (Fig. 4.19E) indicating downwelling conditions. Moreover, the AS transport in the upper layer (Fig. 4.19B)

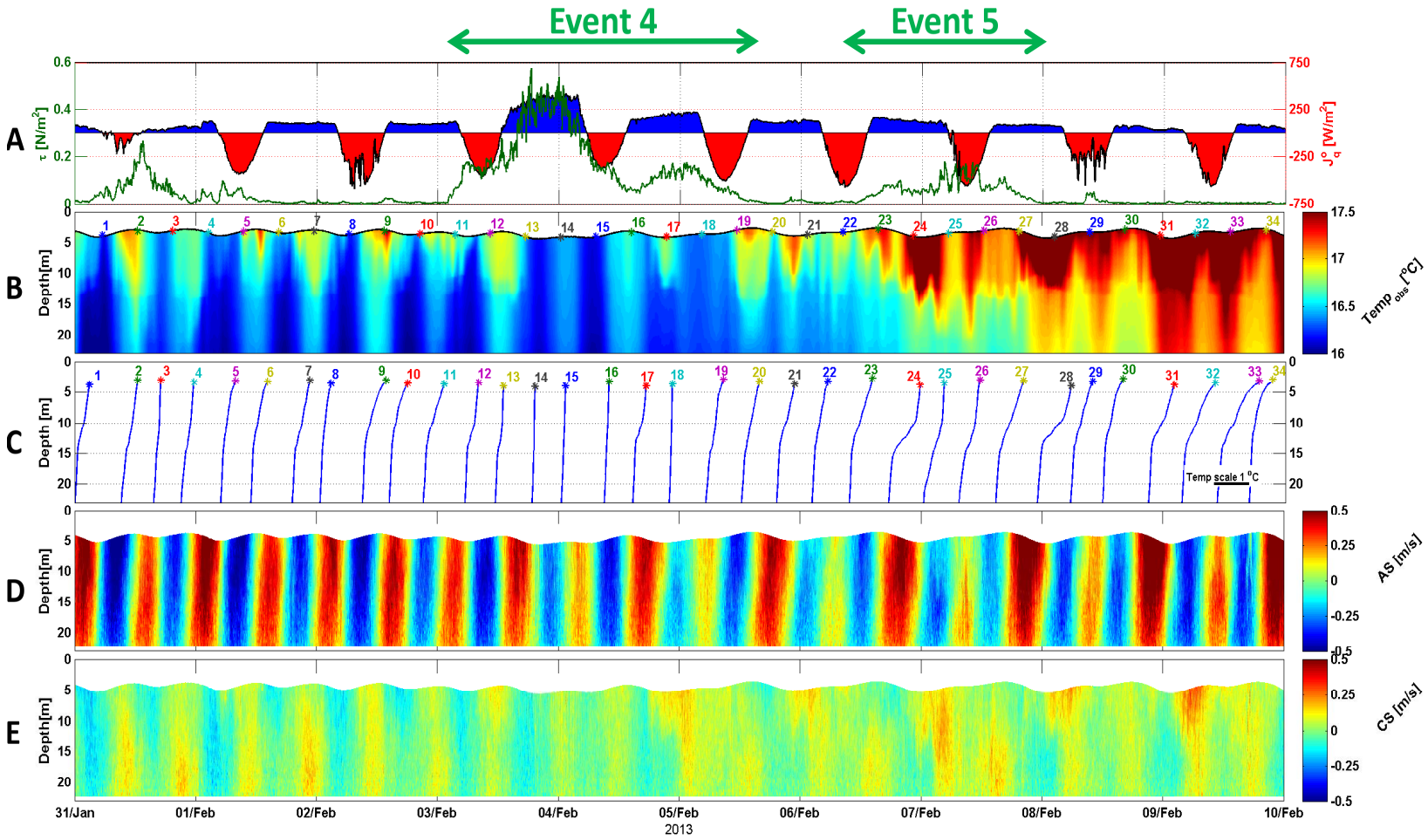

Figure 4.15: Hydrographic observations during February 2013. The green arrows on top represent the durations of two upwelling / downwelling favorable wind events. (A) wind stress (green) and net surface heat flux (shaded), (B) potential temperature, (C) potential temperature profiles, (D) AS (315^o), and (E) CS (45^o) currents. Time is UTC.

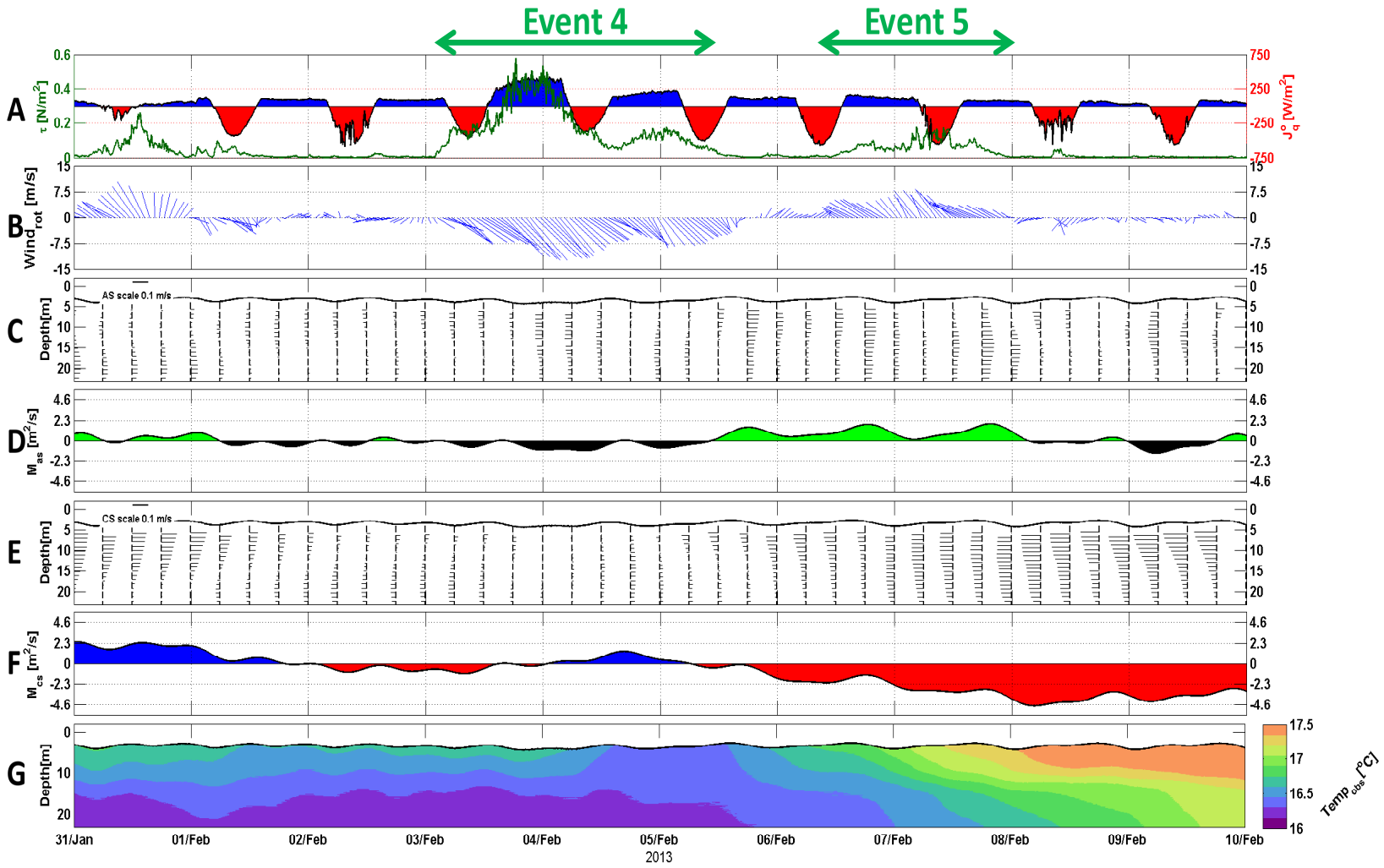

Figure 4.16: Same as Figure 4.7 but for February.

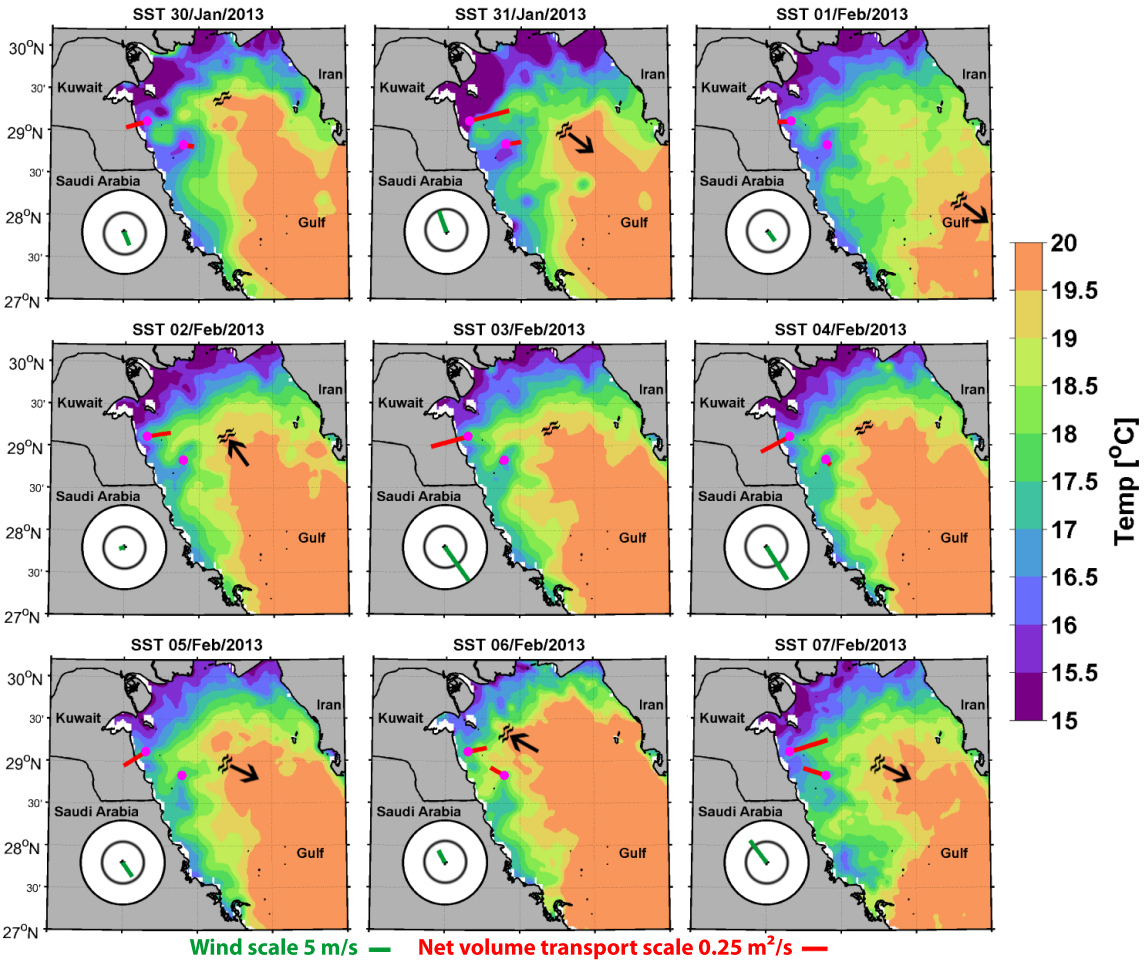

Figure 4.17: Same as Figure 4.8 but for February.

at the Sea Island mooring followed the general direction of the wind that was similar to the Qarooh region with a maximum volume transport of 1.92 m^2/s, while the lower AS volume transport was in the opposite direction (Fig. 4.19C). Based on the above, we are led to suggest a similar conclusion to the previous northwesterly event (Event #2) that downwelling did occur at the region close to shore but did not extend to the Qarooh region.

4.3.6 Event #5- upwelling favorable wind

4.3.6.1 Meteorological conditions

The fifth event was a southeasterly event (Kous) starting at Feb 6 17:00 and ending on Feb 8 1:00. The 1.5 day event produced hourly wind speeds up to 9.33 m/s (Fig. 4.14A and B). Consistent with the previous two southeasterly events (Events #1 and #3), the event resulted in an increase in temperature by 2.41 ^oC and humidity by 28.22 % as the winds traveled over the Gulf and from the southern regions (Fig. 4.14C and D). Furthermore, a decrease in barometric pressure by 7.1 mb was measured during this event (Fig. 4.14E). The surface net heat flux followed a diurnal heating pattern (Fig. 4.14J) with a peak value of 563 W/m^2 occurring mid-day in response to the shortwave radiation (Fig. 4.14F) and a maximum net heat flux loss of 148.62 W/m^2 during the evening. The average longwave radiation of 73.40 W/m^2 (72.04, 75.05) and latent heat flux of 36.75 W/m^2 (34.01, 39.58) were lower compared to Event #4, due to the relatively higher humidity, weaker winds, and warmer air temperatures during this southeasterly event.

4.3.6.2 Hydrographic conditions

The thermal structure followed a warming trend with the water column average temperature changing from 16.79 ^oC (16.78, 16.82) at the start of the event to 17.35 ^oC (17.29, 17.41) at the end of the event (Fig. 4.15B). This warming trend in the

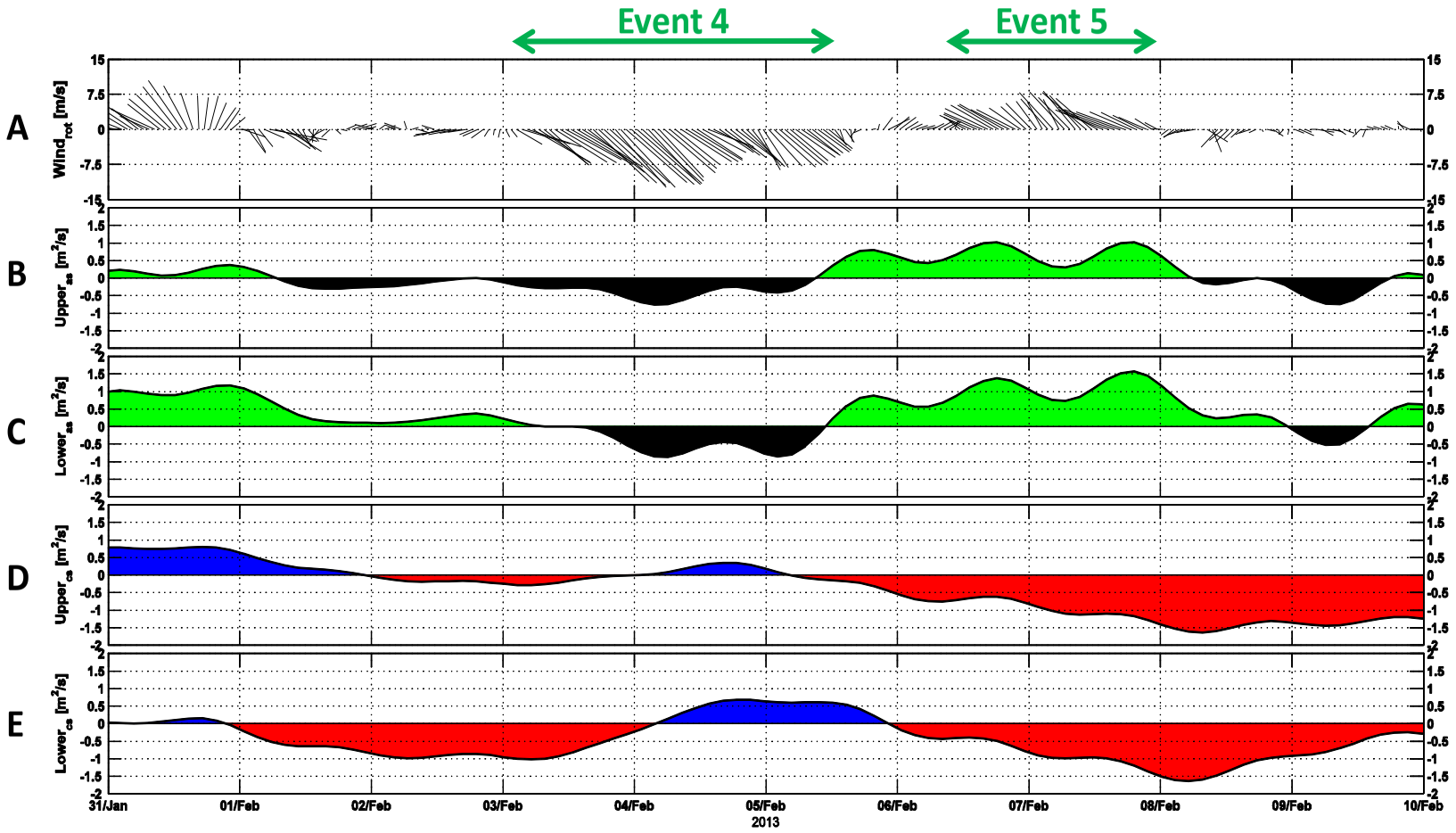

Figure 4.18: Along and cross shore volume transport in the upper (0 - 8 m) and lower (8 - 23 m) layers during February 2013 at Qarooh mooring. The green arrows on top represent the durations of two upwelling / downwelling favorable wind events. (A) rotated (315^o) wind speed vectors, (B) upper AS volume transport, (C) lower AS volume transport, (D) upper CS volume transport, and (E) lower CS volume transport. Time axis is in UTC.

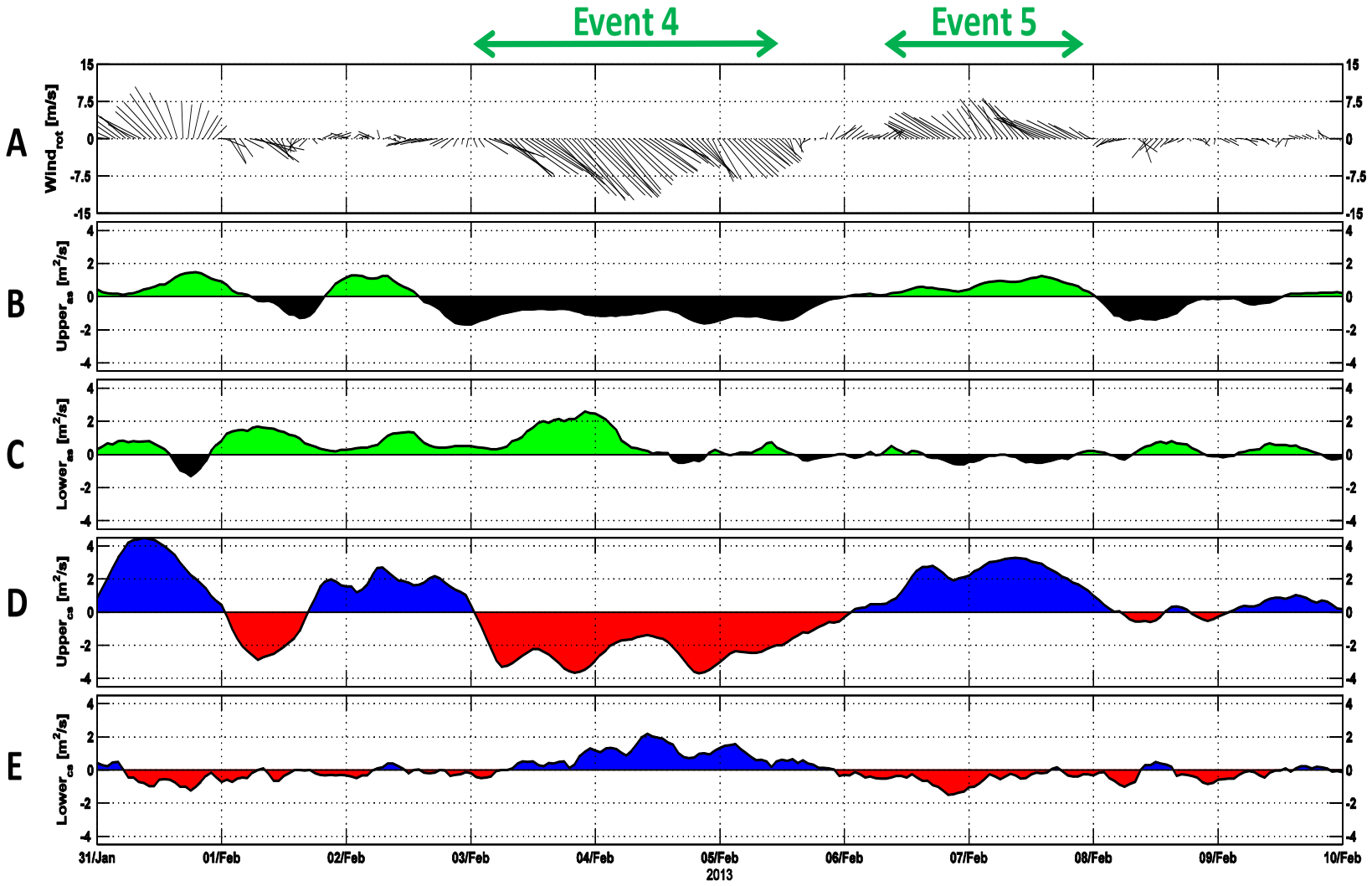

Figure 4.19: Same as Figure 4.18 but for Sea Island mooring.

thermal structure started post-Event #4 (mid-Feb 5th) responding to the gradual change in wind direction from northwest to southeast (Fig. 4.14B). Furthermore, the heating rate of the thermal structure increased from 0.05 ^{o}C/day during pre-Event #5 to reach a maximum rate of 0.49 ^{o}C/day on Feb 7 4:00 during mid-Event #4. The increase in water temperature occurred along with the net AS volume transport reverting directions from southerly to northerly and the net CS volume transport reverting from offshore to onshore post-Event #4 mid-Feb 5th (Fig. 4.16D and F). Moreover, the net CS transport peaked (4.83 m^2/s) toward the end of Event #4 when the water column reached its warmest temperature (17.35 ^{o}C) during this event. This led us to suggest that the volume transport from the southeast regions have resulted in a warmer temperatures. This is further supported by the GHRSST images (Fig. 4.17). The SST images shows the warm 'tongue' advancing in the northwesterly direction toward the Qarooh region between the Feb 5 and 6.

4.3.6.3 Examining upwelling conditions

Consistent with the previous four events, the AS volume transport at Qarooh followed the general wind direction at both depth layers (Fig. 4.18B and C). Similarly to the Qarooh region, the Sea Island upper layer AS transport was in the same direction as the wind (Fig. 4.19B) but the lower layer transport flowed in the opposite direction (Fig. 4.19C). Furthermore, the upper layer CS transport at the Sea Island was offshore (Fig. 4.19D) while the lower layer flow was onshore (Fig. 4.19E), indicating upwelling conditions. The upper layer offshore transport responded to the southeasterly wind within 1.75 hours.

As in the November period, scatter plots were constructed to quantify and clarify the relation between the wind direction and the upper layer AS transport at Qarooh, and between the wind direction and upper layer CS volume transport at the Sea

Island mooring (Fig. 4.20). The results indicate that the southeasterly wind is closely associated with an average offshore transport of 2.56 m^2/s (2.24, 2.88) at the Sea Island region, suggesting upwelling favorable conditions. This offshore transport is higher compared to the 1.47 m^2/s from the November period. At the Sea Island region the northwesterly wind was closely associated with an onshore transport of 1.78 m^2/s (1.49, 2.04), again suggesting downwelling favorable conditions. This onshore transport is consistent with the 1.80 m^2/s from the November period. At at the Qarooh the southeasterly wind resulted in an average upper layer AS transport of 0.47 m^2/s (0.36, 0.60), while a northwesterly wind resulted in a -0.32 m^2/s (-0.40, -0.23) upper layer AS transport suggesting that the volume transport in the Qarooh region followed the general wind direction. Both the AS and CS upper layer transport averages at Qarooh during the February period were similar to those in November.

4.3.6.4 February period model results

Similar model simulation approaches from the November segment were applied in this period (31 Jan to 10 Feb). The simulated net AS volume transport was in the general direction of the wind (Fig. 4.21A and B) which is consistent with the simulation results for November. The northwesterly event (Event #4) generated a southerly net AS volume transport while the southeasterly event (Event #5) generated a northerly net AS transport. These simulation results are in agreement with the observations net AS volume transport (Fig. 4.21B).

The shifting of the net AS volume transport from southerly to northerly or northerly to southerly resulted in the progression of the warm 'tongue' in the northwest direction or the regression of the warm 'tongue' in the southeasterly direction respectively. The regression of the warm 'tongue' to the southeast and advance of

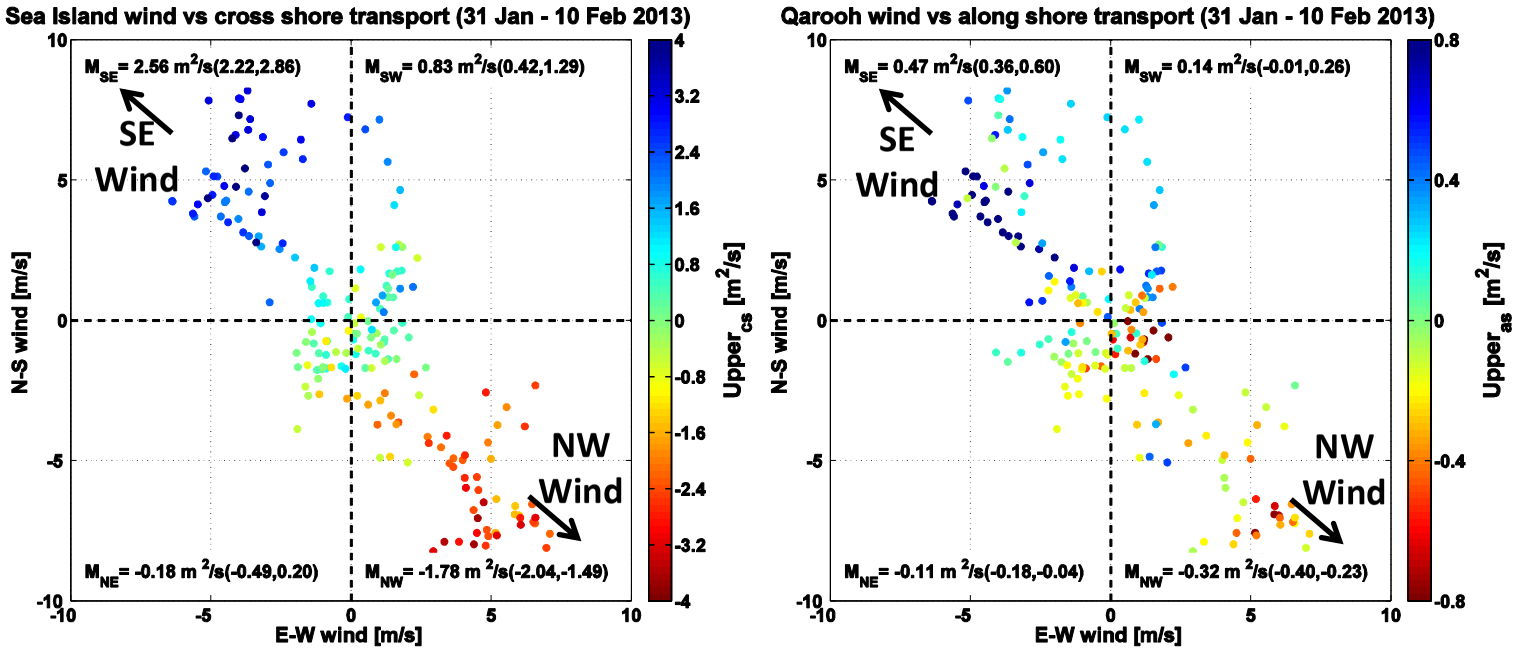

Figure 4.20: Same as Figure 4.12 but for February.

the cooler waters at the Gulf head toward Qarooh during Event #4 were captured well by the model with a low MBE of -0.01 ^{o}C (-0.01, 0.00) and RMSE 0.04 ^{o}C (0.03, 0.04) (Fig. 4.21D and E). However similar to the previous segment, the model over estimated the vertical mixing during the peak phase of Event #4 (Fig. 4.21F numbers 14 and 15). This resulted in a deeper ML depth of 13 m compared to the observations ML depth of 7 m. The mixing of the warmer surface waters with deeper cooler waters caused the surface waters to cool. As a result, the simulated ML waters were cooler than the observations by 0.2 ^{o}C.

Furthermore the model captured well the progression of the warm 'tongue' to the northwest and the northerly net AS transport generated by the southeasterly winds (Event #5) with a MBE of 0.02 ^{o}C (0.02, 0.03) and RMSE of 0.04 ^{o}C (0.03, 0.04). Overall the model simulations during both the events were in a good agreement with the observations' thermal structure as indicated by significant (p-values $<$0.05) correlations of 0.78 (0.78, 0.79) and a positive Nash-Sutcliffe values of 0.76 (0.75, 0.77). Similar to the November period, the non-event period simulations of the thermal structure were unsatisfactory with insignificant (p-values $>$0.05) weak correlations of -0.16 (-0.17, -0.14) and negative Nash-Sutcliffe values of -0.15 (-0.18, -0.12). It is suggested that during non-event periods, the simulated transport (AS and CS) were negligible due to the weak wind stress (Fig. 4.21B and C). Following this, the horizontal advection was suppressed, which was the dominate process in the thermodynamics.

4.4 Conclusion

The regional winds and topography led to a surface flow that was perpendicular to the Kuwaiti Coast. The CS flow near the coast mainly responded to the wind. The southeasterly winds led to an offshore surface volume transport at a rate up to 2.56

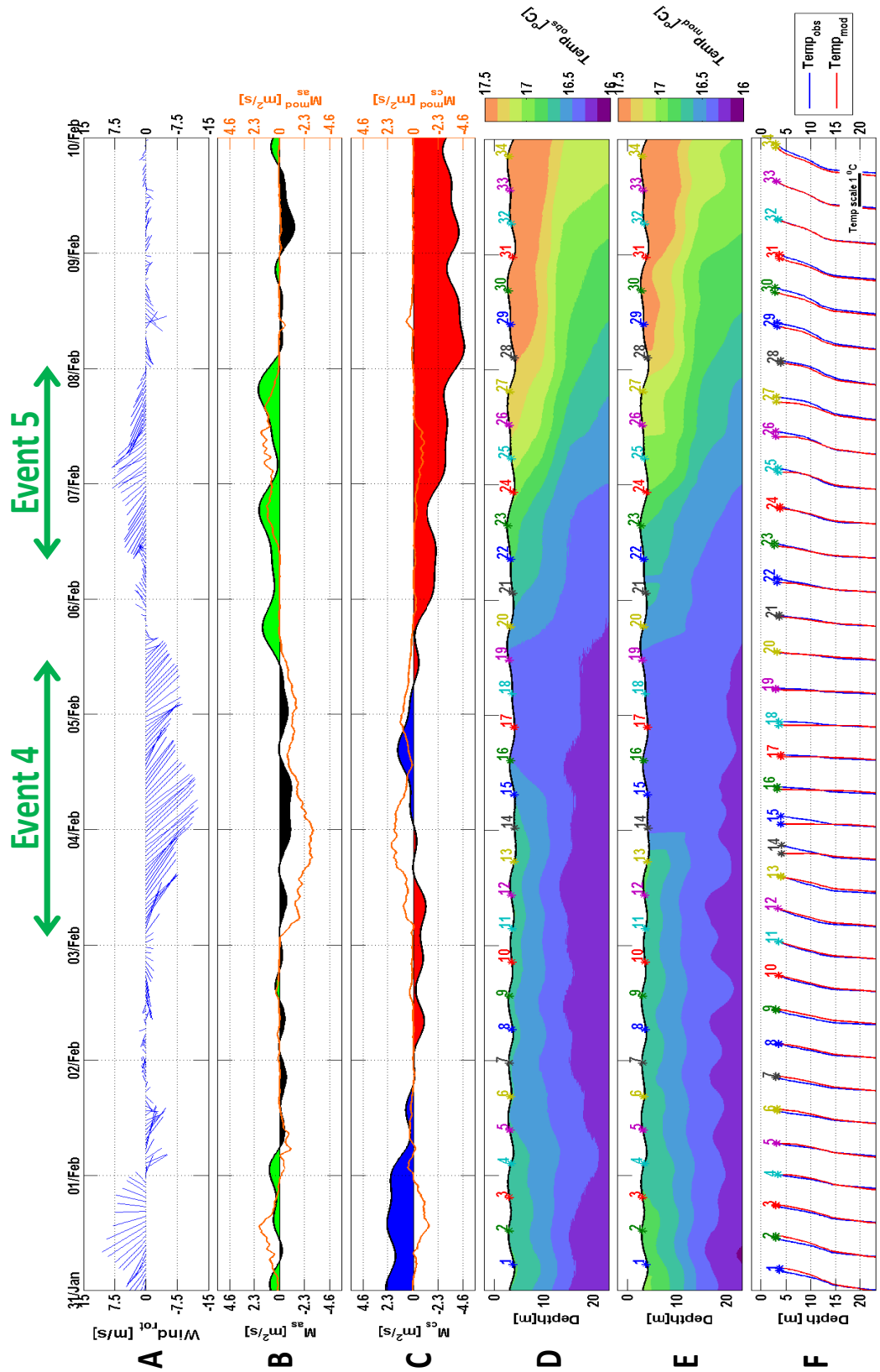

Figure 4.21: Same as Figure 4.13 but for February.

m^2/s and a return flow in the opposite direction in the lower layer. These conditions generated coastal upwelling causing relatively cooler surface water temperatures in the region near the coast. The northwesterly winds led to an onshore surface volume transport at a rate of 1.80 m^2/s and a return flow in the opposite direction in the lower layer. These conditions resulted in coastal downwelling causing relatively warmer surface water temperatures in the region near the coast. The coastal upwelling and downwelling did not extend to the Qarooh region that was located 44 km offshore. Unlike the near coast region, the AS flow at Qarooh responded to the wind. A southeasterly wind generated a northerly AS transport at a rate up to 0.88 m^2/s. These conditions caused the warm 'tongue' to advance northwest and resulted in warmer temperatures. A northwesterly wind generated a southerly AS transport at a rate of 0.37 m^2/s. This caused the warm 'tongue' to regress southeast and the cooler waters at the Gulf head to advance thus resulting in cooler water temperatures.

The comparison of measured and simulated thermal structure at the Qarooh region during the three wind events demonstrated good agreement. These results signify that the advectional processes can be described in 1D turbulence models once accurately addressing the advectional limitations of 1D models. The model produced net AS transports in the general direction of the wind, which captured the warm 'tongue' progression/regression well. However, during the non-event periods, simulations of the net AS and CS transports were unsatisfactory. The absence of momentum flux (wind stress) at the air-sea interface limited the horizontal advection, which was the dominant process for the regions thermodynamics. Furthermore, the model over estimated the ML depth during the strong wind events. This resulted in simulated water temperatures in the ML to be cooler than the observations and the water temperature below the ML to be warmer than the observations.

The results of the study encourage future observational and numerical studies

of the warm 'tongue' that extends from the southeast of Qarooh and upwelling and downwelling off the Kuwaiti Coast. The width and length of the upwelling region is unidentified. Furthermore, the physical processes that take place at the front separating the upwelling waters and Gulf waters is still unknown. Finally, the study focused on the winter period, further observations during the summer period are needed to assess seasonal variability, as well as extension of the results in other possible regions of upwelling in the Gulf.

Table 4.2: Averages and their 95% CI (in parenthesis) for the observed and simulated hydrographic conditions during three upwelling/downwelling favorable wind events.

			Hydrographic Observations		
Event no.	length [hrs]	wind speed [m/s]	net AS transport [m^2/s]	net CS transport [m^2/s]	temperature [^oC]
1	72	6.67 (6.38, 6.97)	1.88 (1.84, 1.91)	0.54 (0.49, 0.59)	26.09 (26.08, 26.09)
2	64	6.47 (6.02, 6.85)	-0.31 (-0.34, -0.27)	0.78 (0.75, 0.82)	25.82 (25.81, 25.83)
3	54	6.99 (6.22, 7.78)	1.79 (1.72, 1.86)	2.37 (2.29, 2.45)	25.28 (25.27, 25.30)
			Hydrographic numerical model simulations		
1			1.70 (1.68, 1.73)	-0.73 (-0.75, -0.71)	26.04 (26.03, 26.04)
2			-0.98 (-0.95, -1.01)	1.38 (1.35, 1.41)	25.73 (25.72, 25.74)
3			1.89 (1.86, 1.92)	-0.16 (-0.20, -0.13)	25.19 (25.18, 25.21)

5. CONCLUSION

In the three studies presented in Chapters 2 - 4 we have investigated Shamals and their influences on the regional meteorology and hydrodynamics in the Northern Arabian / Persian Gulf. The first study focused on the frequency of Shamals between 1973 to 2012 and examined their effects on meteorological parameters: wind speed, air temperature, humidity, visibility and barometric pressure. The second study investigated the BBL mixing processes during three Shamal events and compared the estimated turbulence parameters (Reynolds stresses, eddy diffusivities, TKE, and its dissipation rates) to two equation turbulence model (k-kl and k-ε) simulations. The third study examined the sea current structure and volume transport in response to the Kous and Shamal events using observational data collected over two periods (mid-January to mid-April 2013 and mid-October to mid-January 2014) in Kuwaiti waters. The results of the three studies are summarized in the following:

- Relating Shamal events to climate variability necessitates an operational definition of such events; however, we could not find a standard and agreed upon definition of a Shamal in the literature. Thus, we defined a Shamal event in the study as a WNW-N (287^0 $<$ direction $<$ 360^0) wind with an hourly average speed $\geq$ 9.85 m/s blowing at least 3 hours/day. Two consecutive Shamal days are required for a Shamal to be classified as a Shamal event. Based on this definition, and comparison to preShamal conditions, Shamal events were found to cause abrupt changes in meteorological parameters: an increase in wind speed of 2.7 m/s (0.4, 5.8), an increase in temperature during summer of 0.8 ^{0}C (0.4, 1.2); and a decrease of 1.5 ^{0}C (0.3, 2.8) during winter, a decrease in barometric pressure during summer of 0.6 mb (0.1, 1.5) and a increase of 7.8 mb (2.1,

14.6) during winter, a decrease in visibility of 1.7 km (1.1, 4.9), and reduction in humidity of 4.3 % (6.9, 25.0). A total of 421 Shamal events compromised of 1165 days occurred during the study period with 77% of Shamal days occurring in the summer season. The overall number of Shamal event days decreased by 46% between 1973 and 2012. However, further analysis suggests an increase of 1.63 Shamal days/year in the last 15 years of the study period.

- The comparison of the measured and simulated turbulence parameters (Reynolds stresses, eddy diffusivities, TKE, and its dissipation rates) during the three examined Shamal events demonstrated satisfactory agreement between the two. Mixing in the BBL was mainly controlled by two main forcings. The first forcing was the increase in mixing resulting from the current shear generated by tides. The second was by the Shamal induced convection. The highest averages of the estimated turbulence parameters from the observations during the three studied periods were TKE 9.33 x 10^4 m^2/s^2, TKE dissipation rate 2.48 x 10^{-5} m^2/s^3, Reynold stress 0.44 Pa, and vertical eddy diffusivity 5.47 x 10^{-2} m^2/s. The satisfactory agreement between the observed and simulated turbulence parameters has led us to suggest that tidal current shear and convection driven turbulence are reproduced by two equation turbulence models (k-kl and k-ε). This conclusion was further supported by the significant correlations, low MBE, low RMSE, and positive N_s values.

- The regional winds and topography led to a surface flow that was perpendicular to the Kuwaiti Coast. The CS flow near the coast mainly responded to the wind. The southeasterly winds led to an offshore surface volume transport at a rate up to 2.56 m^2/s and a return flow in the opposite direction in the lower layer. These conditions generated coastal upwelling causing relatively cooler

surface water temperatures in the region near the coast. The northwesterly winds led to an onshore surface volume transport at a rate of 1.84 m^2/s and a return flow in the opposite direction in the lower layer. These conditions resulted in coastal downwelling causing relatively warmer surface water temperatures in the region near the coast. The coastal upwelling and downwelling did not extend to the Qarooh region that was located 44 km offshore. Unlike the near coast region, the AS flow at Qarooh responded to the wind. A southeasterly wind generated a northerly AS transport at a rate up to 0.88 m^2/s. These conditions caused the warm 'tongue' to advance northwest and resulted in warmer temperatures. A northwesterly wind generated a southerly AS transport at a rate of 0.32 m^2/s. This caused the warm 'tongue' to regress southeast and the cooler waters at the Gulf head to advance thus resulting in cooler water temperatures.

REFERENCES

Al-dousari, A. L. I. M., & Al-awadhi, J. (2012). Dust fallout in northern Kuwait , major sources and characteristics. *Kuwait Journal of Science*, *39*, 171–187.

Ali, A. (1994). *Wind meteorology of the summer Shamal in the Arabian Gulf region* (Unpublished master's thesis). Boston University.

Almazroui, M., Islam, M. N., Jones, P., Athar, H., & Rahman, M. A. (2012). Recent climate change in the Arabian Peninsula: seasonal rainfall and temperature climatology of Saudi Arabia for 1979-2009. *Atmospheric Research*, *111*, 29–45.

Almazroui, M., Nazrul Islam, M., Athar, H., Jones, P. D., & Rahman, M. A. (2012). Recent climate change in the Arabian Peninsula: annual rainfall and temperature analysis of Saudi Arabia for 1978-2009. *International Journal of Climatology*, *32*(6), 953–966.

Anis, A., & Moum, J. (1994). Prescriptions for heat flux and entrainment rates in the upper ocean during convection. *Journal of Physical Oceanography*, *24*(10), 2142–2155.

Anis, A., & Singhal, G. (2006). Mixing in the surface boundary layer of a tropical freshwater reservoir. *Journal of Marine Systems*, *63*(3-4), 225–243.

Arpe, K., & Leroy, S. A. G. (2009). Atlantic hurricanes testing impacts of local SSTs, ENSO, stratospheric QBO implications for global warming. *Quaternary International*, *195*(12), 4–14.

Arun, C., Swadhin, B., Mujumdar, M., Ohba, R., & Yamagata, T. (2005). Diagnosis of tropospheric moisture over Saudi Arabia and influences of IOD and ENSO. *Monthly Weather Review*, 598–617.

Attrill, M. J. (2009). Sea temperature change as an indicator of global change. In T. M. Letcher (Ed.), *Climate change* (pp. 337–347). Amsterdam: Elsevier.

Bakhoday Paskyabi, M., Fer, I., & Jenkins, A. D. (2012). Surface gravity wave effects on the upper ocean boundary layer: modification of a one-dimensional vertical mixing model. *Continental Shelf Research*, *38*, 63–78.

Barlow, M., Wheeler, M., Lyon, B., & Cullen, H. (2005). Modulation of daily precipitation over Southwest Asia by the Madden Julian Oscillation. *Monthly Weather Review*, *133*(12), 3579–3594.

Barnston, A., & Livezey, R. (1987). Classification, seasonality and persistence of low-frequency atmospheric circulation patterns. *Monthly Weather Review*, *115*(6), 1083–1126.

Bartlett, K. S. (2004). *Dust storm forecasting for Al Udeid Ab, Qatar: an empirical analysis* (Unpublished master's thesis). Air University.

Benedetti, A., Morcrette, J.-J., Boucher, O., Dethof, A., Engelen, R. J., Fisher, M., ... Suttie, M. (2009). Aerosol analysis and forecast in the European Centre for Medium-Range Weather Forecasts Integrated Forecast System: 2. Data assimilation. *Journal of Geophysical Research*, *114*, 1–18.

Blanton, J., Amft, J., Oey, L., & Lee, T. (1989). Advection of momentum and buoyancy in a coastal frontal zone. *Journal of Physical Oceanography*, *19*, 98–115.

Blasing, T. (2013). *Recent greenhouse gas concentrations.* Retrieved 2013-03-03, from `http://cdiac.ornl.gov/pns/current_ghg.html`

Boehm, A. B., Sanders, B. F., & Winant, C. D. (2002). Cross-shelf transport at Huntington beach. Implications for the fate of sewage discharged through an offshore ocean outfall. *Environmental Science & Technology*, *36*(9), 1899–1906.

Bolding, K., Burchard, H., Pohlmann, T., & Stips, A. (2002). Turbulent mixing in

the Northern North Sea: a numerical model study. *Continental Shelf Research*, *22*(18-19), 2707–2724.

Booth, J. A. T., McPhee-Shaw, E. E., Chua, P., Kingsley, E., Denny, M., Phillips, R., ... Gilly, W. F. (2012). Natural intrusions of hypoxic, low pH water into nearshore marine environments on the California coast. *Continental Shelf Research*, *45*, 108–115.

Boussinesq, J. (1903). Sur un mode simple d'écoulement des nappes d'eau d'infiltration à lit horizontal, avec rebord vertical tout autour lorsqu'une partie de ce rebord est enlevée depuis la surface jusqu'au fond. *C. R. Acad. Sci*, *137*, 5–11.

Brewer, P. G., & Dyrssen, D. (1985). Chemical oceanography of the Persian Gulf. *Progress in Oceanography*, *14*(5529), 41–55.

Brunke, M., Fairall, C., Zeng, X., Eymard, L., & Curry, J. (2003). Which bulk aerodynamic algorithms are least problematic in computing ocean surface turbulent fluxes? *Journal of Climate*, *16*(3), 619–635.

Burchard, H. (1999). Recalculation of surface slopes as forcing for numerical water column models of tidal flow. *Applied Mathematical Modelling*, *23*(10), 737–755.

Burchard, H. (2002). *Applied turbulence modelling in marine waters*. New York: Springer Berlin / Heidelberg.

Burchard, H., & Bolding, K. (2001). Comparative analysis of four second-moment turbulence closure models for the oceanic mixed layer. *Journal of Physical Oceanography*, *31*(8), 1943–1968.

Burchard, H., Bolding, K., Kühn, W., Meister, A., Neumann, T., & Umlauf, L. (2006). Description of a flexible and extendable physicalbiogeochemical model system for the water column. *Journal of Marine Systems*, *61*(3-4), 180–211.

Burchard, H., Craig, P. D., Gemmrich, J. R., van Haren, H., Mathieu, P.-P., Meier, H. M., ... Wijesekera, H. W. (2008). Observational and numerical modeling methods for quantifying coastal ocean turbulence and mixing. *Progress in Oceanography*, *76*(4), 399–442.

Burchard, H., Petersen, O., & Rippeth, T. P. (1998). Comparing the performance of the Mellor-Yamada the two-equation turbulence models and the Kolmogorov. *Journal of Geophysical Research*, *103*, 10,543–10,554.

Canuto, V., Howard, A., Cheng, Y., & Dubovikov, M. (2001). Ocean turbulence. Part I: one-point closure model-momentum and heat vertical diffusivities. *Journal of Physical Oceanography*, *31*, 1413–1426.

Chang, C., Harr, P., & Ju, J. (2000). Possible roles of Atlantic Circulations on the weakening Indian Monsoon rainfall ENSO relationship. *Journal of Climate*, *14*, 2376–2380.

Chao, S.-Y., Kao, T. W., & Al-Hajri, K. R. (1992). A numerical investigation of circulation in the Arabian Gulf. *Journal of Geophysical Research*, *97*(C7), 11219–11236.

Chin, M., Ginoux, P., Kinne, S., Torres, O., Holben, B., Duncan, B., ... Nakajima, T. (2002). Tropospheric aerosol optical thickness from the GOCART model and comparisons with satellite and sun photometer measurements. *Journal of the Atmospheric Sciences*, *59*, 461–483.

Clements, T., Stone, R., Mann, J., & Eymann, J. (1963). *A study of windborne sand and dust in desert areas* (Tech. Rep.). Univesrity of South California.

Cohen, J., & Barlow, M. (2005). The NAO, the AO, and global warming: how closely related? *Journal of Climate*, *18*(21), 4498–4513.

Crook, J. (2009). *Climate analysis and long range forecasting of dust stroms in Iraq* (Unpublished master's thesis). Naval Postgraduate School.

Cullen, H., & Demenocal, P. (2000). North Atlantic influence on Tigris Euphrates. *International Journal of Climatology*, *863*, 853–863.

Dai, A. (2006). Recent climatology, variability, and trends in global surface humidity. *Journal of Climate*, *19*(15), 3589–3606.

Dash, P., Ignatov, A., Martin, M., Donlon, C., Brasnett, B., Reynolds, R. W., ... Poulter, D. (2012). Group for High Resolution Sea Surface Temperature (GHRSST) analysis fields inter-comparisonsPart 2: Near real time web-based level 4 SST Quality Monitor (L4-SQUAM). *Deep Sea Research Part II: Topical Studies in Oceanography*, *77-80*, 31–43.

Davidson, P. (2004). *Turbulence, an introduction for scientists and engineers*. New York: Oxford University Press.

Dewey, R., Crawford, W., Gargett, A., & Oakey, N. (1986). A microstructure instrument for profiling oceanic turbulence in coastal bottom boundary layers. *Journal of Atmospheric & Oceanic Technology*, *4*, 288–297.

Donat, M. G., Peterson, T. C., Brunet, M., King, a. D., Almazroui, M., Kolli, R. K., ... Al Shekaili, M. N. (2014). Changes in extreme temperature and precipitation in the Arab region: long-term trends and variability related to ENSO and NAO. *International Journal of Climatology*, *34*(3), 581–592.

Doron, P., Bertuccioli, L., Katz, J., & Osborn, T. (2001). Turbulence characteristics and dissipation estimates in the coastal ocean bottom boundary layer from PIV data. *Journal of Physical Oceanography*, *31*, 2108–2134.

Dorrestein, R. (1979). On the Vertical Buoyancy Flux below the Sea Surface as Induced by Atmospheric Factors. *Journal of Physical Oceanography*, *9*(1), 229–231.

Drennan, W. M. (2003). On the wave age dependence of wind stress over pure wind seas. *Journal of Geophysical Research*, *108*(C3), 8062.

Eager, R. E., Raman, S., Wootten, A., Westphal, D. L., Reid, J. S., & Al Mandoos, A. (2008). A climatological study of the sea and land breezes in the Arabian Gulf region. *Journal of Geophysical Research*, *113*(D15), D15106.

Efron, B., & Tibshirani, R. (1986). Bootstrap methods for standard errors, confidence intervals, and other measures of statistical accuracy. *Statistical Science*, *1*(1), 54–75.

El Kenawy, A., López-Moreno, J. I., & Vicente-Serrano, S. M. (2012). Trend and variability of surface air temperature in northeastern Spain (1920-2006): Linkage to atmospheric circulation. *Atmospheric Research*, *106*, 159–180.

Elsanabary, M. H., & Gan, T. Y. (2013). Wavelet analysis of seasonal rainfall variability of the upper Blue Nile Basin, its teleconnection to global sea surface temperature, and its forecasting by an artificial neural network. *Monthly Weather Review*, *142*(5), 1771.

Emery, K. O. (1956). Sediments and water of Persian Gulf. *AAPG Bulletin*, *40*(10), 2354–2383.

EPA. (2012). *Climate change.* Retrieved 2013-03-03, from `http://www.epa.gov/climatechange/`

Fairall, C. W., Bradley, E. F., Hare, J. E., Grachev, A. A., & Edson, J. B. (2003). Bulk parameterization of airsea fluxes: Updates and verification for the COARE algorithm. *Journal of Climate*, *16*(4), 571–591.

Fairall, C. W., Bradley, E. F., Rogers, D. P., Edson, J. B., & Young, G. S. (1996). Bulk parameterization of air-sea fluxes for tropical ocean- global atmosphere coupled-ocean atmosphere response experiment difference relative analysis. , *101*, 3747–3764.

Fofonoff, N., & Millard, R. (1983). *Algorithms for computation of fundamental properties of seawater* (Tech. Rep.). UNESCO.

Galperin, B., Sukoriansky, S., & Anderson, P. S. (2007). On the critical Richardson number in stably stratified turbulence. *Atmospheric Science Letter*, *8*, 65–69.

García Berdeal, I. (2002). Influence of wind stress and ambient flow on a high discharge river plume. *Journal of Geophysical Research*, *107*(C9), 3130.

García-Reyes, M., & Largier, J. L. (2012). Seasonality of coastal upwelling off central and northern California: New insights, including temporal and spatial variability. *Journal of Geophysical Research*, *117*(C3), C03028.

Giannakopoulou, E. M., & Toumi, R. (2012). The Persian Gulf summertime low-level jet over sloping terrain. *Quarterly Journal of the Royal Meteorological Society*, *138*(662), 145–157.

Glibert, P. M., Landsberg, J. H., Evans, J. J., Al-Sarawi, M. a., Faraj, M., Al-Jarallah, M. a., ... Shoemaker, C. (2002). A fish kill of massive proportion in Kuwait Bay, Arabian Gulf, 2001: the roles of bacterial disease, harmful algae, and eutrophication. *Harmful Algae*, *1*(2), 215–231.

Gloor, M., Wiiest, A., & Imboden, D. M. (2000). Dynamics of mixed bottom boundary layers and its implications for diapycnal transport in a stratified, natural water basin. , *105*(1999), 8629–8646.

Goes, J. I., Thoppil, P. G., Gomes, H. D. R., & Fasullo, J. T. (2005). Warming of the Eurasian landmass is making the Arabian Sea more productive. *Science*, *308*(5721), 545–7.

Gordon, L., Lohrmann, A., & Jonas, T. (1999). *Internal Wave Generation in Lakes with Very Slow Flow (N4000-707)* (Tech. Rep.). Nortek.

Goudie, A. S. (2009). Dust storms: recent developments. *Journal of environmental management*, *90*(1), 89–94.

Grimes, C., & Kingsfrod, M. (1996). How do riverine plumes of different sizes influence fish larvae : do they enhance recruitment ? *Marine Freshwater*

Resources, *47*, 191–208.

Gupta, H. V., & Kling, H. (2011). On typical range, sensitivity, and normalization of Mean Squared Error and Nash-Sutcliffe Efficiency type metrics. *Water Resources Research*, *47*(W10601), 1–3.

Hansen, J., Lacis, A., Rind, D., Russell, G., Stone, P., Fung, I., ... Lerner, J. (1984). Climate sensitivity: analysis of feedback mechanisms. *Climate Processes and Climate Sensitivity*, *5*(29), 130–163.

Hartmann, M., Lange, H., Seibold, E., & Walger, E. (1971). Oberflachensedimente in Persichen Golf and Golf von Oman, I, Geologisch-hydrologischer Rahmen und erste sedimentologische Ergebnisse. *Meteor Forschungsergeb*, *4*, 1–76.

Hickey, B., Geier, S., Kachel, N., & MacFadyen, A. (2005). A bi-directional river plume: the Columbia in summer. *Continental Shelf Research*, *25*(14), 1631–1656.

Hickey, B. M., Pietrafesa, L. J., Jay, D. A., & Boicourt, W. C. (1998). The Columbia river plume study : subtidal variability in the velocity and salinity fields. *Journal of Geophysical Research*, *103*(C5), 339–368.

Hollingsworth, a., Engelen, R. J., Benedetti, A., Dethof, A., Flemming, J., Kaiser, J. W., ... Schultz, M. G. (2008). Toward a monitoring and forecasting system for atmospheric composition: the GEMS project. *Bulletin of the American Meteorological Society*, *89*(8), 1147–1164.

Huber, P. J. (1964). Robust estimation of a location parameter. *Annals of Mathematical Statistics*, *35*(1), 73–101.

Huber, P. J., & Ronchetti, E. M. (2009). *Generalities, in robust statistics* (2nd ed.). John Wiley & Sons, Inc.

Hurrell, J. (1995). Decadal trends in the North Atlantic Oscilation: regional temperatures and precipitation. *Science*, *269*(5224), 676–679.

Huyer, A. (1983). Coastal upwelling in the California current system. *Progress in Oceanography*, *12*(3), 259–284.

IPCC. (2014). *Climate change 2014: impacts, adaptation, and vulnerability. Part A: global and sectoral aspects. Contribution of working group II to the fifth assessment report of the intergovernmental panel on climate change* (Tech. Rep. No. October 2013). New York: UNEP.

Iraq Foundation. (2003). Physical characteristics Mesopotamian marshlands of Southern Iraq. (January), 1–45.

Janabi, H. (2010). *Water security in Iraq* (Tech. Rep.). UN Food and Agriculture Organization.

Jia, B., Xie, Z., Dai, A., Shi, C., & Chen, F. (2013). Evaluation of satellite and reanalysis products of downward surface solar radiation over East Asia: Spatial and seasonal variations. *Journal of Geophysical Research: Atmospheres*, *118*(9), 3431–3446.

Jin, F.-F. (2003). Strong El Niño events and nonlinear dynamical heating. *Geophysical Research Letters*, *30*(3), 1120.

Johns, W. E., Jacobs, G. A., Kindle, J. C., Murray, S. P., & Carron, M. (1999). *Arabian marginal seas and gulfs* (Tech. Rep.). University of Miami.

Jones, P., Wigley, T., & Wright, P. (1986). Global temperature variations between 1861 and 1984. *Nature*, *322*, 430–434.

Jones, P. D. (2003). Global change: surface temperature trends. In E.-i.-C. J. R. Holton (Ed.), *Encyclopedia of atmospheric sciences* (pp. 898–910). Oxford: Academic Press.

Joseph, P., Eischeid, J., & Pyle, R. (1994). Interannual variability of the onset of the Indian summer monsoon and its association with atmospheric features, El Niño, and sea surface temperature anomalies. *Journal of Climate*, *7*(81),

81–105.

Kanamitsu, M., Ebisuzaki, W., Woollen, J., Yang, S.-K., Hnilo, J. J., Fiorino, M., & Potter, G. L. (2002). NCEPDOE AMIP-II reanalysis (R-2). *Bulletin of the American Meteorological Society*, *83*(11), 1631–1643.

Kantha, L. H., & Clayson, C. A. (1994). An improved mixed layer model for geophysical applications. *Journal of Geophysical Research*, *99*(25), 235–266.

Kimn, S., Friedrichs, C., Maa, J., & Wright, L. (2000). Estimating bottom stress in tidal boundary layer from Acoustic Doppler Velocimeter data. *journal of hydraulic Engineering*, *126*(6), 399–406.

Klein, P., & Coste, B. (1984). Effects of wind-stress variability on nutrient transport into the mixed layer. *Deep Sea Research Part A. Oceanographic Research Papers*, *31*(1), 21–37.

Koch, M., & El-Baz, F. (1998). Identifying the effects of the Gulf War on the geomorphic features of Kuwait by remote sensing and GIS. *Photogrammetric Engineering & Remote Sensing*, *64*(7), 739–747.

Kolmogorov, A. (1941). Dissipation of energy in the locally isotropic turbulence. *Proceedings: Mathematical and Physical Sciences*, *434*(1890), 15–17.

Krause, P., Boyle, P., & Base, F. (2005). Comparison of different efficiency criteria for hydrological model assessment. *Advances in Geosciences*, *5*, 89–97.

Kumar, K. N., & Ouarda, T. B. M. J. (2014). Precipitation variability over UAE and global SST teleconnections. *Journal of Geophysical Research: Atmospheres*, *119*, 1–10.

Kundu, P., & Cohen, I. (2008). *Fluid mechanics* (4th ed.). San Diego: Academic Press.

Kutiel, H., & Furman, H. (2003). Dust storms in the Middle East: sources of origin and their temporal characteristics. *Indoor and Built Environment*, *12*(6), 419–

426.

Launder, B., & Spalding, D. (1972). *Mathematical models of turbulence.* London: Academic Press.

Lee, C., Askari, F., Book, J., Carniel, S., Cushman-Roisin, B., Dorman, C., & Doyle, J. (2005). Northern Adriatic response to a wintertime Bora wind event. *Eos, Transactions American Geophysical Union*, *86*(16), 157–165.

Leichter, J. J., Stewart, H. L., & Miller, S. L. (2003). Episodic nutrient transport to Florida coral reefs. *Limnology and Oceanography*, *48*(4), 1394–1407.

Leroy, S. A. (2006). From natural hazard to environmental catastrophe: Past and present. *Quaternary International*, *158*(1), 4–12.

Liu, W.-C., Chen, W.-B., Cheng, R. T., & Hsu, M.-H. (2008). Modelling the impact of wind stress and river discharge on Danshuei River plume. *Applied Mathematical Modelling*, *32*(7), 1255–1280.

Lohrmann, A., Hackett, B., & Roed, L. (1990). High resolution measurments of turbulence, velocity and stress using a pulse-to-pulse coherent sonar. *Journal of Atmospheric and Oceanic Technology*, *7*, 19–37.

Lumley, J., & Terray, E. (1983). Kinematics of turbulence convected by a random wave field. *Journal of Physical Oceanography*, *13*, 2000–2007.

MacIntyre, S. (1993). Vertical mixing in a shallow, eutrophic lake: possible consequences for the light climate of phytoplankton. *Limnology and Oceanography*, *38*(4), 798–817.

Martin, M., Dash, P., Ignatov, A., Banzon, V., Beggs, H., Brasnett, B., ... Roberts-Jones, J. (2012). Group for High Resolution Sea Surface temperature (GHRSST) analysis fields inter-comparisons. Part 1: A GHRSST multi-product ensemble (GMPE). *Deep Sea Research Part II: Topical Studies in Oceanography*, *77-80*, 21–30.

Meehl, G., & Loon, H. V. (1979). The seesaw in winter temperatures between Greenland and Northern Europe. Part III: teleconnections with lower latitudes. *Monthly Weather Review*, *107*(9), 1095–1106.

Mellor, G., & Yamada, T. (1974). A Hierarchy of Turbulence Closure Models for Planetary Boundary Layers. *Journal of the Atmospheric Sciences*, *31*, 1791–1806.

Mellor, G., & Yamada, T. (1982). Development of a turbulence closure model for Geophysical Fluids. *Reviews of Geophysics*, *20*(4), 851–875.

Miles, J. W. (1961). On the stability of heterogeneous shear flows. *Journal of Fluid Mechanics*, *10*, 496–508.

Mirza, M. M. Q. (2002). Global warming and changes in the probability of occurrence of floods in Bangladesh and implications. *Global Environmental Change*, *12*(2), 127–138.

Morcrette, J.-J., Beljaars, A., Benedetti, A., Jones, L., & Boucher, O. (2008). Sea-salt and dust aerosols in the ECMWF IFS model. *Geophysical Research Letters*, *35*(24), 1–5.

Moum, J. N., Klymak, J. M., Nash, J. D., Perlin, A., & Smyth, W. D. (2007). Energy transport by nonlinear internal waves. *Journal of Physical Oceanography*, *37*(7), 1968–1988.

Naidu, C., Satyanarayana, G., Durgalakshmi, K., Malleswara Rao, L., Jeevana Mounika, G., & Raju, a. D. (2012). Changes in the frequencies of north-east monsoon rainy days in the global warming. *Global and Planetary Change*, *92-93*, 40–47.

NASA. (2013). *Earth Science Data and Information System.* Retrieved from `https://lance-modis.eosdis.nasa.gov/imagery/subsets/?area=af`

Nash, J., & Sutcliffe, J. (1970). River flow forecasting through conceptual models

part I A discussion of principles. *Journal of Hydrology*, *10*(3), 282–290.

Nasrallah, H., & Balling, R. (1995). Impact of desertification on temperature trends in the Middle East. *Environmental Monitoring and Assessment*, *37*(1-3), 265–271.

Nasrallah, H. A., Nieplova, E., & Ramadan, E. (2004). Warm season extreme temperature events in Kuwait. *Journal of Arid Environments*, *56*(2), 357–371.

Nezlin, N. P., Polikarpov, I. G., Al-Yamani, F. Y., Subba Rao, D. V., & Ignatov, A. M. (2010). Satellite monitoring of climatic factors regulating phytoplankton variability in the Arabian (Persian) Gulf. *Journal of Marine Systems*, *82*(1-2), 47–60.

Oakey, N. (1985). Statistics of mixing parameters in the upper ocean during jasin phase 2. , *15*, 1662–1675.

Osborn, T. (1980). Estimates of the local rate of vertical diffusion from dissipation measurements. *Journal of Physical Oceanography*, *10*, 83–89.

Partow, H. (2001). *The Mesopotamian marshlands : demise of an ecosystem* (Tech. Rep.). United Nations Environment Programme.

Pauly, D., & Christensen, V. (1995). Primary production required to sustain global fisheries. *Nature*, *374*, 255–257.

Pavlidis, T., & Horowitz, S. (1974). Segmentation of plane curves. *IEEE Transactions on Computers*, *c-23*(8), 860–870.

Pawlowicz, R., Beardsley, B., & Lentz, S. (2002). Classical tidal harmonic analysis including error estimates in MATLAB using T_TIDE. *Computers & Geosciences*, *28*(8), 929–937.

Perrone, T. (1979). *Winter Shamal in the Persian Gulf, Technical Report 79-06* (Tech. Rep.). Montery: Naval Environmental Prediction Research Facility.

Philandras, C., Nastos, P., Kapsomenakis, I., & Repapis, C. (2013). Climatology of upper air temperature in the Eastern Mediterranean region. *Atmospheric Research*.

Pinker, R. T., Bentamy, A., Katsaros, K. B., Ma, Y., & Li, C. (2014). Estimates of net heat fluxes over the Atlantic Ocean. *Journal of Geophysical Research: Oceans*, *119*(1), 410–427.

Pope, S. (2000). *Turbulent flows*. Cambridge: Cambridge University Press.

Preining, O. (1992). Global warming: greenhouse gases versus aerosols. *Science of The Total Environment*, *126*(12), 199–204.

Press, W., Teukolsky, S., Vetterling, W., & Flannery, B. (2007). *Numerical recipes: the art of scientific computing* (3rd ed.). Cambridge: Cambridge University Press.

Privett, D. (1959). Monthly charts of evaporation from the N . Indian Ocean (including the Red Sea and the Persian Gulf). *Quarterly Journal of the Royal Meteorological Society*, *85*(366), 424–428.

Rao, P. G., Al-Sulaiti, M., & Al-Mulla, A. H. (2001). Winter shamals in Qatar, Arabian Gulf. *Weather*, *56*(12), 444–451.

Rao, P. G., Al-Sulaiti, M. H., & Al-Mulla, A. H. (2003). Summer shamals over the Arabian Gulf. *Weather*, *58*, 471–478.

Reddy, M. S. (2005). Estimates of global multicomponent aerosol optical depth and direct radiative perturbation in the Laboratoire de Météorologie Dynamique general circulation model. *Journal of Geophysical Research*, *110*, D10S16.

Reynolds, O. (1895). On the dynamical theory of incompressible viscous fluids and the determination of the criterion. *Philosophical Transactions of the Royal Society of London*, *186*, 123–164.

Reynolds, R. M. (1993). Physical oceanography of the Persian Gulf , Strait of

Hormuz , and the Gulf of Oman results from the Mt . Mitchell expedition. *Marine Pollution Bulletin*, *27*, 35–59.

Rice, W. (1988). Analyzing tables of statistical tests. *Evolution*, *43*(1), 223–225.

Roberts, J., & Roberts, T. D. (1978). Use of the Butterworth low-pass filter for oceanographic data. *Journal of Geophysical Research*, *83*(8), 5510–5514.

Rodi, W. (1987). Examples of calculation methods for flow and mixing in stratified fluids. *Journal of Geophysical Research*, *92*(6), 5305–5328.

Rusello, P. (2009). *A practical primer for pulse coherent instruments (TN-027)* (Tech. Rep.). Nortek.

Saeed, T. M., Al-Dashti, H., & Spyrou, C. (2014). Aerosol's optical and physical characteristics and direct radiative forcing during a shamal dust storm, a case study. *Atmospheric Chemistry and Physics*, *14*(7), 3751–3769.

Saji, N. H., Goswami, B. N., Vinayachandran, P. N., & Yamagata, T. (1999). A dipole mode in the tropical Indian Ocean. *Nature*, *401*(6751), 360–3.

Saji, N. H., & Yamagata, T. (2003). Possible impacts of Indian Ocean Dipole mode events on global climate. *Climate Research*, *25*, 151–169.

Schneider, N., & Muller, P. (1990). The meridional and seasonal structures of the mixed-layer depth and its diurnal amplitude observed during the Hawaii-to-Tahiti shuttle experiment. *Journal of Physical Oceanography*, *20*(9), 1395–1404.

Schott, F. A., Visbeck, M., Desaubies, Y., Send, U., Fishcher, J., & Stramma, L. (1996). Observations of deep convection in the Gulf of Lions, Northern Mediterranean, during the winter of 1991/92. *Journal of Physical Oceanography*, *26*, 505–524.

Shakula, J., & Paolino, D. (1983). The southern oscillation and long-range forecasting of the summer monsoon rainfall over India. *Monthly Weather Review*, *111*,

1830–1837.

Simpson, J. H., Burchard, H., Fisher, N. R., & Rippeth, T. P. (2002). The semi-diurnal cycle of dissipation in a ROFI: model-measurement comparisons. *Continental Shelf Research*, *22*(11-13), 1615–1628.

Soman, K., & Slingo, J. (1997). Sensitivity of the Asian summer monsoon to aspects of sea-surface-temperature anomalies in the tropical Pacific Ocean. *Quarterly Journal of the Royal Meteorological Society*, *123*, 309–336.

Sprintall, J., & Roemmich, D. (1999). Characterizing the structure of the surface layer in the. *Journal of Geophysical Research*, *104*, 23,91–23,311.

Stapleton, K. R., & Huntley, D. A. (1995). Seabed stress determinations using the inertial dissipation method and the turbulent kinetic energy method. *Earth Surface Processes aand Landforms*, *20*, 807–815.

Stips, A., Burchard, H., Bolding, K., & Eifler, W. (2002). Modelling of convective turbulence with a two-equation k-ϵ turbulence closure scheme. *Ocean Dynamics*, *52*(4), 153–168.

Sutherland, G., Reverdin, G., Marié, L., & Ward, B. (2014). Mixed and mixing layer depths in the ocean surface boundary. *Geophysical Research Lettershysical re*, *41*, 1–8.

Swift, S., & Bower, A. (2003). Formation and circulation of dense water in the Persian/Arabian Gulf. *Journal of Geophysical Research*, *108*(C1), 3004.

Thomas, A., & Weatherbee, R. (2006). Satellite-measured temporal variability of the Columbia River plume. *Remote Sensing of Environment*, *100*(2), 167–178.

Thomson, R., & Fine, I. (2003). Estimating mixed layer depth from oceanic profile data. *Journal of Atmospheric and Oceanic Technology*, *20*, 319–329.

Thoppil, P. G., & Hogan, P. J. (2010). Persian Gulf response to a wintertime shamal wind event. *Deep Sea Research Part I: Oceanographic Research Papers*, *57*(8),

946–955.

Thorpe, S. (2005). *The turbulent ocean.* Cambridge: Cambridge University Press.

Torrence, C., & Webster, P. (1999). Interdecadal changes in the ENSO monsoon system. *Journal of Climate*, *12*, 2679–2690.

Trowbridge, J. (1991). Asymmetric behavior of an oceanic boundary layer above sloping bottom. *Journal of Physical Oceanography*, *21*, 1171–1185.

Trowbridge, J., & Elgar, S. (2001). Turbulence measurements in the surf zone. *Journal of Physical Oceanography*, *31*, 2403–2417.

Tsagareli, K. N., Babanin, a. V., Walker, D. J., & Young, I. R. (2010). Numerical investigation of spectral evolution of wind waves. Part I: wind-input source function. *Journal of Physical Oceanography*, *40*(4), 656–666.

UCAR/COMET. (2010). *Forecasting dust storms v2.* Retrieved from `http://www.meted.ucar.edu/mesoprim/dust/`

Ullman, D., & Codiga, D. (2004). Seasonal variation of a coastal jet in the Long Island Sound outflow region based on HF radar and Doppler current observations. *Journal of Geophysical Research*, *109*(C7), C07S06.

UNEP. (2013). *Forecasting and early warning of dust storms.* Retrieved from `http://www.unep.org/geas/`

van Vliet, M. T., Franssen, W. H., Yearsley, J. R., Ludwig, F., Haddeland, I., Lettenmaier, D. P., & Kabat, P. (2013). Global river discharge and water temperature under climate change. *Global Environmental Change*.

Vishkaee, F., Flamant, C., Cuesta, J., Oolman, L., Flamant, P., & Khalesifard, H. R. (2012). Dust transport over Iraq and northwest Iran associated with winter Shamal: A case study. *Journal of Geophysical Research*, *117*(D3), D03201.

Walker, G., & Bliss, E. (1937). World weather, VI. *Memoirs Royal Meteorological Society*, *39*, 119–139.

Walters, K. (1990). *The Persian Gulf region, a climatological study* (Tech. Rep.). Asheville: United States Air Force.

Webster, P. (1995). The annual cycle and the predictability of the tropical coupled ocean-atmosphere system. *Meteorology and Atmospheric Physics*, *56*, 33–55.

Webster, P. J., Magafia, V. O., Palmer, T. N., Shukla, J., Tomas, R. A., Yanai, M., & Yasunari, T. (1998). Monsoons : Processes , predictability , and the prospects for prediction. *Journal of Geophysical Research*, *103*, 14451–14510.

Webster, P. J., Moore, A. M., Loschnigg, J. P., Leben, R. R., & Nin, E. (1999). Coupled ocean-atmosphere dynamics in the Indian Ocean during 1997-98. *Nature*, *401*(6751), 356–360.

Wilkerson, W. (1991). *Dust and sand forecasting in Iraq and adjoining countries* (Tech. Rep.). Air Weather Service, Scott Air Fore Base.

WMO. (2010). *A decade of climate extremes 2001-2010 (WMO-No. 1103)* (Tech. Rep. No. 1103).

Woodson, C. B., Washburn, L., Barth, J. a., Hoover, D. J., Kirincich, a. R., McManus, M. a., ... Tyburczy, J. (2009). Northern Monterey Bay upwelling shadow front: Observations of a coastally and surface-trapped buoyant plume. *Journal of Geophysical Research*, *114*(C12), C12013.

Yamazaki, H., & Osborn, T. (1993). Direct estimation of heat flux in a seasonal thermocline. *Journal of Physical Oceanography*, *23*, 503–516.

Yao, F., & Johns, W. E. (2010). A HYCOM modeling study of the Persian Gulf: 2. Formation and export of Persian Gulf Water. *Journal of Geophysical Research*, *115*(C11), C11018.

Yosef, Y., Saaroni, H., & Alpert, P. (2009). Trends in daily rainfall intensity over Israel 1950/1-2003/4. *The Open Atmospheric Science Journal*, *3*(1), 196–203.

Zaron, E. D., & Moum, J. N. (2009). A new look at Richardson number mixing

schemes for Equatorial ocean modeling. *Journal of Physical Oceanography*, *39*(10), 2652–2664.

Zhao, Q., He, K., Rahn, K. a., Ma, Y., Jia, Y., Yang, F., ... Wang, S. (2010). Dust storms come to Central and Southwestern China, too: implications from a major dust event in Chongqing. *Atmospheric Chemistry and Physics*, *10*(6), 2615–2630.